

Theory, design and measurement of near-optimal graphene reconfigurable and non-reciprocal devices at terahertz frequencies

THÈSE N° 7025 (2016)

PRÉSENTÉE LE 23 JUIN 2016

À LA FACULTÉ DES SCIENCES ET TECHNIQUES DE L'INGÉNIEUR
LABORATOIRE D'ÉLECTROMAGNÉTISME ET ANTENNES
PROGRAMME DOCTORAL EN GÉNIE ÉLECTRIQUE

ÉCOLE POLYTECHNIQUE FÉDÉRALE DE LAUSANNE

POUR L'OBTENTION DU GRADE DE DOCTEUR ÈS SCIENCES

PAR

Michele TAMAGNONE

acceptée sur proposition du jury:

Prof. J.-Ph. Thiran, président du jury
Prof. J. R. Mosig, Prof. M. A. Ionescu, directeurs de thèse
Prof. F. Koppens, rapporteur
Prof. G. Eleftheriades, rapporteur
Prof. H. Altug, rapporteuse



ÉCOLE POLYTECHNIQUE
FÉDÉRALE DE LAUSANNE

Suisse
2016

To the memory of my early supervisor
Prof. Julien Perruisseau-Carrier

To my parents

Acknowledgements

The results in this thesis would not have been possible without the help of a great number of people (colleagues, collaborators, friends and, of course, family).

First of all I would like to dedicate this thesis to the memory of my early thesis advisor, Prof. Julien Perruisseau-Carrier, who passed away during the third year of my Ph. D. He was a very supporting advisor and friend, always available to help me whenever I needed. I am very grateful to him for the things he taught me and for his unconditional support. Several of the ideas shown in this thesis are his own, and I tried to do my best to complete the work he started on graphene.

I wish to express my deepest gratitude to Prof. Juan R. Mosig, my early thesis co-advisor and late thesis advisor. He helped me during the most difficult moments of my stay in Switzerland, and he managed to save and continue the projects started by Julien. I would like to thank him for his patience, for his precious advices and for the support that he gave me in countless occasions.

A big thanks to Prof. Adrian M. Ionescu, my late thesis co-advisor, for the stimulating and useful discussions, for the access to Nanolab infrastructures and for his support.

Thanks to the other members of my Jury for the time dedicated to the evaluation of my thesis and for the very useful hints and advice that they gave me: Prof. Jean-Philippe Thiran, Prof. Hatice Altug, Prof. Frank Koppens, Prof. George V. Eleftheriades.

Thanks to all the previous members of the GRJPC group at EPFL. In particular thanks to Juan Sebastian Gomez-Diaz, Eduardo Carrasco Yépez and Daniel Rodrigo for the time and the research we shared and for teaching me a lot of tricks on numerical modeling and about academic research in general! Thanks to Pietro Romano for the great collaboration on PDMS and for his advice in many occasions! Thanks to Mohsen Yousefbeiki for the discussions about MIMO and multi-port antennas.

A huge thanks to all EPFL-LEMA current and past members! Special thanks to Santiago Capdevila for the incredible support (technical, moral, logistic,...) you provided me! It was a real pleasure to share with you countless and never-ending discussions on so many topics. You are the best working mate a Ph. D. student can hope to have. Thanks to Prof. Anja Skrivervik, for the discussions on novel RF switching technologies and more, for the help with

Acknowledgements

the thesis and the support. Thanks to Michael Mattes for the discussions and the help for the teaching part. Thanks to Desscan David for his help for IT, for the support and for the great discussions. Big thanks to Eulalia Durussel and Mercedes Quintas for their help in many, many occasions! Thanks to Hamed Hasani and to Joana Silva for our collaboration on terahertz reflectarrays and MIMO-lens antennas. Thanks to Baptiste Hornecker for the discussions and collaborations on complex analysis, graphene quantum capacitance, Green's functions and mathematics in general, and to Mina Bjelogrić for her help with translations in French. Thanks to Hussein Seyyed Esfahlani for the discussions about analogies among Electromagnetics and Acoustics. Big thanks to Tomislav Debogovic, Jean-François Zurcher, Maria Garcia Viguera, Marc Esquius Morote, Roberto Torres-Sanchez, Eden Sorolla, Ioannis Koufogiannis, Marco Letizia, Athanasios Polimeridis, Anton Ivanov, Pedro Robustillo, Apostolos Sounas, Nuno Pires, Mohsen Koohestani, Ioannis Iliopoulos, Rafal Glogowski, Nevena Saponjic, Erio Gandini, Gabriele Rosati, Benjamin Fuchs, Maddalena Violetti, Elena Diaz, Francesco Merli, Laleh Golestanirad, Frédéric Bongard, Marcos Alvarez, Esteban Menargues, Danelys Rodríguez, Jovanche Trajkovikj, Miroslav Veljovic, Lei Wang, for the great time we had together at LEMA, for the discussions and for your help!

Big thanks also to all the EPFL-Nanolab members! Thanks to Clara Moldovan, Wolfgang Vitale, Pakaj Sharma and Emanuele Casu for our great collaborations on graphene and vanadium dioxide and for your help in the clean room and for measurements. It was really a pleasure to work with you and spend so much time together. Thanks to Mariazel Maqueda López, Arnab Biswas, Maneesha Rupakula and Erick Garcia for the time together and the discussions!

Thanks to the EPFL-BIOS (prof. Hatice Altug) laboratory for the access to the infrastructures and for the help and discussions, in particular Odeta Limaj, Andreas Tittel and, again, Daniel Rodrigo.

Thanks to all the EPFL-CMi staff for the help, training and discussions for clean room processes. Thanks also to Pietro Maoddi, Mohsen Bramippanah, Valentin Flauraud and Xiaolong Wang for the discussions.

Thanks to all our collaborators for the supports and help. In particular Alexey Kuzmenko and Jean-Marie Poumirol from University of Geneva, Arya Fallahi from DESY, Prof. Tony Low from University of Minnesota, Prof. Andrea Ferrari and Antonio Lombardo from Cambridge University, Amaia Zurutuza and Alba Centeno from Graphenea, Prof. Frank Koppens and his Group at ICFO, Nicholas Emond from INRS, Québec.

Thanks also to Prof. Christophe Craeye, Prof. Ove Edfors, Prof. Federico Capasso, Dimitrios Sounas, Prof. Andrea Alu, Fabio Pavanello, Prof. Christophe Caloz, Prof. Javier Garcia de Abajo, Prof. Valerio Pruneri, Simone Zanotto, Clemens Nyffeler for the very useful discussions.

Last but not least I would like to thank my parents, for their moral and “logistical” support. Without their support this thesis and my Ph. D. would certainly have not been possible.

Lausanne, 8 June 2016

M. T.

Abstract

This thesis explores the applications of graphene for terahertz and far infrared optical components and antennas, with particular emphasis on tunable and non-reciprocal devices. Both terahertz technologies and graphene are emerging fields which hold many promises for a number of future applications, including ultra-broadband communications, sensing and security. A very important amount of research has been devoted to explore the potential applications of graphene and its advantages over existing technologies. Conversely, there is a clear set of applications that could benefit from the development of terahertz technologies, but there are several technical challenges in terms of very limited availability of materials and components to generate, manipulate and detect terahertz waves. The main idea of this work is to bring these two topics together to demonstrate that terahertz and mid infrared technologies can greatly benefit from the unique optical and electromagnetic properties of graphene.

The first original contribution of this thesis is an important theoretical upper bound for the performance of non-reciprocal and tunable devices, demonstrating that both these components can achieve a target performance at the expense of an unavoidable optical loss, which depends uniquely on the properties of graphene. If graphene with higher mobility is used, this unavoidable loss can be reduced; however, independently of the design geometry (waveguide devices, free space planar devices, ...), the loss will always appear. This theoretical limit is an important guideline for the design of graphene optical devices, as it can predict the best possible performances prior to any design effort or numerical simulation. It is also demonstrated that devices able to reach the upperbound are actually possible, and hence these devices (modulators, isolators among others) are optimal.

The thesis explores then a number of designs of graphene antennas for terahertz and mid infrared frequencies, where it is shown that gated graphene can be used to achieve frequency reconfiguration in resonant plasmonic antennas and beam steering in graphene based reflectarrays. Circuit models are provided as a simple way to understand the behavior of the device. Furthermore, an experimental technique able to measure the complex conductivity of graphene at infrared frequencies is demonstrated, providing a very useful evaluation of graphene quality at those frequencies.

The potential of graphene for non-reciprocal applications is then demonstrated experimentally, with the design, fabrication and measurement of the first terahertz isolator (operating between 1 THz and 10 THz). The isolator is a device which allows the unilateral propagation of light, and for that reason is often called “optical diode”. Our isolator uses graphene immersed in a magnetostatic field, and exhibits approximately 7 dB of loss in one direction and more

Abstract (English)

than 25 dB in the other. Thus, our device is shown to be quasi-optimum according to the theoretical bound and greatly improved performances are predicted for devices with next generation chemically deposited graphene.

Finally, the first tunable graphene reflectarray is presented, which is a metasurface able to steer in a desired direction an incoming beam of terahertz radiation. The device acts as a mirror, but, upon graphene gating, the direction of the reflected beam can be controlled and the beam itself can be modulated with complex modulation schemes. This device provides the first example of electronic beam steering of terahertz radiation.

Key words:

Graphene, Terahertz, Non-reciprocity, Modulators, Beam steering, Upper bounds, Optical isolator, Tunable antenna, Plasmonics, Infrared.

Sommario

Questa tesi esplora le applicazioni del grafene per componenti ed antenne operanti a frequenze terahertz e infrarosso, con un' enfasi particolare su dispositivi riconfigurabili e non-reciproci. Sia la tecnologia terahertz sia il grafene sono temi emergenti molto promettenti per molte applicazioni future, incluse telecomunicazioni a banda ultralarga, sensori e sistemi di sicurezza. Molti studi in letteratura hanno esplorato le applicazioni del grafene e i suoi vantaggi rispetto a tecnologie esistenti. Vice versa, ci sono chiare applicazioni che possono trarre beneficio dall' utilizzo delle frequenze terahertz ma esistono anche importanti sfide tecniche in termini di limitata disponibilità di materiali e dispositivi per generare, manipolare e rilevare le onde terahertz. L' idea principale di questa tesi è di portare questi due temi insieme per dimostrare che le tecnologie a terahertz e infrarosso possono trarre grandi benefici dall' uso del grafene grazie alle sue proprietà ottiche uniche.

Il primo contributo originale di questa tesi è un importante limite teorico sulle performances di dispositivi non-reciproci e riconfigurabili, dimostrando che entrambi possono raggiungere determinate figure di merito a scapito di perdite ottiche che non possono essere evitate, le quali dipendono unicamente dalle proprietà del grafene. Se grafene ad alta mobilità è utilizzato, queste perdite possono essere ridotte, ma, indipendentemente dalla geometria del dispositivo (in guida d' onda, planare, ...) il limite minimo di perdite non può essere superato. Questa teoria fornisce indicazioni importanti per il progetto di dispositivi ottici basati sul grafene, dato che può predire le migliori performances prima del progetto e senza bisogno di alcuna simulazione numerica. Inoltre, esempi di dispositivi (modulatori, isolatori e altro) che raggiungono questo limite sono presentati, i quali possono essere considerati ottimi.

Successivamente, diversi progetti di antenne per frequenze terahertz e infrarosse basate sul grafene sono presentate, dimostrando che il grafene controllato elettrostaticamente può essere usato per regolare la frequenza di lavoro di antenne plasmoniche e per orientare un fascio terahertz usando antenne reflectarray riconfigurabili. Circuiti equivalenti sono presentati al fine di fornire un modo per meglio comprendere il comportamento del dispositivo. Inoltre, una tecnica per misurare la conduttività complessa del grafene a frequenze infrarosse è presentata e utilizzata per stimare la qualità del grafene misurato.

Il potenziale del grafene per applicazioni non-reciproche è quindi dimostrata sperimentalmente grazie al progetto, fabbricazione e misura del primo isolatore a frequenze terahertz (primo nella banda da 1 a 10 THz). Un isolatore è un dispositivo che consente la propagazione della luce in una sola direzione, e per questo è anche chiamato "diodo ottico". L' implemen-

Sommario (Italiano)

tazione proposta utilizza grafene sottoposto a un campo magnetostatico e mostra 7 dB di attenuazione e 25 dB nella direzione opposta. L'isolatore è quasi ottimo secondo il limite teorico e performances molto migliori sono previste per il grafene di prossima generazione. Infine, la prima antenna reflectarray riconfigurabile a frequenze terahertz basata sul grafene è presentata. Essa è una metasuperficie in grado di riflettere le onde terahertz incidenti in una direzione che può essere modificata dinamicamente (beam steering) applicando diverse tensioni sugli elementi che includono grafene. Inoltre è possibile modulare il raggio riflesso con varie modulazioni complesse. Questo è il primo dispositivo in grado di ottenere beam steering con controllo elettronico per onde terahertz.

Parole chiave:

Grafene, Terahertz, Non-reciprocità, Modulatori, Beam steering, Limite teorico, Isolatore ottico, Antenna riconfigurabile, Plasmoni, Infrarosso.

Résumé

L'objet de cette thèse est d'explorer les applications du graphène pour les composants et antennes dans la bande du terahertz et de l'infrarouge lointain, en mettant un accent particulier sur les dispositifs ajustables et non-réciproques. Les deux technologies du terahertz et du graphène sont des champs émergents qui promettent beaucoup d'applications futures, y compris pour les communications ultra-large bande, la détection et la sécurité intérieure. Un grand nombre de recherches ont été consacrées à explorer les applications potentielles du graphène et ses avantages par rapport aux technologies existantes. En parallèle, il existe un ensemble d'applications qui pourraient bénéficier du développement des technologies terahertz ; mais ils présentent plusieurs défis techniques en termes de disponibilité très limitée des matériaux et des composants pour générer, manipuler et détecter les ondes terahertz. L'idée principale de ce travail est d'associer ces deux sujets pour démontrer que les technologies du terahertz et de l'infrarouge lointain peuvent grandement bénéficier des propriétés électromagnétiques uniques du graphène.

La première contribution originale de cette thèse est l'établissement d'une borne supérieure théorique pour les performances des dispositifs non-réciproques et ajustables. Elle démontre qu'une performance ciblée peut être obtenue avec ces deux dispositifs au détriment d'une perte optique inévitable, qui dépend uniquement des propriétés du graphène. Si on emploie du graphène avec une plus grande mobilité, cette perte inévitable peut être réduite ; cependant, et indépendamment de la géométrie en question (dispositifs de guide d'ondes, dispositifs planaires pour l'espace libre ...), les pertes seront toujours présentes. Cette limite théorique est une ligne directrice importante pour la conception de dispositifs optiques en graphène, car elle permet de prédire les meilleures performances possibles avant tout effort de conception ou de simulation numérique. Il est également démontré qu'on peut réaliser en pratique des dispositifs (modulateurs, isolateurs...) capables d'atteindre la limite supérieure, et par conséquent optimaux.

La thèse explore ensuite un certain nombre de conceptions d'antennes terahertz/infrarouge en graphène, et on trouve que le graphène biaisé peut être utilisé pour modifier la fréquence de reconfiguration pour les antennes plasmoniques de résonance et la direction du faisceau dans les reflectarrays basés sur le graphène. Des modèles de circuit sont fournis en tant que moyen simple pour comprendre le comportement du dispositif. En outre, une technique expérimentale capable de mesurer la conductivité complexe du graphène dans l'infrarouge est introduite, fournissant une évaluation très utile de la qualité du graphène à ces fréquences.

Résumé (Français)

Le potentiel du graphène pour les applications non-réciproques est ensuite démontré expérimentalement, avec la conception, fabrication et mesure du premier isolateur terahertz (fréquence de fonctionnement entre 1 THz et 10 THz). L'isolateur est un dispositif qui permet la propagation unilatérale de la lumière et pour cette raison est souvent appelé "diode optique". On utilise du graphène polarisé par un champ magnétostatique, qui présente environ 7 dB de perte dans une direction et plus de 25 dB dans l'autre. On démontre que ce dispositif est quasi-optimal, du point de vue de ses performances comparées à la limite théorique. Des améliorations très conséquentes pour les dispositifs montrés dans cette thèse sont à attendre avec la prochaine génération de graphène CVD.

Enfin, le premier réflecteur ajustable en graphène, composé d'une métasurface capable de dépointer un faisceau terahertz entrant, est présenté dans cette thèse. Le dispositif agit comme un miroir, mais lorsque un champ électrique est appliqué au graphène, la direction du faisceau réfléchi peut être commandée et le faisceau lui-même peut être modulé d'une façon complexe. Ce dispositif fournit la première implémentation de contrôle électronique de la direction d'un faisceau rayonné aux fréquences terahertz.

Mots-clés :

Graphène, Terahertz, Non-réciprocité, Modulateurs, Beam steering, Borne supérieure théorique, Isolateur optique, Antenne reconfigurable, Plasmons, Infrarouge.

Contents

Acknowledgements	v
Abstract (English/Italian/French)	vii
List of figures	xvii
List of tables	xxi
Notation and symbols	xxiii
1 Introduction	1
1.1 Graphene for photonics and electromagnetic applications: state of the art	1
1.2 Applications of terahertz technology	5
1.3 Reflectarrays at terahertz frequencies: state of the art	7
1.4 Non-reciprocal devices for terahertz frequencies: state of the art	9
1.5 Thesis organization and original contributions	11
1.6 Other contributions of the doctoral candidate	12
1.7 Funding sources	13
2 Two-dimensional materials theory in the framework of Maxwell's equations	15
2.1 The Maxwellian framework	15
2.1.1 Electromagnetic propagation in vacuum	15
2.1.2 Electromagnetic propagation in generic 3D medium	19
2.1.3 Interface/boundary conditions and 2D materials modelling	20
2.1.4 1D and 0D materials	21
2.1.5 Constitutive equations: particular cases	23
2.2 Lorentz reciprocity principle	29
2.3 Passive, active and lossless materials	31
2.4 The scattering matrix formalism	32
2.4.1 Scattering matrix for antennas	35
2.4.2 Transmission line models of layered structures and metasurfaces	37
2.4.3 Metasurfaces: linear and circular four waves scattering matrix	38
2.5 Drude and Drude-Lorentz models for plasmas, metals and semiconductors	43
2.6 Graphene conductivity formulae	46
2.6.1 Band structure	46
	xiii

Contents

2.6.2	Graphene gating and doping	49
2.6.3	Quantum capacitance of graphene	51
2.6.4	Scalar conductivity	52
2.6.5	Magnetostatically biased graphene	58
2.6.6	Non-locality (spatial dispersion) in graphene	59
2.7	Numerical simulations	60
3	Theoretical non-reciprocity and modulation upper bounds	63
3.1	Introduction	63
3.2	General scattering upper bound: derivation	64
3.2.1	Multiple and non-homogeneous functional materials	71
3.3	Reconfigurability vs non-reciprocity	72
3.3.1	Inversion of magnetostatic field	72
3.4	Graphene figure of merits	73
3.4.1	Graphene reconfigurability figure of merit	73
3.4.2	Graphene non-reciprocity figure of merit	75
3.5	Device specific upper bounds	76
3.5.1	Modulators	77
3.5.2	Non-reciprocal devices specific upper bounds	81
3.5.3	Bounds for reconfigurable and non-reciprocal antennas	83
3.6	Design of optimal planar devices	87
3.6.1	Optimal amplitude modulators	87
3.6.2	Optimal isolators	91
3.6.3	Optimal Kerr rotators	93
3.7	Applications to nanophotonics	94
3.8	Conclusions	95
4	Graphene plasmonics for antenna applications	97
4.1	Introduction	97
4.2	Theory of plasmon polaritons for 3D materials	97
4.3	Theory of graphene surface plasmon polaritons	100
4.4	Numerical simulations of graphene plasmon waveguides	105
4.5	Graphene tuneable plasmonic dipole	108
4.5.1	Introduction	108
4.5.2	Graphene plasmonic dipole	108
4.5.3	Frequency tuning	111
4.5.4	Circuit model	114
4.5.5	Metal graphene hybrid antenna	117
4.5.6	Graphene plasmonic reflectarrays	118
4.6	Fabry-Perot infrared complex conductivity measurement	118
4.6.1	Introduction	118
4.6.2	Measurement results	119

5	Non-reciprocal devices based on graphene	123
5.1	Introduction	123
5.2	Faraday rotation	124
5.3	Faraday rotation enhancement	124
5.3.1	Magnetoplasmonic enhanced Faraday rotator	125
5.3.2	Ring resonators enhanced Faraday rotator	126
5.4	Terahertz isolator based on graphene	126
5.4.1	Introduction	127
5.4.2	Working principle and Design	128
5.4.3	Measurement and elaboration	131
5.5	Conclusions	135
6	Beam steering reflectarray at terahertz frequencies	137
6.1	Introduction	137
6.2	Reflectarray: working principle	137
6.3	Fixed beam terahertz reflectarray	139
6.4	Graphene beam steering reflectarray	140
6.5	Conclusions	145
7	Conclusions and perspectives	147
A	Micro-nano fabrication of graphene devices	151
A.1	Introduction	151
A.2	Devices based on THz/IR silicon transmission substrate	151
A.2.1	Introduction	151
A.2.2	Infrared and terahertz characterization of graphene	153
A.2.3	Magnetoplasmonic enhanced Faraday rotator	153
A.2.4	Ring resonators enhanced Faraday rotator	154
A.3	Reflection substrate based on SOI silicon device layer	155
A.3.1	Introduction	155
A.3.2	Graphene terahertz isolator	157
A.3.3	Fabry Perot based measurement of graphene conductivity	157
A.3.4	Fixed beam terahertz multiband reflectarray	158
A.3.5	Graphene terahertz reflectarray	159
	Bibliography	171
	Curriculum Vitae	179

List of Figures

1.1	Exfoliated versus CVD graphene	2
1.2	Graphene publications until August 2014	2
1.3	Graphene applications	3
1.4	Graphene photonics phenomena and applications	5
1.5	Applications of terahertz technology for security and airports	6
1.6	Terahertz stand-off imaging	6
1.7	0.28 THz beam scanning on CMOS technology	7
1.8	The first terahertz reflectarray	8
1.9	Polarization beam splitting terahertz reflectarray	8
1.10	Polarization sensitive terahertz reflectarray	9
1.11	Wide phase range terahertz reflectarray	9
1.12	Gold ions implanted terahertz reflectarray	9
1.13	Reflectarrays in this work	10
1.14	Ferrite based Faraday isolator	10
1.15	Thesis organization	11
2.1	Scattering parameters definition	32
2.2	Conventions for circularly polarized scattering	39
2.3	Conventions on representing circularly polarized waves.	40
2.4	Band diagram of graphene	47
2.5	Electrostatic gating of graphene	49
2.6	Carriers and quantum capacitance modulation	51
2.7	Graphene parameters conversion chart	54
2.8	Graphene conductivity with Kubo formula	55
2.9	Conductivity plot: Fermi level sweep	56
2.10	Conductivity plot: τ sweep	57
3.1	Reconfigurability figure of merit of graphene	74
3.2	Non reciprocity figure of merit of graphene	76
3.3	Graphene-based device capabilities	77
3.4	General modulation bound	79
3.5	Amplitude and phase modulation bound	80
3.6	Schematic of a reconfigurable antenna	85

List of Figures

3.7	Reconfigurability antenna upper bound	86
3.8	Optimal graphene amplitude modulator	88
3.9	Optimal non-reciprocal isolators	92
3.10	Optimal Kerr rotators	93
3.11	(Reproduced) Bound for nanophotonic modulators	95
3.12	(Reproduced) Electro-optical materials figures of merit	95
4.1	Surface plasmon polaritons	98
4.2	Graphene surface plasmon polaritons	101
4.3	Computed propagation factor	103
4.4	Computed attenuation factor	104
4.5	Computed mode confinement	104
4.6	Computed quality factor	105
4.7	Numerical simulation of plasmons on infinite graphene sheet	106
4.8	Numerical simulation of plasmons on ribbon waveguides	106
4.9	Simulated propagation constants	108
4.10	Geometry of the proposed graphene plasmonic dipole	109
4.11	Electric field and current on the antenna	110
4.12	Input impedance of the graphene plasmonic dipole	110
4.13	Efficiency of the graphene plasmonic dipole	111
4.14	Radiation pattern of the proposed graphene plasmonic dipole	111
4.15	Geometry of the tuneable graphene plasmonic dipole	112
4.16	Tuneable input impedance	113
4.17	Efficiency of the tuneable plasmonic graphene antenna	113
4.18	Comparison among different number of layers	114
4.19	Radiation pattern of the proposed graphene tuneable dipole	114
4.20	Circuit model of the plasmonic dipole	115
4.21	Detail of the plasmonic fringing fields at the end of a ribbon waveguide	115
4.22	Impedance comparison	116
4.23	Total efficiency comparison	116
4.24	Geometry of the proposed hybrid dipole	117
4.25	Impedance tuning of the proposed hybrid dipole	117
4.26	Radiation efficiency of the proposed hybrid dipole	118
4.27	Fabry-Perot periodic dips in the reflection coefficient of the bare substrate	120
4.28	Perturbation of a single Fabry-Perot absorption dip	121
4.29	Measured complex conductivity of graphene	121
4.30	Measured complex conductivity of gated graphene	122
5.1	Faraday rotation: circuit model	124
5.2	Faraday rotation in CVD graphene	124
5.3	Patterned graphene for plasmonically enhanced Faraday rotation	125
5.4	Measured enhanced Faraday rotation	126
5.5	Decorated graphene for enhanced Faraday rotation	126

5.6 The proposed graphene terahertz isolator	128
5.7 Simplified transmission line circuit model	129
5.8 Measurement of the isolator	132
5.9 Full characterization of the isolator	133
5.10 Device optimality	134
5.11 Linearly polarized light operation	135
6.1 Refelctarray working principle	138
6.2 Beam steering working principle	138
6.3 Geometry and performance of the fixed beam reflectarray	140
6.4 Measurement of fixed beam reflectarray	141
6.5 Unit cell	141
6.6 Reflection coefficient	142
6.7 Layout of the reflectarray	142
6.8 SEM picture of reflectarray	142
6.9 Cross section of the reflectarray	143
6.10 Reflectarray and control unit	143
6.11 Measured beam steering	144
6.12 Beam scanning normalized radiation pattern	145
6.13 PSK modulation schemes	145
A.1 Process flow for THz/IR transmission chip	152
A.2 Process flow for graphene transfer	153
A.3 Process flow for graphene Magnetoplasmonic enhanced Faraday rotator	154
A.4 Process flow for Ring resonators enhanced Faraday rotator	155
A.5 Process flow for reflection substrates (parylene bonding)	156
A.6 FIB section of reflection substrate	157
A.7 Process flow for reflection substrates (anodic bonding)	158
A.8 Process flow for the isolator	158
A.9 Process flow for Fabry Perot resonant chip	159
A.10 Process flow for the fixed beam terahertz multiband reflectarray	159
A.11 Process flow for graphene terahertz reflectarray	160

List of Tables

1.1	Examples of graphene photonics and electromagnetics applications	3
1.2	Terahertz reflectarray fabrication technologies	8
1.3	Technology for terahertz non-reciprocity	10
2.1	Low dimensional systems with impedance and conductance units	22
2.2	Classification of 2D and 3D materials according to chirality and isotropy	28
3.1	Examples of graphene amplitude modulators from literature	90
3.2	Examples of graphene isolators from literature	93
4.1	Proposed antennas and corresponding working points	109
6.1	Control strings for beam steering	144

Notation and symbols

In the remainder of this document scalars are represented in italic, vectors are boldface, matrices and tensors are underlined. The normalized unit vector parallel to a given vector \mathbf{v} is indicated with $\hat{\mathbf{v}}$. Imaginary unit is j , the superscript T is used to indicate matrix or operator transposition, $*$ indicates the complex conjugate and H the Hermitian (transposed and conjugate). When used in a matrix context, vectors are always assumed to be column vectors, so that $\mathbf{v} \cdot \mathbf{v} = \mathbf{v}^{\text{T}}\mathbf{v}$.

For complex phasors notation of time-harmonic fields, the Engineering sign convention $e^{j\omega t}$ with $\omega = 2\pi f$ is used (which differs from the Physics one $e^{-i\omega t}$), so that, for instance, inductors have a positive imaginary impedance and time derivatives are obtained multiplying by $j\omega$; this is in agreement with the commonly used definition of Fourier transform, namely:

$$F(\omega) = \int_{-\infty}^{+\infty} f(t)e^{-j\omega t} dt \quad f(t) = \frac{1}{2\pi} \int_{-\infty}^{+\infty} F(\omega)e^{+j\omega t} d\omega$$

This time-harmonic notation implies that plane waves propagating along the complex wavevector \mathbf{k} are expressed as $e^{-j\mathbf{k}\cdot\mathbf{r}}$ or as $e^{-\gamma\cdot\mathbf{r}}$. The complex wavevector \mathbf{k} is related to the complex vector propagation constant γ as $\gamma = j\mathbf{k}$. The real and imaginary parts of γ are indicated as $\gamma = \alpha + j\beta$. If α and β are parallel, then the scalars k , γ , α , β can be defined analogously along the propagation direction.

The time-domain expression for a time-harmonic quantity A can be obtained as $\text{Re}(Ae^{j\omega t})$. Phasors are expressed using the root mean square (RMS) effective value, so that the complex Poynting vector is $\mathbf{E} \times \mathbf{H}^*$. The norm of a vector \mathbf{v} is expressed as $|\mathbf{v}|$ or v and defined, to be consistent with complex absolute value of a scalar, as $|\mathbf{v}| \triangleq \sqrt{\sum_i |v_i|^2} = \sqrt{\mathbf{v}^* \cdot \mathbf{v}} = \sqrt{\mathbf{v}^{\text{H}}\mathbf{v}}$.

All quantities are expressed following the International System of Units (SI). Some quantities (such as mobility and carrier density) are expressed using centimeters instead of meters for historical reasons. When a frequency is indicated with ω it is to be interpreted as an angular frequency measured in $\text{rad}\cdot\text{s}^{-1}$, if it is indicated as f or Γ then it is a frequency or rate expressed in Hz. The symbol \triangleq is used when defining new quantities.

Notation and symbols

References are indicated by square brackets: [<N>]. If the reference is a journal article written by the author of this thesis, then it is indicated as [JA<N>], if it is a conference article it is indicated as [CA<N>]

1 Introduction

This short introductory chapter presents a concise state of the art for graphene used in photonic and electromagnetic applications. It also illustrates the currently existing solutions for terahertz reflectarrays and isolators, which are the two specific devices targeted in this thesis. Then the original achievements of this thesis are highlighted and the contributions of the candidate are summarized in the frame of chapters organization of the thesis.

1.1 Graphene for photonics and electromagnetic applications: state of the art

Graphene, a 2D material based on a monolayer honeycomb lattice of carbon atoms, was isolated in 2004 [84] and has since then been an extremely important research topic due to its outstanding physical properties [83, 33, 34].

Originally graphene was obtained by a process of micro-mechanical exfoliation, using scotch tape to repeatedly peel small graphite samples and transfer them onto a desired substrate. Graphite, in fact, is a solid composed of several graphene sheets which are weakly coupled to each other. Hall conductivity measures and electric field effects demonstrated the properties of these first mono-atomic flakes [84], sparking an enormous interest in this material. Field effect measurement, in particular, demonstrated that graphene conductivity (also at terahertz and infrared) can be tuned dynamically by applying an electric field on it. The exfoliation technique is still used today to produce high quality graphene samples, but the achievable size is limited to few hundreds of microns in the best cases.

For larger areas other techniques have been proposed, which however, because of lattice defects and contaminations, show worse carrier mobility and therefore lower performances for applied devices. These include epitaxial graphene [21] obtained on the face of SiC wafers and, most importantly, chemically vapor deposited (CVD) graphene [90, 57, 6]. The CVD process is usually performed on copper, obtaining the formation of a graphene layer on it. Graphene is then transferred on the target substrate by spin coating a polymer, wet-etching

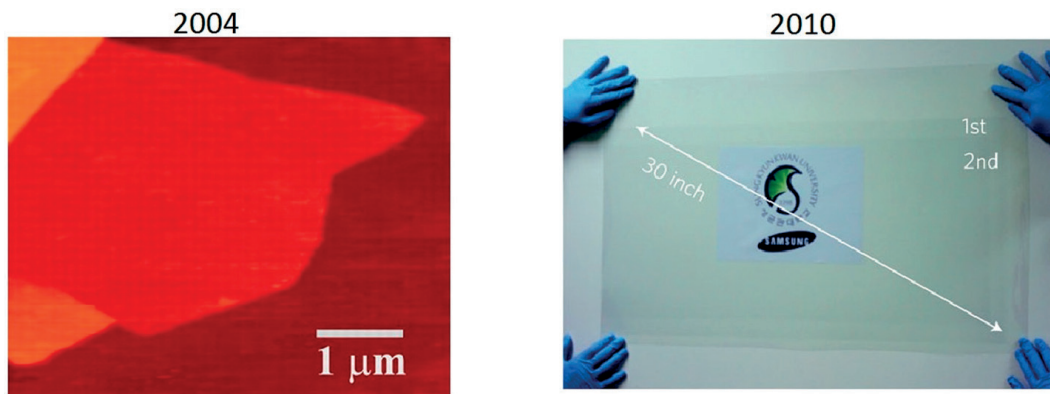


Figure 1.1 – Exfoliated (left) versus CVD graphene (right), reproduced from [33]. In this example two CVD layers (indicated in the figures) are used.

the copper, depositing the film on the substrate and dissolving the polymer. More recently, roll-to-roll graphene production was developed to achieve direct transfer from copper to a transparent polymer [2]. Large area graphene (up to tens of centimeters) on arbitrary substrates can be obtained by CVD process, being it limited only by the size of copper and of the CVD reactor. The process is also cheap and therefore promising for industrial applications.

The technological gap bridged in the first seven years of graphene's life is well represented in Figure 1.1 which shows a comparison between exfoliated and CVD graphene samples [33].

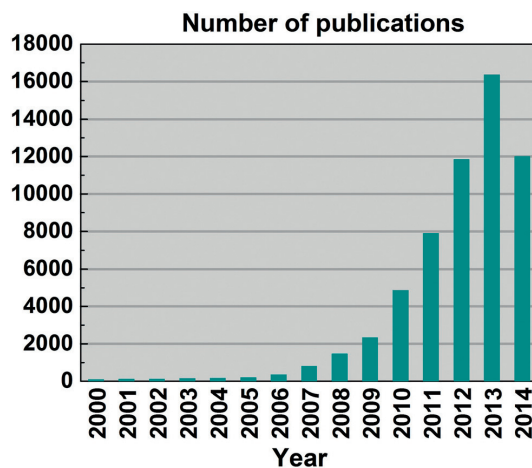


Figure 1.2 – Graphene publications until August 2014, reproduced from [33]

Figures 1.2 and 1.3 also give a very clear indication of the impact of this material in the scientific literature and the potential impact on everyday life. Figures 1.2 illustrates the number of publications on graphene per year, while 1.3 shows examples of the properties of graphene and their applications.

This thesis will focus in particular on the interactions of graphene with electromagnetic waves and light [5, 51], where several important optical properties and related phenomena are

1.1. Graphene for photonics and electromagnetic applications: state of the art

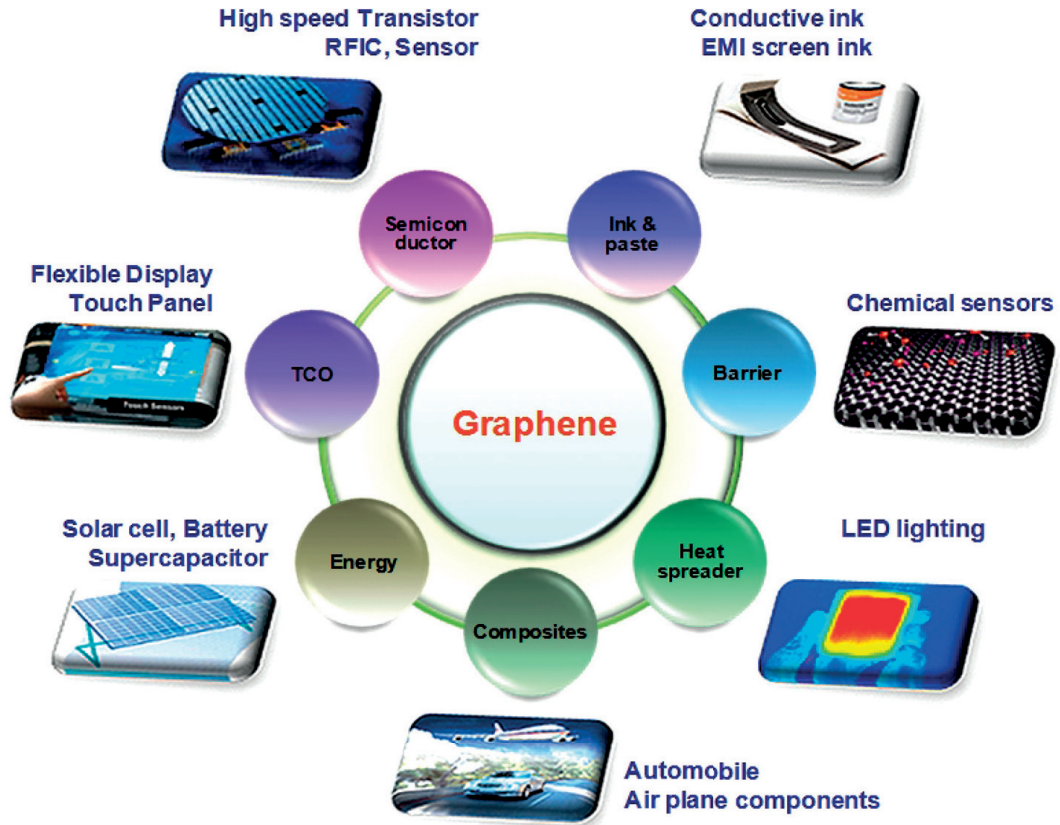


Figure 1.3 – Graphene applications, reproduced from [33]

found. This rich behavior has been exploited for many devices and has the potential of deeply affecting many photonics disciplines. Figure 1.4 and Table 1.1 summarize the most important phenomena and applications related to graphene photonics and examples from the literature are listed in Table 1.1. These properties highly depend on parameters such as graphene quality, wavelength (or frequency), power and device geometry.

Table 1.1 – Examples of graphene photonics and electromagnetics applications

Phenomenon/device	Applications	Figure	References
Transparent conductivity	Touch screens	1.4a	[2]
	Solar panels	1.4b	[75]
Transistors	RF Amplifiers	1.4c	[119]
Tuneable conductivity	Modulators and switches	1.4d,e,f	[66, 98, 123, 124]
	Tuneable lasers	1.4g	[15]
Interband transitions	Photodetectors	1.4h	[126, 60]
Non linearity	Long wavelength detectors	1.4i	[60]
	Saturable absorber	1.4j	[72]
	Mixers	1.4k	[71]
Raman scattering	2D materials characterization	1.4l	[32]
Ohmic losses	Absorbers	1.4m	[125]
Plasmonic resonances	Chemical and bio-sensors	1.4n	[93]
Non-reciprocity	Faraday rotators and Isolators	1.4o	[21, 22, 110]

One of the most interesting properties of graphene is the fact that this material has at the same time a significant DC conductivity (in the order of tens of ohms) and very good transparency for visible light (an isolated graphene sheet in vacuum absorbs approximately 2.3% of visible light [63]). This property makes it appealing for those situations where transparent electrodes are needed, and in particular for touch screens (Figure 1.4a [2]) and solar panels (Figure 1.4b [75]). More recently, graphene was proposed as a transparent protection layers for copper and silver plasmonic [61], since it can act as a barrier against corrosion of these two metals without interfering with plasmons at visible frequencies.

Graphene tunable conductivity via electric field effects can be used at DC to create graphene field effect transistors (GFETs) or at terahertz and infrared frequencies to create tunable optical devices. GFETs have been proposed to create amplifiers and RF circuits (Figure 1.4c [119]). For amplification, unilateral gain larger than unity and useful modulations can be achieved up to tens of GHz. Optical modulators and switches can be designed both for plane and guided waves [66, 98, 123, 124]. Graphene can perform as a switch for microwaves (where however there are technologies showing better performances, such PIN diodes and MEMS), terahertz waves (Figure 1.4d [98]), far and mid infrared (Figure 1.4e [123, 124]) and near infrared (Figure 1.4f [66]), while for visible light absorption is constant and modulation is not possible. In addition, including graphene in a laser cavity provides a way to tune the laser emission in a dynamic way (Figure 1.4g [15]).

Graphene has been proposed to create photo-detectors as well. For visible and infrared light, this can be achieved thanks to graphene interband transitions, which occur for photons having energy larger than two times graphene Fermi level. When a photon induces an interband transition, it is absorbed and an electron-hole couple is created, which can be then detected as a current (Figure 1.4h [60]). For lower frequency (terahertz band) a similar effect can be obtained exploiting non linearities in a GFET (Figure 1.4i [60]).

Non-linearities can be used to create other components as well, such as saturable absorbers operating at visible frequencies (Figure 1.4j [72]) and radio-frequency mixers (Figure 1.4k [71]). Graphene exhibits Raman scattering (Figure 1.4l [32]) which can be used as way to estimate the number of layers and other important graphene parameters.

Two different loss mechanism act in graphene, namely ohmic losses and interband transitions. Ohmic losses dominates at low frequencies, and can be used to create electromagnetic absorbers (Figure 1.4m [125]) with operation frequency which extends from microwaves to mid-infrared.

Graphene exhibits plasmons at mid infrared frequencies, and they provide a way to confine electromagnetic radiation in extremely small volumes, enabling sensing of biological molecules (Figure 1.4n [93]). Finally, the high graphene mobility can be used to create non-reciprocal devices, such as Faraday rotators (Figure 1.4o [21, 22, 110]) which are key elements for one way non-reciprocal isolators.

1.2. Applications of terahertz technology

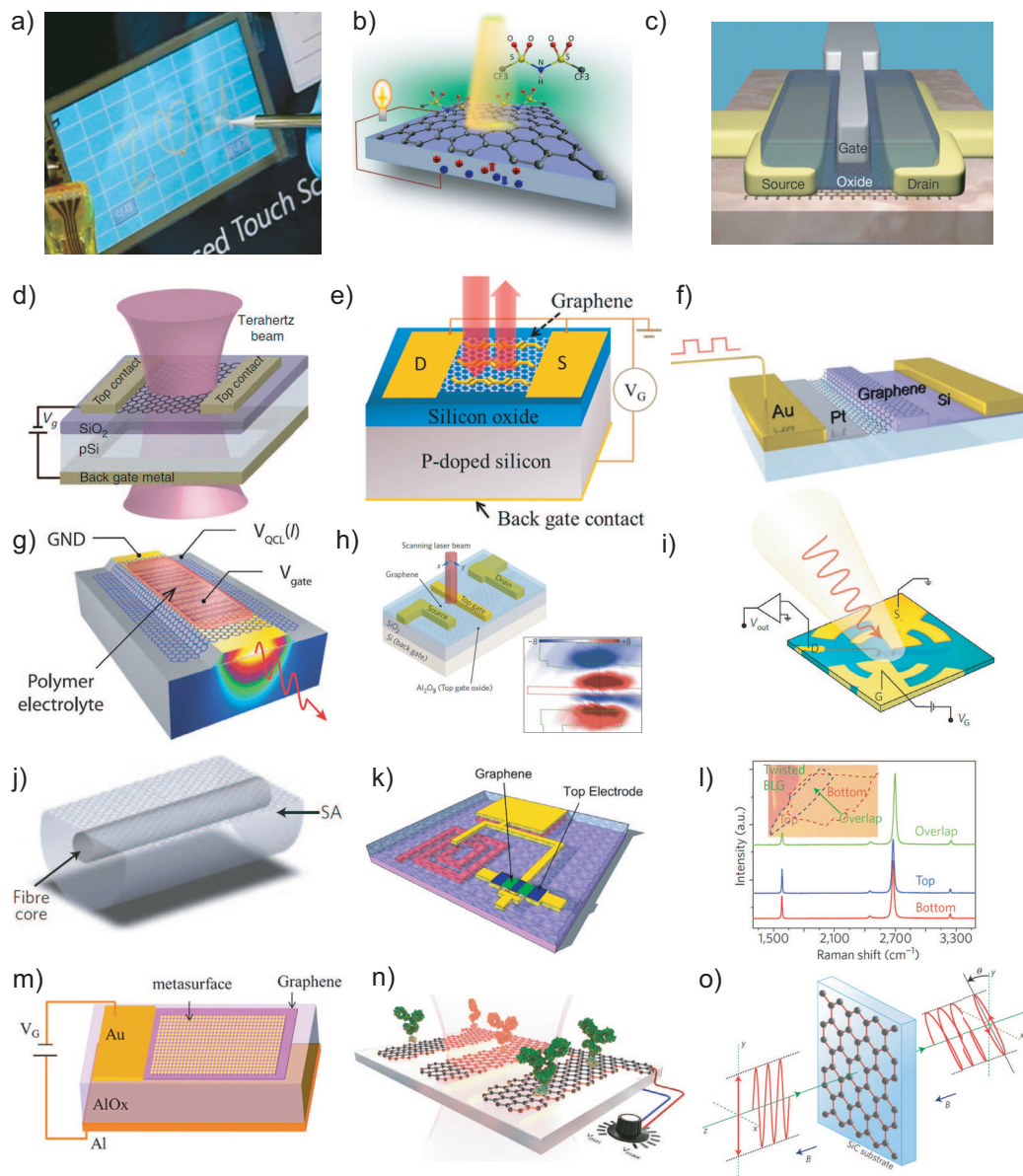


Figure 1.4 – Graphene photonics phenomena and applications. a) Graphene touch screen [2]. b) Graphene solar panels [75]. c) High frequency graphene transistors [119]. d,e,f) Graphene modulators [66, 98, 123, 124]. g) Tuneable lasers using graphene [15]. h) Graphene photodetectors [60]. i) Long wavelength (THz) detectors [60]. j) Graphene saturable absorbers [72]. k) Graphene RF mixers [71]. l) Raman spectroscopy on graphene [32]. m) Graphene optical absorbers [125]. n) Graphene plasmonic biosensors [93]. o) Graphene Faraday rotators [21].

1.2 Applications of terahertz technology

Terahertz science is the study of physical phenomena, devices and systems operating in the range conventionally defined from 0.3 to 3 THz (or alternatively in the extended range 0.1 to 10 THz). Due to important technological challenges, terahertz technology is still emerging,

Chapter 1. Introduction

but it possesses a clear set of important applications [86].

Firstly, terahertz spectroscopy provides an excellent platform for sensing [23], since most molecular vibration resonances can be resolved spectrally at these frequencies. In particular, the detection of drugs and explosives [31] is very promising.

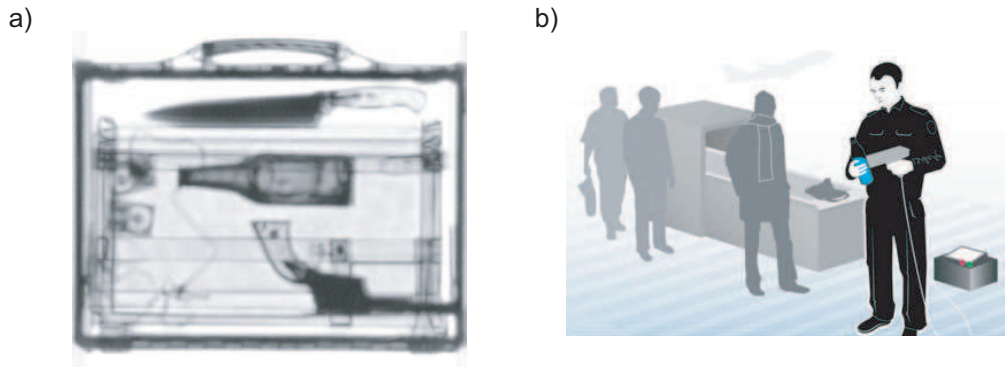


Figure 1.5 – Applications of terahertz technology for security and airports, reproduced from [52]. a) Terahertz transmission image of dangerous items concealed in a suitcase. b) Determination of contents of PET bottles with handheld terahertz sensing scanner.

Terahertz has an important potential as a platform for medical diagnosis, e.g. for skin cancer [127] and cornea hydration analysis [3]. Radioastronomy [62] and telecommunications [1] are other important applications. For example, radioastronomy in this band allows the study of interstellar dust, and in particular it allows the discrimination of different isotopes in the dust, which is of key importance for interstellar chemistry [62].

Another very important field of application is homeland security. Terahertz radiation can, in fact, propagate with low loss through many materials such as paper, cardboard and fabrics, and therefore can be used for security imaging (see Figure 1.5) [52]. Unlike millimeter waves body scanners, terahertz scanners can achieve the same or better resolution in a stand-off radar configuration [19, 20]. Figure 1.6 shows an example of stand-off terahertz imaging setup, which uses a rotating mirror to focus a terahertz beam on various parts of the target.

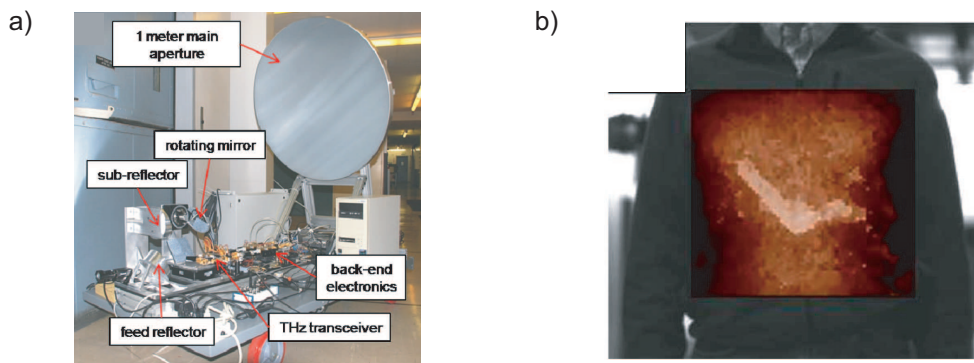


Figure 1.6 – Terahertz stand-off imaging, reproduced from [19, 20]. a) A THz scanner which uses a rotating mirror to achieve beam steering. b) THz imaging of a gun concealed below clothes.

1.3. Reflectarrays at terahertz frequencies: state of the art

The use of mechanically rotating mirrors has, however, important limitations. First of all, the speed of the mirror is limited, and therefore the acquisition of a single frame usually requires times in the order of seconds because of this speed bottleneck [20]. In addition, these systems are usually bulky and lack in reliability, due to the fact that the mirror oscillates with frequency of tens of hertz.

Alternative solutions for beam-steering at terahertz frequencies are therefore an important research topic. A possibility was proposed in [97], where chips based on CMOS technology demonstrated beam steering at 0.28 THz (see figure 1.7). Unfortunately, this approach is limited in frequency by the used CMOS technology.

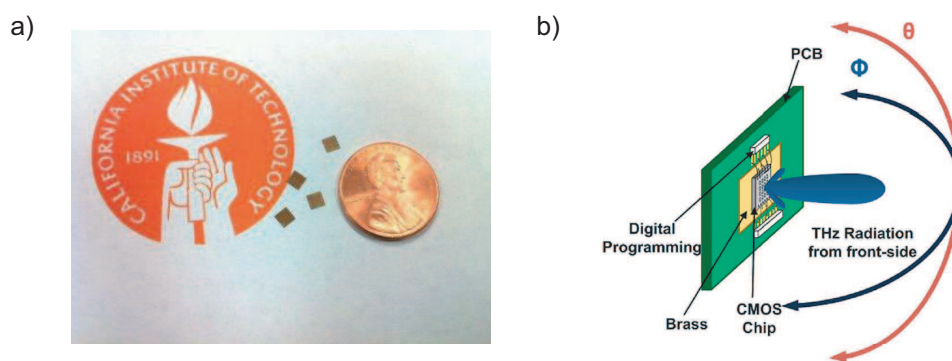


Figure 1.7 – 0.28 THz beam scanning on CMOS technology, reproduced from [97]. a) Beam scanning chips. b) Electrically controlled beam scanning.

While this frequency band has a clear set of applications, there are also important technical challenges for devices operating at terahertz frequencies, and therefore there is currently a very important research effort finalized to overcome these challenges. The latter include the limited availability of high power miniaturized terahertz sources, the propagation losses that occur in many substrates commonly used for other bands and the lack of terahertz low-loss non-reciprocal materials. The solution of these challenges is also the main motivation of this thesis, where it is demonstrated that graphene can be beneficial for several terahertz devices, focusing on reconfigurable antennas and non-reciprocal devices. In particular, a beam-steering reflectarray based on graphene is demonstrated here as a very promising alternative to mechanical beam-scanning. The reminder of the chapter presents a state of the art of terahertz reflectarrays and isolators, which in this thesis have been implemented for the first time using graphene.

1.3 Reflectarrays at terahertz frequencies: state of the art

The concept of reflectarray antennas [47] has been known since decades in the microwave community. More recently, similar phase gradient structures were explored at visible and near infrared frequencies [129], while no examples were available at terahertz frequencies until a few years ago. This section summarizes the current state of the art of experimental reflectarray

Chapter 1. Introduction

antennas at terahertz frequencies.

Table 1.2 – Terahertz reflectarray fabrication technologies

Reference	Figure	Dielectric spacer	Ground plane	Frequency
[81]	1.8	PDMS	Platinum	1 THz
[82]	1.9	PDMS	Platinum	1 THz
[80]	1.10	PDMS (freestanding)	Thin gold strips	1 THz
[89]	1.11	BCB	Aluminum	0.2-0.3 THz
[95, CA15]	1.12	PDMS (freestanding)	Ion implanted gold	1 THz
This work	1.13	High resistivity silicon	Silver and aluminum	0.7, 1, 1.3 THz

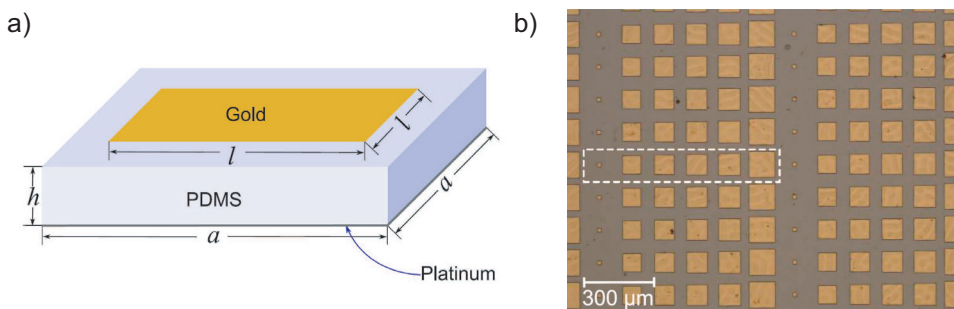


Figure 1.8 – The first terahertz reflectarray, reproduced from [81].

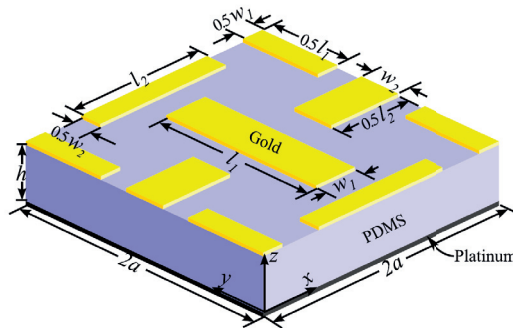


Figure 1.9 – Polarization beam splitting terahertz reflectarray, reproduced from [82].

The main challenge for terahertz reflectarrays is the dielectric spacer. This has, in fact, to be a material with low losses at terahertz frequencies and at the same time with thickness in the order of a fraction of the terahertz wavelength. Table 1.2 shows solutions existing in literature.

Organic substrates such as PDMS (Polydimethylsiloxane) and BCB (Benzocyclobutene) have been considered (figures 1.8, 1.9, 1.10, 1.11) [95, 81, 82, 80, 89], which however do not allow the integration of reconfigurable technology because of the limited compatibility of the substrate with nano-fabrication technologies. In this work we demonstrate the first reflectarray at terahertz based on silicon and we demonstrate the possibility of integrating graphene to achieve beam steering.

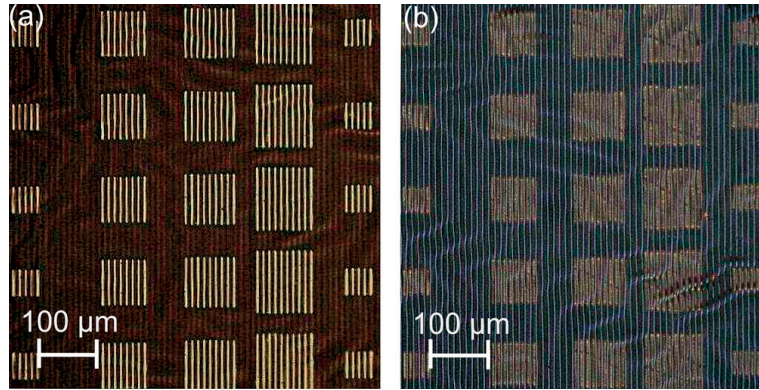


Figure 1.10 – Polarization sensitive terahertz reflectarray, reproduced from [80].

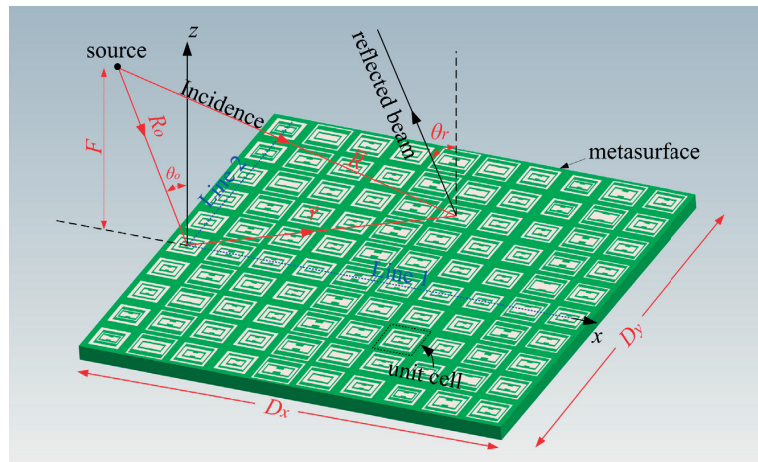


Figure 1.11 – Wide phase range terahertz reflectarray, reproduced from [89]. a) Front view. b) Back view.

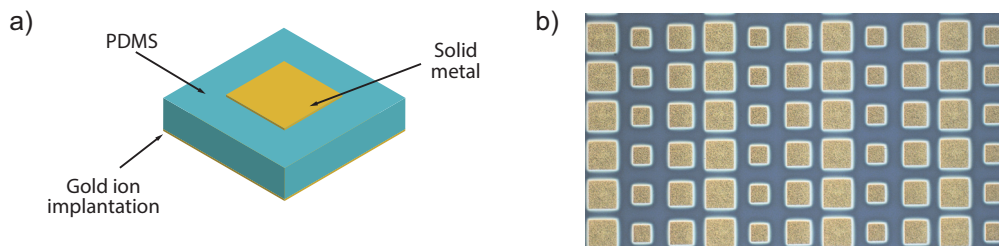


Figure 1.12 – Gold ions implanted terahertz reflectarray, reproduced from [95, CA15]. a) Cell structure. b) Optical picture.

1.4 Non-reciprocal devices for terahertz frequencies: state of the art

The creation of isolators and circulators at terahertz is a very important open challenge. In this thesis, the first isolator working in the band 1-10THz is presented and it is based on graphene [JA12]. Before this work, ferrite has been considered and used to create an isolator up to 0.8 THz (see figure 1.14) [100]. However, despite its moderate frequency remaining below 1 THz,

Chapter 1. Introduction

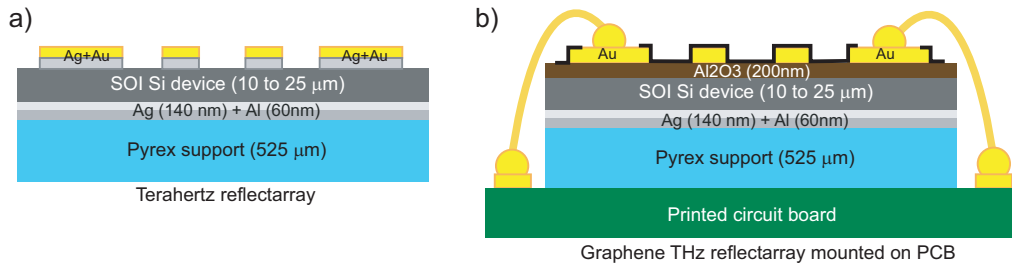


Figure 1.13 – Reflectarrays in this work. a) Fixed beam, multiband terahertz reflectarray on silicon. b) Reconfigurable reflectarray with graphene

this device has very large insertion loss in the order of tens of dB.

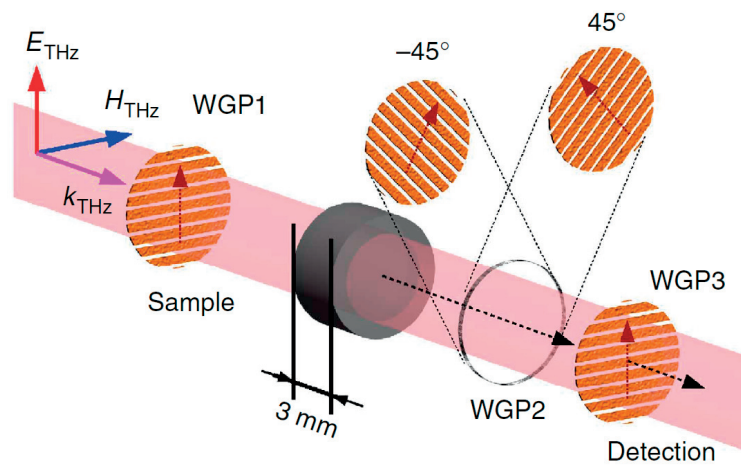


Figure 1.14 – Ferrite based Faraday isolator, reproduced from [100]

Graphene has been considered in a theoretical paper as possible material for terahertz plasmonic isolators [16, 65], and for experimental isolators at microwave frequencies [103, 107, 108]. Table 1.3 illustrates available technologies for terahertz non-reciprocity.

Table 1.3 – Technology for terahertz non-reciprocity

Technology	Status	References
Graphene	Isolator at 2.9 and 7.6 THz	This work
Ferrite	Isolator up to 0.8 THz	[100]
Doped Silicon	Material properties measured	[78]
HgTe	Material properties measured	[78]
Multiferroic materials	Material properties measured	[56, 55]
Ferrofluid materials	Material properties measured	[99]

It is clear that graphene is currently the best material available for terahertz non-reciprocal isolators.

1.5 Thesis organization and original contributions

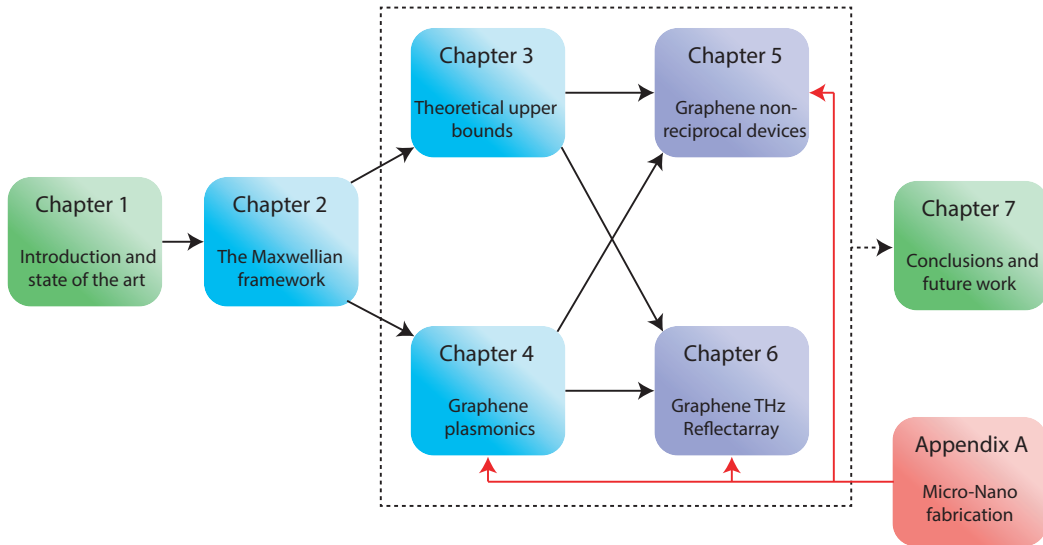


Figure 1.15 – Thesis organization

The contents of this thesis include both theoretical and experimental work, which is organized in chapters as follows.

- **Chapter 1:** Introduction to the state of the art of graphene and terahertz technologies and description of the thesis structure.
- **Chapter 2:** Theoretical framework to model graphene and 2D materials in Maxwell's equations. The chapter reviews the framework of Maxwell's Equations and defines quantities used in the reminder of the thesis. This chapter presents also all the conductivity formulas used in the other chapters.
Original contributions: 2D materials are organized according to properties (locality, anisotropy, chirality, reciprocity, gyrotropy,...). Such a detailed classification has not been done previously, to the best of the candidate's knowledge.
- **Chapter 3:** Theoretical upper-bound of graphene based reconfigurable and non-reciprocal devices.
Original contributions: A bound introduced in [96] is extended to 2D materials, corrected from some mistakes and extended to isolators and modulators performanc. Optimal graphene transmission modulators, reflection modulators, isolators and Kerr rotation are demonstrated. A bound is also given for phase modulators and reconfigurable or non-reciprocal antennas.
Publications:[JA8, JA12, JA13, CA28, CA19, CA17, CA22, CA23]
- **Chapter 4:** Plasmonic devices. The chapters begins with a review of plasmonics in graphene.
Original contributions: propagation in narrow waveguides is addressed, plasmonic antennas based on graphene are developed and are found to be frequency tunable. Finally a new experimental method to measure the complex conductivity of graphene

associated to plasmon propagation is discussed. Both the method and the realized devices are original contributions.

Publications:[JA9, JA1, JA3, JA14, JA10, JA2, CA27, CA2, CA16, CA12, CA11, CA24, CA21, CA13, CA8, CA3]

- **Chapter 5:** Graphene non reciprocal devices.

Original contributions: An ongoing research in collaboration with University of Geneva (Dr. Alexey Kuzmenko) is described, resulting in metasurfaces to enhance Faraday rotation in graphene and in the first THz non-reciprocal isolator based on graphene. To the best of the author's knowledge, this is also the first experimental isolator to work in the high terahertz frequency (1 THz to 10 THz). The author designed the device and analyzed the data. Nanolab (Dr. Clara Moldovan) fabricated the device and the group of Alexey Kuzmenko (University of Geneva) measured the device.

Publications:[JA12]

- **Chapter 6:** This chapter describes the first terahertz graphene reflectarray able to perform beam steering.

Original contributions: First a fixed beam version of the reflectarray (without graphene) is proposed. The multiband reflectarray pattern was designed by Dr. Hamed Hasani, while the design of the fabrication process flow and fabrication itself are original contributions of the author. The device was measured by Dr. Santiago Capdevila. The final graphene reflectarray, a deliverable for the European Graphene Flagship project, was designed, fabricated and measured by the author with the help of Dr. Santiago Capdevila. Dr. Capdevila also designed the control unit to gate the reflectarray columns.

Publications:[JA4, CA5, CA19, CA15, CA20, CA17]

- **Chapter 7:**Conclusions and prospects for future research related to the topics of this thesis.
- **Appendix A:** This appendix summarizes the fabrication process flows of the fabricated devices.

1.6 Other contributions of the doctoral candidate

Additional contributions of the doctoral candidate (not included in this thesis) are:

- The development of vanadium dioxide modulated scatterers at terahertz, second author, in collaboration with EPFL Nanolab (Dr. Wolfgang Vitale) and INRS-EMT.[JA15, CA17, 114]
- The development of stretchable terahertz reflectarrays (third author, in collaboration with Dr. Pietro Romano)[CA15, 95].
- The design and fabrication of graphene quantum capacitance (second author, in collaboration with EPFL Nanolab (Dr. Clara Moldovan and Dr. Pankaj Sharma))[76].
- The development of a method to measure the phase response of optical nano-antennas.
- The integration of graphene quantum capacitance in an integral equations based electrostatic method of moment code (second author, collaboration with Dr. Baptiste

Hornecker) [46].

- Formal comments on the use of orbital angular momentum for radio communications [JA6, JA7, CA30].
- The study of non-locality in graphene (third author, in collaboration with Dr. Arya Fallahi and Dr. Tony Low) [JA3].
- Theoretical study of graphene NEMS in microwave phase shifters (collaboration with Dr. Clara Moldovan and Dr. Wolfgang Vitale) [CA9, 76].

1.7 Funding sources

This work has been financially supported by the Swiss National Science Foundation (SNSF) under grant 133583, the Hasler Foundation under Project 11149 and the European Commission under Graphene Flagship (Contract No. CNECT-ICT-604391)

2 Two-dimensional materials theory in the framework of Maxwell's equations

This chapter describes the theoretical modelling of graphene as a two-dimensional material in the framework of Maxwell's Equations for electromagnetism and photonics problems. First, the Maxwellian framework with related definitions and assumptions is introduced. Second, graphene is introduced in this framework and the conductivity formulas used in the remainder of this thesis are presented. A discussion on which models are adequate for each condition is also provided.

The majority of the contents shown in this chapters are well known, but are often fragmented in literature. This chapter collects these concepts and aims at organizing them organically, bridging optics, solid state physics and electromagnetism. The reader who is already accustomed to this framework may skip this chapter or parts of it.

2.1 The Maxwellian framework

The electromagnetic and photonics phenomena considered in this thesis can be modeled using Maxwell's equations. These equations describe the mutual interaction between electric and magnetic field, explaining the propagation of electromagnetic waves. Importantly, Maxwell's equations are not the ultimate theory of light propagation, as they do not consider quantum aspects such as photon entanglement. Nevertheless they can still be used to understand a broad range of phenomena that are observed in graphene. In spite of the fundamental quantum nature of graphene interaction with light, a semi-classical approach can be defined where these effects are modeled as a macroscopic medium constitutive equations for electromagnetic fields. More specifically, the interaction between graphene and light is described by its optical conductivity.

2.1.1 Electromagnetic propagation in vacuum

Even though Maxwell's equations are well known, it is instructive to review here their definition and, even more important, the assumptions that can be made with respect to each considered

Chapter 2. Two-dimensional materials theory in the framework of Maxwell's equations

medium. Two-dimensional materials such as graphene can then be introduced by analogy. Maxwell's equations in the differential time-domain form in vacuum are:

$$\begin{aligned}\nabla \cdot \mathbf{D} &= \rho_E \\ \nabla \cdot \mathbf{B} &= \mathbf{0} \\ \nabla \times \mathbf{E} &= -\frac{\partial \mathbf{B}}{\partial t} \\ \nabla \times \mathbf{H} &= \frac{\partial \mathbf{D}}{\partial t} + \mathbf{J}_E \\ \mathbf{D} &= \varepsilon_0 \mathbf{E} \\ \mathbf{B} &= \mu_0 \mathbf{H}\end{aligned}\tag{2.1}$$

where \mathbf{E} is the electric field, \mathbf{D} is the displacement field, \mathbf{H} is the magnetic field, \mathbf{B} is the magnetic induction field, \mathbf{J}_E is the electric current density and ρ_E is the electric charge density. All these quantities are vector fields (except the latter which is scalar) defined on space and time.

Because in the following a complete framework for 2D materials is presented, it is useful to include here the magnetic current density \mathbf{J}_M and the magnetic charge density ρ_M . The updated equations read:

$$\begin{aligned}\nabla \cdot \mathbf{D} &= \rho_E \\ \nabla \cdot \mathbf{B} &= \rho_M \\ \nabla \times \mathbf{E} &= -\frac{\partial \mathbf{B}}{\partial t} - \mathbf{J}_M \\ \nabla \times \mathbf{H} &= \frac{\partial \mathbf{D}}{\partial t} + \mathbf{J}_E \\ \mathbf{D} &= \varepsilon_0 \mathbf{E} \\ \mathbf{B} &= \mu_0 \mathbf{H}\end{aligned}\tag{2.2}$$

Even though there are currently no evidences on the existence of magnetic monopoles, the response of many materials can be magnetic in the most general case, so it is useful to include in Maxwell's equations these auxiliary quantities from the beginning as they will simplify conceptually the mathematical passages.

Because these equations are linear, taking Fourier's transform in time they can be rewritten in

frequency domain:

$$\begin{aligned}
 \nabla \cdot \mathbf{D} &= \rho_E \\
 \nabla \cdot \mathbf{B} &= \rho_M \\
 \nabla \times \mathbf{E} &= -j\omega \mathbf{B} - \mathbf{J}_M \\
 \nabla \times \mathbf{H} &= j\omega \mathbf{D} + \mathbf{J}_E \\
 \mathbf{D} &= \varepsilon_0 \mathbf{E} \\
 \mathbf{B} &= \mu_0 \mathbf{H}
 \end{aligned} \tag{2.3}$$

At frequencies $\omega \neq 0$ the first two equalities derive immediately from the second couple, also considering charge conservation (continuity equations):

$$\begin{aligned}
 \nabla \cdot \mathbf{J}_E &= -j\omega \rho_E \\
 \nabla \cdot \mathbf{J}_M &= -j\omega \rho_M
 \end{aligned} \tag{2.4}$$

which clearly show that all information about sources is contained in the current densities, while full knowledge of charge densities is not sufficient. So the final set of equations needed to fully describe the propagation of electromagnetic waves in vacuum in the electrodynamic case ($\omega \neq 0$) is:

$$\begin{aligned}
 \nabla \times \mathbf{E} &= -j\omega \mathbf{B} - \mathbf{J}_M \\
 \nabla \times \mathbf{H} &= j\omega \mathbf{D} + \mathbf{J}_E \\
 \mathbf{D} &= \varepsilon_0 \mathbf{E} \\
 \mathbf{B} &= \mu_0 \mathbf{H}
 \end{aligned} \tag{2.5}$$

Replacing the \mathbf{D} and \mathbf{B} fields one finally gets:

$$\begin{aligned}
 \nabla \times \mathbf{E} &= -j\omega \mu_0 \mathbf{H} - \mathbf{J}_M \\
 \nabla \times \mathbf{H} &= j\omega \varepsilon_0 \mathbf{E} + \mathbf{J}_E
 \end{aligned} \tag{2.6}$$

If no sources are considered (homogeneous Maxwell's equations), the possible solutions can

Chapter 2. Two-dimensional materials theory in the framework of Maxwell's equations

be decomposed in plane waves:

$$\begin{aligned}
 \mathbf{E} &= \mathbf{E}_0 e^{-j\mathbf{k}\cdot\mathbf{r}} \\
 \mathbf{H} &= \mathbf{H}_0 e^{-j\mathbf{k}\cdot\mathbf{r}} \\
 \mathbf{k}\cdot\mathbf{E}_0 &= 0 \\
 \mathbf{H}_0 &= \frac{\mathbf{k}\times\mathbf{E}_0}{\omega\mu_0} \\
 k^2 &= \mathbf{k}\cdot\mathbf{k} = \omega^2\varepsilon_0\mu_0
 \end{aligned} \tag{2.7}$$

The vector propagation phase and group velocities are defined respectively as:

$$\mathbf{v}_p \triangleq \hat{\mathbf{k}} \frac{\omega}{|\mathbf{k}|} = \mathbf{k} \frac{\omega}{k^2} \tag{2.8}$$

$$\mathbf{v}_g \triangleq \nabla_{\mathbf{k}}\omega \tag{2.9}$$

and for the considered vacuum case they are both equal to the speed of light c :

$$c = \sqrt{\frac{1}{\varepsilon_0\mu_0}} \simeq 2.99792 \cdot 10^8 \text{ m}\cdot\text{s}^{-1} \tag{2.10}$$

For non-evanescent waves, i.e. if the imaginary part of \mathbf{k} are null, \mathbf{E}_0 , \mathbf{H}_0 and \mathbf{k} are all orthogonal at each instant of time. The vector \mathbf{E}_0 is in general complex, and it encodes the *polarization* of the propagating wave. The time evolution of the vector can be obtained, as for any time-harmonic quantity, as $\text{Re}(\mathbf{E}_0 e^{j\omega t})$, and the trajectory of the \mathbf{E}_0 field as it evolves is in the general case an ellipse in space. For non-evanescent plane waves the ellipse lies in the plane orthogonal to \mathbf{k} . Particular cases are the linear polarization ($\text{Re}\mathbf{E}_0 \times \text{Im}\mathbf{E}_0 = 0$) and the circular polarization ($\text{Re}\mathbf{E}_0 \cdot \text{Im}\mathbf{E}_0 = 0$). The ratio between the electric and magnetic field is the vacuum impedance, defined as:

$$\eta \triangleq \frac{E_0}{H_0} = \sqrt{\frac{\mu_0}{\varepsilon_0}} \simeq 376.73 \Omega \tag{2.11}$$

The Poynting vector is defined as:

$$\mathbf{S} \triangleq \mathbf{E} \times \mathbf{H} \quad \text{in time domain} \tag{2.12}$$

$$\mathbf{S} \triangleq \mathbf{E} \times \mathbf{H}^* \quad \text{in frequency domain} \tag{2.13}$$

and this definition is maintained for propagation in media. The stored electromagnetic energy

density is:

$$u = u_E + u_M = \frac{1}{2} \mathbf{D} \cdot \mathbf{E} + \frac{1}{2} \mathbf{B} \cdot \mathbf{H} \quad \text{in time domain} \quad (2.14)$$

2.1.2 Electromagnetic propagation in generic 3D medium

The study of the propagation of electromagnetic waves in materials different from vacuum can be accomplished more easily by redefining the \mathbf{D} and \mathbf{B} fields. The first step to do so is to distinguish two possible origins for the currents \mathbf{J}_M and \mathbf{J}_E :

- Actual external source currents ($\mathbf{J}_E^{\text{src}}$ and $\mathbf{J}_M^{\text{src}}$)
- Currents induced in the medium by the fields \mathbf{E}_0 and \mathbf{H}_0 ($\mathbf{J}_E^{\text{mat}}$ and $\mathbf{J}_M^{\text{mat}}$)

Maxwell equations then are written as:

$$\begin{aligned} \nabla \times \mathbf{E} &= -j\omega \mathbf{B} - \mathbf{J}_M^{\text{mat}} - \mathbf{J}_M^{\text{src}} \\ \nabla \times \mathbf{H} &= j\omega \mathbf{D} + \mathbf{J}_E^{\text{mat}} + \mathbf{J}_E^{\text{src}} \end{aligned} \quad (2.15)$$

and the \mathbf{D} and \mathbf{B} fields are redefined as

$$\begin{aligned} \mathbf{B} &\longleftarrow \mathbf{B} + \frac{\mathbf{J}_M^{\text{mat}}}{j\omega} \\ \mathbf{D} &\longleftarrow \mathbf{D} + \frac{\mathbf{J}_E^{\text{mat}}}{j\omega} \end{aligned} \quad (2.16)$$

The final set of equations needed to describe propagation in the medium becomes then:

$$\begin{aligned} \nabla \times \mathbf{E} &= -j\omega \mathbf{B} - \mathbf{J}_M^{\text{src}} \\ \nabla \times \mathbf{H} &= j\omega \mathbf{D} + \mathbf{J}_E^{\text{src}} \\ \mathbf{D} &= f_{\mathbf{D}}(\mathbf{E}, \mathbf{H}) \\ \mathbf{B} &= f_{\mathbf{B}}(\mathbf{E}, \mathbf{H}) \end{aligned} \quad (2.17)$$

The first two equations are referred to as the *macroscopic Maxwell's equations*, while the last two are the *constitutive equations* of the medium, and represent the full physical model of the remaining phenomena occurring in the material. The two functionals $f_{\mathbf{D}}$ and $f_{\mathbf{B}}$ characterize the materials and relate the displacement field \mathbf{D} and the induced magnetic field \mathbf{B} to the electric and magnetic fields \mathbf{E} and \mathbf{H} . In the most general case, this relation can be quite complex, as the \mathbf{D} and \mathbf{B} in a given point can depend on the \mathbf{E} and \mathbf{H} field in all the points in space and time (with some constraints imposed by causality). Fortunately, for most

Chapter 2. Two-dimensional materials theory in the framework of Maxwell's equations

materials, important simplifications take place in these relationships and are explored in the next sections.

2.1.3 Interface/boundary conditions and 2D materials modelling

Interface conditions are a set of additional equations required when solving electromagnetic problems involving more than one material, and they provide constraints on the electromagnetic fields at the interface of the two materials. Importantly, these conditions can be extended to include the presence of electric or magnetic currents existing exactly at the interface of the two materials (and for this reason called surface currents). This is a crucial step to formalize a model for 2D materials in the Maxwellian framework. Surface current can be described in the distributional sense as a delta function; if the 2D material surface can be described by an equation $f(x, y, z) = 0$ then it must be possible to represent the surface current as a 3D distribution:

$$\begin{aligned} \mathbf{J}_{sE} &= \mathbf{J}_E \delta(f(x, y, z)) \\ \mathbf{J}_{sM} &= \mathbf{J}_M \delta(f(x, y, z)) \end{aligned} \quad (2.18)$$

with the constraint of being parallel to the surface. A similar form must exist for the surface charges. In the reminder, these kind of distributions are referred to as *deltiform*.

The following boundary conditions can then be deduced directly from macroscopic Maxwell's equations:

$$\begin{aligned} \hat{\mathbf{n}}_{12} \times (\mathbf{E}_2 - \mathbf{E}_1) &= \mathbf{J}_{sM} \\ \hat{\mathbf{n}}_{12} \times (\mathbf{H}_2 - \mathbf{H}_1) &= \mathbf{J}_{sE} \\ \hat{\mathbf{n}}_{12} \cdot (\mathbf{B}_2 - \mathbf{B}_1) &= \rho_{sM} \\ \hat{\mathbf{n}}_{12} \cdot (\mathbf{D}_2 - \mathbf{D}_1) &= \rho_{sE} \end{aligned} \quad (2.19)$$

where \mathbf{J}_{sM} and \mathbf{J}_{sE} are the magnetic and electric surface current densities while ρ_{sM} and ρ_{sE} are the magnetic and electric charge densities. One more time, charge densities can be completely determined from the current densities because of charge conservation.

As

(surface) currents in response to the surrounding fields, namely:

$$\begin{aligned} \mathbf{J}_{sE} &= f_{\mathbf{J}_E}(\mathbf{E}_{1\parallel}, \mathbf{E}_{2\parallel}, \mathbf{H}_{1\parallel}, \mathbf{H}_{2\parallel}, \mathbf{B}_{1\perp}, \mathbf{B}_{2\perp}, \mathbf{D}_{1\perp}, \mathbf{D}_{2\perp}) \\ \mathbf{J}_{sM} &= f_{\mathbf{J}_M}(\mathbf{E}_{1\parallel}, \mathbf{E}_{2\parallel}, \mathbf{H}_{1\parallel}, \mathbf{H}_{2\parallel}, \mathbf{B}_{1\perp}, \mathbf{B}_{2\perp}, \mathbf{D}_{1\perp}, \mathbf{D}_{2\perp}) \end{aligned} \quad (2.20)$$

with:

$$\begin{aligned} \mathbf{E}_{1\parallel} &= \hat{\mathbf{n}}_{12} \times \mathbf{E}_1 & \mathbf{E}_{2\parallel} &= \hat{\mathbf{n}}_{12} \times \mathbf{E}_2 & \mathbf{H}_{1\parallel} &= \hat{\mathbf{n}}_{12} \times \mathbf{H}_1 & \mathbf{H}_{2\parallel} &= \hat{\mathbf{n}}_{12} \times \mathbf{H}_2 \\ \mathbf{B}_{1\perp} &= (\hat{\mathbf{n}}_{12} \cdot \mathbf{B}_1) \hat{\mathbf{n}}_{12} & \mathbf{B}_{2\perp} &= (\hat{\mathbf{n}}_{12} \cdot \mathbf{B}_2) \hat{\mathbf{n}}_{12} & \mathbf{D}_{1\perp} &= (\hat{\mathbf{n}}_{12} \cdot \mathbf{D}_1) \hat{\mathbf{n}}_{12} & \mathbf{D}_{2\perp} &= (\hat{\mathbf{n}}_{12} \cdot \mathbf{D}_2) \hat{\mathbf{n}}_{12} \end{aligned} \quad (2.21)$$

Because the differences in Equations 2.19 are actually determined by the surface current themselves, the dependence can be expressed as the sum (or equivalently the average) of these quantities. More specifically, defining:

$$\begin{aligned} \mathbf{E}_{\parallel} &= \frac{1}{2} (\mathbf{E}_{1\parallel} + \mathbf{E}_{2\parallel}) & \mathbf{H}_{\parallel} &= \frac{1}{2} (\mathbf{H}_{1\parallel} + \mathbf{H}_{2\parallel}) \\ \mathbf{D}_{\perp} &= \frac{1}{2} (\mathbf{D}_{1\perp} + \mathbf{D}_{2\perp}) & \mathbf{B}_{\perp} &= \frac{1}{2} (\mathbf{B}_{1\perp} + \mathbf{B}_{2\perp}) \end{aligned} \quad (2.22)$$

we have:

$$\begin{aligned} \mathbf{J}_{sE} &= f_{JE}(\mathbf{E}_{\parallel}, \mathbf{H}_{\parallel}, \mathbf{D}_{\perp}, \mathbf{B}_{\perp}) \\ \mathbf{J}_{sM} &= f_{JM}(\mathbf{E}_{\parallel}, \mathbf{H}_{\parallel}, \mathbf{D}_{\perp}, \mathbf{B}_{\perp}) \end{aligned} \quad (2.23)$$

The latter are the *constitutive equations* of the 2D material.

It is now worthy discussing which conditions are physically necessary to use this particular description of 2D materials. First of all the thickness of the material has to be much smaller than the wavelength in the host 3D material(s). Graphene is, for example, 0.34 nm thick (this is an approximation because the indetermination principle actually “smears out” the position of the electrons), which is three order of magnitude smaller than the wavelength of visible light, and even electrically smaller for infrared or terahertz.

Secondly, the phase of the actual current distribution in the material must have a uniform phase with depth. This rules out, for example, thin metallic films, which do not behave as 2D materials because of variable current phase due to the skin depth effect. Examples of other systems, a part from true 2D materials, are 2D electron gases (2DEGS) obtained, e.g., at the interface of semiconductors, quantum wells or the surface of topological insulators. The latter are 3D materials characterized by conducting states on their surface and, more in general, at each interface between topological insulators and other insulators.

2.1.4 1D and 0D materials

In the previous section it was demonstrated that the modeling of true 2D materials (*deltiform* in one dimensions) is possible in the framework of Maxwell’s equations without the need of modeling them as thin anisotropic 3D materials. It is interesting at this point to briefly address

Chapter 2. Two-dimensional materials theory in the framework of Maxwell's equations

a related question: can this approach be extended also to even lower dimensional systems? For instance carbon nano-tubes (CNT) are an example of 1D materials where the size in two dimensions is very small when compared to the wavelength. Similarly, quantum dots (QD) or even directly single atoms (for optical frequencies and at a single photon level) are electrically small in all three spatial dimensions, and hence can be considered as 0D entities.

The question can be made more precise by asking whether it is possible to determine a value for the impedance of the object directly extending the approach used for 2D materials. The unit of impedance (or reciprocally the conductance) clearly would depend on the number of dimension of the systems, as shown in Table 2.1.

Table 2.1 – Low dimensional systems with impedance and conductance units

Number of dimensions	Examples	Impedance unit	Conductivity unit	Well defined ?
3	Common 3D materials	$\Omega \cdot \text{m}$	$\text{S} \cdot \text{m}^{-1}$	Yes
2	2D materials, quantum wells	Ω	S	Yes
1	1D materials, quantum wires	$\Omega \cdot \text{m}^{-1}$	$\text{S} \cdot \text{m}$	No
0	Nano-particles, quantum dots	$\Omega \cdot \text{m}^{-2}$	$\text{S} \cdot \text{m}^2$	No

Unfortunately, while 2D materials conductivity and impedance are well-defined, it is impossible to describe objects which are *deltiform* in 2 dimensions (1D materials) or in 3 dimensions (0D materials). The reason is that for such low dimensional objects the electromagnetic energy stored in proximity of the electric or magnetic currents tends to infinity, forcing the currents to be null. This is not the case for a surface current, which generates a finite discontinuity in the field, and hence a finite amount of electromagnetic energy. To illustrate this point let us consider the magnetic energy stored in proximity of a 1D material with length l supporting a current I , within a distance r_0 . In the static case (which holds also in the dynamical case if r_0 is much smaller than the wavelength) the total stored energy is given by:

$$\begin{aligned}
 B &= \frac{\mu_0 I}{2\pi r} \\
 U_M &= \frac{1}{2\mu_0} \int_0^l \int_0^{r_0} \int_0^{2\pi} r B^2 d\theta dr dz = \\
 &= \frac{I^2 \mu_0 l}{4\pi} \left[\ln|r| \right]_0^{r_0} = \\
 &= \infty
 \end{aligned} \tag{2.24}$$

A similar demonstration holds for the 0D case.

In conclusions the modeling of truly *deltiform* materials is impossible for the 1D and 0D case, and the actual size of the object (e.g. the CNT diameter) is required to model it in the framework of Maxwell's equations. This is also the reason why the modeling of wire antennas

with numerical methods always requires the actual wire thickness to provide meaningful results. In contrast, graphene, independently of its actual physical thickness, can be modeled as a true 2D material consistently with Maxwell's equations.

2.1.5 Constitutive equations: particular cases

The general constitutive equations for 2D and 3D materials (Equations 2.17,2.23) are expressed in the most general form, and hence little conclusions can be drawn unless more particular cases are explored. Fortunately, most 2D and 3D materials are accurately modeled in these particular cases. In the remainder of this section these simplifications are introduced sequentially and the constitutive equations (for both the 3D and 2D cases) are casted in the corresponding particular form.

In plane 2D response

The first considered particular case concerns 2D materials: for most practical cases, one can neglect the effect of the out-of-plane fields \mathbf{D}_\perp and \mathbf{B}_\perp , and so the corresponding equations become:

$$\begin{aligned} \mathbf{J}_{sE} &= f_{JE}(\mathbf{E}_\parallel, \mathbf{H}_\parallel) \\ \mathbf{J}_{sM} &= f_{JM}(\mathbf{E}_\parallel, \mathbf{H}_\parallel) \end{aligned} \quad (2.25)$$

Notably there is an important exception, which concerns the terahertz response of graphene under strong magnetostatic bias. There the biasing field \mathbf{B}_\perp modifies the response at terahertz frequencies. However, the effect can be modeled including the magnetostatic field as a simple parameter, preserving linearity (see below) for terahertz radiation.

Linear media

Linear media are defined as media where the linear combination of possible field configurations is also a possible field configuration. Hence the constitutive relations for 3D and 2D materials can be rewritten as:

$$\begin{aligned} \mathbf{D} &= \iiint_{\text{space}} \int_{-\infty}^t \left[\underline{f_{EE}}(\mathbf{r}, \mathbf{r}', t, t') \mathbf{E}(\mathbf{r}', t') + \underline{f_{EM}}(\mathbf{r}, \mathbf{r}', t, t') \mathbf{H}(\mathbf{r}', t') \right] dt' d\mathbf{r}' \\ \mathbf{B} &= \iiint_{\text{space}} \int_{-\infty}^t \left[\underline{f_{ME}}(\mathbf{r}, \mathbf{r}', t, t') \mathbf{E}(\mathbf{r}', t') + \underline{f_{MM}}(\mathbf{r}, \mathbf{r}', t, t') \mathbf{H}(\mathbf{r}', t') \right] dt' d\mathbf{r}' \end{aligned} \quad (2.26)$$

Chapter 2. Two-dimensional materials theory in the framework of Maxwell's equations

$$\begin{aligned}
 \mathbf{J}_{sE} &= \iiint_{\text{space}} \int_{-\infty}^t [\underline{\sigma}_{EE}(\mathbf{r}, \mathbf{r}', t, t') \mathbf{E}_{\parallel}(\mathbf{r}', t') + \underline{\sigma}_{EM}(\mathbf{r}, \mathbf{r}', t, t') \mathbf{H}_{\parallel}(\mathbf{r}', t')] dt' d\mathbf{r}' \\
 \mathbf{J}_{sM} &= \iiint_{\text{space}} \int_{-\infty}^t [\underline{\sigma}_{ME}(\mathbf{r}, \mathbf{r}', t, t') \mathbf{E}_{\parallel}(\mathbf{r}', t') + \underline{\sigma}_{MM}(\mathbf{r}, \mathbf{r}', t, t') \mathbf{H}_{\parallel}(\mathbf{r}', t')] dt' d\mathbf{r}' \quad (2.27)
 \end{aligned}$$

Importantly the tensors \underline{f} are 3×3 dyadics as they linearly relate two 3D fields, while the tensors $\underline{\sigma}$ are 2×2 dyadics as they relate 2D fields (i.e. surface currents and tangential \mathbf{E} and \mathbf{H} fields)

Time invariance and frequency dispersion

Time invariance is an important property which applies to most media, which holds when a material does not change its properties with time. If, in addition to linearity, also time invariance is assumed (as done in the remainder of this document) then the constitutive relations for 3D and 2D material can be written as convolutions in time domain:

$$\begin{aligned}
 \mathbf{D} &= \iiint_{\text{space}} \int_{-\infty}^t [\underline{f}_{EE}(\mathbf{r}, \mathbf{r}', t - t') \mathbf{E}(\mathbf{r}', t') + \underline{f}_{EM}(\mathbf{r}, \mathbf{r}', t - t') \mathbf{H}(\mathbf{r}', t')] dt' d\mathbf{r}' \\
 \mathbf{B} &= \iiint_{\text{space}} \int_{-\infty}^t [\underline{f}_{ME}(\mathbf{r}, \mathbf{r}', t - t') \mathbf{E}(\mathbf{r}', t') + \underline{f}_{MM}(\mathbf{r}, \mathbf{r}', t - t') \mathbf{H}(\mathbf{r}', t')] dt' d\mathbf{r}' \quad (2.28)
 \end{aligned}$$

$$\begin{aligned}
 \mathbf{J}_{sE} &= \iiint_{\text{space}} \int_{-\infty}^t [\underline{\sigma}_{EE}(\mathbf{r}, \mathbf{r}', t - t') \mathbf{E}_{\parallel}(\mathbf{r}', t') + \underline{\sigma}_{EM}(\mathbf{r}, \mathbf{r}', t - t') \mathbf{H}_{\parallel}(\mathbf{r}', t')] dt' d\mathbf{r}' \\
 \mathbf{J}_{sM} &= \iiint_{\text{space}} \int_{-\infty}^t [\underline{\sigma}_{ME}(\mathbf{r}, \mathbf{r}', t - t') \mathbf{E}_{\parallel}(\mathbf{r}', t') + \underline{\sigma}_{MM}(\mathbf{r}, \mathbf{r}', t - t') \mathbf{H}_{\parallel}(\mathbf{r}', t')] dt' d\mathbf{r}' \quad (2.29)
 \end{aligned}$$

Taking the Fourier transform in time it is possible to write the relation in the ω spectral domain in a frequency-wise manner as:

$$\begin{aligned}
 \mathbf{D} &= \iiint_{\text{space}} [\underline{f}_{EE}(\mathbf{r}, \mathbf{r}') \mathbf{E}(\mathbf{r}') + \underline{f}_{EM}(\mathbf{r}, \mathbf{r}') \mathbf{H}(\mathbf{r}')] d\mathbf{r}' \\
 \mathbf{B} &= \iiint_{\text{space}} [\underline{f}_{ME}(\mathbf{r}, \mathbf{r}') \mathbf{E}(\mathbf{r}') + \underline{f}_{MM}(\mathbf{r}, \mathbf{r}') \mathbf{H}(\mathbf{r}')] d\mathbf{r}' \quad (2.30)
 \end{aligned}$$

$$\begin{aligned}
 \mathbf{J}_{\text{SE}} &= \iiint_{\text{space}} [\underline{\sigma}_{\text{EE}}(\mathbf{r}, \mathbf{r}') \mathbf{E}_{\parallel}(\mathbf{r}') + \underline{\sigma}_{\text{EM}}(\mathbf{r}, \mathbf{r}') \mathbf{H}_{\parallel}(\mathbf{r}')] d\mathbf{r}' \\
 \mathbf{J}_{\text{SM}} &= \iiint_{\text{space}} [\underline{\sigma}_{\text{ME}}(\mathbf{r}, \mathbf{r}') \mathbf{E}_{\parallel}(\mathbf{r}') + \underline{\sigma}_{\text{MM}}(\mathbf{r}, \mathbf{r}') \mathbf{H}_{\parallel}(\mathbf{r}')] d\mathbf{r}'
 \end{aligned} \tag{2.31}$$

where the dependence on ω of all the quantities has been omitted. If at least one among the kernels ($f_{\text{DE}}, f_{\text{DH}} \dots$) is not constant with ω then the medium is said to be *frequency dispersive* (or simply *dispersive*), otherwise it is *non-dispersive*.

Spatial homogeneity and locality

The analogous of time invariance in the spatial domain is the medium homogeneity, namely the fact that the medium has the same properties at any position in space. If that is assumed in addition to time invariance, the kernels further simplifies:

$$\begin{aligned}
 \mathbf{D} &= \iiint_{\text{space}} [\underline{f}_{\text{EE}}(\mathbf{r} - \mathbf{r}') \mathbf{E}(\mathbf{r}') + \underline{f}_{\text{EM}}(\mathbf{r} - \mathbf{r}') \mathbf{H}(\mathbf{r}')] d\mathbf{r}' \\
 \mathbf{B} &= \iiint_{\text{space}} [\underline{f}_{\text{ME}}(\mathbf{r} - \mathbf{r}') \mathbf{E}(\mathbf{r}') + \underline{f}_{\text{MM}}(\mathbf{r} - \mathbf{r}') \mathbf{H}(\mathbf{r}')] d\mathbf{r}'
 \end{aligned} \tag{2.32}$$

$$\begin{aligned}
 \mathbf{J}_{\text{SE}} &= \iiint_{\text{space}} [\underline{\sigma}_{\text{EE}}(\mathbf{r} - \mathbf{r}') \mathbf{E}_{\parallel}(\mathbf{r}') + \underline{\sigma}_{\text{EM}}(\mathbf{r} - \mathbf{r}') \mathbf{H}_{\parallel}(\mathbf{r}')] d\mathbf{r}' \\
 \mathbf{J}_{\text{SM}} &= \iiint_{\text{space}} [\underline{\sigma}_{\text{ME}}(\mathbf{r} - \mathbf{r}') \mathbf{E}_{\parallel}(\mathbf{r}') + \underline{\sigma}_{\text{MM}}(\mathbf{r} - \mathbf{r}') \mathbf{H}_{\parallel}(\mathbf{r}')] d\mathbf{r}'
 \end{aligned} \tag{2.33}$$

Taking the Fourier transform in space it is possible to write the relation in the \mathbf{k} spectral domain as:

$$\begin{aligned}
 \mathbf{D} &= \underline{f}_{\text{EE}} \mathbf{E} + \underline{f}_{\text{EM}} \mathbf{H} \\
 \mathbf{B} &= \underline{f}_{\text{ME}} \mathbf{E} + \underline{f}_{\text{MM}} \mathbf{H}
 \end{aligned} \tag{2.34}$$

$$\begin{aligned}
 \mathbf{J}_{\text{SE}} &= \underline{\sigma}_{\text{EE}} \mathbf{E}_{\parallel} + \underline{\sigma}_{\text{EM}} \mathbf{H}_{\parallel} \\
 \mathbf{J}_{\text{SM}} &= \underline{\sigma}_{\text{ME}} \mathbf{E}_{\parallel} + \underline{\sigma}_{\text{MM}} \mathbf{H}_{\parallel}
 \end{aligned} \tag{2.35}$$

Chapter 2. Two-dimensional materials theory in the framework of Maxwell's equations

where each equation holds for each considered wave-vector \mathbf{k} . If the kernels (now simple coefficients) are constant with \mathbf{k} (this is the case for most cases) then the material is said to be *local*. Otherwise it is said to be *spatially dispersive* or *non-local*. Importantly, for a local non-homogeneous medium, equations 2.34 and 2.35 still hold, but they hold for each point \mathbf{r} in space rather than for each point in the spectral \mathbf{k} domain.

In most cases, materials can be treated as local. If, however, the fields are forced in very confined regions or have very large spatial variability, spatial dispersion might become relevant. For example, the anomalous skin effect occurs when the mean free path of carriers in a conductor (typically metal at low temperature) becomes comparable with the skin depth. The effect can only be explained in a non local way, because the electron's inertia causes, for each point in space, electric currents dependent on the fields in a surrounding area, rather than just in the point itself. Another example are graphene plasmons, which in certain extreme confinement regions are expected to be affected by non-locality. Again, this is due to carrier's dynamics.

For 3D materials, the four tensor quantities in equation 2.34 have specific names:

$$\underline{\mathbf{D}} = \underline{\varepsilon}\underline{\mathbf{E}} + \underline{\xi}\underline{\mathbf{H}} \quad (2.36)$$

$$\underline{\mathbf{B}} = \underline{\zeta}\underline{\mathbf{E}} + \underline{\mu}\underline{\mathbf{H}} \quad (2.37)$$

$$\underline{\varepsilon}_r = \underline{\varepsilon}_0^{-1}\underline{\varepsilon} \quad (2.38)$$

$$\underline{\mu}_r = \underline{\mu}_0^{-1}\underline{\mu} \quad (2.39)$$

and can be represented in a single linear relationship:

$$\begin{pmatrix} \underline{\mathbf{D}} \\ \underline{\mathbf{B}} \end{pmatrix} = \underline{\mathbf{C}} \begin{pmatrix} \underline{\mathbf{E}} \\ \underline{\mathbf{H}} \end{pmatrix} \quad \underline{\mathbf{C}} = \left(\begin{array}{c|c} \underline{\varepsilon} & \underline{\xi} \\ \hline \underline{\zeta} & \underline{\mu} \end{array} \right) \quad (2.40)$$

where $\underline{\mathbf{C}}$ is the material matrix, $\underline{\varepsilon}$ is the material permittivity tensor, $\underline{\mu}$ is the permeability tensor, while $\underline{\xi}$ and $\underline{\zeta}$ are the magneto-electric dyadics. The latter are usually represented as $\underline{\xi} = \underline{\chi}^T - j\underline{\kappa}^T$ and $\underline{\zeta} = \underline{\chi} + j\underline{\kappa}$, so that [102]:

$$\begin{pmatrix} \underline{\mathbf{D}} \\ \underline{\mathbf{B}} \end{pmatrix} = \underline{\mathbf{C}} \begin{pmatrix} \underline{\mathbf{E}} \\ \underline{\mathbf{H}} \end{pmatrix} \quad \underline{\mathbf{C}} = \left(\begin{array}{c|c} \underline{\varepsilon} & \underline{\chi}^T - j\underline{\kappa}^T \\ \hline \underline{\chi} + j\underline{\kappa} & \underline{\mu} \end{array} \right) \quad (2.41)$$

This representation has two serious drawbacks, which were highlighted already in [96]. The first drawback is that it is not easy to express a condition for causality in the considered material using this representation. The second is that the conditions for reciprocity are not straightforward (the meaning and importance of reciprocity are recalled later). In fact reciprocity implies symmetry in the permittivity and permeability tensors, but this is not the case for the full $\underline{\mathbf{C}}$ matrix. On the contrary, the $\underline{\chi}$ tensor is referred to as the non-reciprocal Tellegen dyadic and $\underline{\kappa}$ as the reciprocal chiral dyadic [54].

To solve these issues it was proposed [96] to redefine the material matrix in order to be always consistent with the concept of impedance in terms of passivity, causality and reciprocity:

$$\mathbf{Q} = \underline{\mathbf{Y}}\mathbf{R} \quad \underline{\mathbf{Y}} = j\omega \left(\begin{array}{c|c} \underline{\boldsymbol{\varepsilon}} & j\underline{\boldsymbol{\chi}}^T + \underline{\boldsymbol{\kappa}}^T \\ \hline -j\underline{\boldsymbol{\chi}} + \underline{\boldsymbol{\kappa}} & \underline{\boldsymbol{\mu}} \end{array} \right) = \left(\begin{array}{c|c} \underline{\boldsymbol{\varepsilon}} & j\underline{\boldsymbol{\xi}} \\ \hline -j\underline{\boldsymbol{\zeta}} & \underline{\boldsymbol{\mu}} \end{array} \right) \quad (2.42)$$

$$\mathbf{Q} = j\omega \left(\frac{j\mathbf{D}}{\mathbf{B}} \right) = j\omega \begin{pmatrix} j\mathbf{D}_x \\ j\mathbf{D}_y \\ j\mathbf{D}_z \\ \mathbf{B}_x \\ \mathbf{B}_y \\ \mathbf{B}_z \end{pmatrix} \quad \mathbf{R} = \left(\frac{j\mathbf{E}}{\mathbf{H}} \right) = \begin{pmatrix} j\mathbf{E}_x \\ j\mathbf{E}_y \\ j\mathbf{E}_z \\ \mathbf{H}_x \\ \mathbf{H}_y \\ \mathbf{H}_z \end{pmatrix} \quad (2.43)$$

The $\underline{\mathbf{Y}}$ matrix has in particular the property of being symmetrical for reciprocal materials. Importantly, although the matrix was called $\underline{\mathbf{Z}}$ in [96] to recall similar properties with respect to the impedances, it contains terms with multiple dimensions in the SI system, and it is renamed here as $\underline{\mathbf{Y}}$ because of its closer resemblance with an admittance matrix, as will be evident in the following. In fact, as a further step, Equation 2.35 can be extended to 3D materials:

$$\begin{aligned} \mathbf{J}_E &= \underline{\sigma}_{EE}\mathbf{E} + \underline{\sigma}_{EM}\mathbf{H} \\ \mathbf{J}_M &= \underline{\sigma}_{ME}\mathbf{E} + \underline{\sigma}_{MM}\mathbf{H} \end{aligned} \quad (2.44)$$

and the quantities replaced in the $\underline{\mathbf{Y}}$ matrix:

$$\underline{\mathbf{Y}} = \left(\begin{array}{c|c} j\omega\varepsilon_0 + \underline{\sigma}_{EE} & j\underline{\sigma}_{EM} \\ \hline -j\underline{\sigma}_{ME} & j\omega\mu_0 + \underline{\sigma}_{MM} \end{array} \right) \quad (2.45)$$

By analogy, the 2D material matrix is:

$$\underline{\mathbf{Y}} = \left(\begin{array}{c|c} \underline{\sigma}_{EE} & j\underline{\sigma}_{EM} \\ \hline -j\underline{\sigma}_{ME} & \underline{\sigma}_{MM} \end{array} \right) \quad (2.46)$$

The absence of the diagonal constant terms is linked to the fact that 2D materials have no volume, and hence no background vacuum permittivity or permeability. These matrices will be used especially in the next chapter.

Isotropy, chirality and reciprocity

The previously described cases are still very general, and a further classification is possible accordingly to the properties of the material matrix. Table 2.2 is a classification of the main types of 3D materials (and by extension 2D) including relevant parameters and number of complex scalar values needed to fully describe the material. The most general case are bi-

Table 2.2 – Classification of 2D and 3D materials according to chirality and isotropy

	3D materials	2D materials
Bi-anisotropic	$\underline{\varepsilon}, \underline{\chi}, \underline{\zeta}, \underline{\mu}$: 36 parameters	$\underline{\sigma}_{EE}, \underline{\sigma}_{EM}, \underline{\sigma}_{ME}, \underline{\sigma}_{MM}$: 16 parameters
↳ [reciprocal case]	$\underline{\varepsilon}, \underline{\zeta}, \underline{\mu}$: 21 parameters	$\underline{\sigma}_{EE}, \underline{\sigma}_{EM}, \underline{\sigma}_{ME}, \underline{\sigma}_{MM}$: 10 parameters
Bi-isotropic	$\underline{\varepsilon}, \underline{\chi}, \underline{\zeta}, \underline{\mu}$: 4 parameters	$\underline{\sigma}_{EE}, \underline{\sigma}_{EM}, \underline{\sigma}_{ME}, \underline{\sigma}_{MM}$: 4 parameters
↳ [reciprocal case]	$\underline{\varepsilon}, \underline{\zeta}, \underline{\mu}$: 3 parameters	$\underline{\sigma}_{EE}, \underline{\sigma}_{EM}, \underline{\sigma}_{ME}, \underline{\sigma}_{MM}$: 3 parameters
Anisotropic	$\underline{\varepsilon}, \underline{\mu}$: 18 parameters	$\underline{\sigma}_{EE}, \underline{\sigma}_{MM}$: 8 parameters
↳ [reciprocal case]	$\underline{\varepsilon}, \underline{\mu}$: 12 parameters	$\underline{\sigma}_{EE}, \underline{\sigma}_{MM}$: 6 parameters
Gyrotropic	$\underline{\varepsilon}, \underline{\mu}$: 6 parameters	$\underline{\sigma}_{EE}, \underline{\sigma}_{MM}$: 4 parameters
Isotropic	$\underline{\varepsilon}, \underline{\mu}$: 2 parameters	$\underline{\sigma}_{EE}, \underline{\sigma}_{MM}$: 2 parameters
Anisotropic amagnetic	$\underline{\varepsilon}$: 9 parameters	$\underline{\sigma}_{EE}$: 4 parameters
↳ [reciprocal case]	$\underline{\varepsilon}$: 6 parameters	$\underline{\sigma}_{EE}$: 3 parameters
Gyrotropic amagnetic	$\underline{\varepsilon}$: 3 parameters	$\underline{\sigma}_{EE}$: 2 parameters
Isotropic amagnetic	$\underline{\varepsilon}$: 1 parameter	$\underline{\sigma}_{EE}$, 1 parameter

anisotropic materials which requires the full specification of the full \underline{Y} matrix. This implies 36 complex parameters to be specified for 3D materials and 16 for 2D materials. The term *anisotropic* refers to the fact that the material is not invariant with a 3D rotation (or 2D for 2D materials), i.e. its behavior depends on the material orientation, while the prefix *bi-* refers to the fact that there is a crossed dependence of electrical properties and magnetic properties (magneto-electric media). Bi-isotropic materials are invariant to 3D rotations but still have magneto-electric properties – for example a non-racemic suspension of chiral molecules falls in this category. Anisotropic materials have pure magnetic and electric interaction, and are dependent on the orientation, while isotropic materials are rotationally invariant. Gyrotropic materials are invariant to rotations along a specific axis (typically the tensor is given assuming that this axis is z). For 3D materials the tensors then take the following form:

$$\underline{\varepsilon} = \begin{pmatrix} \varepsilon_d & \varepsilon_o & 0 \\ -\varepsilon_o & \varepsilon_d & 0 \\ 0 & 0 & \varepsilon_z \end{pmatrix} \quad \underline{\mu} = \begin{pmatrix} \mu_d & \mu_o & 0 \\ -\mu_o & \mu_d & 0 \\ 0 & 0 & \mu_z \end{pmatrix} \quad (2.47)$$

and for 2D materials

$$\underline{\sigma}_{EE} = \begin{pmatrix} \sigma_{dEE} & \sigma_{oEE} \\ -\sigma_{oEE} & \sigma_{dEE} \end{pmatrix} \quad \underline{\sigma}_{MM} = \begin{pmatrix} \sigma_{dMM} & \sigma_{oMM} \\ -\sigma_{oMM} & \sigma_{dMM} \end{pmatrix} \quad (2.48)$$

The term *amagnetic* is used to indicate that the material has negligible magnetic properties.

Reciprocal materials satisfy the **Lorentz reciprocity principle**, which means that the \underline{Y} matrix is symmetrical, adding more constraints and reducing the number of parameters needed to fully describe the material. Importantly, isotropic materials are always reciprocal and gyrotropic ones are always non-reciprocal (a part from trivial sub-cases). Reciprocity is discussed in details in the reminder of this chapter.

All the considered 2D materials in this thesis are assumed to be amagnetic, and the interaction is only of electrical nature. Consequently the tensor $\underline{\sigma}_{EE}$ is sufficient to describe the material, and from now on it will be referred to simply as $\underline{\sigma}$. Relevant 2D materials examples are graphene (amagnetic isotropic), black phosphorus (reciprocal, amagnetic anisotropic) and graphene under magnetic bias (gyrotropic amagnetic).

Finally, perfect electric conductors (PEC) and perfect magnetic conductors (PMC) are 2D materials where $\underline{\sigma}_{EE}$ or $\underline{\sigma}_{MM}$ respectively tend to infinity times the identity matrix.

2.2 Lorentz reciprocity principle

Lorentz reciprocity principle is an extremely important principle which, expressed in a very simplified way, claims that if the source of electromagnetic and an observer are switched of positions then the observer will perceive the same amount of electromagnetic radiation. Because the discussion of the validity of this principle involves also different cases of media, let us rewrite here Equation 2.15 as

$$\begin{aligned}\nabla \times \mathbf{E} &= -j\omega\mu_0\mathbf{H} - \mathbf{J}_M^{\text{mat}} - \mathbf{J}_M^{\text{src}} \\ \nabla \times \mathbf{H} &= j\omega\varepsilon_0\mathbf{E} + \mathbf{J}_E^{\text{mat}} + \mathbf{J}_E^{\text{src}}\end{aligned}\tag{2.49}$$

Defining $\mathbf{J}_E^{\text{tot}} \triangleq \mathbf{J}_E^{\text{mat}} + \mathbf{J}_E^{\text{src}}$ and $\mathbf{J}_M^{\text{tot}} \triangleq \mathbf{J}_M^{\text{mat}} + \mathbf{J}_M^{\text{src}}$ the Maxwell's equations takes the microscopic form (i.e. in vacuum):

$$\begin{aligned}\nabla \times \mathbf{E} &= -j\omega\mu_0\mathbf{H} - \mathbf{J}_M^{\text{tot}} \\ \nabla \times \mathbf{H} &= j\omega\varepsilon_0\mathbf{E} + \mathbf{J}_E^{\text{tot}}\end{aligned}\tag{2.50}$$

Let us now consider the same electromagnetic system under two different excitations conditions, namely $\mathbf{J}_E^{\text{src}}$ and $\mathbf{J}_M^{\text{src}}$ change from one condition to the other and consequently all the fields do. We name these two conditions 'A' and 'B', and we use these as subscripts in all the

Chapter 2. Two-dimensional materials theory in the framework of Maxwell's equations

resulting fields. Let us then define the following fields:

$$\mathbf{W} \triangleq \mathbf{E}_A \times \mathbf{H}_B - \mathbf{E}_B \times \mathbf{H}_A \quad (2.51)$$

$$W_{J,E}^{\text{tot}} \triangleq (\mathbf{J}_{E,A}^{\text{tot}} \cdot \mathbf{E}_B - \mathbf{J}_{E,B}^{\text{tot}} \cdot \mathbf{E}_A) \quad (2.52)$$

$$W_{J,H}^{\text{tot}} \triangleq -(\mathbf{J}_{M,A}^{\text{tot}} \cdot \mathbf{H}_B - \mathbf{J}_{M,B}^{\text{tot}} \cdot \mathbf{H}_A) \quad (2.53)$$

$$W_J^{\text{tot}} \triangleq W_{J,E}^{\text{tot}} + W_{J,H}^{\text{tot}} \quad (2.54)$$

$$W_{J,E}^{\text{mat}} \triangleq (\mathbf{J}_{E,A}^{\text{mat}} \cdot \mathbf{E}_B - \mathbf{J}_{E,B}^{\text{mat}} \cdot \mathbf{E}_A) \quad (2.55)$$

$$W_{J,H}^{\text{mat}} \triangleq -(\mathbf{J}_{M,A}^{\text{mat}} \cdot \mathbf{H}_B - \mathbf{J}_{M,B}^{\text{mat}} \cdot \mathbf{H}_A) \quad (2.56)$$

$$W_J^{\text{mat}} \triangleq W_{J,E}^{\text{mat}} + W_{J,H}^{\text{mat}} \quad (2.57)$$

$$W_{J,E}^{\text{src}} \triangleq (\mathbf{J}_{E,A}^{\text{src}} \cdot \mathbf{E}_B - \mathbf{J}_{E,B}^{\text{src}} \cdot \mathbf{E}_A) \quad (2.58)$$

$$W_{J,H}^{\text{src}} \triangleq -(\mathbf{J}_{M,A}^{\text{src}} \cdot \mathbf{H}_B - \mathbf{J}_{M,B}^{\text{src}} \cdot \mathbf{H}_A) \quad (2.59)$$

$$W_J^{\text{src}} \triangleq W_{J,E}^{\text{src}} + W_{J,H}^{\text{src}} \quad (2.60)$$

These fields are not physical fields, in the sense that they are not defined in a given space and moment because they actually depend on two distinct situations. Hence they can be used to compare the propagation in these two cases. For the moment we assume that only excitation changes in the two conditions 'A' and 'B', later we will also assume that the materials involved can change, always to compare the propagation in different conditions.

Let us now consider the divergence of the \mathbf{W} field:

$$\begin{aligned} \nabla \cdot \mathbf{W} &= \nabla \cdot (\mathbf{E}_A \times \mathbf{H}_B - \mathbf{E}_B \times \mathbf{H}_A) \\ &= (\nabla \times \mathbf{E}_A) \cdot \mathbf{H}_B - (\nabla \times \mathbf{H}_B) \cdot \mathbf{E}_A - (\nabla \times \mathbf{E}_B) \cdot \mathbf{H}_A + (\nabla \times \mathbf{H}_A) \cdot \mathbf{E}_B \end{aligned} \quad (2.61)$$

Replacing Maxwell's Equations in the curls we obtain:

$$\nabla \cdot \mathbf{W} = W_J^{\text{tot}} \quad (2.62)$$

which is known as the Lorentz reciprocity principle. This principle will be also used in its integral formulation in the reminder of this thesis, which reads:

$$\oiint_S \mathbf{w} \cdot d\mathbf{S} = \iiint_V W_J^{\text{tot}} dV \quad (2.63)$$

where V is a volume of space and S is the closed surface delimiting this volume. If we assume that in volume V there are no sources then inside it we have $W_J^{\text{src}} = 0$ and $W_J^{\text{tot}} = W_J^{\text{mat}}$. Using

the formalism of the Y matrix shown above, it is possible rewriting this quantity as:

$$W_J^{\text{mat}} = \mathbf{R}_A \underline{Y} \mathbf{R}_B - \mathbf{R}_B \underline{Y} \mathbf{R}_A = \mathbf{R}_A (\underline{Y} - \underline{Y}^T) \mathbf{R}_B \quad (2.64)$$

If the \underline{Y} matrix is symmetric then the material is said to be *reciprocal* and the following holds:

$$\nabla \cdot \mathbf{W} = 0 \quad (2.65)$$

$$\oiint_S \mathbf{W} \cdot d\mathbf{S} = 0 \quad (2.66)$$

The importance of this relation will be evident when defining the *scattering matrix* formalism. All the above passages apply both for 3D and 2D materials.

2.3 Passive, active and lossless materials

Materials can be classified according to their ability to attenuate or amplify propagating electromagnetic waves in the following categories:

Lossless materials: cannot absorb or amplify electromagnetic fields.

Passive materials: can absorb electromagnetic energy but not provide it

Active materials: can provide electromagnetic energy and hence amplify waves.

The power flow is given by the real part of the Poynting vector $\mathbf{S} \triangleq \mathbf{E} \times \mathbf{H}^*$. The capability of generating or absorbing optical power in a material is hence linked to $\text{Re}(\nabla \cdot \mathbf{S})$. Following similar passages as in the reciprocity case we find that the power generated in the material is:

$$\text{Re}(\nabla \cdot \mathbf{S}) = -\text{Re}(\mathbf{R}^* \cdot \mathbf{Q}) = -\text{Re}(\mathbf{R}^H \underline{Y} \mathbf{R}) = -\frac{1}{2} \mathbf{R}^H (\underline{Y} + \underline{Y}^H) \mathbf{R} \quad (2.67)$$

If we consider without loss of generality $|\mathbf{R}| = 1$ then the range of possible values for this expression is bounded by the real part of the eigenvalues of \underline{Y} . Negative divergence means that energy is being absorbed in the material and vice versa. Hence:

Lossless materials: All eigenvalues of \underline{Y} have zero real part.

Passive materials: At least one eigenvalue of \underline{Y} has positive real part, no one has negative real part.

Active materials: At least one eigenvalue of \underline{Y} has negative real part.

This is exactly the behavior of a generic admittance matrix, confirming the advantage of using

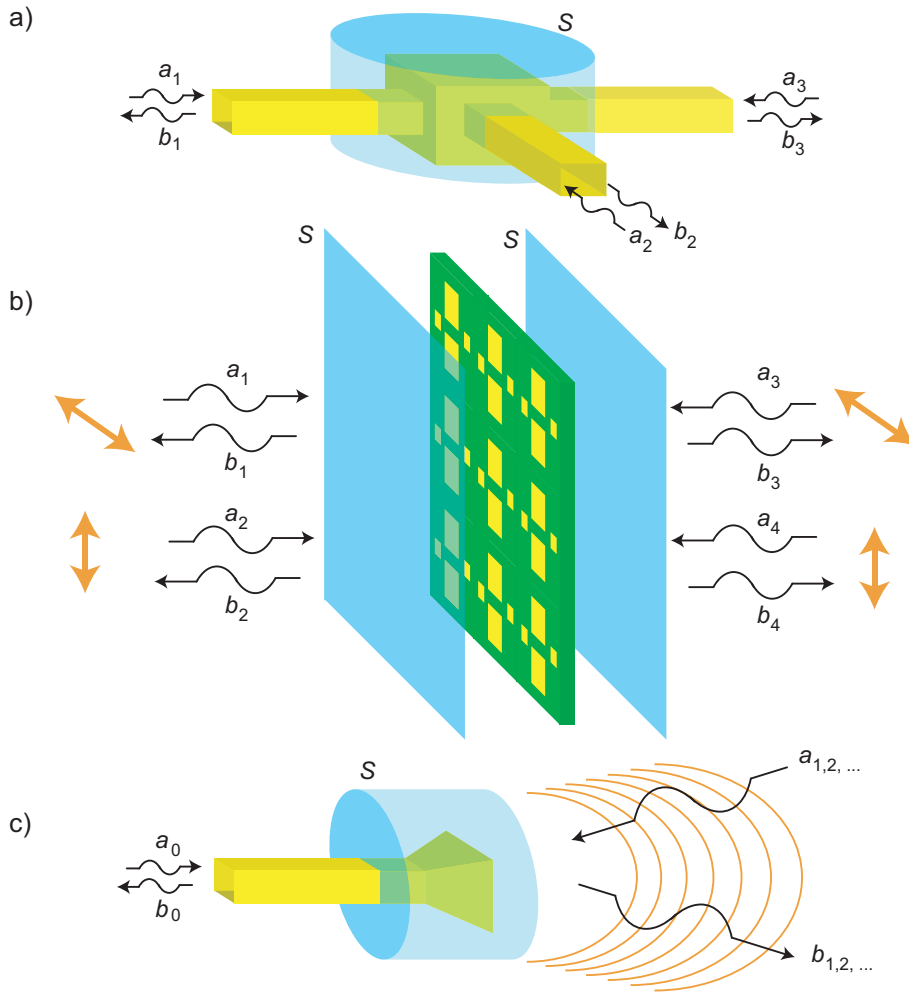


Figure 2.1 – Definition of scattering parameters for a) guided structures, b) layered structures and metasurfaces, c) antennas.

the \underline{Y} notation.

2.4 The scattering matrix formalism

Most of the photonic devices considered in this thesis interact with lights propagating as known *modes*. The concept of *mode* is very general and it indicates a particular way in which light can propagate resulting as a solution of Maxwell's Equations potentially in presence of waveguides. Three cases are of particular interest for this dissertation (see Figure 2.1):

- Electromagnetic wave propagating in waveguides (for guided devices).
- Electromagnetic wave propagating in free space (for planar devices).
- Electromagnetic waves radiating from antennas.

In all cases the considered modes are supported – for simplicity – by lossless reciprocal media (e.g. vacuum, PEC or lossless dielectrics). Each mode can propagate semi-infinitely in one direction, while on the other it terminates on the device. Because of reciprocity, each of these *access modes* can support a *progressive* (or *incident*) wave towards the device and a *regressive* (or *scattered*) one propagating away from it. The device is surrounded by a surface S which encloses it and that is sufficiently large to ensure that the fields existing on S are solely due to the considered access modes and not to, e.g., evanescent fields from the structure. S is called *enveloping surface* after the concept is introduced in [77], chapter 5. Importantly, the access modes must be orthogonal on S , as described in the following.

Figure 2.1a shows an example where S encloses a device (*junction*) whose terminals are waveguides. Figure 2.1b instead represents a planar device, which operates with plane waves; the S surface is simply the union of two planes which are taken sufficiently distant from the planar device. Polarization can be described using horizontal and vertical components, and 2D infinite periodic structures (metasurfaces) can be modeled provided that the unit cell is smaller than the wavelength. If it is larger, additional grating plane waves modes need to be considered in the scattering matrix formalism. Figure 2.1c shows that also antennas (i.e. structures converting guided modes to free space propagation) can be described in this formalism, by considering a feeding mode and decomposing the radiated field in orthogonal modes (e.g. spherical harmonics).

Once the access modes have been identified – and assuming that linearity holds – the structure can be completely described using a **scattering matrix** \underline{S} [77]. The scattering matrix describes the linear relationship between the incident and scattered waves; the latter are modeled assuming that each mode can be written as [77]:

$$\begin{aligned} \mathbf{E}_{\parallel i} &= (a_i e^{-\gamma z} + b_i e^{+\gamma z}) \mathbf{e}_{\parallel i}(x, y) \\ \mathbf{H}_{\parallel i} &= (a_i h^{-\gamma z} - b_i h^{+\gamma z}) \mathbf{h}_{\parallel i}(x, y) \end{aligned} \quad (2.68)$$

a_i and b_i represent the progressive and regressive amplitudes of the i -th mode and they are expressed in $W^{1/2}$. The complex scalar γ is the propagation coefficient along the modal propagation coordinate z while e and h are the tangential electric and magnetic fields distributions along the two transversal coordinates x and y .

These distributions must be orthonormal for a proper mode decomposition, hence:

$$\oint_S \mathbf{e}_{\parallel i} \times \mathbf{h}_{\parallel j}^* = \delta_{ij} \quad (2.69)$$

where δ_{ij} is the Kronecker delta. In this formalism, the device internal details are completely

Chapter 2. Two-dimensional materials theory in the framework of Maxwell's equations

described by \underline{S} :

$$\mathbf{b} = \underline{S}\mathbf{a} \quad (2.70)$$

A number of properties of the device can be expressed in a simple form using \underline{S} . For example, for lossless devices \underline{S} is unitary, that is $\underline{S}\underline{S}^H = \underline{I}$ where \underline{I} is the identity matrix. More in general, the eigenvalues of \underline{S} provide information on device passivity, in a similar way as the \underline{Y} matrix does for a material, however the magnitude of the eigenvalues is involved here:

Lossless device All eigenvalues of \underline{S} have magnitude 1.

Passive device At least one eigenvalue of \underline{S} has magnitude < 1 , none has magnitude > 1 .

Active device At least one eigenvalue of \underline{S} has magnitude > 1 .

This is due to the fact that the total power entering the device is

$$\begin{aligned} P_{\text{in}} &= P_{\text{inc}} - P_{\text{scatt}} \\ &= \mathbf{a}^H \mathbf{a} - \mathbf{b}^H \mathbf{b} \\ &= \mathbf{a}^H \mathbf{a} - \mathbf{a}^H \underline{S}^H \underline{S} \mathbf{a} \\ &= \mathbf{a}^H (\underline{I} - \underline{S}^H \underline{S}) \mathbf{a} \\ &= - \oiint_S \text{Re}(\mathbf{S} \cdot d\mathbf{S}) \\ &= - \iiint_V \text{Re}(\nabla \cdot \mathbf{S} dV) \\ &= \frac{1}{2} \mathbf{R}^H (\underline{Y} + \underline{Y}^H) \mathbf{R} \end{aligned} \quad (2.71)$$

and the eigenvalues of $\underline{S}^H \underline{S}$ are the absolute value squared of the eigenvalues of \underline{S} .

Similarly, if the device contains only reciprocal materials, then it is possible to consider two excitations $\mathbf{a}_A, \mathbf{a}_B$ and knowing already that:

$$\oiint_S \mathbf{W} \cdot d\mathbf{S} = 0 \quad (2.72)$$

we have [77, 96]:

$$\begin{aligned}
 \iiint_V \nabla \cdot \mathbf{W} dV &= \iiint_V \mathbf{R}_A (\underline{Y} - \underline{Y}^T) \mathbf{R}_B dV \\
 &= \oiint_S \mathbf{W} \cdot d\mathbf{S} \\
 &= \oiint_S (\mathbf{E}_A \times \mathbf{H}_B - \mathbf{E}_B \times \mathbf{H}_A) \cdot d\mathbf{S} \\
 &= 2(\mathbf{a}_B^T \mathbf{b}_A - \mathbf{a}_A^T \mathbf{b}_B) \\
 &= 2(\mathbf{a}_B^T \mathbf{b}_A - \mathbf{b}_B^T \mathbf{a}_A) \\
 &= 2(\mathbf{a}_B^T \underline{S} \mathbf{a}_A - \mathbf{a}_B^T \underline{S}^T \mathbf{a}_A) \\
 &= 2\mathbf{a}_B^T (\underline{S} - \underline{S}^T) \mathbf{a}_A
 \end{aligned} \tag{2.73}$$

Importantly, the first passage above is just a sketch of the full demonstration, which makes use of Maxwell's equations for \mathbf{e} and \mathbf{h} to prove this result. If the materials are reciprocal, this result implies $\underline{S} = \underline{S}^T$, namely the scattering matrix of reciprocal devices is symmetric.

In Chapter 3 this result will be generalized, and it will be demonstrated that, if the device contains a single non-reciprocal material, the transposition of the \underline{Y} matrix of the material causes the transposition of the \underline{S} matrix of the device. More in general, if all the \underline{Y} matrices of the used materials are transposed (and only non reciprocal materials are affected by this operation), the final \underline{S} matrix of the transformed device is also transposed. Most optical non-reciprocal materials, including graphene, need a biasing magnetostatic field to acquire non-reciprocal properties. Usually, if this magnetic field is reversed, the \underline{Y} matrix of the device is transposed, and, consequently, the scattering matrix is also transposed. This theorem is already known in literature [113, 54], but it can be demonstrated as a straightforward corollary of the theory presented in Chapter 3.

2.4.1 Scattering matrix for antennas

In Chapter 3 a description of antennas based on scattering parameters is needed. This is a relatively unusual approach, and hence it is fully derived in this subsection. This can be achieved by decomposing the radiated pattern in a summation of orthogonal modes. These could be for instances spherical harmonics, but any set of modes $\mathbf{E}_i(\theta, \varphi)$ satisfying orthonormality can be used, i.e.:

$$\frac{1}{4\pi\eta} \oiint \mathbf{E}_i(\theta, \varphi) \cdot \mathbf{E}_j^*(\theta, \varphi) d\Omega = \delta_{ij} P_{\text{ref}} \tag{2.74}$$

Chapter 2. Two-dimensional materials theory in the framework of Maxwell's equations

where the integral is taken on the sphere to infinity, η is the free space impedance and P_{ref} is some reference power. We can then fully describe the electromagnetic properties of the antenna with an infinite-dimensional scattering matrix \underline{S} defined for convenience with 0-based indexing, where the 0 index refers to the antenna input port and the other indexes to the radiation modes. In this formalism $S_{00} = \Gamma$ refers to the antenna input reflection coefficient, S_{i0} for $i \geq 1$ to the radiation pattern, S_{0j} for $j \geq 1$ to the reception pattern and S_{ij} for $i, j \geq 1$ to the scattering behavior of the antenna when loaded with a matched load. In practice, this infinite scattering matrix can be truncated in order to include only relevant modes, especially for electrically small antennas; however we will not make use of such truncation in the reminder as it is not needed. The total field radiated by the antenna can then be expressed assuming an incident forward power wave a_0 on the input port with power $P_{\text{forw}} = |a_0|^2 P_{\text{ref}}$. Notice that we are assuming here (and only for the antenna case) that the power waves a_i and b_j are dimensionless complex numbers, normalized to a the reference power P_{ref} . This is useful as it simplifies following expressions and reconciles the results to the orthonormality relation above which needs a reference power to be defined. The expression for the total radiated field is:

$$\mathbf{E}_{\text{rad}}(\theta, \varphi) = a_0 \sum_{i=1}^{\infty} S_{i0} \mathbf{E}_i(\theta, \varphi) \quad (2.75)$$

The radiated power can then be expressed exploiting the orthogonality of the radiation modes:

$$P_{\text{rad}} = \frac{1}{4\pi\eta} \iint \mathbf{E}_{\text{rad}}(\theta, \varphi) \cdot \mathbf{E}_{\text{rad}}^*(\theta, \varphi) d\Omega = |a_0|^2 P_{\text{ref}} \sum_{i=1}^{\infty} |S_{i0}|^2 \quad (2.76)$$

We can then compute the total radiation efficiency ϵ_{rad} defined as the ratio of the radiated power P_{rad} to the incident power P_{forw} on the input port:

$$\epsilon_{\text{rad}} = \frac{P_{\text{rad}}}{P_{\text{forw}}} = \sum_{i=1}^{\infty} |S_{i0}|^2 \quad (2.77)$$

The conventional radiation efficiency η_{rad} defined as the ratio of the radiated power P_{rad} to the input power P_{in} can be found noting that $P_{\text{in}} = P_{\text{forw}}(1 - |\Gamma|^2)$:

$$\eta_{\text{rad}} = \frac{P_{\text{rad}}}{P_{\text{in}}} = \frac{1}{1 - |\Gamma|^2} \sum_{i=1}^{\infty} |S_{i0}|^2 \quad (2.78)$$

Since in the remainder also non reciprocal antennas are considered, it is convenient to introduce here also the equivalent quantities in reception:

$$\varepsilon_{\text{rec}} = \frac{P_{\text{rec}}}{P_{\text{bacw}}} = \sum_{j=1}^{\infty} |S_{0j}|^2 \quad (2.79)$$

$$\eta_{\text{rec}} = \frac{P_{\text{rec}}}{P_{\text{out}}} = \frac{1}{1-|\Gamma|^2} \sum_{j=1}^{\infty} |S_{0j}|^2 \quad (2.80)$$

where P_{out} is the output power at the antenna port and P_{bacw} is given by the relation $P_{\text{out}} = P_{\text{back}}(1 - |\Gamma|^2)$. Notice that, with respect to the transmission case, in reception the index of the scattering terms are reversed. For reciprocal antennas this leads to the same efficiency as in the transmission case. For non-reciprocal antennas, however, these quantities might differ. Recalling that the inversion of the magnetostatic field causes the transposition of the scattering matrix, it is also possible to claim that the reception pattern and efficiency are the transmission pattern and efficiency for opposite magnetic bias.

2.4.2 Transmission line models of layered structures and metasurfaces

In the following, transmission line theory is used to simulate numerically simple layered structures. First, considering linear local isotropic 3D materials, macroscopic Maxwell's equations in absence of sources read:

$$\begin{aligned} \nabla \times \mathbf{E} &= -j\omega \mathbf{B} \\ \nabla \times \mathbf{H} &= j\omega \mathbf{D} \\ \mathbf{D} &= \varepsilon \mathbf{E} \\ \mathbf{B} &= \mu \mathbf{H} \end{aligned} \quad (2.81)$$

In analogy to the vacuum case the solutions are plane waves:

$$\begin{aligned} \mathbf{E} &= \mathbf{E}_0 e^{-j\mathbf{k} \cdot \mathbf{r}} \\ \mathbf{H} &= \mathbf{H}_0 e^{-j\mathbf{k} \cdot \mathbf{r}} \\ \mathbf{k} \cdot \mathbf{E}_0 &= 0 \\ \mathbf{H}_0 &= \frac{\mathbf{k} \times \mathbf{E}_0}{\omega \mu} \\ k^2 &= \mathbf{k} \cdot \mathbf{k} = \omega^2 \varepsilon \mu \end{aligned} \quad (2.82)$$

Chapter 2. Two-dimensional materials theory in the framework of Maxwell's equations

Assuming without loss of generality that the propagation occurs in the z direction ($\mathbf{k} = k_z \hat{\mathbf{z}}$) and that the electric field is parallel to the x axis ($\mathbf{E} = E_x \hat{\mathbf{x}}$) we get:

$$\mathbf{E} = (E_{0x}^+ e^{-jk_z z} + E_{0x}^- e^{+jk_z z}) \hat{\mathbf{x}} \quad (2.83)$$

$$\mathbf{H} = Z_0^{-1} (E_{0x}^+ e^{-jk_z z} - E_{0x}^- e^{+jk_z z}) \hat{\mathbf{y}} \quad (2.84)$$

$$Z_0 = \sqrt{\frac{\mu}{\epsilon}} \quad (2.85)$$

$$k_z = \omega \sqrt{\epsilon \mu} \quad (2.86)$$

which is analogous to a transmission line model with parameters Z_0 and k_z , depending on the material properties. A part from this mode (horizontal polarization) another one exist (vertical) if the electric field is chosen parallel to the y axis.

Using the boundary conditions it is then possible to include 2D materials in this transmission line model. More precisely, the following substitutions are made:

- Dielectric layers: replaced with a transmission line having characteristic impedance $Z_0 = \sqrt{\mu \epsilon^{-1}}$ and propagation constant $\gamma = jk = \alpha + j\beta = j\omega \sqrt{\epsilon \mu}$.
- Metallic layers: modeled as a dielectric layers with $\mu = \mu_0$ and an equivalent ϵ computed from the conductivity (see Section 2.5).
- 2D materials: assumed to be amagnetic, modeled as conductance in parallel, identical to the 2D conductivity of the 2D material.
- electrically thin metasurfaces, modeled as conductance in parallel, equal to their meta-conductivity. This approach can be used only if the evanescent waves from the meta-surface are confined in a space much smaller than the thickness of the surrounding dielectric layers.

If two polarizations are relevant, one transmission line is used for each polarization (e.g. horizontal and vertical), possibly coupled by non-isotropic 2D materials.

2.4.3 Metasurfaces: linear and circular four waves scattering matrix

A metasurface is a 2D periodic arrangement of structures including 3D materials, 2D materials or both. A metasurface can also include layered structure along the propagation direction z . If the incidence is normal, the periodicity of the metasurface must be smaller than the wavelength in the access media (usually vacuum). For arbitrary incidence direction, the periodicity must be smaller than half a wavelength. Figure 2.2 shows two conventions used in this thesis for the scattering parameters of a metasurface, for linear and circular polarizations. This approach is equivalent to a generalized Jones's Matrix formalism [18]. Notice that, for circularly polarized waves, modes are identified by the handedness of the polarization rather than by the absolute rotation direction in the xy plane. This is linked to the fact that handedness is preserved in a time reversal transformation, satisfying the condition that the regressive wave

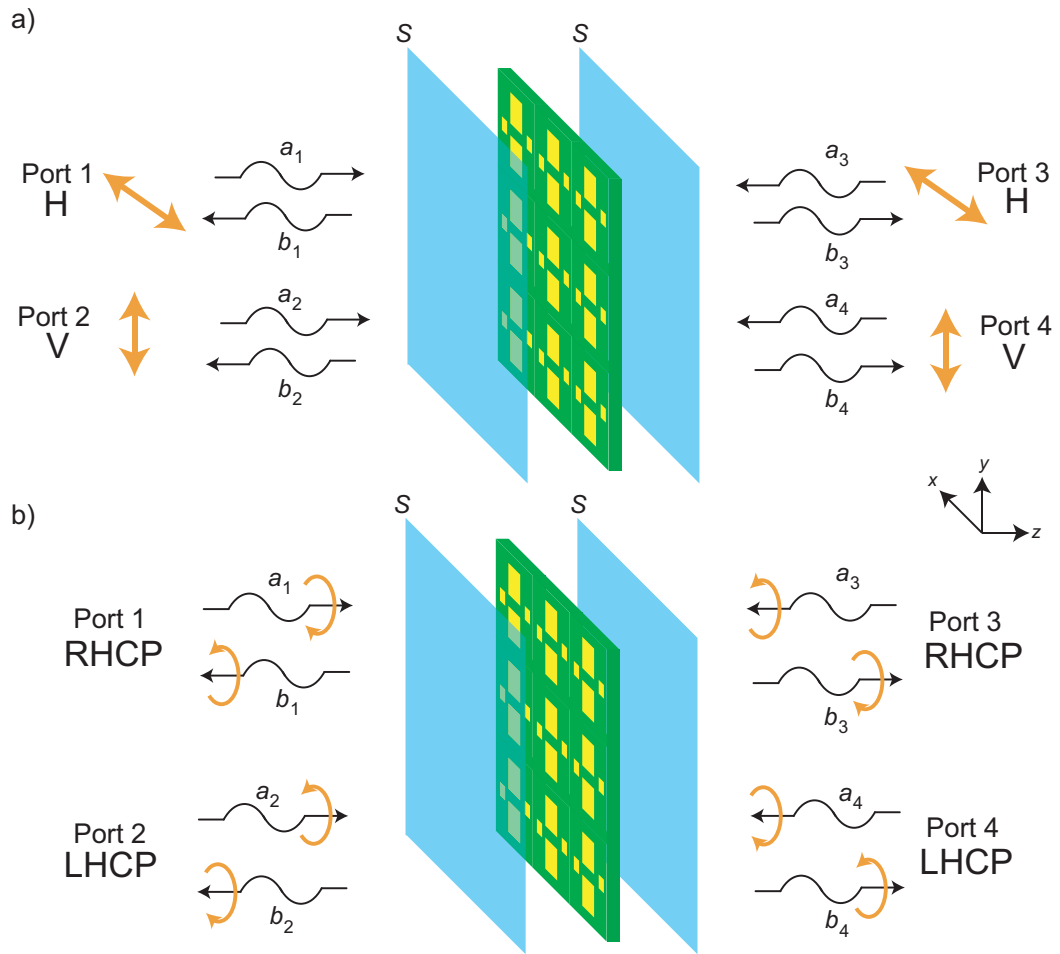


Figure 2.2 – Scattering matrix conventions for a) linearly and b) circularly polarized light for planar devices.

must be a time reversed version of the progressive wave. In this thesis the wave handedness is abbreviated as either:

- RHCP: right hand circularly polarized
- LHCP: left hand circularly polarized

When referring to the absolute rotation in the xy plane, these will be referred as:

- CW: clockwise
- CCW: counterclockwise

Figure 2.3a represents these conventions when the z axis is taken in the same direction of progressive waves, while Figure 2.3b illustrates the case where the z axis is reversed, which is useful for devices operating in reflection (such as the isolator in chapter 5).

Both for linear and circular polarization conventions, the metasurface can be represented

Chapter 2. Two-dimensional materials theory in the framework of Maxwell's equations

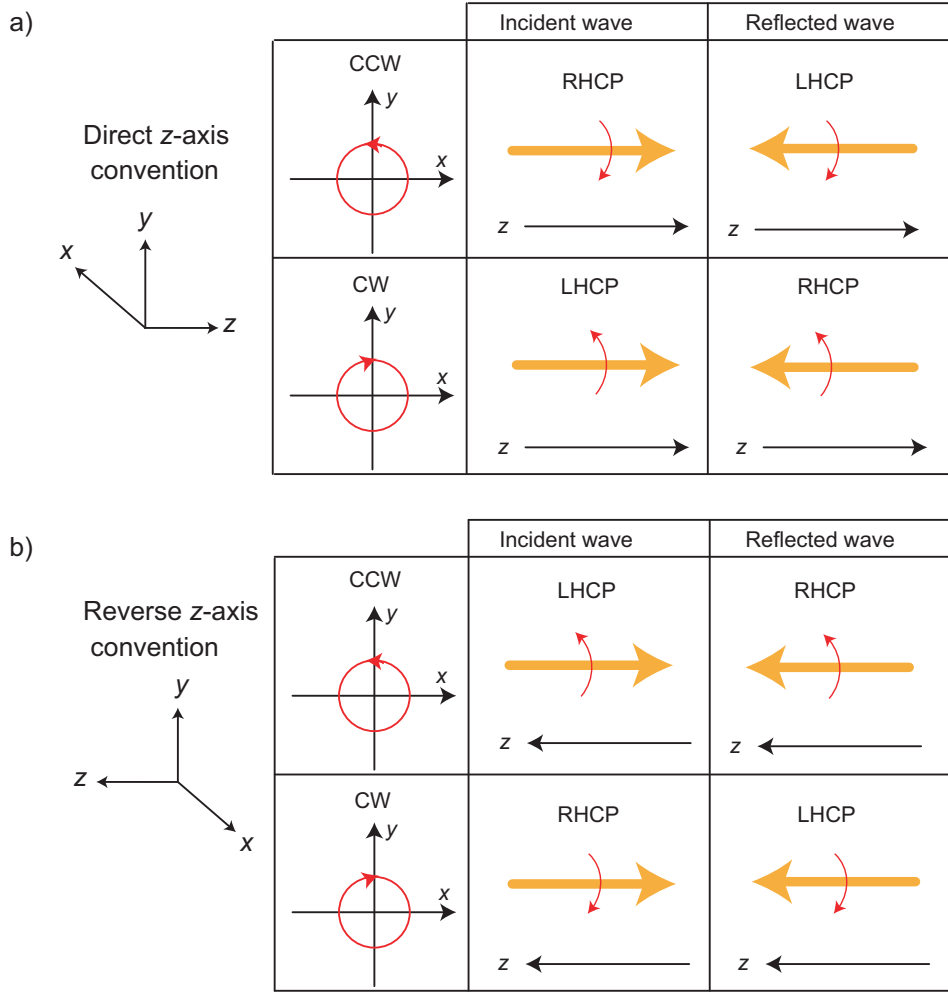


Figure 2.3 – Conventions on representing circularly polarized waves.

with a 4×4 scattering matrix, with 16 complex degrees of freedom (CDOFs).

$$\underline{S}_{\text{lin}} = \begin{pmatrix} S_{11} & S_{12} & S_{13} & S_{14} \\ S_{21} & S_{22} & S_{23} & S_{24} \\ S_{31} & S_{32} & S_{33} & S_{34} \\ S_{41} & S_{42} & S_{43} & S_{44} \end{pmatrix} \quad \underline{S}_{\text{circ}} = \begin{pmatrix} S_{11} & S_{12} & S_{13} & S_{14} \\ S_{21} & S_{22} & S_{23} & S_{24} \\ S_{31} & S_{32} & S_{33} & S_{34} \\ S_{41} & S_{42} & S_{43} & S_{44} \end{pmatrix} \quad (2.87)$$

In both cases, the matrices can be divided in four blocks:

$$\underline{S} = \begin{pmatrix} \underline{J}_{LL} & \underline{J}_{LR} \\ \underline{J}_{RL} & \underline{J}_{RR} \end{pmatrix} \quad (2.88)$$

where:

- \underline{J}_{LL} is the Jones matrix representing reflection on the left side.

- \underline{J}_{LR} is the Jones matrix representing transmission from right to left.
- \underline{J}_{RL} is the Jones matrix representing transmission from left to right.
- \underline{J}_{RR} is the Jones matrix representing reflection on the right side.

The following relation can be used to convert between linearly polarization matrices and circular ones:

$$\underline{S}_{\text{circ}} = \sqrt{2} \left(\begin{array}{cc|cc} 1 & -j & 0 & 0 \\ 1 & j & 0 & 0 \\ \hline 0 & 0 & 1 & j \\ 0 & 0 & 1 & -j \end{array} \right) \underline{S}_{\text{lin}} \sqrt{2} \left(\begin{array}{cc|cc} 1 & 1 & 0 & 0 \\ -j & j & 0 & 0 \\ \hline 0 & 0 & 1 & 1 \\ 0 & 0 & j & -j \end{array} \right) \quad (2.89)$$

Important simplifications in the scattering matrix take place for some particular cases listed below, which are relevant for many devices considered in the following.

Reciprocal metasurfaces

Reciprocal devices always have symmetric scattering matrices, and as a consequence the device is described by 10 complex degrees of freedom:

$$\underline{S}_{\text{lin}} = \left(\begin{array}{cc|cc} S_{11} & S_{12} & S_{13} & S_{14} \\ \color{green}S_{12} & S_{22} & S_{23} & S_{24} \\ \hline S_{13} & \color{green}S_{23} & S_{33} & S_{34} \\ S_{14} & S_{24} & \color{green}S_{34} & S_{44} \end{array} \right) \quad \underline{S}_{\text{circ}} = \left(\begin{array}{cc|cc} S_{11} & S_{12} & S_{13} & S_{14} \\ \color{green}S_{12} & S_{22} & S_{23} & S_{24} \\ \hline S_{13} & \color{green}S_{23} & S_{33} & S_{34} \\ S_{14} & S_{24} & \color{green}S_{34} & S_{44} \end{array} \right) \quad (2.90)$$

In this equations and in the following cases, the green quantities represent non-free parameters which depends on the free ones (in black).

C3, C4, C6 and C ∞ structures

If the metasurface is either:

- C3: invariant to a rotation of 120° in the xy plane.
- C4: invariant to a rotation of 90° in the xy plane.
- C6: invariant to a rotation of 60° in the xy plane.
- C ∞ : invariant to any rotation in the xy plane.

Chapter 2. Two-dimensional materials theory in the framework of Maxwell's equations

then several parameters in the circular matrix representation are null:

$$\underline{S}_{\text{circ}} = \left(\begin{array}{cc|cc} 0 & S_{12} & S_{13} & 0 \\ S_{21} & 0 & 0 & S_{24} \\ \hline S_{31} & 0 & 0 & S_{34} \\ 0 & S_{42} & S_{43} & 0 \end{array} \right) \quad (2.91)$$

This property is of special importance for the isolator presented in chapter 5. The number of CDOFs is 8.

Electrically thin metasurface

A metasurface is said to be electrically thin if it has the following properties:

- The metasurface includes only amagnetic materials
- Its thickness is much smaller than the wavelength in surrounding media
- The current in the metasurface is uniform along z (at least in phase)

Then the tangential component of the electric field \mathbf{E} has the same value on each side of the metasurface and the number of CDOFs is reduced to just 4:

$$\underline{S}_{\text{lin}} = \left(\begin{array}{cc|cc} S_{11} & S_{12} & S_{11} + 1 & S_{12} \\ S_{21} & S_{22} & S_{21} & S_{22} + 1 \\ \hline S_{11} + 1 & S_{12} & S_{11} & S_{12} \\ S_{21} & S_{22} + 1 & S_{21} & S_{22} \end{array} \right) \quad (2.92)$$

$$\underline{S}_{\text{circ}} = \left(\begin{array}{cc|cc} S_{11} & S_{12} & S_{12} + 1 & S_{11} \\ S_{21} & S_{22} & S_{22} & S_{21} + 1 \\ \hline S_{21} + 1 & S_{22} & S_{22} & S_{21} \\ S_{11} & S_{12} + 1 & S_{12} & S_{11} \end{array} \right) \quad (2.93)$$

An electrically thin metasurface can be modeled equivalently as a 2D *meta-conductivity* $\underline{\sigma}_{\text{META}}$, which also has 4 CDOFs, and the scattering matrix in linear polarization form is given by:

$$\underline{S}_{\text{lin}} = \left(\begin{array}{c|c} \underline{\Gamma} & \underline{\Gamma} + \underline{I} \\ \hline \underline{\Gamma} + \underline{I} & \underline{\Gamma} \end{array} \right) \quad \underline{\Gamma} = -\underline{\sigma}_{\text{META}} (2\eta^{-1}\underline{I} + \underline{\sigma}_{\text{META}})^{-1} \quad (2.94)$$

Graphene and patterned graphene both belong to this category, and the same applies to any 2D material. Patterns obtained with metallic films may or may not fall in this category accordingly to the film thickness and to the skin depth. In fact, if the thickness is comparable or larger than the skin depth, then the induced current will not be uniform in the material and hence the tangential electric field will be discontinuous. If the thickness is much smaller than the skin depth of the metal (e.g. low frequency and thin metal) then the film falls in this category and can be modeled as a resistive sheet.

2.5 Drude and Drude-Lorentz models for plasmas, metals and semiconductors

As mentioned in the previous sections, the constitutive equations describe the physical phenomena in the optical materials. In a wide category of conducting materials, these interactions are dominated by free carriers, i.e. electrons or holes (missing electrons in the valence band); these include plasmas, metals and semiconductors (at different frequencies). In most cases, their optical properties can be predicted by a simple semi-classical model, called Drude model, which takes into account both the carrier dynamic in the metal and the intrinsic polarizability of the atoms in the lattice. This model is important since it can be used also as a first low-frequency ($f \leq 5$ THz) approximation for graphene.

This model assumes the following about the conductor:

- The naked atomic lattice (imagining all carriers to be removed) has a permittivity of ϵ_∞ .
- The carrier density (either electrons or holes) per unit volume is n , and carriers have elementary charge q_e .
- The carrier's movement is predominantly thermal, and the thermal velocity is v_{th} .
- The carriers collide with lattice imperfections and/or other scatterers (e.g. phonons); the average time between collisions is τ , and the average length covered by the carriers during this time (ballistic length) is $l = v_{th}\tau$.
- The mass of the carriers is m . This can be in general different from the electron mass, and given by a semi-classical approximation obtained from the band structure.
- The drift velocity $v_d = q\tau m^{-1}E$ is a small perturbation caused by the electric field E on the carriers.
- The total current density at DC $J = \sigma E$ is given by $J = nqv_d$
- The material is considered isotropic, but extension to anisotropic cases are often straightforward (e.g. different m and τ for different crystal axes)

Then the DC conductivity (only carriers without background) is given by:

$$\sigma_{DC} = \frac{nq_e^2\tau}{m} \quad (2.95)$$

and the optical conductivity is given by

$$\sigma = \frac{\sigma_{DC}}{1 + j\omega\tau} = \frac{nq_e^2m^{-1}}{\tau^{-1} + j\omega} \quad (2.96)$$

Notice that the resistivity can be written as the series between a resistive and an inductive

Chapter 2. Two-dimensional materials theory in the framework of Maxwell's equations

component:

$$\rho = \sigma^{-1} = \frac{1}{\sigma_{\text{DC}}} + j\omega \frac{\tau}{\sigma_{\text{DC}}} = \frac{m}{nq_e^2\tau} + j\omega \frac{m}{nq_e^2} = R + j\omega L \quad (2.97)$$

$$R = \frac{1}{\sigma_{\text{DC}}} = \frac{m}{nq_e^2\tau} \quad (2.98)$$

$$L = \frac{\tau}{\sigma_{\text{DC}}} = \frac{m}{nq_e^2} \quad (2.99)$$

$$L = \tau R \quad (2.100)$$

The inductive component is very important for plasmonic propagation, as explained in the following, and it is basically due to the inertia of the carriers. In fact, it dominates when the optical frequency is larger than the collision rate, and it can be understood as follows: a free electron will be accelerated by a sinusoidally oscillating electric field, but with a delay of 90° . The resulting current has then the same delay that is found in an inductor driven by an alternating voltage. The energy associated to this inductive term is stored as kinetic energy of the carriers, and hence the inductance in the Drude model is referred to as *kinetic inductance*.

The total equivalent permittivity is:

$$\varepsilon = \varepsilon_\infty + \frac{\sigma}{j\omega} = \varepsilon_\infty + \frac{nq_e^2}{m} \frac{1}{j\omega\tau^{-1} - \omega^2} \quad (2.101)$$

Two important frequencies are the collision rate Γ :

$$\Gamma = \tau^{-1} \quad (2.102)$$

and the plasma frequency ω_p :

$$\omega_p = \sqrt{\frac{nq_e^2}{m\varepsilon_\infty}} = \sqrt{\frac{nq_e^2}{m\varepsilon_{r\infty}\varepsilon_0}} \quad (2.103)$$

The permittivity can then be expressed as:

$$\varepsilon = \varepsilon_\infty \left(1 - \frac{\omega_p^2}{\omega^2 - j\Gamma\omega} \right) \quad (2.104)$$

$$\varepsilon_r = \varepsilon_{r\infty} \left(1 - \frac{\omega_p^2}{\omega^2 - j\Gamma\omega} \right) \quad (2.105)$$

2.5. Drude and Drude-Lorentz models for plasmas, metals and semiconductors

If $\omega \geq 2\pi\Gamma$ and $\omega \leq \omega_p$ then the equivalent permittivity has a dominant negative real part, and the material behaves as a plasma. In this case, propagation is impossible, while the material is transparent again for frequencies above the plasma frequency. Typical values for noble metals are in the order of ultraviolet for the plasma frequency and mid to near infrared for the collision rate, which means that noble metals exhibit plasmonic behavior at visible frequencies [109]. Another important quantity is the carrier mobility μ , defined by:

$$v_d = \mu E \quad (2.106)$$

and hence it is given by:

$$\mu = \frac{q_e \tau}{m} \quad (2.107)$$

The following relation between μ and σ_{DC} holds:

$$\sigma_{DC} = nq_e \mu \quad (2.108)$$

When a magnetostatic field \mathbf{B}_0 is applied to the material, it affects carrier's trajectories through Lorentz forces (Hall effect). The conductivity becomes a gyrotropic tensor [118, 105], and the new conductivity model is referred to as Drude-Lorentz model. Assuming the field is parallel to z axis ($\mathbf{B}_0 = B_0 \hat{z}$):

$$\underline{\sigma} = \begin{pmatrix} \sigma_d & \sigma_o & 0 \\ -\sigma_o & \sigma_d & 0 \\ 0 & 0 & \sigma_z \end{pmatrix} \quad (2.109)$$

where the diagonal conductivity σ_d is:

$$\sigma_d = \sigma_{DC} \frac{1 + j\omega\tau}{(\omega_c\tau)^2 + (1 + j\omega\tau)^2} \quad (2.110)$$

and the off-diagonal conductivity σ_o is:

$$\sigma_o = \sigma_{DC} \frac{\omega_c\tau}{(\omega_c\tau)^2 + (1 + j\omega\tau)^2} \quad (2.111)$$

where ω_c is the cyclotron angular frequency, namely the angular frequency of a carrier orbiting in the magnetostatic field. This quantity is independent of the velocity v of the particle, and it

Chapter 2. Two-dimensional materials theory in the framework of Maxwell's equations

is obtained equating the Lorentz force $\nu B_0 q_e$ and the centrifugal force $m\nu\omega_c$:

$$\omega_c = \frac{B_0 q_e}{m} \quad (2.112)$$

The conductivity along the magnetic axis is instead unaffected:

$$\sigma_z = \sigma = \frac{\sigma_{\text{DC}}}{1 + j\omega\tau} \quad (2.113)$$

and the final permittivity tensor is simply (assuming no effect of magnetic field on ε_∞):

$$\underline{\varepsilon} = \varepsilon_\infty \underline{I} + \frac{1}{j\omega} \underline{\sigma} \quad (2.114)$$

Importantly, if the magnetic field is very strong, the Drude Lorentz model might fail, as more complex effects can occur, such as energy level quantization in the quantum Hall effect.

2.6 Graphene conductivity formulae

This section presents useful formulas found in literature to model the complex conductivity tensor of graphene as a function of several parameters. The formulas show excellent agreement with experimental results, including the ones presented in this thesis.

2.6.1 Band structure

The conductivity of graphene depends on its band structure, which can be computed using a tight-binding approximation considering only the nearest neighbor terms. The structure of graphene is depicted in Figure 2.4a, and the computation leads to [14, 105]:

$$E_\pm = \pm t \sqrt{3 + 2 \cos(\sqrt{3} k_y a) + 4 \cos\left(\frac{\sqrt{3}}{2} k_y a\right) \cos\left(\frac{3}{2} k_x a\right)} \quad (2.115)$$

where $\mathbf{k} = (k_x, k_y)$ is the electron wave-vector, E is the electron energy, $a = 1.42 \text{ \AA}$ is the inter-atomic distance between carbon atoms and $t = 2.8 \text{ eV}$ is the nearest neighbor hopping energy. The periodicity of graphene is $\sqrt{3}a = 2.46 \text{ \AA}$.

The first Brillouin zone (Figure 2.4b) is characterized by a number of interesting features. First of all it is composed of two branches which, for the nearest neighbor approximation, are exactly one the opposite of the other (*ambipolarity*). The positive band is called *conduction*

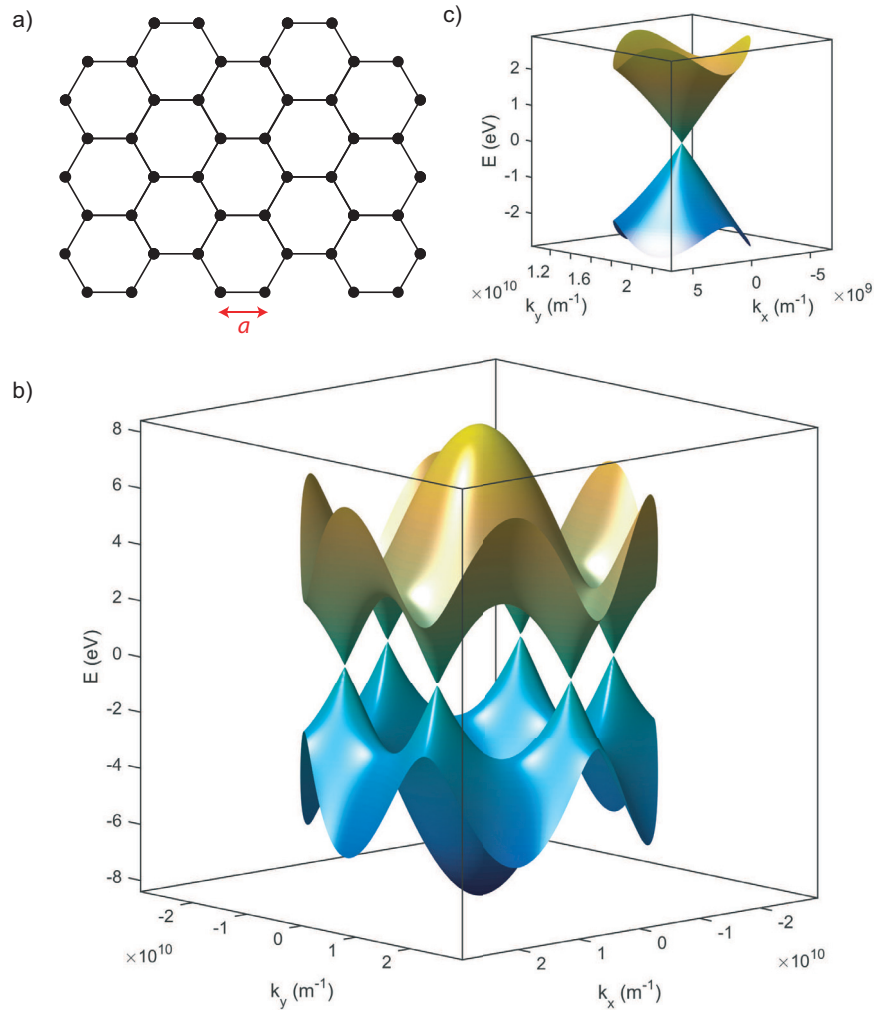


Figure 2.4 – Structure and band diagram of graphene. a) Exagonal honeycomb arrangement of carbon atom in graphene, b) band-structure of graphene in an area slightly larger than the first Brillouin zone, c) detail of a Dirac point.

band and the negative one *valence* band. The two branches touch each other in six points (around the first Brillouin zone) which are named Dirac Points. Because of the ambipolarity, for ideal graphene, the Fermi level (which separates occupied states and empty states) falls exactly at the Dirac point (0 eV in Figure 2.4). Hence, at absolute 0 temperature ($T = 0\text{K}$) the valence band is fully occupied by electrons, while the conduction band is empty, i.e. fully occupied by holes. The terms “Fermi level” and “chemical potential” will be used as synonyms in this thesis.

Because conductivity phenomena often concern the interface between electrons and holes, the relevant portion of the band structure is the one located around the Dirac points (e.g. Figure 2.4c shows a neighborhood of a Dirac point). Strikingly, the band structure here can be approximated with an excellent accuracy with a cone (called *Dirac cone*). This approximation simplifies the conductivity models, also leading to closed form expressions. First of all, with a

Chapter 2. Two-dimensional materials theory in the framework of Maxwell's equations

simple Taylor development, the approximating cone can be expressed as:

$$E_{\pm} = \pm \frac{3at}{2} |\mathbf{k} - \mathbf{k}_{\text{dirac}}| \quad (2.116)$$

where $\mathbf{k}_{\text{dirac}}$ is the position of the Dirac point in the \mathbf{k} space. This constant offset can be neglected for the phenomena considered in this thesis, and hence we can write:

$$E_{\pm} = \pm \frac{3at}{2} |\mathbf{k}| \quad (2.117)$$

The proportionality between energy and momentum is typical also of photons in free space, and it is associated to their lack of rest mass. For a photon in fact we have $E = \hbar c |\mathbf{k}|$, which is associated to a constant speed c . Similarly we can write here:

$$E_{\pm} = \pm \hbar v_f |\mathbf{k}| \quad (2.118)$$

$$v_f \triangleq \frac{3at}{2\hbar} \simeq 9.1 \cdot 10^5 \text{ m} \cdot \text{s}^{-1} \quad (2.119)$$

where \hbar is the reduced Planck constant ($\hbar \simeq 6.582 \cdot 10^{-16} \text{ eV} \cdot \text{s}$) and v_f is called Fermi velocity in graphene and it usually approximated as $10^6 \text{ m} \cdot \text{s}^{-1}$ or $c/300$. Because of this, carriers in graphene are usually referred to as *massless fermions*. The approximated conical band structure can be used to compute the density of electronic states (DOS) as a function of the energy E , with good validity in the range $-1 \text{ eV} < E < 1 \text{ eV}$. Considering a graphene square patch with area L^2 (though the analysis holds for any arbitrary shape), the possible electron states are described by two quantum numbers m, n with:

$$\mathbf{k} = \frac{2\pi}{2L} (m, n) \quad (2.120)$$

Two additional degrees of freedom have to be considered [14, 30]. First a factor $g_s = 2$, due to the fact that each electron state in the \mathbf{k} space can hosts two electrons with opposite spins. Secondly, each Brillouin zone contains six Dirac cones. However, each cone is shared among three Brillouin zones, and hence the actual number of distinct valleys multiplicity is $g_v = 2$. The number of states with energy between 0 and $|E|$ is:

$$\# = g_s g_v \frac{1}{4} \pi \left(\frac{L|E|}{\pi \hbar v_f} \right)^2 \quad (2.121)$$

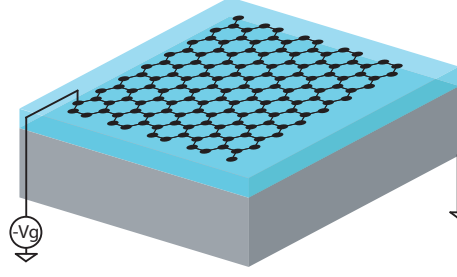


Figure 2.5 – Electrostatic gating of graphene. A thin oxide layer (light blue) separates graphene from a semiconducting substrate (gray)

the final density of states is then:

$$\rho(E) = \frac{1}{L^2} \frac{\partial \#}{\partial E} = \frac{g_s g_v}{2\pi(\hbar v_f)^2} |E| = \frac{2|E|}{\pi(\hbar v_f)^2} \quad (2.122)$$

Just as for 3D crystals, at $T = 0$ K all the states with energy below the Fermi level μ_c are occupied while the ones above it are free. For arbitrary temperature T , the electrons follow the Fermi statistics, i.e. the probability of occupancy depends on its energy as [14, 30]:

$$f_d(E - \mu_c) = \left(1 + e^{\frac{E - \mu_c}{k_B T}} \right)^{-1} \quad (2.123)$$

where k_B is Boltzmann's constant and f_d is called Fermi distribution. At room temperature ($T = 300$ K) we have $k_B T = 26$ meV.

2.6.2 Graphene gating and doping

For pristine graphene the Fermi level is located exactly at the Dirac point. This implies that at 0 K all the electrons are in the valence band while all the holes are in the conduction band. If the temperature is larger, then some holes appear in the valence band and some electrons in the conduction band, and both these particles (called thermal carriers) can participate in electrical conduction with relatively low conductivity. The Fermi level of graphene, however, can be changed with at least two techniques:

Chemical doping other atoms are added to graphene (e.g. adatoms) and they become ions either releasing an electron in graphene (donor dopant) or capturing one creating a hole (acceptor dopant). The created carriers are then free to move in the atomic lattice participating in the conduction.

Electrostatic gating a voltage is applied between graphene and another conductor through an insulating gate layer (typically an oxide). The system behaves as a parallel plate capacitor

Chapter 2. Two-dimensional materials theory in the framework of Maxwell's equations

and the induced electrons or holes on graphene can participate to the conduction (Figure 2.5). The free carriers create a bi-dimensional electron gas (2DEG) very similar to the one found silicon field effect transistors (FETs)

In both cases, these techniques act on the net number of carriers on graphene. The latter can be defined as a function of the temperature T and Fermi level μ_c (both constant and well defined in equilibrium conditions). Defining n as the number of electrons in the conduction band and p as the density of holes per unit surface we have:

$$n = \int_0^{\infty} \rho(E) f_d(E - \mu_c) dE \quad (2.124)$$

$$p = \int_{-\infty}^0 \rho(E) (1 - f_d(E - \mu_c)) dE = \int_0^{\infty} \rho(E) f_d(E + \mu_c) dE \quad (2.125)$$

The net induced surface carrier density n_s and the surface charge σ_q are then (Figure 2.6a and b):

$$n_s = n - p = \int_0^{\infty} \rho(E) (f_d(E - \mu_c) - f_d(E + \mu_c)) dE \quad (2.126)$$

$$\sigma_q = -q_e n_s = q_e (p - n) \quad (2.127)$$

It is also useful considering the electric field needed to induce the charges on graphene. This is simply:

$$E = \frac{\sigma_q}{\epsilon_0 \epsilon_r} = \frac{q_e n_s}{\epsilon_0 \epsilon_r} \quad (2.128)$$

Because the field depends on the relative permittivity ϵ_r of the gate oxide it is useful to introduce an equivalent electric field which incorporate this effect and which is independent of the used oxide:

$$E_{eq} \triangleq \epsilon_r E = \frac{q_e n_s}{\epsilon_0} \quad (2.129)$$

The gate voltage is simply given by

$$V_g \triangleq tE = t\epsilon_r^{-1} E_{eq} \quad (2.130)$$

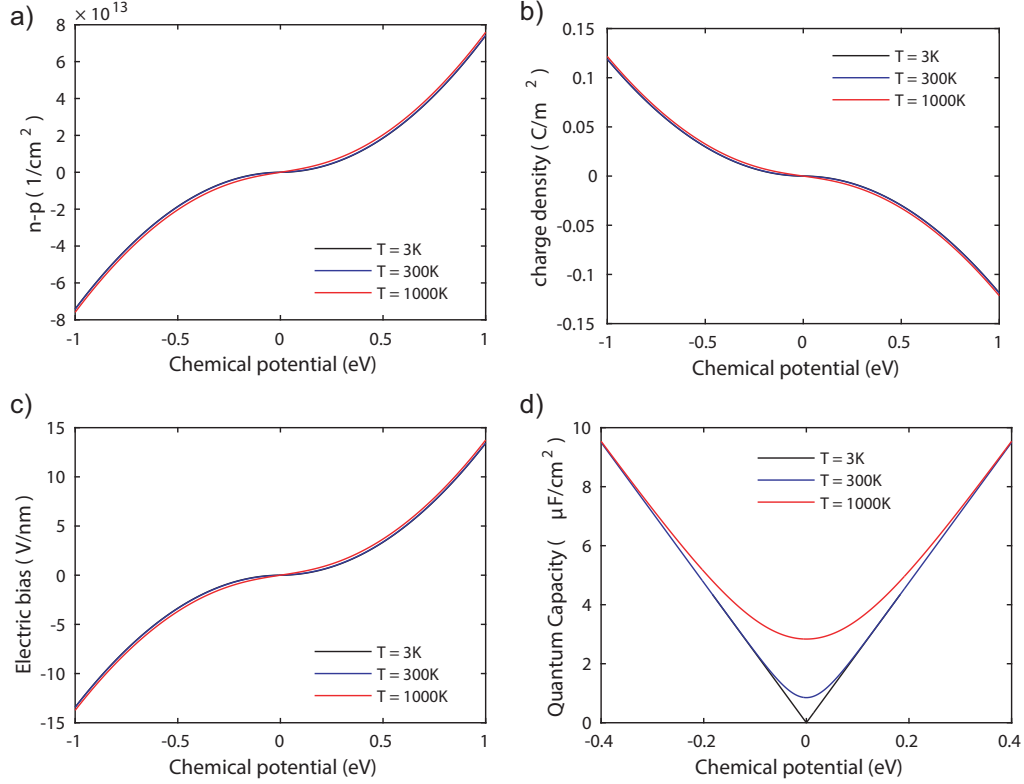


Figure 2.6 – Control of carriers and chemical potential by gating. a) Carrier density n_s versus μ_c . b) Charge density σ_q versus μ_c . c) Effective electric field E_g versus μ_c . d) Quantum capacity per unit area C_q versus μ_c .

where t is the oxide thickness. Finally, for $\mu_c \gg k_B T$ a closed form simplification can be found:

$$n_s \simeq \text{sign}(\mu_c) \frac{\mu_c^2}{\pi(\hbar v_f)^2} \quad (2.131)$$

$$\mu_c \simeq \text{sign}(n_s) \hbar v_f \sqrt{\pi |n_s|} \quad (2.132)$$

2.6.3 Quantum capacitance of graphene

A gated sample of graphene behaves as a parallel plate capacitor. However, for very thin gate oxides (e.g. 10 nm or less) the total capacity (per unit area) of the gated graphene is the series

Chapter 2. Two-dimensional materials theory in the framework of Maxwell's equations

of two capacitive terms:

$$C_{\text{tot}} = C_{\text{ox}}^{-1} + C_{\text{q}}^{-1} \quad (2.133)$$

$$C_{\text{ox}} \triangleq \frac{\epsilon_0 \epsilon_r}{t} \quad (2.134)$$

$$C_{\text{q}} \triangleq \frac{t \sigma_{\text{q}}}{d(q_e \mu_c)} \quad (2.135)$$

The reason for this additional terms is understood as follows: in order to induce a variation in the charge density in graphene, two energy variations must occur. First, the electrostatic energy changes, which is modeled by the electrostatic oxide capacitance C_{ox} ; secondly, the new induced electrons are actually causing a change in the Fermi level in graphene, and hence this energy variation induced by the new charge behaves exactly as a capacitor, and it is defined taking the derivative of the surface charge with respect with the variation of the electron potential $q_E^{-1} \mu_c$. Using Equation 2.126 it is possible to exchange the derivative and the integral obtaining a closed form formula for the quantum capacitance:

$$C_{\text{q}} = \frac{d\sigma_{\text{q}}}{d(q_e \mu_c)} = \frac{2q_e^2 k_B T}{\pi(\hbar v_f)^2} \ln \left(2 + 2 \cosh \left(\frac{\mu_c}{k_B T} \right) \right) \quad (2.136)$$

If the condition $\mu_c \gg k_B T$ holds, then the effect of temperature is negligible and an approximated formula is found:

$$C_{\text{q}} \simeq \frac{2q_e^2}{\pi(\hbar v_f)^2} |\mu_c| \quad (2.137)$$

The most important feature of this capacitance is that it can be tuned applying a different gate voltage (since it depends on the Fermi level). Figure 2.6d illustrates this dependence. In conclusion the quantum capacitance acts as a non linear capacitor since its value depends on the applied voltage, and for a small radio-frequency signal it can be used as a varactor.

2.6.4 Scalar conductivity

Now that the behavior of carriers in the electrostatic case is known, the next step is the development of models to describe the conductivity of the carriers themselves. Graphene conductivity is influenced by several parameters. First of all it depends on the frequency f , showing different behaviours and trends at various frequency bands. It is influenced by the surface carriers density n_s , which in turns depends on the Fermi level μ_c (also known as chemical potential). For low value of the carrier density, the thermal carriers are significant, and hence also the temperature T affects the conductivity. Finally, just as for the Drude

model presented in Section 2.5, the mean free time between carriers collisions (i.e. carriers' scattering time τ) has an important impact on the conductivity, as it directly related to the carrier mobility μ .

All these effects can be modeled using Kubo formula [43, 44, 41, 40], which provides an excellent numerical approximation of graphene conductivity until visible light frequencies. The formula is based on the previously described electronic band structure of graphene using Hamiltonian operators to model the nearest neighbor hopping, and it is given by:

$$\sigma(\omega, \mu_c, \tau, T) = \frac{j q_e^2 (\omega - j\tau^{-1})}{\pi \hbar^2} \left[\frac{1}{(\omega - j\tau^{-1})^2} \int_0^\infty \epsilon \left(\frac{\partial f_d(\epsilon)}{\partial \epsilon} - \frac{\partial f_d(-\epsilon)}{\partial \epsilon} \right) d\epsilon - \int_0^\infty \frac{f_d(-\epsilon) - f_d(\epsilon)}{(\omega - j\tau^{-1})^2 - 4(\epsilon/\hbar)^2} d\epsilon \right] \quad (2.138)$$

The first integral is referred to as *intra-band conductivity*, and it refers to dynamical phenomena in which carriers remain in the same electronic band. The second one is the *inter-band conductivity* and it takes into account the absorption of photons in graphene due to the interband transitions of carrier from the upper Dirac cone to the lower or vice versa. For this second case, a highly energetic photon is needed to create the transition of the electron from one band to the other, and hence this effect is visible only in the mid infrared and above.

While the inter-band integral cannot in general be solved analytically (i.e. requires numerical integration), the intra-band one allows a close form expression. We then obtain:

$$\sigma(\omega, \mu_c, \tau, T) = \sigma_{\text{intra}} + \sigma_{\text{inter}} \quad (2.139)$$

$$\sigma_{\text{intra}} = \frac{-j q_e^2 k_B T}{\pi \hbar^2 (\omega - j\tau^{-1})} \ln \left(2 + 2 \cosh \left(\frac{\mu_c}{k_B T} \right) \right) \quad (2.140)$$

$$\sigma_{\text{inter}} = \frac{j q_e^2 (\omega - j\tau^{-1})}{\pi \hbar^2} \int_0^\infty \frac{f_d(-\epsilon) - f_d(\epsilon)}{(\omega - j\tau^{-1})^2 - 4(\epsilon/\hbar)^2} d\epsilon \quad (2.141)$$

The inter-band term can be neglected if $\hbar\omega \ll 2\mu_c$. Typically, for frequencies lower than 5 THz, this is an excellent approximation.

The intra-band term σ_{intra} can be further simplified if the condition $\mu_c \gg k_B T$ holds, giving a

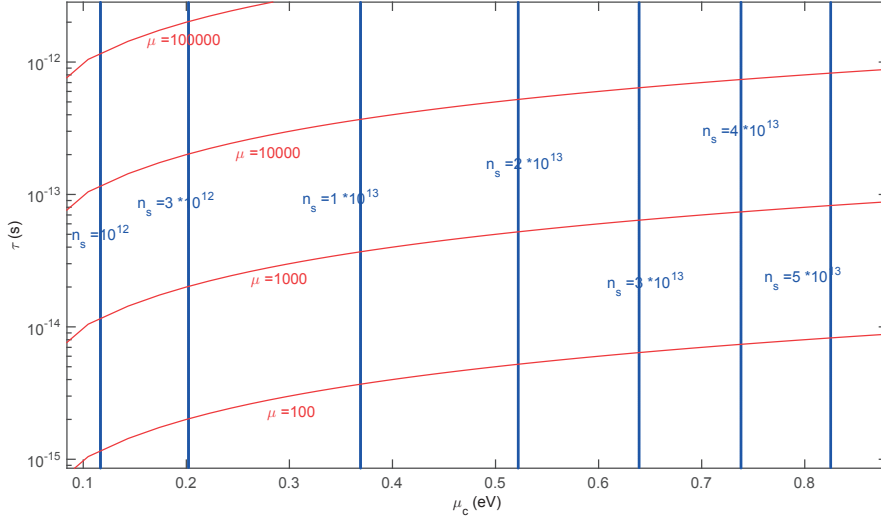


Figure 2.7 – Chart illustrating the relationship between the couples μ_c, τ and μ, n_s in the low temperature approximation. Note: μ, n_s are expressed using centimeters, so μ is measured in $\text{cm}^2 \cdot \text{V}^{-1} \cdot \text{s}^{-1}$ and n_s in cm^{-2}

low temperature approximation:

$$\sigma_{\text{intra}} \simeq \frac{q_e^2 |\mu_c| \tau}{\pi \hbar^2 (1 + j\omega\tau)} \quad (2.142)$$

Comparing this equation with the Drude model, one can find perfect agreement if the following condition is assumed on the carrier's mass:

$$m = |\mu_c| v_f^{-2} \quad (2.143)$$

which matches the fact that for a photon the mass is fully relativistic (i.e. null rest mass) and given by $m = Ec^{-2}$ confirming that massless Dirac fermions really behave as photons in free space. The mobility is then given, by extension, as:

$$\mu = \frac{q_e \tau v_f^2}{\mu_c} = \frac{q_e \tau v_f}{\hbar \sqrt{\pi |n_s|}} \quad (2.144)$$

This relation can be inverted as:

$$\tau = \frac{\pi \hbar^2 n_s \mu}{q_e \mu_c} = \frac{\hbar \mu \sqrt{\pi n_s}}{q_e v_f} \quad (2.145)$$

The conversion from the couple of parameters μ_c, τ to μ, n_s is represented graphically in Figure 2.7. An important remark is that the plasma frequency is undefined in graphene, because, unlike 3D plasma, it cannot completely stop a wave due to its bidimensional nature.

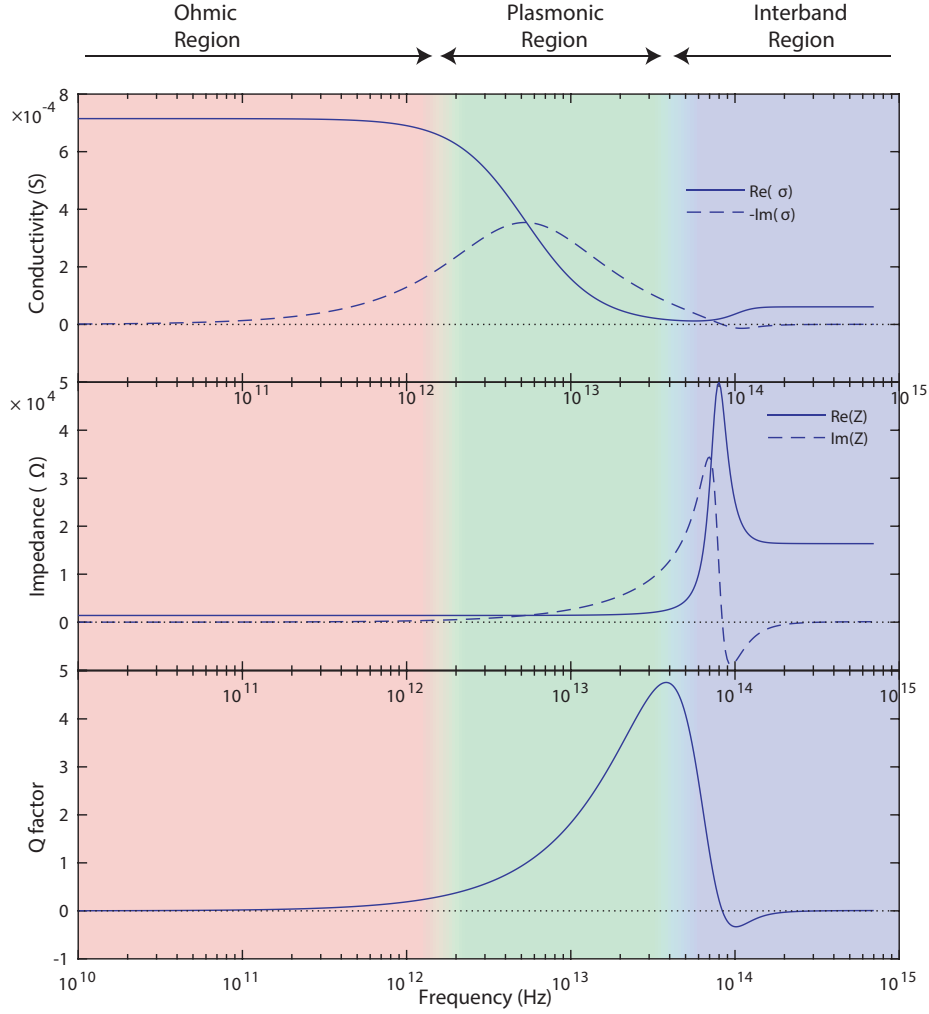


Figure 2.8 – Numerical evaluation of graphene complex conductivity using Kubo formula. The parameters $\tau=30$ fs and $\mu_c=0.2$ eV are typical of CVD graphene. For conductivity, the imaginary part has a reverse sign to allow better comparison with the real part. Impedance (reciprocal of conductivity) and quality factor (imaginary over real part) are also shown

Figure 2.8 shows an example of conductivity computed with Kubo formula for typical CVD graphene parameters ($\tau=30$ fs and $\mu_c=0.2$ eV). Three regions can be clearly identified. For frequencies much lower than τ^{-1} the conductivity is essentially real, namely graphene behaves as a resistor. This range (*ohmic region*) extends from DC to microwaves. At terahertz and far-infrared frequencies, the imaginary part of the conductivity becomes significant and dominates in the near infrared, while the inter-band term is still negligible. Graphene shows a plasma like behavior, and the region is called *plasmonic region*. For frequencies such that $\hbar\omega > 2\mu_c$ the conductivity is dominated by the inter-band contribution (*interband region*), and it takes the constant value of

$$\sigma_{\text{univ}} = q_e^2 \hbar^{-1} = 2\pi R_K^{-1} = \simeq 61 \mu\text{S} \quad (2.146)$$

Chapter 2. Two-dimensional materials theory in the framework of Maxwell's equations

independently of graphene parameters. This value is referred to as the *universal dynamical conductivity* of graphene. $R_K = hq_e^{-2}$ is the Von Klitzing constant. The figure also shows graphene impedance Z and quality factor Q defined as:

$$Z \triangleq \sigma^{-1} \quad (2.147)$$

$$Q \triangleq -\frac{\text{Im}(\sigma)}{\text{Re}(\sigma)} = \frac{\text{Im}(Z)}{\text{Re}(Z)} \quad (2.148)$$

The latter is of fundamental importance for plasmonic propagation in graphene explored in Chapter 4 and it is related to the quality factor of graphene plasmonic resonators. We notice that in the intra-band regime:

$$Q \simeq \omega\tau \quad \text{for } \hbar\omega < 2\mu_c \quad (2.149)$$

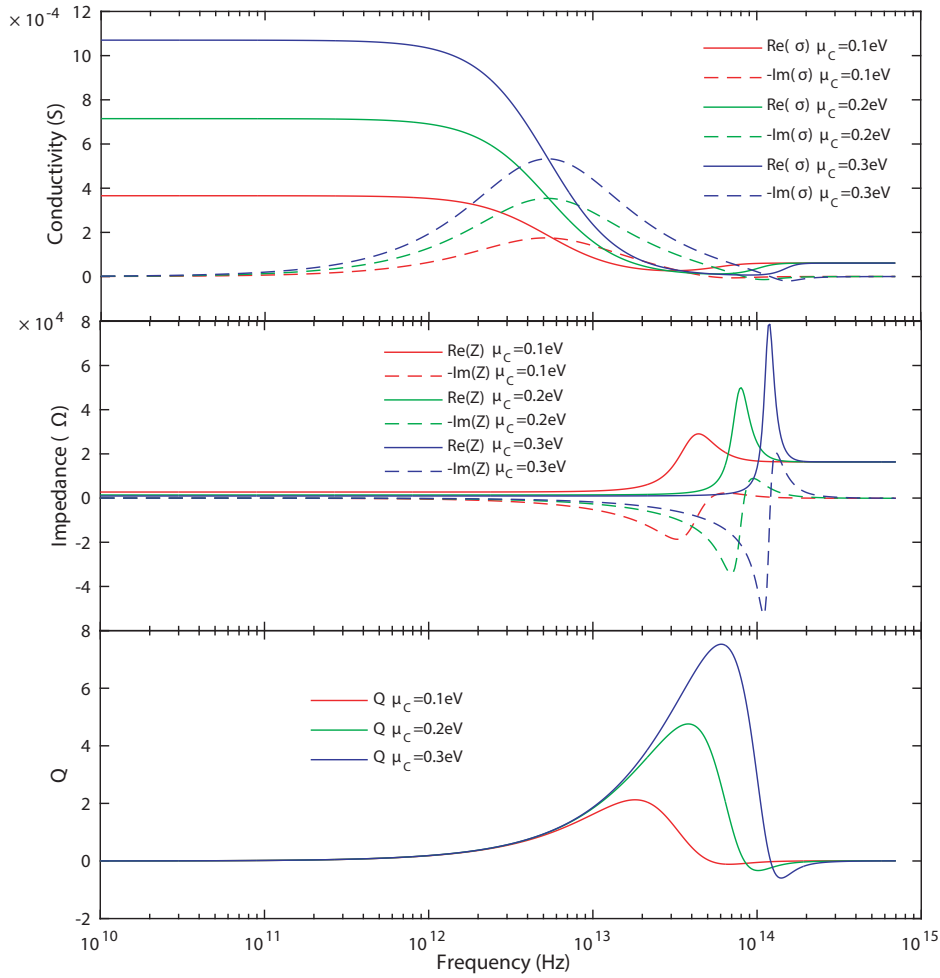


Figure 2.9 – Numerical evaluation of graphene complex conductivity using Kubo formula upon Fermi level sweep.

2.6. Graphene conductivity formulae

Figure 2.9 illustrates the dependence of the conductivity on the Fermi level. An increased Fermi level leads to higher carrier density (and hence higher ohmic conductivity) and to a larger transition frequency between plasmonic behavior and inter-band one.

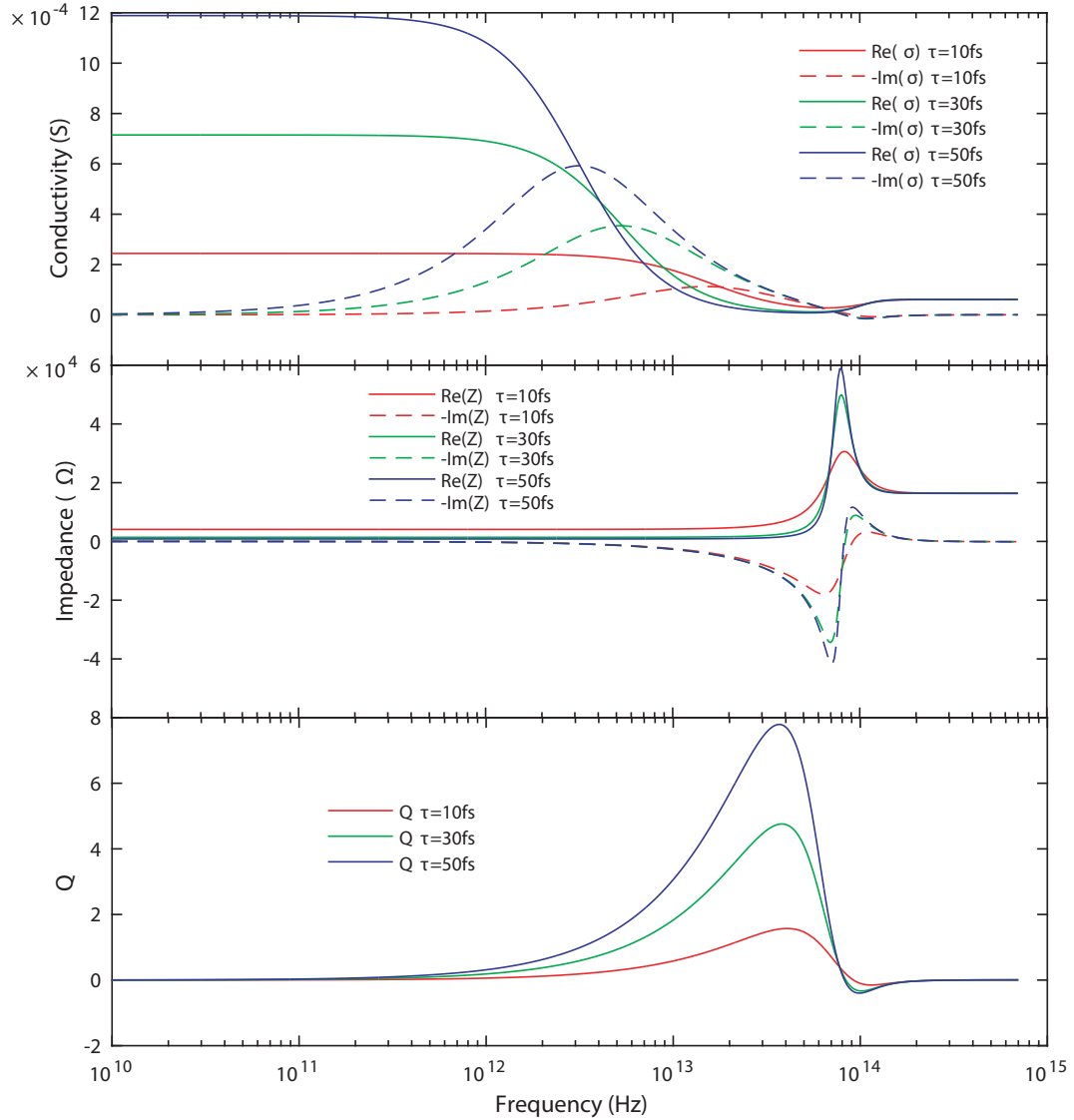


Figure 2.10 – Numerical evaluation of graphene complex conductivity using Kubo formula for different values of τ .

Figure 2.10 illustrates the dependence of conductivity on the carrier scattering time. Larger τ imply higher mobility and DC conductivity, and a lower transition frequency to the plasmonic region. Importantly, when electrostatic bias is applied μ_c is changed and the conductivity of graphene can be tuned. Upon change in the chemical potential, both τ and μ can change accordingly to a number of factors. Typically, in high quality exfoliated graphene samples τ is left approximately unchanged upon field effect tuning, while for chemically deposited (CVD) graphene the impurities induce a different behavior, and μ tends to be constant instead.

2.6.5 Magnetostatically biased graphene

When a magneto-static field is applied orthogonally to graphene a number of important phenomena occur [105, 41]. Firstly, the band structure is not continuous anymore showing instead discrete energy levels called Landau levels:

$$E_n = \sqrt{n}L \quad (2.150)$$

$$L = \sqrt{2\hbar q_e B_0 v_f^2} \quad (2.151)$$

The conductivity is then expressed as [105, 41]:

$$\mathbf{J} = \underline{\sigma} \mathbf{E} \quad \underline{\sigma} = \begin{pmatrix} \sigma_d & \sigma_o \\ -\sigma_o & \sigma_d \end{pmatrix} \quad (2.152)$$

with:

$$\begin{aligned} \sigma_d = & \frac{j q_e^2 v_f^2 |q_e B_0| \hbar (\omega - j\tau^{-1})}{\pi} \\ & \cdot \sum_{n=0}^{\infty} \left\{ \frac{1}{M_{n+1} - M_n} \cdot \frac{f(M_n) - f(M_{n+1}) + f(-M_{n+1}) - f(-M_n)}{(M_{n+1} - M_n)^2 - \hbar^2 (\omega - j\tau^{-1})^2} + \right. \\ & \left. + \frac{1}{M_{n+1} + M_n} \cdot \frac{f(-M_n) - f(M_{n+1}) + f(-M_{n+1}) - f(M_n)}{(M_{n+1} + M_n)^2 - \hbar^2 (\omega - j\tau^{-1})^2} \right\} \quad (2.153) \end{aligned}$$

and

$$\begin{aligned} \sigma_o = & -\frac{q_e^3 v_f^2 B_0}{\pi} \sum_{n=0}^{\infty} \left\{ f(M_n) - f(M_{n+1}) + f(-M_{n+1}) - f(-M_n) \right\} \\ & \cdot \left\{ \frac{1}{(M_{n+1} - M_n)^2 - \hbar^2 (\omega - j\tau^{-1})^2} + \frac{1}{(M_{n+1} + M_n)^2 - \hbar^2 (\omega - j\tau^{-1})^2} \right\} \quad (2.154) \end{aligned}$$

with

$$M_n = \sqrt{2n v_f^2 |q_e B_0| \hbar} \quad (2.155)$$

$$f(\epsilon) = f_d(\epsilon - \mu_c) \quad (2.156)$$

A low-temperature, low-magnetic-field approximation holds if the number of levels to be considered is so large that the summations can be approximated as integrals and if inter-band

transitions can be neglected. In that case the Drude Lorentz model can be used:

$$\begin{aligned}\sigma_d &= \sigma_{\text{DC}} \frac{1 + j\omega\tau}{(\omega_c\tau)^2 + (1 + j\omega\tau)^2} \\ \sigma_o &= \sigma_{\text{DC}} \frac{\omega_c\tau}{(\omega_c\tau)^2 + (1 + j\omega\tau)^2}\end{aligned}\quad (2.157)$$

where the DC conductivity and cyclotron frequency take a special form in graphene:

$$\sigma_{\text{DC}} = \sigma_{\text{intra}}(\omega = 0, T \rightarrow 0) = \frac{q_e^2\tau|\mu_c|}{\pi\hbar^2} \quad (2.158)$$

$$\omega_c \simeq \frac{L^2}{2\hbar\mu_c} = \frac{q_e B_0 v_f^2}{\mu_c} \quad (2.159)$$

The cyclotron frequency is consistent with the Drude Lorentz model if we assume, one more time, that $m = |\mu_c|v_f^{-2}$.

It is worth mentioning here that the conductivity of graphene takes a particular simple form with circular polarization. In fact, assuming that graphene lies on the xy plane, then the conductivity tensor has two eigenvalues for the circularly polarized light:

$$\begin{aligned}\sigma_{\text{cw}} &= \sigma_d + j\sigma_o \\ \sigma_{\text{ccw}} &= \sigma_d - j\sigma_o\end{aligned}\quad (2.160)$$

So for circularly polarized light, gyrotropic graphene behaves again as a scalar conductivity, but with two different values accordingly to the polarization handedness. This principle is linked to the presence of Faraday rotation, where a linearly polarized wave pass through magnetostatically biased graphene and undergoes a rotation, because the phase of σ_{cw} is different from the one of σ_{ccw}

2.6.6 Non-locality (spatial dispersion) in graphene

This thesis also briefly explores spatial dispersion effects in graphene. The physical phenomenon that causes spatial dispersion is the fact that carriers have a relatively high speed in graphene ($v_f \simeq c/300$) and a good ballistic behavior (in the best samples the mean free path l is in the order of microns). Furthermore, graphene supports plasmonic modes, which show very sharp spatial variations (i.e. very confined waves with k wavevectors much larger than in free space). Because of these effects, in some cases, non-local behavior cannot be neglected. Below is one example of spatially dispersive graphene conductivity presented by Lovat et al in

[69] and used in [JA3]. This is a particular case for a low k-vector approximation:

$$\underline{\sigma} = \begin{pmatrix} \sigma_{XX} & \sigma_{XY} \\ \sigma_{YX} & \sigma_{YY} \end{pmatrix} \quad (2.161)$$

$$\begin{aligned} \sigma_{XX} &= \gamma \frac{\pi}{\alpha} \left[1 + \frac{v_f^2}{4\alpha^2} \left(3 - j \frac{2}{\omega\tau} \right) k_x^2 + \frac{v_f^2}{4\alpha^2} k_y^2 \right] \\ \sigma_{XY} &= \gamma \frac{\pi}{\alpha} \frac{v_f^2}{2\alpha^2} \left(1 - j \frac{1}{\omega\tau} \right) k_x k_y \\ \sigma_{YX} &= \gamma \frac{\pi}{\alpha} \frac{v_f^2}{2\alpha^2} \left(1 - j \frac{1}{\omega\tau} \right) k_x k_y \\ \sigma_{YY} &= \gamma \frac{\pi}{\alpha} \left[1 + \frac{v_f^2}{4\alpha^2} k_x^2 + \frac{v_f^2}{4\alpha^2} \left(3 - j \frac{2}{\omega\tau} \right) k_y^2 \right] \end{aligned} \quad (2.162)$$

with

$$\gamma = -j \frac{q_e k_B T}{\pi^2 \hbar^2} \ln \left[2 + 2 \cosh \left(\frac{\mu_c}{k_B T} \right) \right] \quad (2.163)$$

$$\alpha = \omega - j\tau^{-1} \quad (2.164)$$

which depends on the wavevector components k_x and k_y , and hence it is spatial dispersive. Importantly, even if not obvious, the operator $\underline{\sigma}$ is isotropic (invariant to rotation) because, upon rotation, also the components k_x and k_y are transformed and the total tensor is unchanged.

2.7 Numerical simulations

Simulations of the graphene based devices presented in this thesis have been performed using several softwares.

ANSYS HFSS: The software ANSYS HFSS allows the simulation of truly 2D materials modeled as an impedance boundary condition, and has been used for most of the simulations in this thesis. A general 2D local electrical conductivity tensor can be used as input, allowing the simulation of magneto-statically biased graphene. Plasmonic propagation on graphene can be simulated and plasmons can be excited directly with wave-ports.

Homemade periodic MoM code: A periodic method of moment code developed by Dr. Arya Fallahi has been used to model periodic metasurfaces including graphene. The code supports magnetostatically biased graphene and spatial dispersion. Because of the nature itself of the method of moment code (which reduces the problem to an impedance

matrix) this software computes in a very precise way the \mathbf{W} field involved in tunable and non-reciprocal devices.

CST Studio Suite: CST has been used in simulations of graphene-only reflectarrays in collaboration with Dr. Eduardo Carrasco. As HFSS, it supports truly 2D materials but has been tested in this framework only for plasmonic resonators.

More details on the simulation techniques will be provided in the remaining chapters of this thesis.

3 Theoretical non-reciprocity and modulation upper bounds

Note: this chapter report work previously published by the Ph.D. candidate in references [CA17, JA8, JA13].

3.1 Introduction

Graphene offers interesting possibilities for tunable and non reciprocal devices in a very wide frequency spectrum spanning from microwaves to near infrared. However, it is also characterized by optical losses, which can limit the performances of the devices. While developing the concepts presented in this thesis, it soon became clear that the issue of optical losses in graphene had to be tackled by answering very fundamental questions such as “What is the minimum insertion loss to achieve a given reconfigurability function?” or “Is it possible to build an ideal non-reciprocal isolator using graphene?”. Revisiting a theory developed in [96], this chapter presents several fundamental limits on non-reciprocal and tunable devices based on graphene.

The limits are expressed in the form of upper bound on several key performances of the selected devices, and typically the outcome of these upper bounds is that there is a minimum amount of insertion loss that has to be accepted in order to achieve a given functionality (e.g. 100 % modulation depth in a graphene modulator or infinite isolation in a graphene non reciprocal isolator). This minimum amount of loss, strikingly, depends only on graphene conductivity, and it is independent of the particular geometry of the device. The bound is, therefore, a very important tool to estimate the best possible performances as a function of modulators and isolators based on graphene prior any actual design, just accordingly to graphene parameters. Second, the bound provides important guidelines to the designer, because it reveals how close an actual design is to the best possible performance, so that no useless optimizations are run once the optimal performance has been reached. The theory presented here has been used in the subsequent chapters to ensure the optimality of the presented devices.

The theory proposed here continues a research line started in 1954 by Mason [73, 39], who found out that it is possible to define a value U (the unilateral amplifier gain) for an active two-ports device. This value has the following property: if the two-ports device is embedded in a lossless reciprocal network to obtain a new transformed two-ports device, the value U does not change in this transformation. If the transformation is such that the transmission coefficient S_{12} from port 2 to port 1 becomes null, then the transmission in the opposite direction has a magnitude $|S_{21}| = \sqrt{U}$. The theory can be applied to amplifiers but also to non reciprocal passives, and in that case U is a figure of merit for isolators, which are devices that ideally transmit power waves perfectly in one direction, while blocking them in the other.

Five years later the theory was extended by Shaug-Pettersen and Tønning [96] showing an important mathematical inequality for variable and non-reciprocal networks. Unfortunately, although the inequality is correct, the demonstration provided in [96] contains several errors, which were corrected in our work [JA8]. In [JA8] we also extended the bound to 2D materials, and demonstrated a number of theoretical bounds expressed directly as a function of modulators' and isolators' figures of merit. More recently, we also extended this concept to antennas [JA13]. In this chapter the main results of [JA8, JA13] are presented, and a full demonstration is given for the theoretical bound. Equations up to 3.39 summarizes the Shaug-Pettersen bound [96], including our corrections to the demonstration and presenting the results for general 3D and 2D materials. Subsequently we derive the figures of merit of graphene and we demonstrate the possibility of designing optimal graphene devices [JA8, JA13].

3.2 General scattering upper bound: derivation

Let us consider a reconfigurable or nonreciprocal device based on a reconfigurable or nonreciprocal 2D or 3D material such that the device can be described by a passive $n \times n$ scattering matrix. This representation is suitable for any passive n-mode-guided device, layered surfaces, and periodic metasurfaces, as discussed in the previous chapter. We consider the behavior of the device in two distinct situations, 'A' and 'B', characterized by the considered material \underline{Y} matrices \underline{Y}_A and \underline{Y}_B , the corresponding scattering matrices \underline{S}_A and \underline{S}_B , and arbitrary incident waves \mathbf{a}_A and \mathbf{a}_B . We will refer to this tunable and/or non-reciprocal material as the *functional material*, since it enables the device functionality. Let us also assume a general closed surface S that completely surrounds the device, as explained in Chapter 2. If the device is an infinite planar structure, then S is taken as the union of two planes, one on each side of the structure. Among others, here, we address 2D materials, the presence of additional losses in other materials, and the case of multiple or inhomogeneous reconfigurable/non-reciprocal materials. The general inequality obtained is then further developed in the next section to derive specific upper bounds of the graphene-based devices used for our results. All the materials in the device are passive, local and linear; all the materials a part from the functional material are also assumed to be fixed (they do not change in situation 'A' and 'B') and reciprocal.

3.2. General scattering upper bound: derivation

Recalling that (Chapter 2):

$$\oint_S \mathbf{W} \cdot d\mathbf{S} = \oint_S (\mathbf{E}_A \times \mathbf{H}_B - \mathbf{E}_B \times \mathbf{H}_A) \cdot d\mathbf{S} = 2\mathbf{a}_B^T (\underline{S} - \underline{S}^T) \mathbf{a}_A \quad (3.1)$$

we can now perform a similar derivation, considering that this time the functional material and the device can have different properties in cases 'A' and 'B', which was not the case when discussing simply Lorentz non-reciprocity. We then obtain:

$$\begin{aligned} \oint_S \mathbf{W} \cdot d\mathbf{S} &= \oint_S (\mathbf{E}_A \times \mathbf{H}_B - \mathbf{E}_B \times \mathbf{H}_A) \cdot d\mathbf{S} \\ &= 2(\mathbf{a}_B^T \mathbf{b}_A - \mathbf{a}_A^T \mathbf{b}_B) \\ &= 2(\mathbf{a}_B^T \mathbf{b}_A - \mathbf{b}_B^T \mathbf{a}_A) \\ &= 2(\mathbf{a}_B^T \underline{S}_A \mathbf{a}_A - \mathbf{a}_B^T \underline{S}_B^T \mathbf{a}_A) \\ &= 2\mathbf{a}_B^T (\underline{S}_A - \underline{S}_B^T) \mathbf{a}_A \end{aligned} \quad (3.2)$$

Similarly, this quantity can also be expressed in terms of the material properties:

$$\begin{aligned} W_J^{\text{mat}} &= \mathbf{Q}_B \cdot \mathbf{R}_A - \mathbf{Q}_A \cdot \mathbf{R}_B \\ &= \mathbf{R}_A \cdot \mathbf{Q}_B - \mathbf{R}_B \cdot \mathbf{Q}_A \\ &= \mathbf{R}_A^T \underline{Y}_B \mathbf{R}_B - \mathbf{R}_B^T \underline{Y}_A \mathbf{R}_A \\ &= \mathbf{R}_B^T \underline{Y}_B^T \mathbf{R}_A - \mathbf{R}_B^T \underline{Y}_A \mathbf{R}_A \\ &= \mathbf{R}_B^T (\underline{Y}_B^T - \underline{Y}_A) \mathbf{R}_A \end{aligned} \quad (3.3)$$

In absence of sources in the device, $W_J^{\text{mat}} = W_J^{\text{tot}}$ and using:

$$\oint_S \mathbf{W} \cdot d\mathbf{S} = \iiint_V W_J^{\text{tot}} dV = \iiint_V W_J^{\text{mat}} dV \quad (3.4)$$

we obtain:

$$\mathbf{a}_B^T (\underline{S}_A - \underline{S}_B^T) \mathbf{a}_A = \frac{1}{2} \iiint_V \mathbf{R}_B^T (\underline{Y}_B^T - \underline{Y}_A) \mathbf{R}_A dV \quad (3.5)$$

where V is the volume of the functional material and it is assumed that all the remaining materials a part from the functional one are reciprocal and fixed. The equality above holds

Chapter 3. Theoretical non-reciprocity and modulation upper bounds

for 3D materials, but if the considered material is 2D, then the relation can be extended immediately by replacing the volume integral with a surface integral. For example, for an amagnetic 2D material characterized by electric conductivity tensor $\underline{\sigma}$ we obtain:

$$\mathbf{a}_B^T (\underline{S}_A - \underline{S}_B^T) \mathbf{a}_A = \frac{1}{2} \iint_{\text{2Dmaterial}} \mathbf{E}_{tB}^T (\sigma_A - \sigma_B^T) \mathbf{E}_{tA} dS \quad (3.6)$$

where \mathbf{E}_t represents the Electric field component tangential to the 2D material. A more complete discussion on 2D materials is presented later in this chapter.

The thermal power P dissipated in the device in states 'A' and 'B' is given by:

$$P_A = \mathbf{a}_A^H \left(\underline{I} - \underline{S}_A^H \underline{S}_A \right) \mathbf{a}_A = \frac{1}{2} \iiint_V \mathbf{R}_A^H \left(\underline{Y}_A + \underline{Y}_A^H \right) \mathbf{R}_A dV + L_A \quad (3.7)$$

$$P_B = \mathbf{a}_B^H \left(\underline{I} - \underline{S}_B^H \underline{S}_B \right) \mathbf{a}_B = \frac{1}{2} \iiint_V \mathbf{R}_B^H \left(\underline{Y}_B + \underline{Y}_B^H \right) \mathbf{R}_B dV + L_B \quad (3.8)$$

where L_A and L_B represent the losses in other materials apart from the functional material. This integral is always positive because of the passivity of the involved material, which implies that $\underline{Y} + \underline{Y}^H$ is hermitian and positively defined.

Let us now consider the following quantity:

$$\gamma_{\text{dev}} \triangleq \frac{\left| \mathbf{a}_B^T (\underline{S}_A - \underline{S}_B^T) \mathbf{a}_A \right|^2}{\mathbf{a}_A^H \left(\underline{I} - \underline{S}_A^H \underline{S}_A \right) \mathbf{a}_A \mathbf{a}_B^H \left(\underline{I} - \underline{S}_B^H \underline{S}_B \right) \mathbf{a}_B} \quad (3.9)$$

This quantity is always real and positive, and depends uniquely on the final scattering matrices \underline{S}_A and \underline{S}_B of the device in the two states, and on two excitation vectors \mathbf{a}_A and \mathbf{a}_B which can be chosen arbitrarily. This quantity is called, for reasons which will become clear later, the *device figure of merit*. We can rewrite this expression using Equations 3.5, 3.7 and 3.8 as:

$$\gamma_{\text{dev}} = \frac{\left| \iiint_V \mathbf{R}_B^T (\underline{Y}_B^T - \underline{Y}_A) \mathbf{R}_A dV \right|^2}{\left[\iiint_V \mathbf{R}_A^H \left(\underline{Y}_A + \underline{Y}_A^H \right) \mathbf{R}_A dV + L_A \right] \left[\iiint_V \mathbf{R}_B^H \left(\underline{Y}_B + \underline{Y}_B^H \right) \mathbf{R}_B dV + L_B \right]} \quad (3.10)$$

Next, we will make a chain of inequalities to simplify this expression with the aim of reaching an expression depending only on the properties of the functional material (i.e. independently

3.2. General scattering upper bound: derivation

of the actual fields). First we notice that γ_{dev} is maximized when there are no losses L_A and L_B :

$$\gamma_{\text{dev}} = \frac{\left| \iiint_V \mathbf{R}_B^T (\underline{Y}_B^T - \underline{Y}_A) \mathbf{R}_A dV \right|^2}{\left[\iiint_V \mathbf{R}_A^H (\underline{Y}_A + \underline{Y}_A^H) \mathbf{R}_A dV + L_A \right] \left[\iiint_V \mathbf{R}_B^H (\underline{Y}_B + \underline{Y}_B^H) \mathbf{R}_B dV + L_B \right]} \quad (3.11)$$

$$\leq \frac{\left| \iiint_V \mathbf{R}_B^T (\underline{Y}_B^T - \underline{Y}_A) \mathbf{R}_A dV \right|^2}{\left[\iiint_V \mathbf{R}_A^H (\underline{Y}_A + \underline{Y}_A^H) \mathbf{R}_A dV \right] \left[\iiint_V \mathbf{R}_B^H (\underline{Y}_B + \underline{Y}_B^H) \mathbf{R}_B dV \right]} \quad (3.12)$$

Next, because of the integral absolute value theorem we have:

$$\left| \iiint_V \mathbf{R}_B^T (\underline{Y}_B^T - \underline{Y}_A) \mathbf{R}_A dV \right|^2 \leq \left(\iiint_V \left| \mathbf{R}_B^T (\underline{Y}_B^T - \underline{Y}_A) \mathbf{R}_A \right| dV \right)^2 \quad (3.13)$$

and hence

$$\gamma_{\text{dev}} \leq \frac{\left(\iiint_V \left| \mathbf{R}_B^T (\underline{Y}_B^T - \underline{Y}_A) \mathbf{R}_A \right| dV \right)^2}{\left[\iiint_V \mathbf{R}_A^H (\underline{Y}_A + \underline{Y}_A^H) \mathbf{R}_A dV \right] \left[\iiint_V \mathbf{R}_B^H (\underline{Y}_B + \underline{Y}_B^H) \mathbf{R}_B dV \right]} \quad (3.14)$$

The next objective is to remove the integrals from the expression by maximizing it. To this aim, let us consider three general real positive functions $e(r)$, $b(r)$, $c(r)$. These functions can be defined on a domain with an arbitrary number of dimensions. Now we consider the quantity:

$$\left(\int \sqrt{e(r)b(r)c(r)} dr \right)^2 \quad (3.15)$$

if we consider the maximum value of $e(r)$, namely $\max_r e(r)$, we can then write

$$\left(\int \sqrt{e(r)b(r)c(r)} dr \right)^2 \leq \max_r e(r) \left(\int \sqrt{b(r)c(r)} dr \right)^2 \quad (3.16)$$

Chapter 3. Theoretical non-reciprocity and modulation upper bounds

Furthermore, using the Cauchy-Schwarz inequality:

$$\begin{aligned} \left(\int \sqrt{e(r)b(r)c(r)} \, dr \right)^2 &\leq \max_r e(r) \left(\int \sqrt{b(r)c(r)} \, dr \right)^2 \\ &\leq \max_r e(r) \int b(r) \, dr \int c(r) \, dr \end{aligned} \quad (3.17)$$

If we now define:

$$a(r) \triangleq \sqrt{e(r)b(r)c(r)} \quad (3.18)$$

$$e(r) = \frac{a^2(r)}{b(r)c(r)} \quad (3.19)$$

we obtain:

$$\frac{\left(\int a(r) \, dr \right)^2}{\int b(r) \, dr \int c(r) \, dr} \leq \max_r \frac{a^2(r)}{b(r)c(r)} \quad (3.20)$$

We can now apply Equation 3.20 to 3.14 obtaining:

$$\begin{aligned} \gamma_{\text{dev}} &\leq \frac{\left(\iiint_V \left| \mathbf{R}_B^T (\underline{Y}_B^T - \underline{Y}_A) \mathbf{R}_A \right| dV \right)^2}{\left[\iiint_V \mathbf{R}_A^H (\underline{Y}_A + \underline{Y}_A^H) \mathbf{R}_A dV \right] \left[\iiint_V \mathbf{R}_B^H (\underline{Y}_B + \underline{Y}_B^H) \mathbf{R}_B dV \right]} \\ &\leq \max_V \frac{\left| \mathbf{R}_B^T (\underline{Y}_B^T - \underline{Y}_A) \mathbf{R}_A \right|^2}{\mathbf{R}_A^H (\underline{Y}_A + \underline{Y}_A^H) \mathbf{R}_A \mathbf{R}_B^H (\underline{Y}_B + \underline{Y}_B^H) \mathbf{R}_B} \end{aligned} \quad (3.21)$$

After successfully removing the integrals, the next step is to remove the dependence on fields, once again by maximization. To do so, first we define:

$$\underline{T}_A \triangleq \underline{Y}_A + \underline{Y}_A^H \quad (3.22)$$

$$\underline{T}_B \triangleq \underline{Y}_B + \underline{Y}_B^H \quad (3.23)$$

3.2. General scattering upper bound: derivation

obtaining:

$$\gamma_{\text{dev}} \leq \max_V \frac{\left| \mathbf{R}_B^T (\underline{Y}_B^T - \underline{Y}_A) \mathbf{R}_A \right|^2}{\mathbf{R}_A^H \underline{T}_A \mathbf{R}_A \mathbf{R}_B^H \underline{T}_B \mathbf{R}_B} \quad (3.24)$$

Because of passivity, both \underline{T}_A and \underline{T}_B are positive defined Hermitian matrices. Therefore they can be written as [45]:

$$\underline{T}_A = \underline{M}_A^H \underline{M}_A \quad (3.25)$$

$$\underline{T}_B = \underline{M}_B^H \underline{M}_B \quad (3.26)$$

obtaining:

$$\gamma_{\text{dev}} \leq \max_V \frac{\left| \mathbf{R}_B^T (\underline{Y}_B^T - \underline{Y}_A) \mathbf{R}_A \right|^2}{\mathbf{R}_A^H \underline{M}_A^H \underline{M}_A \mathbf{R}_A \mathbf{R}_B^H \underline{M}_B^H \underline{M}_B \mathbf{R}_B} \quad (3.27)$$

Defining the vectors:

$$\mathbf{K}_A \triangleq \underline{M}_A \mathbf{R}_A \quad (3.28)$$

$$\mathbf{K}_B \triangleq \underline{M}_B \mathbf{R}_B \quad (3.29)$$

we get:

$$\begin{aligned} \gamma_{\text{dev}} &\leq \max_V \frac{\left| \mathbf{K}_B^T \underline{M}_B^{-1T} (\underline{Y}_B^T - \underline{Y}_A) \underline{M}_A^{-1} \mathbf{K}_A \right|^2}{\mathbf{K}_A^H \mathbf{K}_A \mathbf{K}_B^H \mathbf{K}_B} \\ &= \max_V \frac{\left| \mathbf{K}_B^T \underline{M}_B^{-1T} (\underline{Y}_B^T - \underline{Y}_A) \underline{M}_A^{-1} \mathbf{K}_A \right|^2}{|\mathbf{K}_A|^2 |\mathbf{K}_B|^2} \end{aligned} \quad (3.30)$$

This quantity does not change if the vectors \mathbf{K} are multiplied by a real scalar, so we can assume, without loss of generality, that $|\mathbf{K}_A| = 1$ and $|\mathbf{K}_B| = 1$; thus

$$\gamma_{\text{dev}} \leq \max_V \left| \mathbf{K}_B^T \underline{M}_B^{-1T} (\underline{Y}_B^T - \underline{Y}_A) \underline{M}_A^{-1} \mathbf{K}_A \right|^2 \quad (3.31)$$

Chapter 3. Theoretical non-reciprocity and modulation upper bounds

In this expression, the only quantities affected by the particular choice of excitation are the vectors \mathbf{K} , whereas the remaining vectors depend only on the conductivities. If the conductivities are constant over the entire functional material (the non-constant case is discussed later), the quantity being maximized is actually bounded by a certain value γ_{mat} :

$$\left| \mathbf{K}_B^T \underline{M}_B^{-1T} (\underline{Y}_B^T - \underline{Y}_A) \underline{M}_A^{-1} \mathbf{K}_A \right|^2 \leq \gamma_{\text{mat}} \quad (3.32)$$

This is due to the fact that \mathbf{K}_A and \mathbf{K}_B are unit vectors and by the fact that the matrix \underline{A} defined as

$$\underline{A} \triangleq \underline{M}_B^{-1T} (\underline{Y}_B^T - \underline{Y}_A) \underline{M}_A^{-1} \quad (3.33)$$

is independent of the choice of \mathbf{K}_A and \mathbf{K}_B and depends only on the conductivities. Then, by definition, the upper bound γ_{mat} is the square of the two-norm of matrix \underline{A} :

$$\gamma_{\text{mat}} = \|\underline{A}\|_2^2 = \text{Largest eigenvalue of } (\underline{A}^H \underline{A}) \quad (3.34)$$

The eigenvalues are not changed by a similarity transformation, so we can write:

$$\gamma_{\text{mat}} = \text{Largest eigenvalue of } (\underline{M}_A^{-1} \underline{A}^H \underline{A} \underline{M}_A) \quad (3.35)$$

Defining:

$$\underline{N} \triangleq \underline{M}_A^{-1} \underline{A}^H \underline{A} \underline{M}_A \quad (3.36)$$

and substituting the values of \underline{M}_A and \underline{A} we find

$$\gamma_{\text{mat}} = \text{Largest eigenvalue of } \underline{N} \quad (3.37)$$

$$\underline{N} = (\underline{Y}_A + \underline{Y}_A^H)^{-1} (\underline{Y}_B^* - \underline{Y}_A^H) (\underline{Y}_B^* + \underline{Y}_B^T)^{-1} (\underline{Y}_B^T - \underline{Y}_A) \quad (3.38)$$

Combining the previous equations we finally find:

$$\gamma_{\text{dev}} \leq \gamma_{\text{mat}} \quad (3.39)$$

$$\gamma_{\text{dev}} \triangleq \frac{\left| \mathbf{a}_B^T (\underline{S}_A - \underline{S}_B^T) \mathbf{a}_A \right|^2}{\mathbf{a}_A^H \left(\underline{I} - \underline{S}_A^H \underline{S}_A \right) \mathbf{a}_A \mathbf{a}_B^H \left(\underline{I} - \underline{S}_B^H \underline{S}_B \right) \mathbf{a}_B} \quad (3.40)$$

$$\gamma_{\text{mat}} \triangleq \text{Largest eigenvalue of } \underline{N} \quad (3.41)$$

$$\underline{N} \triangleq \left(\underline{Y}_A + \underline{Y}_A^H \right)^{-1} \left(\underline{Y}_B^* - \underline{Y}_A^H \right) \left(\underline{Y}_B^* + \underline{Y}_B^T \right)^{-1} \left(\underline{Y}_B^T - \underline{Y}_A \right) \quad (3.42)$$

which is referred to as the *general scattering upper bound*.

Importantly, Equation 3.39 is an inequality relating γ_{dev} , which depends on the final device properties only, and γ_{mat} , which depends on the material properties only. The fact that device performances are bounded by material properties alone is the main strength of this approach, which holds independently of the device geometry and prior to any device design. In the following sections it is shown that, in all cases, devices with lower losses (and hence better performances) possess a larger γ_{dev} , which therefore is named *device figure of merit*. However, because the value of γ_{dev} is bounded by γ_{mat} , a minimum amount of loss is unavoidable, and this loss is determined by γ_{mat} which is then called *material figure of merit*. The two quantities can be used as metrics for the optimality of device and materials respectively, and they take positive real value (from 0 to $+\infty$).

For some materials, the inverse matrices in 3.42 might be singular. In that case, for practical materials, the singularity is compensated by a zero in the other factors of 3.42. These undefined eigenvalues can then be neglected, since they are associated with no loss and no reconfigurability (or no non-reciprocity) at the same time. The vectors \mathbf{a}_A and \mathbf{a}_B are free parameters, namely this upper bound represents actually an infinite set of upper bounds, each holding for a different choice of \mathbf{a}_A and \mathbf{a}_B . It will be shown that an accurate choice of these parameters can lead to specialized upper bounds on relevant figure of merit (such as, for example, isolation and insertion loss of an optical isolator).

3.2.1 Multiple and non-homogeneous functional materials

When a device contains several reconfigurable/non-reciprocal materials, the right term of Equation 3.31 indicates that the total γ_{mat} is equal to the maximum γ_{mat} of the materials involved. Particularly important is the following case: consider a reconfigurable device with two states ('0' and '1'); the device is based on a material with \underline{Y}_A and \underline{Y}_B , but some parts of the material have \underline{Y} matrix \underline{Y}_A on state '0' (and \underline{Y}_B on state '1'), whereas the remainder has \underline{Y} matrix \underline{Y}_B on state '0' (and \underline{Y}_A on state '1'). The γ_{mat} bound still holds in this case because we can consider the two areas as two distinct materials having inverted states and identical γ_{mat} . Finally, if the functional material is non-homogeneous, then it can be thought as an infinite

set of materials, and the figure of merit will be equal to the maximum value of γ_{mat} over the entire material.

3.3 Reconfigurability vs non-reciprocity

The general upper bound can be used to obtain performance upper bounds in two cases of interest:

- **Modulation or reconfigurability:** The material is assumed to be reciprocal and its \underline{Y} matrix takes two different values in situations 'A' and 'B'. This situation includes tunable devices such as switches, modulators, phase shifters and reconfigurable antennas. In this case $\underline{Y}_A^T = \underline{Y}_A \neq \underline{Y}_B = \underline{Y}_B^T$.
- **Non-reciprocity:** The material properties do not change between situations 'A' and 'B' (only the excitation do), but the material is not reciprocal, and hence $\underline{Y}_A^T \neq \underline{Y}_A = \underline{Y}_B \neq \underline{Y}_B^T$. The material matrix is then simply $\underline{Y}^T \neq \underline{Y}$.

For the modulation or reconfigurability case, the material figure of merit γ_{mat} is renamed as γ_M , for the non reciprocal case as γ_{NR} .

3.3.1 Inversion of magnetostatic field

The mixed case (reconfigurable and non-reciprocal) is of difficult interpretation. There is, however, a very simple case falling in this category where the bound gives an immediately useful results. Let us consider the case where non-reciprocal materials are biased by a magnetostatic field; in this case, usually the inversion of the field causes the transposition of the \underline{Y} matrix of the material. Then we consider:

- Situation A: The material is biased by a magnetostatic field \mathbf{B}_0 and the resulting matrix \underline{Y}_A is non-symmetric.
- Situation B: The material is biased by the reverse magnetostatic field $-\mathbf{B}_0$ and the resulting non-symmetric matrix \underline{Y}_B is then $\underline{Y}_B = \underline{Y}_A^T$

Considering the N matrix, it is immediate to see that, because $\underline{Y}_A - \underline{Y}_B^T = \underline{0}$, $N = \underline{0}$. Hence $\gamma_{\text{max}} = 0$ and using the general scattering inequality we immediately obtain $\underline{S}_A - \underline{S}_B^T = \underline{0}$ and hence $\underline{S}_A = \underline{S}_B^T$. This is the demonstration that the scattering matrix is transposed upon inversion of the biasing magnetic field, as mentioned in the previous chapter and in [113, 54].

3.4 Graphene figure of merits

As mentioned above, the presented theory can be extended immediately to linear, local, passive 2D materials, by noting that:

$$\begin{aligned}
 \iiint_V W_J^{\text{mat}} dV &= \iiint_V \mathbf{R}_B^T (\underline{Y}_B^T - \underline{Y}_A) \mathbf{R}_A dV \\
 &= \iiint_V [(\mathbf{J}_{E,A}^{\text{mat}} \cdot \mathbf{E}_B - \mathbf{J}_{E,B}^{\text{mat}} \cdot \mathbf{E}_A) - (\mathbf{J}_{M,A}^{\text{mat}} \cdot \mathbf{H}_B - \mathbf{J}_{M,B}^{\text{mat}} \cdot \mathbf{H}_A)] dV \\
 &= \iint_{2\text{Dmat}} [(\mathbf{J}_{E,A}^{2\text{Dmat}} \cdot \mathbf{E}_B - \mathbf{J}_{E,B}^{2\text{Dmat}} \cdot \mathbf{E}_A) - (\mathbf{J}_{M,A}^{2\text{Dmat}} \cdot \mathbf{H}_B - \mathbf{J}_{M,B}^{2\text{Dmat}} \cdot \mathbf{H}_A)] dS \\
 &= \iint_{2\text{Dmat}} \mathbf{R}_{B,\text{tang}}^T (\underline{Y}_{B,2D}^T - \underline{Y}_{A,2D}) \mathbf{R}_{A,\text{tang}} dS
 \end{aligned} \tag{3.43}$$

which follows from the deltiform distribution of currents on 2D materials. If the material is also amagnetic (with electrical conductivity tensor $\underline{\sigma}$), we have:

$$\underline{N} \triangleq (\sigma_A + \sigma_A^H)^{-1} (\sigma_B^* - \sigma_A^H) (\sigma_B^* + \sigma_B^T)^{-1} (\sigma_B^T - \sigma_A) \tag{3.44}$$

3.4.1 Graphene reconfigurability figure of merit

Let us consider first the reconfigurability case applied to graphene. When an electrostatic field is applied to graphene, its conductivity changes and the scattering properties of the device are modulated (electro-optical modulation). For example, one can design a device having high transmission coefficient in one state and low in the other (amplitude modulator). We assume that τ remains constant while the Fermi level μ_c changes in response to gating. In this case, graphene conductivity is a scalar, and the reconfigurability figure of merit is simplified:

$$\gamma_{\text{mat}} = \gamma_M = \frac{|\sigma_A - \sigma_B|^2}{4\text{Re}(\sigma_A)\text{Re}(\sigma_B)} \tag{3.45}$$

We notice that the figure of merit takes an intuitive form, because its value is decreased if the material has large conductivity real part (associated to ohmic loss) and it is increased proportionally to the absolute value of the difference of the conductivities. If the low temperature intra-band approximation can be used (Equation 2.142), then the figure of merit takes a

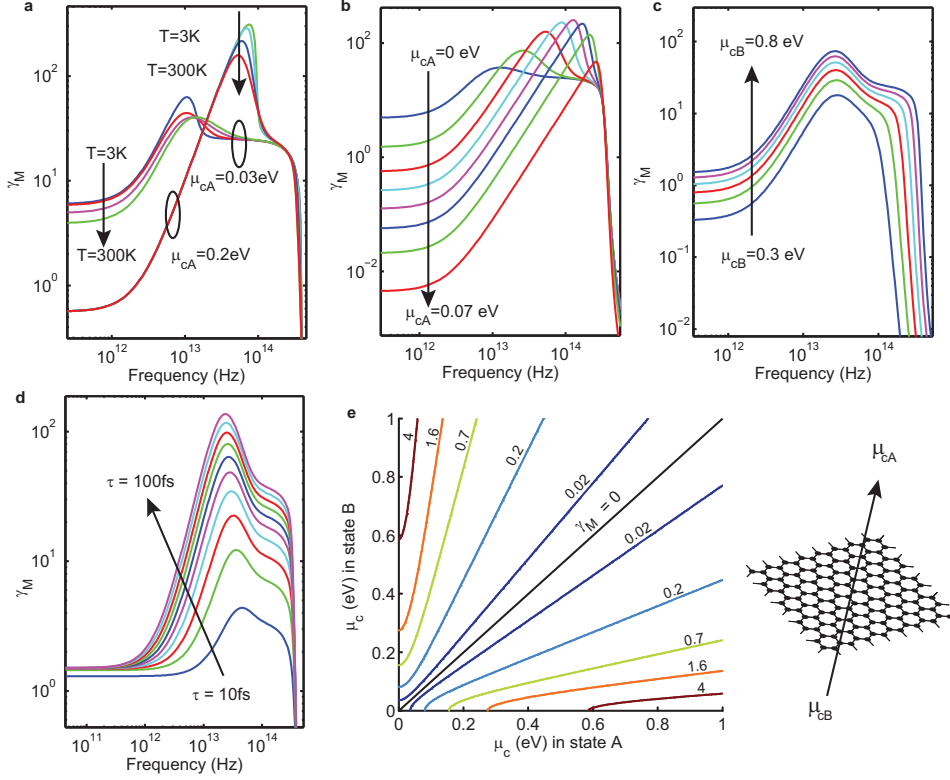


Figure 3.1 – Theoretical upper bound γ_M on the performance of graphene modulators as a function of multiple parameters. In all plots, the quantities that are not swept or otherwise specified have values of $f=1$ THz, $T=300$ K, $\mu_{c,A}=0.1$ eV, $\mu_{c,B}=0.8$ eV, $\tau=66$ fs. a-d) frequency dependence of γ_M for several values of a) temperature, b) $\mu_{c,A}$, c) $\mu_{c,B}$, and d) τ . e) parametric level curves of γ_M for different values of $\mu_{c,A}$ and $\mu_{c,B}$

simpler form:

$$\begin{aligned}
 \sigma_A &\simeq \frac{q_e^2 |\mu_{c,A}| \tau}{\pi \hbar^2 (1 + j\omega\tau)} \\
 \sigma_B &\simeq \frac{q_e^2 |\mu_{c,B}| \tau}{\pi \hbar^2 (1 + j\omega\tau)} \\
 \gamma_{\text{mat}} &\simeq \gamma_M = \frac{(1 + \omega^2 \tau^2) (|\mu_{c,A}|^2 - |\mu_{c,B}|^2)}{4 |\mu_{c,A}| |\mu_{c,B}|} \quad (3.46)
 \end{aligned}$$

and demonstrates that the figure of merit improves with increasing difference of chemical potentials, increasing frequency and τ (once the conductivity is in the plasmonic region).

Figure 3.1 shows values of γ_M as a function of different parameters influencing the conductivity of graphene in the two states, leading to the following conclusions. First, the best modulation performances can be obtained between 10 and 100 THz and, evidently, for larger dynamic variations of the chemical potential. The performance sharply decreases at shorter wavelengths due to the well-known universal conductivity of graphene at optical frequencies (see Equation

2.146), effectively preventing any modulation; hence, $\gamma_M=0$. The transition frequency depends on the largest chemical potential (Figure 3.1c) and is coarsely approximated by twice the Fermi level, corresponding to the emergence of interband transitions. As expected, temperature is only important for low values of Fermi level, whereas the graphene relaxation time τ has a very strong impact on the ultimate performance because it directly affects the loss mechanism.

3.4.2 Graphene non-reciprocity figure of merit

When a magnetostatic field is applied to graphene, the conductivity takes the form in Equation 2.152:

$$\underline{\sigma}_A = \underline{\sigma}_B = \underline{\sigma} = \begin{pmatrix} \sigma_d & \sigma_o \\ -\sigma_o & \sigma_d \end{pmatrix} \quad (3.47)$$

The graphene non-reciprocity figure of merit is then:

$$\gamma_{\text{mat}} = \gamma_{\text{NR}} = \frac{|\sigma_o|^2}{\text{Re}^2(\sigma_d) - \text{Im}^2(\sigma_o)} \quad (3.48)$$

The figure of merit increases for larger off-diagonal conductivities, as expected, and it decreases for larger real part of the diagonal conductivity. Less intuitively, a larger imaginary part of the off-diagonal conductivity can improve the figure of merit, as it compensates for the loss.

If the Drude Lorentz approximation can be used (Equation 2.157), then:

$$\begin{aligned} \sigma_d &\simeq \sigma_{\text{DC}} \frac{1 + j\omega\tau}{(\omega_c\tau)^2 + (1 + j\omega\tau)^2} \\ \sigma_o &\simeq \sigma_{\text{DC}} \frac{\omega_c\tau}{(\omega_c\tau)^2 + (1 + j\omega\tau)^2} \\ \gamma_{\text{NR}} &\simeq (\omega_c\tau)^2 = (\mu B_0)^2 = \left(\frac{q_e\tau v_f^2 B_0}{\mu_c} \right)^2 \end{aligned} \quad (3.49)$$

showing that higher magnetic field and graphene mobility lead to better non-reciprocal figure of merit.

Figure 3.2a illustrates that the optimal performance improves for larger magnetostatic biasing, as expected. A less obvious observation is the fact that isolators perform better at low μ_c if τ is unchanged; this finding can also be inferred by the inspection of (9). This observation can be explained semi-classically by noting that the effective mass $m = |\mu_c| v_f^{-2}$ of the carriers decreases (or similarly, the mobility increases) for low μ_c ; thus, the bending of their trajectories due to the magnetic field increases (higher cyclotron frequency). Figure 3.2b illustrates that temperature is influential at low Fermi level, where the presence of thermal carriers of both

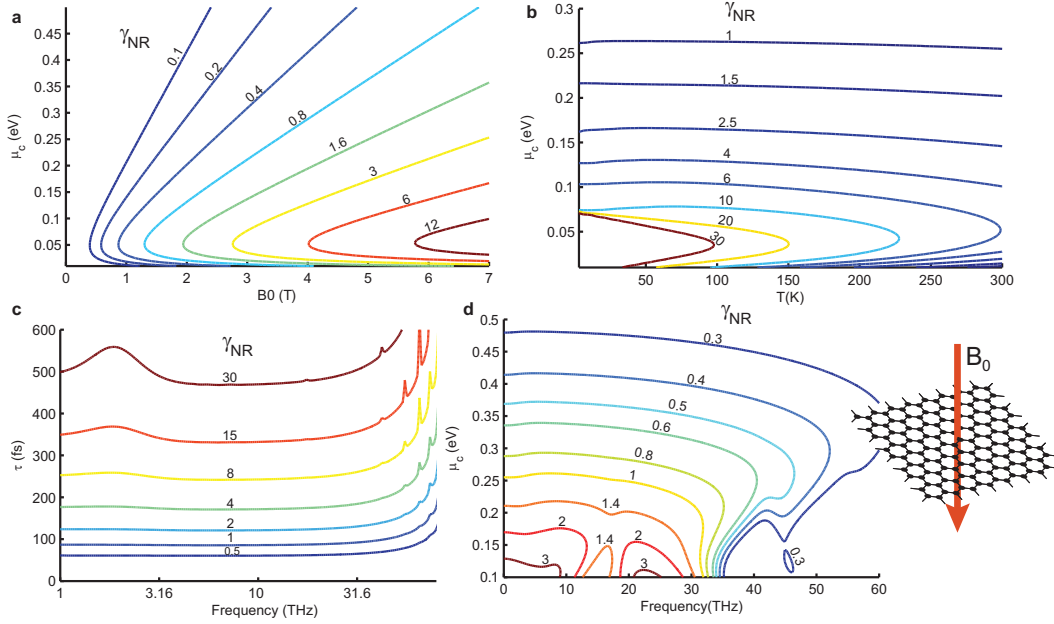


Figure 3.2 – Theoretical upper bound (γ_{NR}) to the performance of graphene non-reciprocal devices as a function of multiple parameters. Full magneto-optical conductivity is used (Equations 2.153 and 2.154). In all plots, the quantities that are not swept have the values of $f=1$ THz, $T=300$ K, $\mu_c=0.34$ eV, $B_0=4$ T, and $\tau=66$ fs. Each contour is marked with the corresponding value of γ_{NR} . a) temperature vs. chemical potential sweep. b) bias magnetic field vs. chemical potential sweep. c) frequency vs. relaxation time sweep. d) frequency vs. chemical potential sweep.

polarities degrades the performance. High values of τ , i.e., high graphene quality, can lead to very high γ_{NR} , as shown in Figure 3.2c. Figures 3.2c and 3.2d illustrate that performance is relatively frequency-invariant until the mid-infrared region, where the frequency drops due to interband transitions and to the universal optical conductivity of graphene. The invariance toward low frequencies can be explained by the independence of γ_{NR} on the imaginary part of σ_d in (8). This behavior contrasts with that of γ_M in the modulation case, which degrades significantly toward low-terahertz and microwave frequencies (see Figure 3.1). This difference in behavior indicates that, unlike in modulators, plasmonic resonances are not instrumental to achieving high performance in graphene-based non-reciprocal devices.

3.5 Device specific upper bounds

In this section several performance upper bounds useful for specific tunable and non-reciprocal devices are presented. Tunability can be used for electro-optical modulators, switches or reconfigurable antennas, while non reciprocity for isolators, circulators, gyrators and Kerr rotators. Figure 3.3 illustrates some examples of these functionalities for planar devices (i.e. operating for incident plane waves).

If graphene (or any material supported by the upper bound) is used to achieve modulation, then the general scattering inequality applies and can be used. The inequality is valid for any

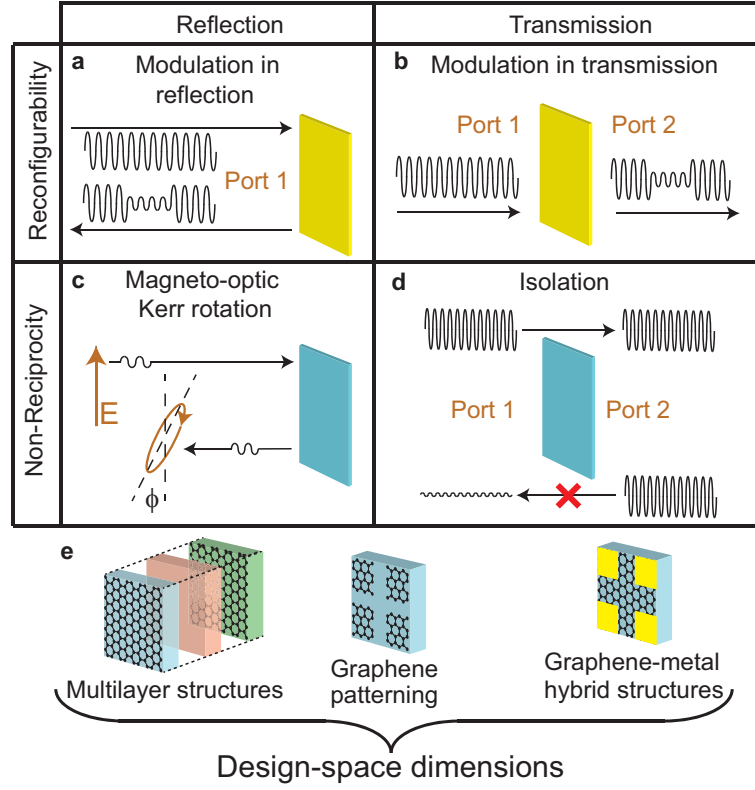


Figure 3.3 – Graphene-based capabilities used for a detailed illustration of the method and ‘design space’ dimensions. The device capabilities are classified according to the direction (reflection or transmission) and framework (non-reciprocity or reconfigurability). a) amplitude modulation in reflection. b) amplitude modulation in transmission. c) magneto-optical Kerr rotation. d) isolation. e) main independent degrees of freedom for the design of the devices.

pair of vectors \mathbf{a}_A and \mathbf{a}_B . In particular, if \mathbf{a}_A and \mathbf{a}_B are both chosen with only one nonzero entry, a specific term of the matrix $\underline{S}_A - \underline{S}_B^T$ is selected to appear in the numerator. The selected entry represents a specific signal path inside the multiport device, and the two vectors \mathbf{a}_A and \mathbf{a}_B determine the source and the observation ports of the signal, respectively. For example if for a 3-ports device $\mathbf{a}_A = [1, 0, 0]^T$ and $\mathbf{a}_B = [0, 1, 0]^T$ then the path from port 1 to port 2 is selected, or if $\mathbf{a}_A = [0, 0, 1]^T$ and $\mathbf{a}_B = [0, 0, 1]^T$ then the reflection coefficient of port 3 is selected. Therefore \mathbf{a}_A and \mathbf{a}_B must be chosen according to the specific device capability considered, as done in the examples below.

3.5.1 Modulators

Electro-optic modulation is the most studied application based on the dynamic reconfiguration of graphene conductivity. The practical feasibility of these devices has been verified at different frequencies, ranging from infrared to kHz. In particular, graphene demonstrates a remarkable potential for modulation at THz frequencies, where alternative technologies exhibit significant limitations¹⁶. Graphene modulators, either in guided-wave systems or

Chapter 3. Theoretical non-reciprocity and modulation upper bounds

as metasurfaces for free space beams, can be rigorously described using scattering matrix formalism. The scattering matrix of the modulator takes two distinct values, \underline{S}_A and \underline{S}_B , for the two scalar conductivities σ_A and σ_B of graphene, obtained by applying different electrostatic bias fields. Here, we consider amplitude modulators both in reflection and in transmission.

Modulators in reflection

An amplitude modulator in reflection is a single port device that reflects electromagnetic waves with different amplitudes in states 'A' and 'B'. The scattering matrix is a complex scalar, namely, $\underline{S}_A = \Gamma_A$ for state 'A' and $\underline{S}_B = \Gamma_B$ for state 'B'. Because a modulator in reflection is a single port device, here simply $\mathbf{a}_A = \mathbf{a}_B = 1$, and we obtain

$$\gamma_{\text{Mod}} \triangleq \frac{|\Gamma_A - \Gamma_B|^2}{(1 - |\Gamma_A|^2)(1 - |\Gamma_B|^2)} \leq \gamma_M \quad (3.50)$$

The numerator indicates that the difference between the reflection coefficients in the two states is affected by the bound. Γ_A and Γ_B can differ in absolute value (amplitude modulator) or have approximately the same magnitude and differ in phase (phase modulator) or a mix of these two cases. The value γ_{Mod} is the *device* modulation figure of merit, and it expresses the optimality of the device modulation.

To better understand the bound, we notice that a common phase factor among Γ_A and Γ_B is irrelevant for modulation purposes. Hence we can represent the bound using these three real numbers instead:

- The magnitude in state 'A' i.e. $|\Gamma_A|$
- The magnitude in state 'B' i.e. $|\Gamma_B|$
- The phase difference $\varphi \triangleq \angle\Gamma_A - \angle\Gamma_B$

We then get:

$$\gamma_{\text{Mod}} = \frac{|\Gamma_A|^2 + |\Gamma_B|^2 - 2|\Gamma_A||\Gamma_B|\cos\varphi}{(1 - |\Gamma_A|^2)(1 - |\Gamma_B|^2)} \leq \gamma_M \quad (3.51)$$

Next we notice, after some algebraic passages:

$$\gamma_{\text{Mod}} = \gamma_{\text{AMod}} + \gamma_{\text{PMod}} \leq \gamma_M \quad (3.52)$$

$$\gamma_{\text{AMod}} \triangleq \frac{(|\Gamma_A| - |\Gamma_B|)^2}{(1 - |\Gamma_A|^2)(1 - |\Gamma_B|^2)} \quad (3.53)$$

$$\gamma_{\text{PMod}} \triangleq \frac{2|\Gamma_A||\Gamma_B|(1 - \cos\varphi)}{(1 - |\Gamma_A|^2)(1 - |\Gamma_B|^2)} \quad (3.54)$$

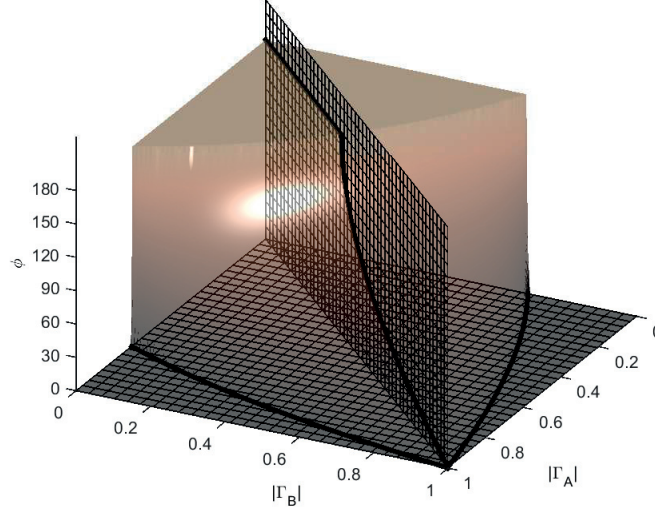


Figure 3.4 – 3D representation of the general modulation bound (Equation 3.51) using as example the value $\gamma_M = 1$

γ_{AMod} and γ_{PMod} are metrics for the optimality of the device as amplitude or phase modulator respectively. Their sum must be lower than the material reconfigurability figure of merit, which means that if the target is the optimization of a phase modulator, then the amplitude modulation must be minimized and vice versa. Clearly, since all γ quantities are real and positive, we can always write $\gamma_{AMod} \leq \gamma_M$ and $\gamma_{PMod} \leq \gamma_M$.

We notice that γ_{AMod} depends on two real parameters only, representing the magnitude of the reflection coefficients. γ_{PMod} depends instead on all the parameters, but it can be reduced to a simpler form at the cost of obtaining a slightly less strict bound. In fact, defining the minimum among reflection coefficients magnitudes $R_{\min} \triangleq \min(|\Gamma_A|, |\Gamma_B|)$, we get:

$$\gamma'_{PMod} \leq \gamma_{PMod} \quad (3.55)$$

$$\gamma_{AMod} + \gamma'_{PMod} \leq \gamma_{AMod} + \gamma_{PMod} = \gamma_{Mod} \leq \gamma_M \quad (3.56)$$

$$\gamma_{AMod} \triangleq \frac{(|\Gamma_A| - |\Gamma_B|)^2}{(1 - |\Gamma_A|^2)(1 - |\Gamma_B|^2)} \leq \gamma_{Mod} \leq \gamma_M \quad (3.57)$$

$$\gamma'_{PMod} \triangleq \frac{2R_{\min}^2(1 - \cos \varphi)}{(1 - R_{\min}^2)^2} \leq \gamma_{Mod} \leq \gamma_M \quad (3.58)$$

$$\gamma_{PMod} \triangleq \frac{2|\Gamma_A||\Gamma_B|(1 - \cos \varphi)}{(1 - |\Gamma_A|^2)(1 - |\Gamma_B|^2)} \leq \gamma_{Mod} \leq \gamma_M \quad (3.59)$$

Notice that if $|\Gamma_A| = |\Gamma_B|$ we actually have $\gamma'_{PMod} = \gamma_{PMod}$, and hence we do not lose in terms of optimality, implying that phase modulators should be designed with $|\Gamma_A| = |\Gamma_B|$ for better performances. It is now useful to graphically represent the upper bound for the various cases.

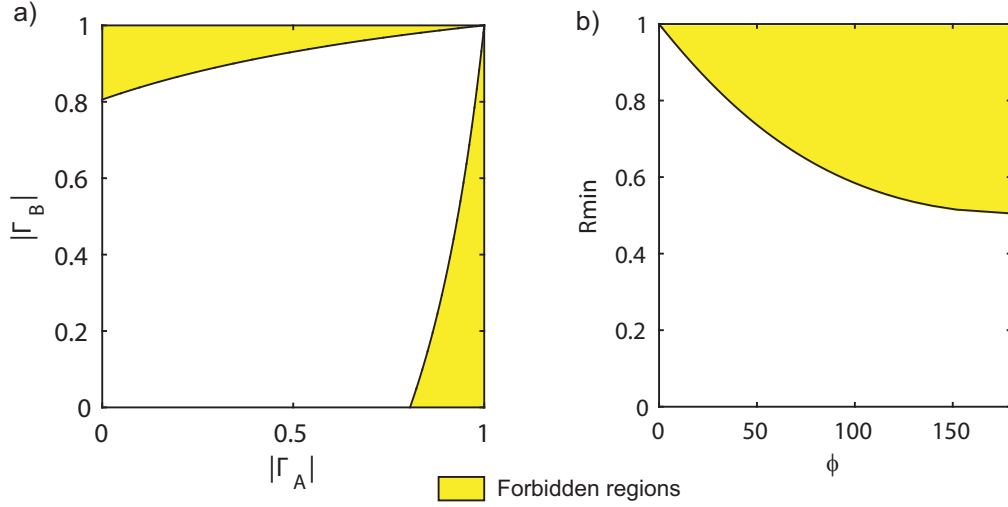


Figure 3.5 – Graphical representation of the amplitude (a) and phase (b) upper bounds (Equations 3.57, 3.58)

First, the general modulation bound (Equation 3.51) can be represented in the selected three real variables as in Figure 3.4. Each modulator (at a given design frequency) is a point in the Cartesian space $(|\Gamma_A|, |\Gamma_B|, \phi)$, called *performance space*, and must lie below the surface represented in the figure (the region above is called *forbidden region*). The value $\gamma_M = 1$ has been used as example, for smaller values the surface becomes smaller, reducing the allowed volume for the modulators. Next, the amplitude modulation bound (Equation 3.57) and the phase modulation bound (Equation 3.58) can be obtained intersecting the surface with the two planes in figure 3.4. The sections are depicted in Figure 3.5, where the forbidden regions are yellow. One can clearly see that there is a trade off between modulation and insertion loss. For example, for amplitude modulation, the ideal modulator has $|\Gamma_A| = 1, |\Gamma_B| = 0$, which is impossible as this point is in the forbidden region. If 100% modulation efficiency is desired ($|\Gamma_B| = 0$), then there is necessarily an insertion loss in the ON state, which is expressed as:

$$|\Gamma_A| \leq \sqrt{\frac{\gamma_M}{\gamma_M + 1}} \quad (3.60)$$

If a lower modulation efficiency is tolerated, then the insertion loss can be reduced. Similarly, if a 180° is needed (BPSK modulation) then the minimum unavoidable loss is given by:

$$|R_{min}| \leq \sqrt{\gamma_M^{-1} + 1} - \sqrt{\gamma_M^{-1}} \quad (3.61)$$

The plots 3.5 also represent a *performance space* which has however a lower number of dimension, accordingly to the relevant performance parameters of the considered class of devices. For amplitude modulators, as explained later, the bound can also be expressed in terms of modulation depth and insertion loss.

Modulators in transmission

The amplitude modulator in transmission is a two-port device in which one port is used as input for the non-modulated wave and the other as output for the modulated signal. The behaviour of the device in states 'A' and 'B' is described by two scattering matrices, \underline{S}_A and \underline{S}_B . If reciprocal materials are used (as in the case of graphene with zero magnetic bias), the scattering matrices are symmetric:

$$\underline{S}_A = \begin{pmatrix} \Gamma_{1A} & T_A \\ T_A & \Gamma_{2A} \end{pmatrix} \quad (3.62)$$

$$\underline{S}_B = \begin{pmatrix} \Gamma_{1B} & T_B \\ T_B & \Gamma_{2B} \end{pmatrix} \quad (3.63)$$

Similar to the reflection modulation case, the general scattering bound can be applied. Because we are interested in the transmission between ports 1 and 2, we select the path from ports 1 and 2 by choosing $\mathbf{a}_A = [1, 0]^T$ and $\mathbf{a}_B = [0, 1]^T$. In the numerator, we obtain an expression that depends only on T_A and T_B :

$$\frac{|T_A - T_B|^2}{(1 - |T_A|^2 - |\Gamma_{1A}|^2)(1 - |T_B|^2 - |\Gamma_{2B}|^2)} \leq \gamma_M \quad (3.64)$$

Unlike the numerator, the denominator contains quantities other than T_A and T_B . However, for passive devices, the two factors in the denominator are always positive, implying

$$\frac{|T_A - T_B|^2}{(1 - |T_A|^2)(1 - |T_B|^2)} \leq \frac{|T_A - T_B|^2}{(1 - |T_A|^2 - |\Gamma_{1A}|^2)(1 - |T_B|^2 - |\Gamma_{2B}|^2)} \leq \gamma_M \quad (3.65)$$

Hence, defining:

$$\gamma_{\text{Mod}} \triangleq \frac{|T_A - T_B|^2}{(1 - |T_A|^2)(1 - |T_B|^2)} \leq \gamma_M \quad (3.66)$$

we obtain a bound which is formally identical to the reflection case. Importantly, reaching optimal performance in transmission requires a much more involved design procedure, as shown in the remainder of this chapter.

3.5.2 Non-reciprocal devices specific upper bounds

The second major class of graphene passive photonic devices is based on the presence of a magnetostatic field bias and the resulting off-diagonal terms in the conductivity tensor of

Chapter 3. Theoretical non-reciprocity and modulation upper bounds

graphene. This class includes Kerr and Faraday polarisation rotators, as well as isolators, which are non-reciprocal devices. These devices are considered in the remainder of the paper. A similar procedure as that used in the case of the modulators can be followed concerning the mathematical derivation, its verification, and the practical exploitation of the results; thus, only the key methodology difference and practical results are considered in detail.

Isolators

An isolator is a non-reciprocal two-port device that enables transmission in one direction but prevents transmission in the other. A generic isolator can be represented by the scattering matrix:

$$\underline{S} = \begin{pmatrix} S_{11} & S_{12} \\ S_{21} & S_{22} \end{pmatrix} \quad (3.67)$$

$$(3.68)$$

The same procedure used for the modulators in transmission leads to:

$$\gamma_{\text{Isol}} \triangleq \frac{(|S_{12}| - |S_{21}|)^2}{(1 - |S_{12}|^2)(1 - |S_{21}|^2)} \leq \gamma_{\text{NR}} \quad (3.69)$$

$$(3.70)$$

This bound indicates that a certain insertion loss is to be accepted if a given level of isolation is required. For perfect isolation, the minimum loss is:

$$|S_{12}| \leq \sqrt{\frac{\gamma_{\text{NR}}}{\gamma_{\text{NR}} + 1}} \quad (3.71)$$

Kerr rotators

Magneto-optic Kerr rotation describes the variation of orientation of a linearly polarised plane wave upon reflection on a magnetostatically-biased material. In the most general case, the reflected wave might exhibit helicity, and in that case, the major axis of the reflected elliptic polarisation is used to define the rotation. Magneto-optic Kerr rotation is well defined if the reflective behaviour of the surface is invariant to a rotation of the surface itself. For a metasurface, this condition is always met if the geometric pattern is invariant to a 90° rotation (a symmetry that is also referred to as C4 symmetry). An immediate consequence of this symmetry is that a normal incident left hand circularly polarized (LHCP) plane wave is always reflected as a left hand circularly polarized (RHCP) one and vice versa. Hence, the scattering matrix of the structure takes a simple form when LHCP and RHCP plane waves are used. Using

the same approach used for phase modulation, it is possible to prove that:

$$\gamma_{\text{Kerr}} \triangleq \frac{|2M \sin \varphi|^2}{(1 - M^2)^2} \leq \gamma_{\text{NR}} \quad (3.72)$$

where M is the magnitude of the major axis of the reflected elliptical polarization and φ is the magneto-optical Kerr rotation.

3.5.3 Bounds for reconfigurable and non-reciprocal antennas

In the remainder of this thesis, as well as in many other works in literature, several designs of reconfigurable antennas based on graphene are presented, exploiting its tunable conductivity to obtain some form of reconfigurability. This section extends the upper bound to the radiation efficiency of graphene antennas with tuneable radiation pattern. Subsequently is also demonstrated that similar bounds exist for non-reciprocal graphene antennas, namely antennas which exhibit a reception pattern different from the radiation pattern (identical in reciprocal antennas). These antennas are possible whenever non-reciprocal materials are included in their structure, including magneto-statically biased graphene. In this case the bound is expressed as a function of the radiation and reception efficiencies. The scattering matrix notation for antennas (described in Chapter 2) will be used together with the general scattering inequality.

Reconfigurable antennas

First we will consider the case of antennas containing gated graphene with tunable scalar reciprocal conductivity. If the complex conductivity is changed from σ_A to σ_B then the overall behavior of the antenna will change, and this can be described using two scattering matrices for these two cases, namely \underline{S}_A and \underline{S}_B (Figure 3.6). Then

$$\gamma_{\text{dev}} \leq \gamma_{\text{mat}} \quad (3.73)$$

$$\gamma_{\text{dev}} \triangleq \frac{\left| \mathbf{a}_B^T (\underline{S}_A - \underline{S}_B^T) \mathbf{a}_A \right|^2}{\mathbf{a}_A^H \left(\underline{I} - \underline{S}_A^H \underline{S}_A \right) \mathbf{a}_A \mathbf{a}_B^H \left(\underline{I} - \underline{S}_B^H \underline{S}_B \right) \mathbf{a}_B} \quad (3.74)$$

$$\gamma_M = \frac{|\sigma_A - \sigma_B|^2}{4\text{Re}(\sigma_A)\text{Re}(\sigma_B)} \quad (3.75)$$

Chapter 3. Theoretical non-reciprocity and modulation upper bounds

If we choose \mathbf{a}_A and \mathbf{a}_B so that $a_0^A = 1$, $a_{i \geq 1}^A = 0$, $a_0^B = 0$, $a_{i \geq 1}^B = (S_{i0}^A - S_{i0}^B)^*$ we obtain the following inequality:

$$\begin{aligned} \gamma_{\max} &\geq \frac{(\sum_{i=1}^{\infty} |S_{i0}^A - S_{i0}^B|^2)^2}{(1 - \sum_{i=1}^{\infty} |S_{i0}^A|^2) \mathbf{a}_B^H (\mathbf{I} - \mathbf{S}_B^H \mathbf{S}_B) \mathbf{a}_B} \\ &\geq \frac{\sum_{i=1}^{\infty} |S_{i0}^A - S_{i0}^B|^2}{1 - |\Gamma^A|^2 - \varepsilon_{\text{rad}}^A} = \frac{\Xi^{\text{AB}}}{1 - |\Gamma^A|^2 - \varepsilon_{\text{rad}}^A} \end{aligned} \quad (3.76)$$

where Ξ^{AB} is called pattern diversity factor, and it is defined as:

$$\Xi^{\text{AB}} = \sum_{i=1}^{\infty} |S_{i0}^A - S_{i0}^B|^2 = \frac{\iint |\mathbf{E}_{\text{rad}}^A - \mathbf{E}_{\text{rad}}^B|^2 d\theta d\phi}{4\pi Z_0 P_{\text{forw}}} \quad (3.77)$$

Finally we notice that an identical bound holds if we exchange \mathbf{a}_A and \mathbf{a}_B . The intersection of the two bounds can be written using the maximum function as:

$$\frac{\Xi^{\text{AB}}}{1 - \max(|\Gamma^A|^2 + \varepsilon_{\text{rad}}^A, |\Gamma^B|^2 + \varepsilon_{\text{rad}}^B)} \leq \gamma_{\max} \quad (3.78)$$

This formula is referred to as the antenna reconfigurability upper bound. An important simplification of the formula takes place if the antenna is matched in both states (a condition which is easily obtained in reconfigurable reflectarrays), namely $\varepsilon_{\text{rad}}^X = \eta_{\text{rad}}^X$:

$$\frac{\Xi^{\text{AB}}}{1 - \max(\eta_{\text{rad}}^A, \eta_{\text{rad}}^B)} \leq \gamma_{\max} \quad (3.79)$$

It is now worth discussing the correct interpretation of the pattern diversity factor Ξ^{AB} . This quantity acts a metric (i.e. as a distance) in the set of all possible radiated field configurations. Note for instance that it $\Xi^{\text{AB}} = 0$ if the radiated field is the same in case A and B, because the difference in the numerator goes to 0. In the simple case where $\varepsilon_{\text{rad}}^X = \eta_{\text{rad}}^X = 1$ (corresponding to a lossless matched antenna) this factor has a maximum value of 4 if $\mathbf{E}_{\text{rad}}^A = -\mathbf{E}_{\text{rad}}^B$, that is if the field undergoes a complete phase reconfiguration of 180° upon state switching, a result which is in general very demanding from this upper bound perspective. If $\mathbf{E}_{\text{rad}}^A$ and $\mathbf{E}_{\text{rad}}^B$ are orthogonal, as defined in Equation 2.74, then $\Xi^{\text{AB}} = 2$. This is because one can distribute the power integral on the two terms, thus obtaining the sum of the powers. This is the case, for instance, when a complete beam steering without beam overlapping is achieved (Figure 3.6b). For this case, if the antenna is lossy, mismatched or both, the maximum value of Ξ^{AB} can be

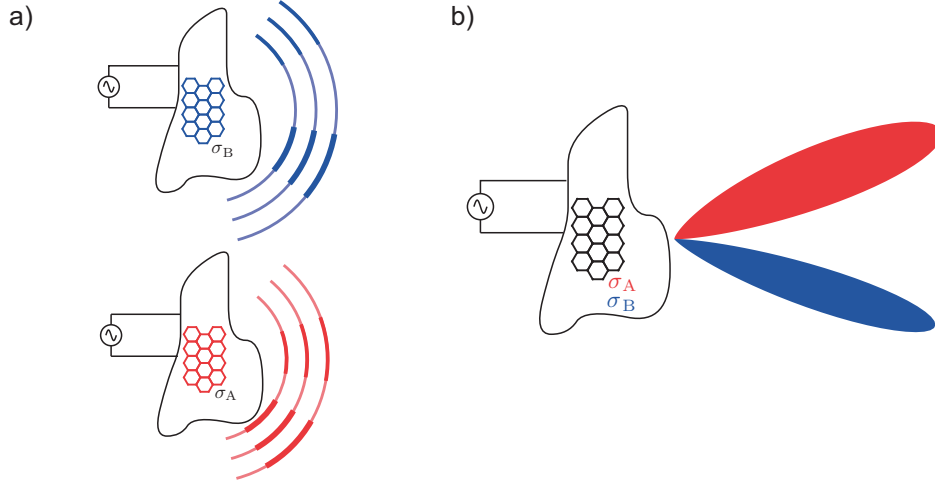


Figure 3.6 – Conceptual schematic of a reconfigurable antenna enabled by graphene field effect tuning. Panel (a) shows that for identical incident waves and different graphene conductivities the radiation pattern is tuned. Panel (b) illustrates the particular case of beam steering, where the radiated beam is directed towards two distinct directions for the two states A and B.

found using the triangular inequality as

$$\Xi_{\max}^{\text{AB}} = \left(\sqrt{\varepsilon_{\text{rad}}^{\text{A}}} + \sqrt{\varepsilon_{\text{rad}}^{\text{B}}} \right)^2 = \varepsilon_{\text{rad}}^{\text{A}} + \varepsilon_{\text{rad}}^{\text{B}} + 2\sqrt{\varepsilon_{\text{rad}}^{\text{A}}\varepsilon_{\text{rad}}^{\text{B}}} \quad (3.80)$$

and in case of orthogonal modes we have $\Xi^{\text{AB}} = \varepsilon_{\text{rad}}^{\text{A}} + \varepsilon_{\text{rad}}^{\text{B}}$. It is also important to mention that another related figure of merit for beam overlapping is the N_{eq} provided in [94]. However, since N_{eq} does not depend on the phase of the electric field and Ξ^{AB} does, it is not possible to write a univocal relationship between the two quantities.

An important consequence of inequality 3.79 is that the higher is the distance that we wish to realize between the two radiation patterns the higher has to be the loss at the denominator, in order to keep satisfying the inequality. Let us for example consider the case of matched antennas with losses ($\varepsilon_{\text{rad}}^{\text{X}} = \eta_{\text{rad}}^{\text{X}} \leq 1$) and orthogonal beams, a situation found in graphene beam steering reflectarrays [JA1, JA2, CA17]. For this case we have:

$$\frac{\Xi^{\text{AB}}}{1 - \max(\eta_{\text{rad}}^{\text{A}}, \eta_{\text{rad}}^{\text{B}})} \leq \gamma_{\max} \quad (3.81)$$

This inequality can be represented in the Cartesian plane $(\eta_{\text{rad}}^{\text{A}}, \eta_{\text{rad}}^{\text{B}})$ as shown in Figure 3.7. The realistic case presented there shows that, using commercial CVD graphene, the bound does not prevent satisfactory values of radiation efficiency (around 70%), while the best

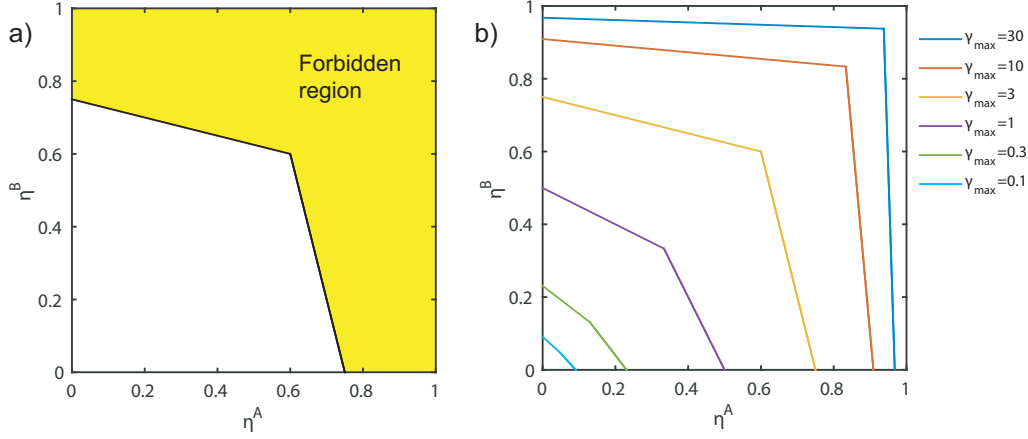


Figure 3.7 – Representation of the reconfigurable antenna upper bound. Panel (a) shows the forbidden region for a realistic case of graphene. Graphene conductivity has been computed with Kubo formula with parameters $T = 300\text{K}$, $f = 5\text{THz}$, $\tau = 50\text{fs}$, $\mu_c = 0.1\text{eV}$ and 0.6eV in cases ‘A’ and ‘B’ respectively. For this case $\gamma_{\text{mat}} = 3.5$. Panel (b) is a parametric sweep of the same limit for different assumed value of γ_{mat} .

possible performances rapidly degrade for $\gamma_{\text{mat}} < 1$.

Non-reciprocal antennas

The theory developed for reconfigurable antennas holds with minor modification also for the non-reciprocal case. Here we are assuming as usual that a strong perpendicular magnetic field is applied to graphene, the conductivity of which takes the gyrotropic form in Equation 3.47:

Following the same steps as above, we obtain the following expression:

$$\frac{\Xi^{\text{TR}}}{1 - |\Gamma| - \max(\varepsilon_{\text{rad}}^A, \varepsilon_{\text{rad}}^B)} \leq \gamma_{\max} \quad (3.82)$$

which is referred to as the *antenna non-reciprocity upper bound*. In this case the pattern diversity factor Ξ^{TR} expresses the distance between the radiation pattern (transmission mode) and the reception pattern (receive mode), and it is defined as:

$$\Xi^{\text{TR}} = \sum_{i=1}^{\infty} |S_{i0} - S_{0i}|^2 = \frac{\iint |\mathbf{E}_{\text{rad}} - \mathbf{E}_{\text{rec}}|^2 d\theta d\phi}{4\pi Z_0 P_{\text{ref}}} \quad (3.83)$$

where \mathbf{E}_{rad} is the radiated field pattern when feeding the antenna port with incident power P_{ref} and \mathbf{E}_{rec} is the reception field pattern. The latter is more easily understood as the radiation pattern in the case of opposite magnetostatic biasing of graphene. In fact, opposite bias has the effect of transposing the scattering matrix, as explained in 2.

Applications

The bound enables an estimation of the loss of the antenna prior to any design, and it applies to any antenna geometry and operation frequency. Furthermore the bound can be readily used for any 2D materials for which the conductivity is known, and likely extended to 3D and lumped reconfigurable elements. The demonstrated upper bound is expressed in a negative form, namely it gives information on which performances cannot be reached. Nevertheless, this theory is of great utility for graphene and technology selection in the early stages of the design, as it helps choosing graphene parameters prior to any numerical simulation. These results are particularly important for the design of reflectarray antennas, later in this thesis.

3.6 Design of optimal planar devices

The theoretical upper bound limits the efficiency of graphene tuneable and non-reciprocal devices, by stating that a minimum insertion loss is unavoidable accordingly to the material property γ_{mat} and to the requested function (e.g. modulation or isolation). The upper bound however does not guarantee that devices reaching the optimal performance (the minimum insertion loss) can actually be designed. Because of this, a very large number of planar devices were simulated with randomly chosen geometrical parameters.

The devices' performances were then plotted in the performance spaces described above. Each device is simulated at the chosen frequency of 1THz and represented as a single point in the performance space. We verified that no devices were found in the forbidden region, validating the bound. Interestingly, some devices were able to be very close to the forbidden region boundary. These devices are optimal, in the Pareto optimality sense [85]. This means that no device can be designed which is better in all the considered performance space dimensions. For example, if an amplitude modulator lies on the boundary of the theoretical limit (Figure 3.5) then no device can be better in terms of insertion loss and modulation depth.

The devices are simulated using a code developed by Dr. Arya Fallahi [25, JA3, 26, 27, 28, 29, JA8, 121] and graphene conductivity is computed using the full Kubo formalism described in Chapter 2. The results are illustrated in the reminder of this section.

3.6.1 Optimal amplitude modulators

The first class of devices considered for optimal design are amplitude modulators. Both reflection and transmission configurations will be explored, as they share the same theoretical

Chapter 3. Theoretical non-reciprocity and modulation upper bounds

bound (Equation 3.57):

$$\gamma_{A\text{Mod}} \triangleq \frac{(|\Gamma_A| - |\Gamma_B|)^2}{(1 - |\Gamma_A|^2)(1 - |\Gamma_B|^2)} \leq \gamma_M \quad \text{Reflection modulator} \quad (3.84)$$

$$\gamma_{A\text{Mod}} \triangleq \frac{(|T_A| - |T_B|)^2}{(1 - |T_A|^2)(1 - |T_B|^2)} \leq \gamma_M \quad \text{Transmission modulator} \quad (3.85)$$

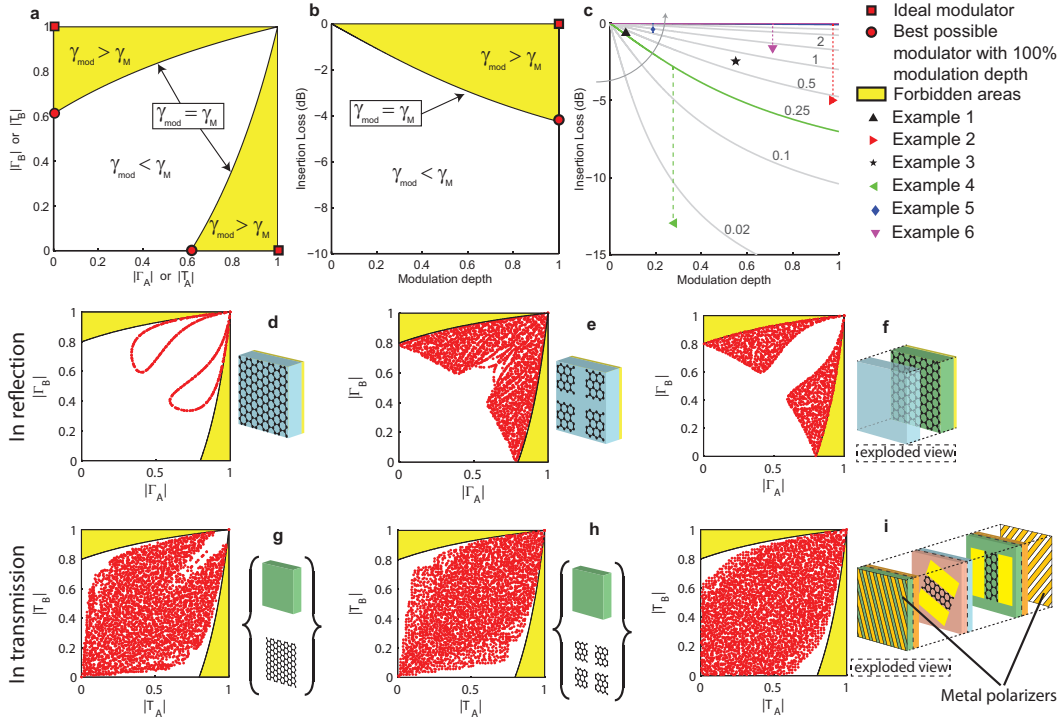


Figure 3.8 – Performances of electro-optical amplitude modulators. a) graphical representation of the amplitude modulation inequality in the Cartesian plane ($|\Gamma_A|, |\Gamma_B|$) [here, $\gamma_M = 0.6$ is used as an example]. The squares represent ideal modulators, and the circles denote the best possible modulators with 100% modulation depth. Forbidden areas (yellow) are delimited by the boundary curve, where $\gamma_{\text{mod}} = \gamma_R$, b) same as a but using the insertion loss and modulation depth coordinates. c) upper bounds for different values of γ_M . The available designs in the literature are represented by coloured symbols, and where possible, the corresponding bound is represented using the same colour. d-f) simulations of randomly generated reflection modulators. Each red point represents a single simulated device. The frequency considered is 1 THz, and the graphene parameters are $T = 300$ K, $\mu_{c,A} = 0.1$ eV, $\mu_{c,B} = 0.8$ eV, and $\tau = 66$ fs (leading to $\gamma_M = 1.76$). A graphene layer on a back metallised dielectric layer (d) can reach optimal performance in a limited range. However, if graphene is patterned in a periodic square array (e) or if an additional dielectric layer is added (f), optimal performances can be reached along the entire boundary curve, including the best possible reflection modulation with 100% modulation depth. g-i) random simulations of different device topologies for transmission modulation. g represents random sequences of graphene sheets and dielectric layers. h represents random sequences of patterned graphene and dielectric layers. i shows an example of a complex structure employing polarisers and hybrid graphene metal structures showing near-optimal performances. Structures d-h are dual polarised, whereas the polarisers in i restrict the operation to single linear polarisation (with a 90° polarisation twist).

As mention earlier, helpful intuition regarding this inequality is obtained by considering the Cartesian plane ($|\Gamma_A|, |\Gamma_B|$), as shown again in Figure 3.8a. The inequality states that there are

some areas in the space of $(|\Gamma_A|, |\Gamma_B|)$ that are strictly ‘forbidden’; these regions are highlighted in yellow in Figure 3.8a. The boundaries of these forbidden regions are determined by γ_M and thus solely by graphene conductivity. In this plot, an ideal modulator corresponds to the red squares, i.e., $|\Gamma_A| = 1$ and $|\Gamma_B| = 0$, or vice versa. However, Inequality 3.84 readily shows that such an ideal modulator is not practically realisable. For example, if the modulator is designed to achieve perfect absorption in its ‘off’ state, such that $|\Gamma_B| = 0$, then $|\Gamma_A|$ cannot exceed the value shown by the red circle in Figure 3.8a.

A more practical view is obtained by representing the same data in the Cartesian plane defined by insertion loss and modulation depth (Figure 3.8b). This representation is accomplished by assuming, without loss of generality, that $|\Gamma_A| \geq |\Gamma_B|$ and by defining the modulation depth as:

$$h \triangleq \frac{|\Gamma_A| - |\Gamma_B|}{|\Gamma_A| + |\Gamma_B|} \quad \text{Reflection modulator} \quad (3.86)$$

$$h \triangleq \frac{|T_A| - |T_B|}{|T_A| + |T_B|} \quad \text{Transmission modulator} \quad (3.87)$$

and the insertion loss IL as:

$$\text{IL} \triangleq |\Gamma_A| \quad \text{Reflection modulator} \quad (3.88)$$

$$\text{IL} \triangleq |T_A| \quad \text{Transmission modulator} \quad (3.89)$$

In this case, Inequality 3.84 writes:

$$\gamma_{\text{AMod}} \triangleq \frac{(2h \text{ IL})^2}{(1 - \text{IL}^2)((1 + h)^2 - \text{IL}^2(1 - h)^2)} \leq \gamma_M \quad (3.90)$$

$$(3.91)$$

As noticed previously, the best possible modulator with 100% modulation depth will have a loss of $\text{IL} = \sqrt{\gamma_M/(1 + \gamma_M)}$ which is obtained by introducing $h = 1$ in Inequality 3.90. This case is represented by the red circle in Figure 3.8b, which corresponds exactly to the red circle in the alternative representation in Figure 3.8a. Insertion loss (and other quantities in the following) can be given in dB, and in that case the $20\log_{10}$ convention has to be used since these quantities are defined on field amplitudes (and not power).

In summary, the theory indicates that a given target value for modulation depth cannot be reached without a minimum value for insertion loss. The general trend is intuitive and related to the loss in graphene. More precisely, a high modulation originates from a strong interaction of the fields with graphene, which in turn increases the loss. However, here, we rigorously demonstrate that although arbitrarily complex designs might potentially allow the modulation

Chapter 3. Theoretical non-reciprocity and modulation upper bounds

depth to be increased without limit, such unbounded increases will always come at the cost of a minimum amount of loss. Importantly, this minimum amount of loss is a known function of the parameters of graphene alone, which allows us to fully utilise the developed theory for practical purposes, as detailed below.

The bound γ_M is a function of graphene conductivity, and Figure 3.8c presents the frontiers corresponding to different values of γ_M . Modulators with different amplitudes that are available in the literature are also reported on the graph, where possible with their corresponding frontiers. Table 3.1 lists the references used for this comparison, which have varying performances accordingly to the working frequency and graphene type.

Table 3.1 – Examples of graphene amplitude modulators from literature

Example number of	Reference number	Operation frequency	Type
Example 1	Ref [98]	0.57–0.63 THz	Experimental
Example 2	Ref [35]	25–30 THz	Theoretical
Example 3	Ref [59]	193 THz	Theoretical
Example 4	Ref [64]	0.5–2 THz	Experimental
Example 5	Ref [70]	193 THz	Theoretical
Example 6	Ref [120]	193 THz	Theoretical

The performance achieved in these initial concept demonstrations is typically significantly below the theoretical upper bound. This result suggests the important potential for improvement if devices approaching the theoretical limit can indeed be designed in practice.

To provide our first answers to this question and subsequently to validate the theoretical prediction, we simulated a very large number of randomly generated modulators. All modulators use graphene of the same conductivities and use the design degrees of freedom depicted in Figure 3.3e. Graphene conductivity is evaluated using Kubo formalism (as in Equation 2.138) for the parameters reported in the caption of Figure 3.8, leading to $\gamma_M = 1.76$ and the corresponding theoretical upper bound plotted in Figure 3.8(d-e-f). The red dots in the figures report the computed performance of each randomly generated modulator.

The simplest possible reflection modulator, namely, uniform graphene over a metalized substrate (Figure 3.8d), can only achieve near-optimal performance for small modulation depths. In this case, the random simulations form a 1D locus. The same behaviour is observed by employing a multilayer dielectric stack between graphene and reflector. The reason is that the admittance seen at the input of the modulator, which determines the complex reflection coefficient, is the sum of graphene conductivity and the admittance seen at the input of the stack. The latter is always an imaginary number; thus, varying the permittivity, thickness, or number of layers provides only a single equivalent degree of freedom, which is the cause of the 1D locus.

Therefore, the logical next step is to consider the simplest modulators that provide additional

design flexibility, namely, graphene patterning (Figure 3.8e) or the use of an additional dielectric layer before graphene (Figure 3.8f). The distribution of the computed results (red dots) provides evidence that these minimal increments in device complexity allow an almost arbitrary approach to the absolute theoretical upper bound, which is of considerable practical importance. The numerical results presented correspond to the conductivity of the given selected graphene, but the conclusions apply to any conductivity. The method is bandwidth-agnostic, thus different near-optimal solutions can be compared and selected according to the bandwidth requirement.

The simulations provide convincing evidence of the bound validity. The frontiers of the performance clouds for the randomly generated modulators almost exactly match the theoretical upper bound. Importantly, many more simulations of complex randomly generated setups were carried out, including combinations of a multilayer substrate, patterned graphene, and the addition of metal. No single result was found to exceed the theoretical limit.

The optimal performances for modulators in transmission are more difficult to attain. Despite closely approaching the bound for most modulation depth, non-patterned and patterned multilayer structures are suboptimal when a 100%-modulation is desired (Figures 3.8g-h). The physical interpretation is that in contrast to modulators in reflection, a good high-transmission modulation state not only requires limiting loss in graphene but also must independently impedance-match the system. The operation of a polarization twist upon transmission, which is achieved in Figure 3.8i by using highly anisotropic hybrid graphene metal patterns, offers a new degree of freedom. The hybrid metasurfaces modulate one polarization, whereas the other polarization is left largely unaffected, allowing for feedback in the structure. However the improvement is only useful for a 100% modulation depth and comes at increased complexity, hence a simpler unpatterned multilayer structures as in Figure 3.8g is in general the best solution (see the Supplementary Methods for designs close to the optimal performance).

3.6.2 Optimal isolators

The second class of graphene passive photonic devices considered are non-reciprocal optical isolators. For isolators, Inequality 3.69 reads:

$$\gamma_{\text{Isol}} \triangleq \frac{(|S_{12}| - |S_{21}|)^2}{(1 - |S_{12}|^2)(1 - |S_{21}|^2)} \leq \gamma_{\text{NR}} \quad (3.92)$$

We will assume, without loss of generality, that $|S_{12}| \geq |S_{21}|$. The inequality can be casted in a different form defining the isolation ISO and insertion loss IL:

$$\text{ISO} \triangleq \frac{|S_{12}|}{|S_{21}|} \geq 1 \quad (3.93)$$

$$\text{IL} \triangleq |S_{21}| \leq 1 \quad (3.94)$$

Chapter 3. Theoretical non-reciprocity and modulation upper bounds

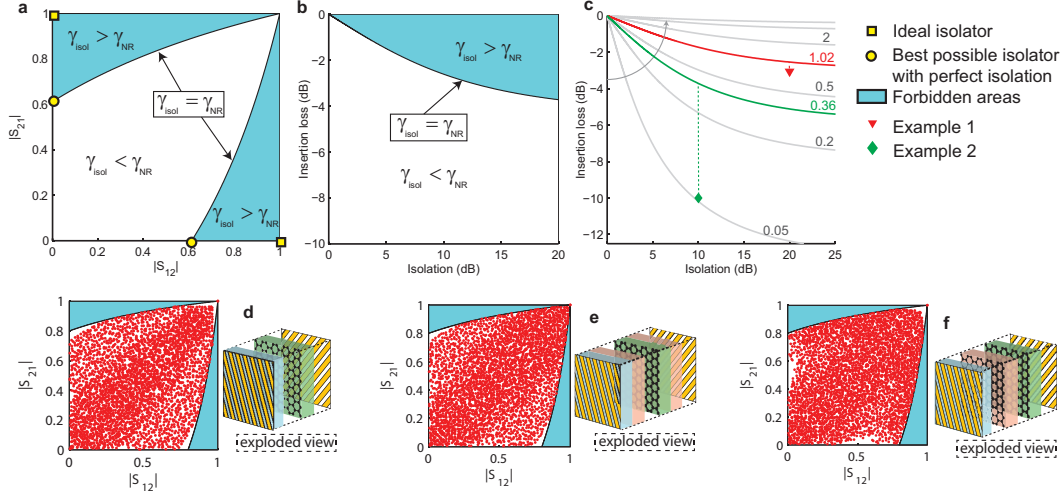


Figure 3.9 – Performances of non-reciprocal isolators. a) graphical representation of the isolation inequality on the Cartesian plane ($|S_{12}|, |S_{21}|$) (here, $\gamma_{\text{NR}}=0.6$ is used as an example). The squares represent ideal isolators, and the circles denote the best possible isolators with perfect isolation. Forbidden areas (cyan) are delimited by the boundary $\gamma_{\text{isol}} = \gamma_{\text{NR}}$. b) same as a but using the insertion loss and the isolation of the isolator as coordinates. c) boundaries for different values of γ_{NR} . The available designs in the literature are represented by coloured symbols, and where possible, the corresponding boundary is represented using the same colour. d-f) random simulations for different device topologies. Each red point represents a single simulated device. The frequency considered is 1 THz, and the graphene parameters are $T=3$ K, $\mu_c=0.2$ eV, $B_0=4$ T, and $\tau=66$ fs ($\gamma_{\text{NR}}=1.78$). All topologies use polarisers at both ends to convert Faraday rotation into isolation. d uses a graphene sheet enclosed by two dielectric layers. e uses two dielectrics on each side of the graphene sheet. f uses two graphene sheets and three dielectric layers in an alternating pattern.

In this case, Inequality 3.92 writes:

$$\gamma_{\text{isol}} \triangleq \frac{\text{IL}^2(\text{ISO} - 1)^2}{(1 - \text{IL})(\text{ISO}^2 - \text{IL}^2)} \leq \gamma_{\text{NR}} \quad (3.95)$$

Figures 3.9a and 3.9b represent the isolation inequality and the ideal and best possible optima. As before, the minimum insertion loss for an isolator having perfect isolation is found setting $\text{ISO} \rightarrow \infty$

$$\text{IL} = \sqrt{\frac{\gamma_{\text{NR}}}{1 + \gamma_{\text{NR}}}}. \quad (3.96)$$

Figure 3.9c presents the variation in the best possible trade-off between isolation and insertion loss for different values of γ_{NR} . The literature examples are listed in Table 3.2:

Figures 3.9d to 3.9f illustrate that the best possible performance can be reached with simple planar structures encapsulated between two polarizers. In the simplest case of a graphene sheet placed between two dielectric slabs (Figure 3.9d), optimality is achieved everywhere

Table 3.2 – Examples of graphene isolators from literature

Example number of	Reference number	Operation frequency	Type
Example 1	Ref [106]	Microwaves	Theoretical
Example 2	Ref [108]	20 GHz	Experimental

except for a small degradation when perfect isolation is required ($ISO \rightarrow \infty$). Increasing the number of dielectric layers between graphene and polarizers does not solve this issue (Figure 3.9e). However, a structure comprised of three dielectric slabs and two graphene sheets in an alternating pattern can reach optimal performances at moderate complexity (Figure 3.9f). Unlike additional dielectric layers, a second graphene layer allows for decorrelating rotation and loss in the system, approaching the theoretical upper bound. Similarly to the transmission modulator case, impedance matching at both ports is essential to achieve optimal performance.

3.6.3 Optimal Kerr rotators

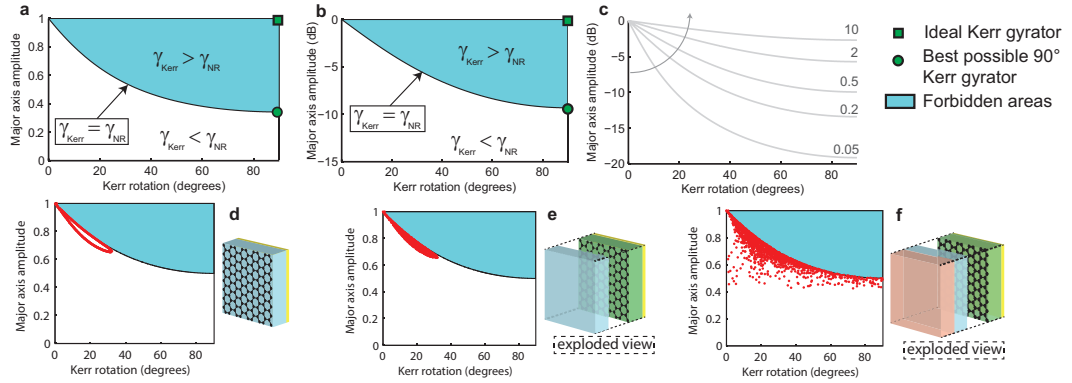


Figure 3.10 – Performances of magneto-optical Kerr rotators. a) graphical representation of the Kerr rotation inequality on the Cartesian plane (M, ϕ) (here, $\gamma_{NR}=0.6$ is used as an example). The squares represent ideal 90° rotators, and the circles denote the best possible 90° rotators with perfect rotation. Forbidden areas (cyan) are delimited by the boundary curve, where $\gamma_{KERR} = \gamma_{NR}$. b) same as a with the major axis expressed in dB. c) theoretical bound curve for different values of γ_{NR} . d-f) random simulations for different device topologies. Each red point represents a single simulated device. The frequency considered is 1 THz, and the graphene parameters are $T=3$ K, $\mu_C=0.2$ eV, $B_0=4$ T, and $\tau=66$ fs ($\gamma_{NR}=1.78$). The topology shown in f) reaches optimal performance values for every rotation in the range $0^\circ - 90^\circ$. d) is a single graphene layer on a back metallised substrate; in e), a superstrate is added; and in f), two superstrates are added, leading to the optimal performances.

Finally, we show that also Kerr polarization rotators can reach optimal upper bound performances. These devices can replace the Faraday rotator in Faraday isolators, by modifying the geometry from transmission to reflection. In that case the amount of rotation needed is 45° . Alternatively, a Kerr rotator of 90° can act as a 180° gyrotor for linearly polarized waves in

reflection. We previously found (Equation 3.72)

$$\gamma_{\text{Kerr}} \triangleq \frac{|2M \sin \varphi|^2}{(1 - M^2)^2} \leq \gamma_{\text{NR}} \quad (3.97)$$

where φ is the Kerr rotation angle, M is the magnitude of the reflected linear polarization. M represents the magnitude of the major ellipse axis when the polarisation of the reflected wave is elliptical. The inequality is graphically represented in Figure 3.10a-c using the same conventions as in Figures 3.8 and 3.9. The ideal (90°) and best possible Kerr rotators are identified by green markers in the figures.

Figure 3.10d presents the Kerr rotation of uniform graphene on a metal-backed substrate. Although optimal performance is obtained in a small region, the lack of degrees of freedom again prevents optimal performance over the full optimal frontier. The insertion of a single superstrate of a dielectric provides an additional degree of freedom but has no particular effect on the performance (Figure 3.10e). However, two different superstrates allow for greatly enhanced Kerr rotations thanks to Fabry-Pérot resonances (Figure 3.10f), leading to optimal performances in a technologically simple structure. This enhancement is also in agreement with a similar effect reported for Faraday rotation^{29, 30, 39}. Finally, a significant number of devices obtained by randomized combinations of the different strategies of Figure 3.10(d-f) were also simulated, all satisfying the upper bound.

3.7 Applications to nanophotonics

In a recent paper (Ref. [130]), Dr. Zanotto *et al.* studied this upper bound and related device optimization for electro-optical modulators based on tunable 3D materials. Figure 3.11 illustrates an important result of this work: optimal devices can be created exploiting resonances, while waveguide modulators based on simple modulation of the propagation constant are suboptimal. Similar considerations hold for graphene, where typical electro-optical waveguide modulators [66] generally exploit the variation of just the real part of graphene conductivity, using only a part of graphene's potential. More complex approaches could be used such as resonators or Mach-Zehnder configurations [120] to improve performances.

Figure 3.11, always taken from [130] provides a comparison of different electro-optical materials using the material figure of merit $\gamma_{\text{mat}} = \gamma_{\text{R}}$ of several electro-optical materials. The method can be used for materials with different physical mechanisms; for example VO_2 (vanadium dioxide) and GST (germanium antimony tellurium) are based on phase change, while ITO (indium tin oxide) and silicon are based on carrier density modulation. This comparison allows to select the best materials accordingly to the target optical frequency.

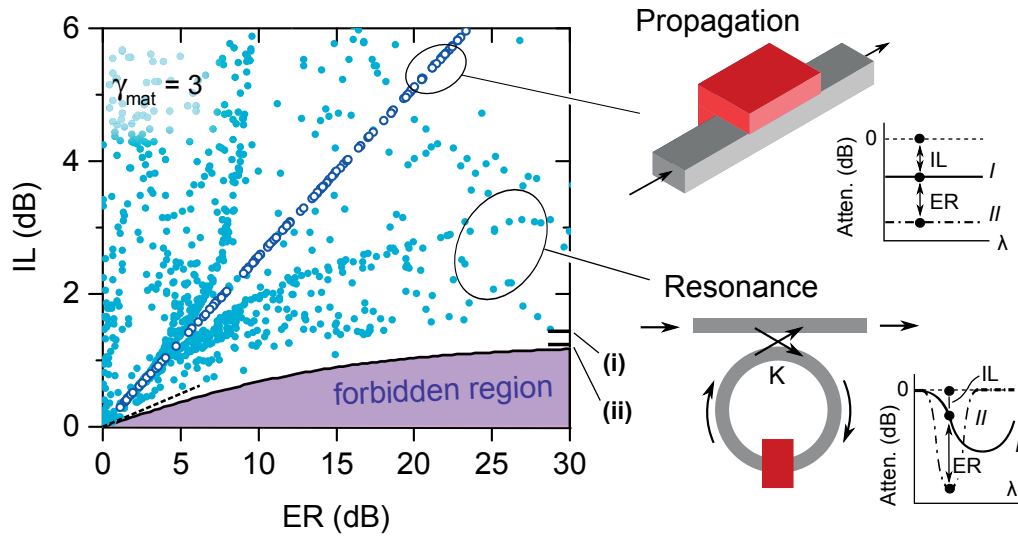


Figure 3.11 – Reproduced from [130]: application of the upperbound to nanophotonic waveguide modulator based on a 3D electro-optical material. One important consideration is that resonance contributes in approaching the bound, while propagation based devices are constrained on a line (blue dots) far from the optimal device frontier. Here resonance is implemented using a ring oscillator

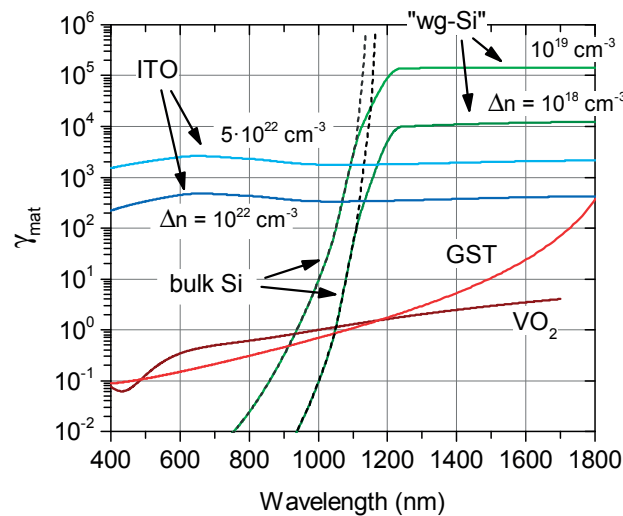


Figure 3.12 – Reproduced from [130]: figure of merit $\gamma_{mat} = \gamma_R$ of several 3D electro-optical materials for nanophotonics modulators in the visible to near infrared range

3.8 Conclusions

The performance of graphene-based modulators and non-reciprocal devices is bounded by absolute upper limits, which solely depend on the conductivity of the graphene employed. This relationship allows the ultimate performance that will be achieved by such devices to be predicted as a function of frequency and the other parameters that influence graphene conductivity. Simple technological implementations allow for very close approaches to the

Chapter 3. Theoretical non-reciprocity and modulation upper bounds

upper limit for the metasurface implementation of an amplitude modulator in reflection and transmission, as well as Kerr rotators and isolators. The observed influence of graphene parameters on the upper bounds, as well as the device topologies allowed to approach them, can be confirmed by physical insight. The developed theory applies to any passive linear structure that can be described in terms of a scattering matrix and can thus be extended to graphene guided devices and other 2DEGs. The method can be used also for 3D materials and is very promising for the optimization of nanophotonic modulators based on tunable materials.

This method, however, has also two minor drawbacks which might be removed by a future more general formulation. Firstly it is frequency-agnostic, that is it holds frequency by frequency. As a consequence, the presented optimal devices might achieve optimality only in a narrow band and frequency-tunable components and filters cannot be studied directly with this method (although they could be analyzed as modulators, and bounds on frequency shifts could be provided with the aid of additional assumptions on the frequency behavior of the device). Secondly, some materials are expected to have very large figures of merit but simultaneously interact very weakly with light (e.g. low mobility band-gap 2D materials as MoS₂). Hence reaching the optimal performance likely requires high-Q resonances, leading to narrowband devices and potentially losses in other parts of the device.

The developed methodology and practical results obtained are believed to constitute an essential milestone toward the optimal operation of numerous future photonic devices.

4 Graphene plasmonics for antenna applications

4.1 Introduction

This chapter illustrates the use of graphene plasmonics for antenna applications. The concept of graphene plasmon polariton mode is introduced in the Maxwellian framework with a full theoretical analysis based on works already published in the literature. Subsequently, the numerical simulation of these modes in the commercial software HFSS is presented and demonstrated to be in excellent agreement with theory for the case of infinitely wide graphene sheet, which can be solved analytically. Then it is illustrated how the graphene plasmons can be used to create a high impedance plasmonic resonant antennas which can be frequency tuned by gating graphene, discussing various geometries and extensions to metallic hybrids. In addition, various designs of graphene plasmonic reflectarrays (done in collaboration with Eduardo Carrasco, who first authored these works) have been designed and it was illustrated how beam steering can be obtained. These reflectarray designs are conceptually different from the experimental presented in Chapter 6, since they require either high quality graphene or high frequency to exploit graphene plasmons. Finally, some preliminary measurement results of a new method (still under development) to measure full graphene complex conductivity are presented.

4.2 Theory of plasmon polaritons for 3D materials

Plasmonics is the branch of optics which studies the propagation and interaction of electromagnetic waves in the presence of materials behaving as plasma. For 3D materials, as mentioned in Chapter 2 this behavior is found in the presence of free charge carriers, when the frequency is larger than the collision rate and lower than the plasma frequency, and it is characterized by a permittivity with dominant negative real part. At infrared and visible frequencies, most metals behave as plasma, in particular noble metals such as silver, gold and copper [116].

While the equivalent dielectric permittivity of these materials is strongly affected by the

Chapter 4. Graphene plasmonics for antenna applications

carriers, the magnetic permeability is usually very close to the value of vacuum ($\mu = \mu_0$, $\mu_r = 1$). This implies that long range waves cannot propagate through the plasma medium and instead they decay exponentially with distance. This is due to the fact that propagation constant in a linear local isotropic medium is given by $\gamma = j\omega\sqrt{\mu\epsilon}$. If ϵ is negative, then the argument of the square root is negative, and γ becomes real, indicating that the wave is evanescent in the medium. These evanescent plasma waves are referred to as plasmons and the material as plasmonic.

An important phenomenon can occur at the interface between a plasmonic material and a dielectric is the coupling between plasmons and evenescent waves in the dielectric. This phenomenon results in long range surface waves, named surface plasmons or transverse magnetic surface plasmon polaritons (TM SPPs). These waves can exist only at the interface (i.e. they are confined to the surface), and the energy associated to the wave decays exponentially with the distance from the interface, both in the plasmonic material and in the dielectric. The waves are usually characterized by very large wave numbers, which prevents them from radiating in the dielectric.

This phenomenon is understood in the Maxwellian framework by solving Maxwell's equations at the interface of the two media [116]. Figure 4.1 shows the geometry of the problem.

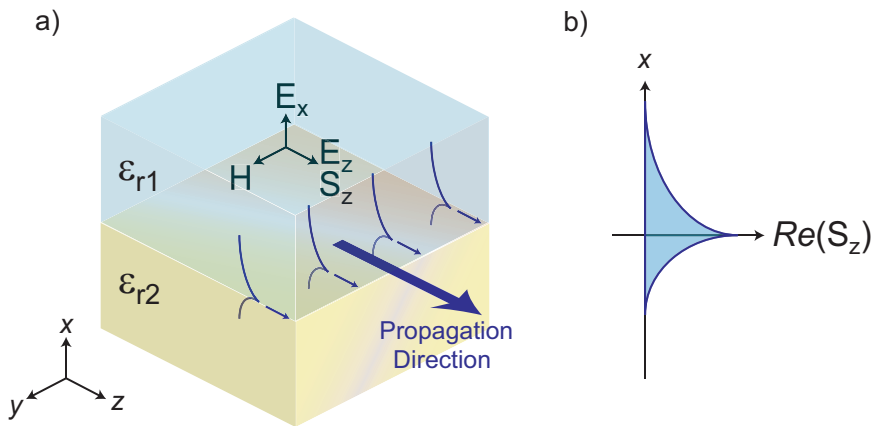


Figure 4.1 – Surface plasmon polaritons at the interface of a plasmonic material and a dielectric

Without loss of generality it can be assumed that the surface wave will propagate in the z direction. TM and TE modes can be studied separately [104], and it is possible to prove that no solution exists for the TE case. For the TM case, the magnetic field \mathbf{H} associated to the mode must be orthogonal to the propagation direction, and by symmetry we can conclude that it is parallel to the y axis. Again by symmetry, the electric field \mathbf{E} must lie in the xz plane. Because here no surface currents are considered, using 2.19, it can be concluded that the tangential components of the electric and magnetic fields are continuous along x . Recalling

4.2. Theory of plasmon polaritons for 3D materials

from Chapter 2 the solution for propagation of plane waves in dielectrics:

$$\begin{aligned}
 \mathbf{E} &= \mathbf{E}_0 e^{-j\mathbf{k}\cdot\mathbf{r}} \\
 \mathbf{H} &= \mathbf{H}_0 e^{-j\mathbf{k}\cdot\mathbf{r}} \\
 \mathbf{k}\cdot\mathbf{E}_0 &= 0 \\
 \mathbf{H}_0 &= \frac{\mathbf{k}\times\mathbf{E}_0}{\omega\mu} \\
 k^2 &= \mathbf{k}\cdot\mathbf{k} = \omega^2\varepsilon\mu \\
 \gamma &= j\mathbf{k}
 \end{aligned} \tag{4.1}$$

with the boundary conditions (Equation 2.19 without surface currents)

$$\begin{aligned}
 \hat{\mathbf{x}}\times(\mathbf{E}_2 - \mathbf{E}_1) &= \mathbf{0} \\
 \hat{\mathbf{x}}\times(\mathbf{H}_2 - \mathbf{H}_1) &= \mathbf{0}
 \end{aligned} \tag{4.2}$$

$$\tag{4.3}$$

and applying them in each half space separately:

$$\mathbf{E}_1 = (E_{1x}\hat{\mathbf{x}} + E_{0z}\hat{\mathbf{z}}) e^{-\gamma_z z - \gamma_{1x} x} \tag{4.4}$$

$$\mathbf{E}_2 = (E_{2x}\hat{\mathbf{x}} + E_{0z}\hat{\mathbf{z}}) e^{-\gamma_z z - \gamma_{2x} x} \tag{4.5}$$

$$\mathbf{H}_1 = H_{1y}\hat{\mathbf{y}} = \frac{\gamma_z E_{1x} - \gamma_{1x} E_{0z}}{j\omega\mu} \hat{\mathbf{y}} \tag{4.6}$$

$$\mathbf{H}_2 = H_{2y}\hat{\mathbf{y}} = \frac{\gamma_z E_{2x} - \gamma_{2x} E_{0z}}{j\omega\mu} \hat{\mathbf{y}} \tag{4.7}$$

$$E_{1x} = -\frac{\gamma_z}{\gamma_{1x}} E_{0z} \tag{4.8}$$

$$E_{2x} = -\frac{\gamma_z}{\gamma_{2x}} E_{0z} \tag{4.9}$$

$$k_0 = \omega c^{-1} \tag{4.10}$$

$$\gamma_z^2 + \gamma_{1x}^2 = -\varepsilon_{r1} k_0^2 \tag{4.11}$$

$$\gamma_z^2 + \gamma_{2x}^2 = -\varepsilon_{r2} k_0^2 \tag{4.12}$$

$$H_{1y} - H_{2y} = 0 \tag{4.13}$$

Confinement of the waves can be enforced as:

$$\operatorname{Re}(\gamma_{1x}) > 0 \tag{4.14}$$

$$\operatorname{Re}(\gamma_{2x}) < 0 \tag{4.15}$$

The following final dispersion relation is then found:

$$\gamma_z = j k_0 \sqrt{\frac{\epsilon_{r1} \epsilon_{r2}}{\epsilon_{r1} + \epsilon_{r2}}} \quad (4.16)$$

In the simplified case of no losses (real permittivities), because $\epsilon_{r1} > 0$ and $\epsilon_{r2} < 0$, the mode can propagate if $|\epsilon_{r2}| > |\epsilon_{r1}|$ because the square root takes a real value. The mode is, in particular, very confined (large imaginary part of the propagation constant γ_z) if the two values are very close.

When a thin plasmonic layer is considered, plasmons can appear at both the interfaces. If the layer is thin enough, the two modes are coupled, leading to an even and an odd mode. If the layer is very thin, substantial alteration of the propagation constant is observed [116]. Graphene can be considered as a thin plasmonic layer, and the supported mode is the even mode of the structure above. However, a more direct and rigorous analysis can be done modeling graphene as a true 2D material in the Maxwellian framework [50, 51], and it is presented in the next section.

4.3 Theory of graphene surface plasmon polaritons

The analysis done for plasmons in 3D plasmonic materials can be extended to the case of graphene with complex conductivity σ to determine the dispersion relation of plasmon polaritons (in the reminder of this work graphene surface plasmon polariton modes are referred to as graphene plasmons for simplicity). Here, graphene included in two dielectrics (a superstrate and substrate) with different permittivity and $\mu_r = 1$ is considered (Figure 4.2). The approach is similar to the previous case, but the boundary condition on magnetic field is

4.3. Theory of graphene surface plasmon polaritons

modified to include the surface electric current supported by graphene:

$$\mathbf{E}_1 = (E_{1x}\hat{\mathbf{x}} + E_{0z}\hat{\mathbf{z}}) e^{-\gamma_z z - \gamma_{1x} x} \quad (4.17)$$

$$\mathbf{E}_2 = (E_{2x}\hat{\mathbf{x}} + E_{0z}\hat{\mathbf{z}}) e^{-\gamma_z z - \gamma_{2x} x} \quad (4.18)$$

$$\mathbf{H}_1 = H_{1y}\hat{\mathbf{y}} = \frac{\gamma_z E_{1x} - \gamma_{1x} E_z}{j\omega\mu} \hat{\mathbf{y}} \quad (4.19)$$

$$\mathbf{H}_2 = H_{2y}\hat{\mathbf{y}} = \frac{\gamma_z E_{2x} - \gamma_{2x} E_z}{j\omega\mu} \hat{\mathbf{y}} \quad (4.20)$$

$$E_{1x} = -\frac{\gamma_z}{\gamma_{1x}} E_{0z} \quad (4.21)$$

$$E_{2x} = -\frac{\gamma_z}{\gamma_{2x}} E_{0z} \quad (4.22)$$

$$k_0 = \omega c^{-1} \quad (4.23)$$

$$\gamma_z^2 + \gamma_{1x}^2 = -\epsilon_{r1} k_0^2 \quad (4.24)$$

$$\gamma_z^2 + \gamma_{2x}^2 = -\epsilon_{r2} k_0^2 \quad (4.25)$$

$$H_{1y} - H_{2y} = J_{sz} = \sigma E_{0z} \quad (4.26)$$

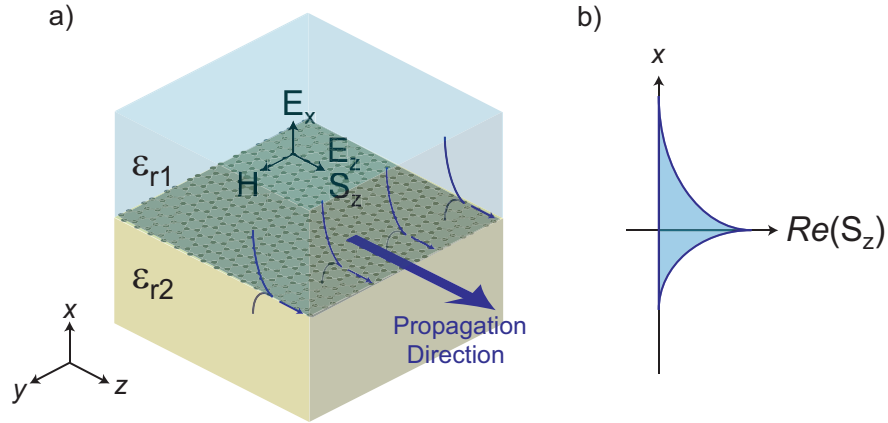


Figure 4.2 – Graphene surface plasmon polaritons

Confinement of the waves can be enforced again as:

$$\text{Re}(\gamma_{1x}) > 0 \quad (4.27)$$

$$\text{Re}(\gamma_{2x}) < 0 \quad (4.28)$$

Chapter 4. Graphene plasmonics for antenna applications

The following final dispersion relation is then found:

$$\frac{\epsilon_{r1}}{\sqrt{\gamma_z^2 + \epsilon_{r1} k_0^2}} + \frac{\epsilon_{r2}}{\sqrt{\gamma_z^2 + \epsilon_{r2} k_0^2}} = \frac{\eta\sigma}{k_0} \quad (4.29)$$

If the superstrate and substrate are identical with permittivity ϵ_r then:

$$\gamma_z = k_0 \sqrt{\epsilon_r} \sqrt{\left(\frac{2\sqrt{\epsilon_r}}{\eta\sigma}\right)^2 - 1} \quad (4.30)$$

If graphene is suspended in vacuum then:

$$\gamma_z = k_0 \sqrt{\left(\frac{2}{\eta\sigma}\right)^2 - 1} \quad (4.31)$$

Solving Equation 4.29 in γ_z the propagation can be determined as function of the considered parameters. Although the full Kubo formula with Equation 4.29 gives the exact analytical value of the propagation constant, to better understand the propagation properties it is useful to consider an approximation for the case of high confinement ($\text{Im}(\gamma_z) \gg k_0$). As shown later, this is obtain for the case of low Fermi level in graphene. The limit of the dispersion relation for large $\text{Im}(\gamma_z)$ is:

$$\gamma_z = (\epsilon_{r1} + \epsilon_{r2}) \frac{k_0}{\eta\sigma} \quad (4.32)$$

Using the low temperature intra-band approximation (Equation 2.142) for graphene conductivity we obtain:

$$\gamma_z = j\epsilon_0(\epsilon_{r1} + \epsilon_{r2}) \frac{\omega^2 \pi \hbar^2}{q_e^2 |\mu_c|} (1 + (j\omega\tau)^{-1}) \quad (4.33)$$

$$\beta = \text{Re}(k) = \text{Im}(\gamma_z) = \epsilon_0(\epsilon_{r1} + \epsilon_{r2}) \frac{\omega^2 \pi \hbar^2}{q_e^2 |\mu_c|} \quad (4.34)$$

$$\alpha = -\text{Im}(k) = \text{Re}(\gamma_z) = (\omega\tau)^{-1} \beta \quad (4.35)$$

4.3. Theory of graphene surface plasmon polaritons

Phase and group velocities (neglecting the losses given by α) are:

$$v_p = \frac{\omega}{\beta} = \frac{q_e^2 |\mu_c|}{\epsilon_0 (\epsilon_{r1} + \epsilon_{r2}) \omega \pi \hbar^2} \quad (4.36)$$

$$v_g = \frac{\partial \omega}{\partial \beta} = \frac{q_e^2 |\mu_c|}{2 \epsilon_0 (\epsilon_{r1} + \epsilon_{r2}) \omega \pi \hbar^2} = \frac{1}{2} v_p \quad (4.37)$$

Figures 4.3, 4.4 and 4.5 illustrate the propagation for $\epsilon_{r1} = 1$ and $\epsilon_{r2} = 4$ and for various graphene parameters.

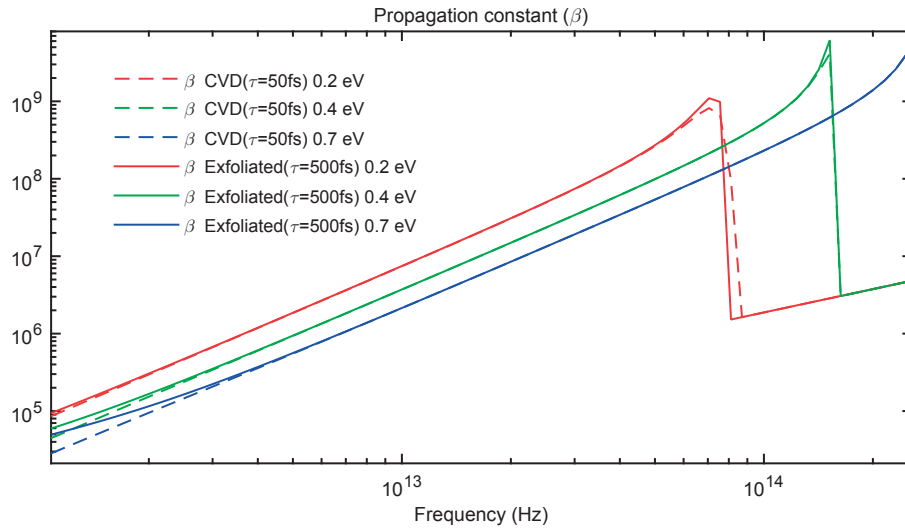


Figure 4.3 – Computed propagation factor for plasmons in graphene between media with relative permittivity 1 and 4

Several important things can be noticed. First, plasma frequency is undefined in graphene, since it concerns only 3D materials. The plasmons are supported by the inductive conductivity of graphene due to the carrier's inertia. The plasmonic mode is dispersive, with both phase and group velocity inversely proportional to the frequency. The wavenumber is proportional to the sum of the surrounding permittivities and not to their square root as in TEM structures (like coplanar waveguides). The propagation is tuneable, since it depends on the Fermi Level which can be controlled by applying a biasing voltage. In particular, the velocity is proportional to the Fermi level, so that for low $|\mu_c|$ the mode is more confined. Losses are dominant for low frequencies and plasmons become significant only for $\omega < \tau^{-1}$. For high quality graphene, plasmons exist already at low terahertz frequencies, while for CVD graphene they appear in the mid infrared starting from approximately 10-20 THz.

A very important figure of merit is the plasmon quality factor $Q = \omega \tau$, as plotted in 2.9. This quantity has at least three consistent interpretations:

- As stated in the definition, it is the ratio between imaginary and real part of the conduc-

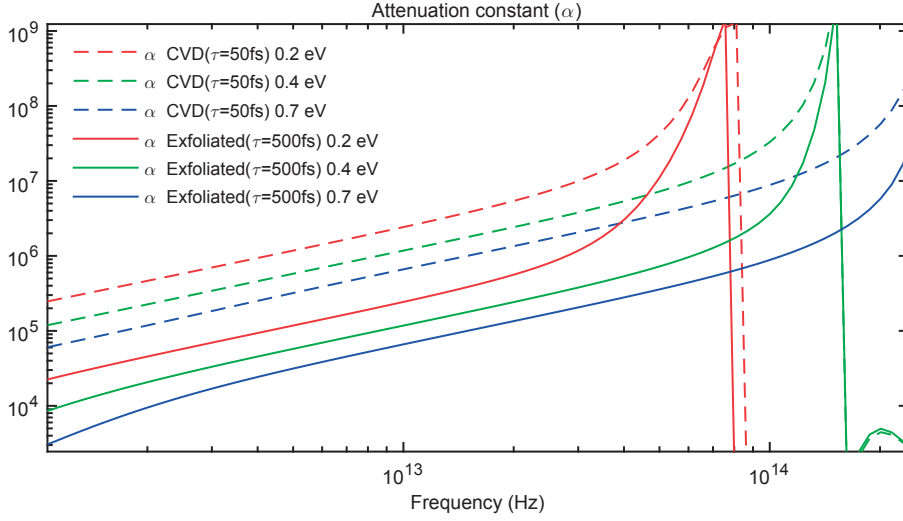


Figure 4.4 – Computed attenuation factor for plasmons in graphene between media with relative permittivity 1 and 4

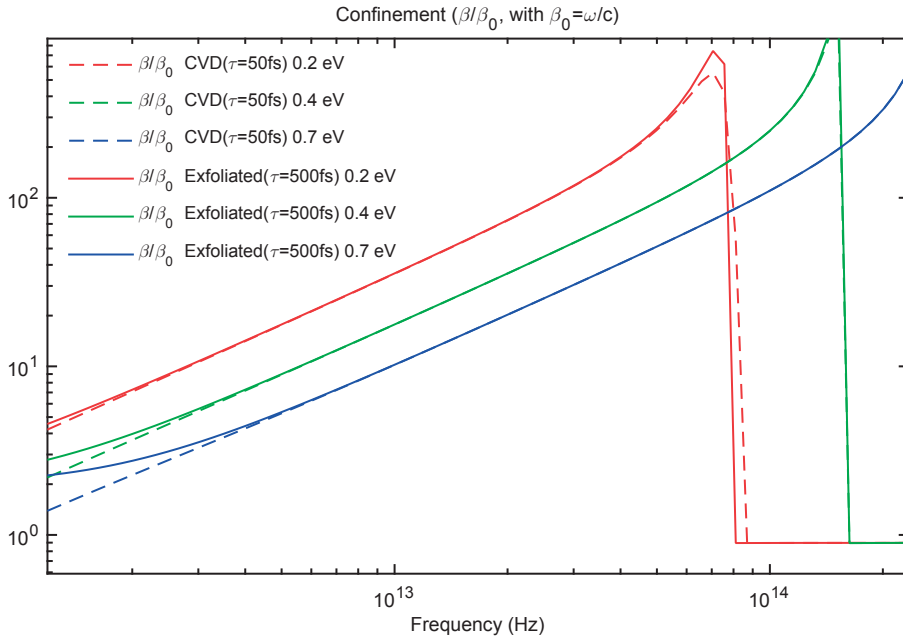


Figure 4.5 – Computed mode confinement for plasmons in graphene between media with relative permittivity 1 and 4

tivity $Q = -\frac{\text{Im}(\sigma)}{\text{Re}(\sigma)} = \omega\tau$, indicating the quality of the inductive behavior of graphene.

- It is also the ratio between imaginary and real part of the propagation constant $Q = \frac{\text{Im}(\gamma)}{\text{Re}(\gamma)} = \omega\tau$, indicating the quality of the plasmons with respect to attenuation.
- If graphene plasmonic resonators are built [122, 53] then the effect of the electromagnetic field is limited to the quasi-static electric field, given that the size of the resonators is very small due to confinement. These resonators can be modeled as an RLC equivalent

4.4. Numerical simulations of graphene plasmon waveguides

circuit, where L and R are given by graphene Kubo/Drude model, and the capacitance depends on the geometry of the device. If the resonance frequency is ω_0 then it is found $Q = \omega_0 \frac{L}{R} = \omega_0 \tau$.

Figure 4.6 illustrates the quality factor using the same graphene parameters as in the previous figures.

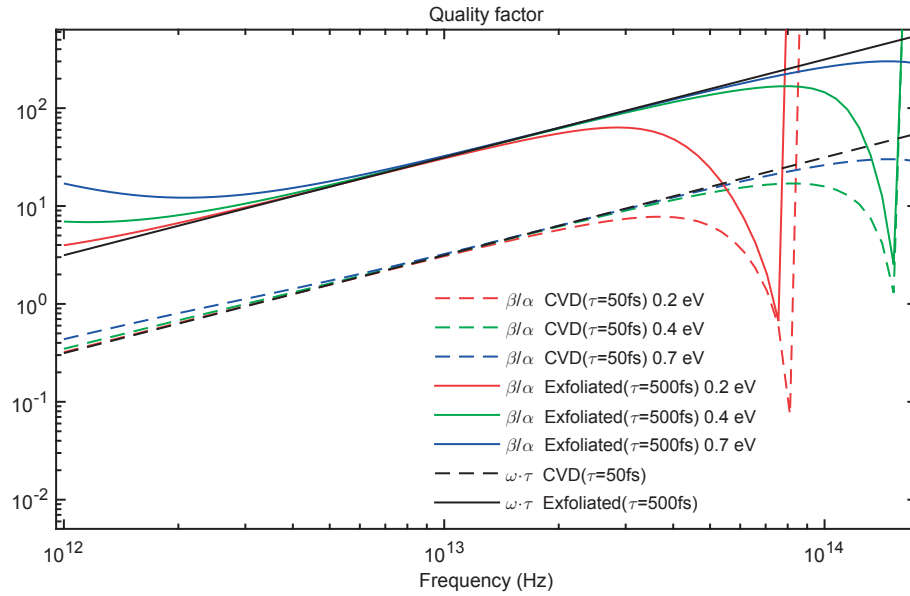


Figure 4.6 – Computed quality factor for plasmons in graphene between media with relative permittivity 1 and 4

Finally, in the plasmonic range, the propagation factor (and hence the mode confinement) depend on the Fermi level but not on τ , while the quality factor is independent of the Fermi level and depends only on τ . These considerations, as well as the equivalence of the three interpretations of the quality factor, apply in the plasmonic region of graphene conductivity, while for lower or higher frequencies ohmic and interband losses dominate respectively and plasmonic modes are not supported.

4.4 Numerical simulations of graphene plasmon waveguides

Before analyzing graphene based plasmonic antennas, it is important to identify and validate an electromagnetic solver which can handle correctly this phenomenon with 2D materials [JA9]. In the following, Ansys HFSS and CST have been used; this section summarizes the validation of HFSS, while CST has been validated by Dr. Eduardo Carrasco and used for plasmonic reflectarrays based on graphene [JA1, JA2, 13].

The dispersion of plasmonic modes on graphene infinite sheets has been studied using the HFSS model in Figure 4.7a. Graphene is modeled using the *impedance boundary condition* using as impedance the inverse of graphene conductivity. Two *H-symmetry* planes are used

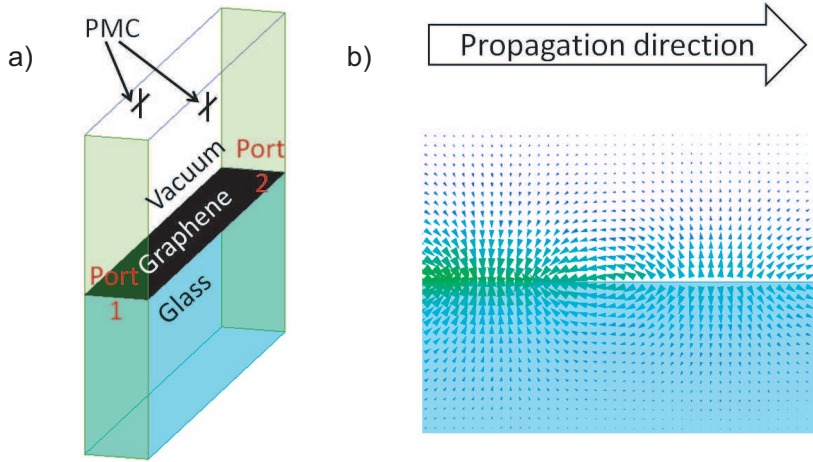


Figure 4.7 – Numerical simulation of plasmons on infinite graphene sheet. a) Geometry of HFSS model. b) Electrical field lateral view.

on the side exploiting the fact that the mode is transverse magnetic. The substrate considered here is glass ($\epsilon_r = 4$) and the excitation is obtained using two wave ports on each side of the structure. Top and bottom side of the box can be modeled as either *radiation boundary condition* or *perfect magnetic conductors*. The last choice motivated by the fact that the fields are in any case very weak there and no additional modes are supported by the box, since all the structure is electrically small. Figure 4.7b shows the excited fields demonstrating successful excitation of the plasmonic mode on graphene.

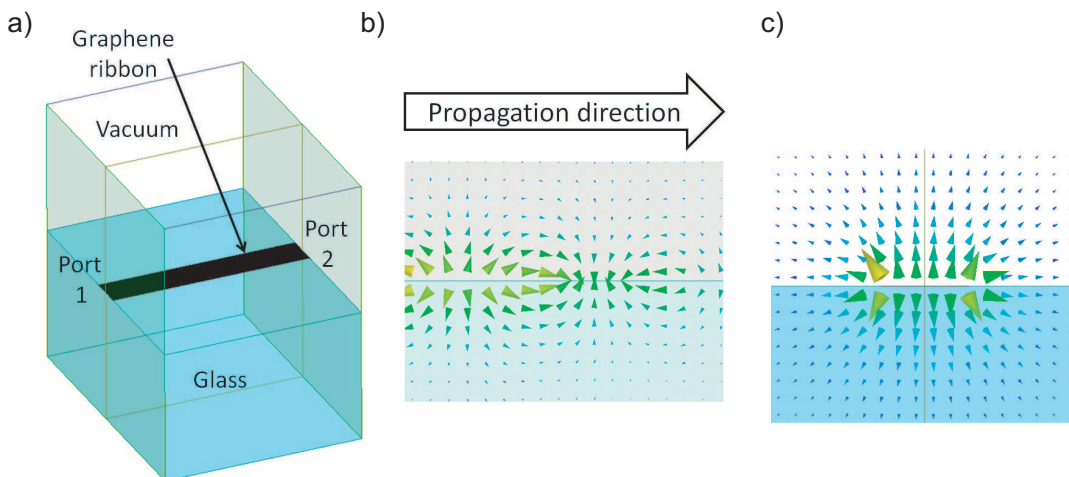


Figure 4.8 – Numerical simulation of plasmons on ribbon waveguides. a) Geometry of HFSS model. b) Electrical field lateral view. c) Electrical field transversal view.

For graphene strips (Figure 4.8a) graphene is again modeled with an impedance boundary condition and wave-ports are used; however the radiation boundary condition (or alternatively

4.4. Numerical simulations of graphene plasmon waveguides

the perfect magnetic conductor) is used in all the remaining four faces of the box. Figures 4.8b and 4.8c illustrate the obtained electric fields.

Results can be exported from HFSS in the form of scattering parameters of the simulated structure. When a substrate is used, care must be exercised to select the proper mode at the waveport, since the structure can support other modes associated to the dielectric. This problem is greatly attenuated using the perfect magnetic boundary condition instead of the radiation one. When simulating plain homogeneous waveguides, as in this case, it is expected to obtain a scattering matrix with null S_{11} and S_{22} ; however, due to the very confined nature of the mode, there exist a mismatch between the mode computed by the wave port and the one actually propagating. As a result, the final S_{11} and S_{22} are not null. However, using an ABCD matrix approach as suggested in [87], it is possible to retrieve the actual propagation parameters. This is done by converting the scattering matrix in an ABCD matrix (alias transmission matrix):

$$\begin{pmatrix} V_2 \\ I_2 \end{pmatrix} = \begin{pmatrix} A & B \\ C & D \end{pmatrix} \begin{pmatrix} V_1 \\ -I_1 \end{pmatrix} \quad (4.38)$$

and computing its eigenvalues. If ζ is an eigenvalue of the ABCD matrix, then the associated propagation constant is given by:

$$\zeta = e^{-\gamma\Delta L} \quad (4.39)$$

$$\gamma = -\frac{\ln(\zeta)}{\Delta L} \quad (4.40)$$

where ΔL is the geometrical length of the simulated waveguide. Because the exponential function is periodic in the complex plane, multiple solutions are to be considered when taking the logarithm, and the ambiguity is solved repeating the simulation with a different ΔL . Another approach could be to select a sufficiently small ΔL to remain in the first branch of the logarithm. However this technique has the drawback of being influenced by the evanescent higher order mode excited by the wave-ports, which are not matched perfectly to the waveguide, and hence it is avoided here.

Figure 4.9 illustrates the propagation constants on infinite sheet and ribbons for $\tau = 1$ ps, $\mu C = 0.25$ eV, $T = 300$ K. For the infinite sheet case, the propagation matches very well the theory prediction, and for the strip we can notice a further mode confinement and wave slow down, associated to the larger overall capacitance of the equivalent transmission line (the electric field is now completely surrounding graphene, and is not only found above and below as in the infinite plane case). The used value of $\tau = 1$ ps corresponds to high quality exfoliated graphene [74], which is required to obtain plasmons at terahertz frequencies.

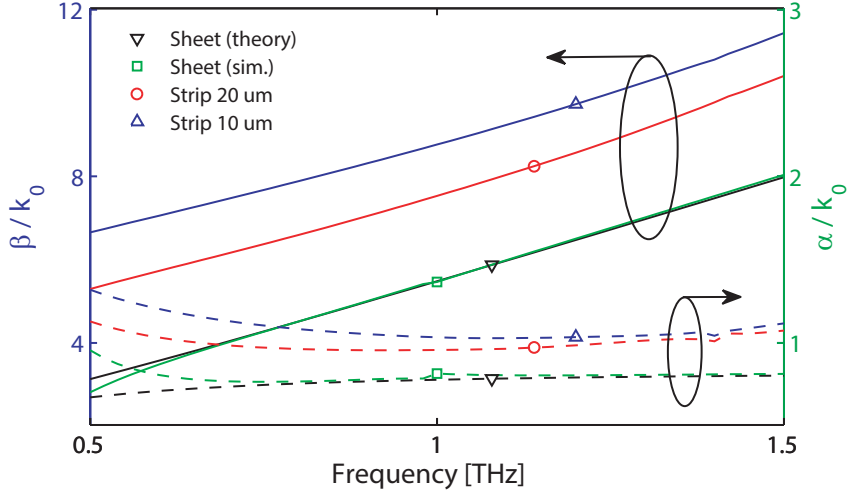


Figure 4.9 – Simulated propagation constants on infinite sheet and ribbons for $\tau = 1\text{ps}$, $uC = 0.25\text{eV}$, $T = 300\text{K}$, substrate $\epsilon_r = 3.8$

4.5 Graphene tuneable plasmonic dipole

4.5.1 Introduction

The slow and tuneable propagation constant can be used to create miniaturized plasmonic antennas based on graphene. This mechanism was explored in [68, 67], which however provide only a study of the antenna scattering without modeling a proper source for the energy to be radiated. In contrast, as we demonstrated in [JA9, JA14, JA10], it is indeed possible to design a proper radiator based on terahertz graphene plasmons. The considered terahertz source is a terahertz photo-mixer[36], which has generally a very high impedance in the order of 10 k Ω . Photo mixers, also, are sufficiently miniaturized to fit in the gap of the graphene plasmonic antenna. The rest of this section presents a theoretical study of these antennas.

4.5.2 Graphene plasmonic dipole

The geometry of the antenna is shown in Figure 4.10. Two rectangular patches of graphene are separated by a gap ($G = 2\mu\text{m}$) which hosts the source (e.g. a photomixer). The design is obtained creating a gap in a rectangular $W \times L$ graphene patch, which can be regarded as a finite length L strip with width W . Since the SPP mode can propagate on finite-width strips, the patch is expected to support standing wave resonances approximately (due to fringing fields) given by $L = n\lambda/2 = n\pi/\beta$, where β is the wave number of the finite-width strip plasmon previously computed. We focus on the first resonance ($n = 1$) for smallest size and best-behaved input impedances. The length of the antenna is selected using the resonance condition and considering a target resonance frequency of 1 THz.

As mentioned before, we aim here at designing actual antennas acting as interfaces between

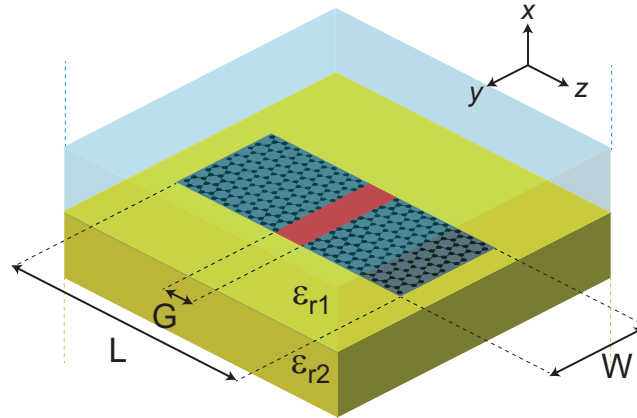


Figure 4.10 – Geometry of the proposed graphene plasmonic dipole

Table 4.1 – Proposed plasmonic antennas and corresponding working points (W.P.). The last column shows the electrical length with respect to the free space wavelength.

Antenna	μ_c (eV)	L (μm)	W (μm)	W.P.	f (THz)	Z_{in} (Ω)	L/λ_0
1	0.13	17	10	L	1.023	77	0.06
				H	1.35	1020	0.08
2	0.25	23	20	L	1.172	33	0.09
				H	1.534	425	0.12

free space propagation and a lumped source/detector, rather than simple scatterers. Radiation is achieved placing a THz continuous-wave (CW) photomixer in the gap. In transmission, the photomixer excites the patch resonance which enables radiation (note that a DC bias must be applied between both graphene half-sections here). Reciprocally, in reception the incident power is delivered to the photomixer that can operate also as a detector. Different antennas were designed using the strip plasmon mode simulation approach, assuming different chemical potentials μ_c . Table 4.1 shows the corresponding antenna dimensions for two representative examples, hereafter referred to as Antenna 1 and 2, respectively.

Figure 4.11 illustrates the electric field and surface current of the antenna, which agree to the expected plasmon resonance. Figure 4.12 shows the input impedance Z_{in} of the antennas. Each antenna shows two frequency working points where Z_{in} is real: the first one (referred to as L) with a low resistance value, the second one (H) with a high value. The latter is particularly interesting since THz photomixers generally show a very high and real output impedance. The second working point occurs when each of the patches support a single plasmonic mode (rather than exciting the overall mode of the antenna). This does not occur for the double of the frequency, as one would initially expect, but at a frequency of approximately $\sqrt{2}$ times larger. This is due to the fact that β is proportional to ω^2 , as in equation 4.34. Hence, beta is doubled for a frequency $\sqrt{2}$ times larger.

It is noticeable that placing the source in an asymmetric position (closer to one extremity than

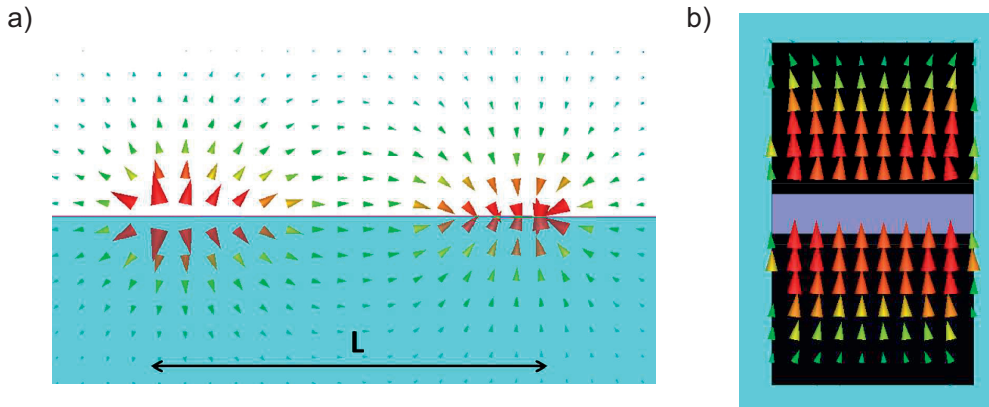


Figure 4.11 – Electric field (a) and surface current (b) on the proposed graphene dipole

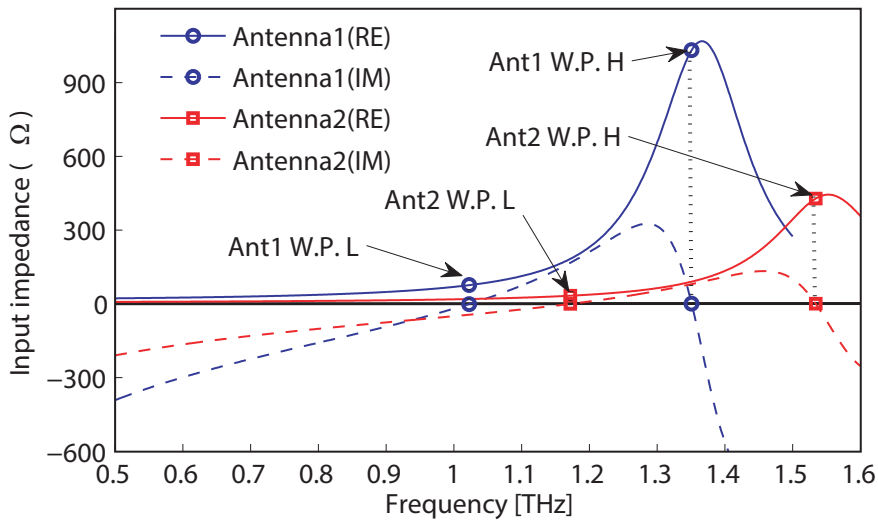


Figure 4.12 – Input impedance of the graphene plasmonic dipole

the other) provides an additional degree of freedom for Z_{in} . However this leads in general to lower Z_{in} .

Figure 4.13 shows that higher μ_c values lead to larger radiation efficiencies η_r . This effect is mainly due to the larger resonating size of the antenna for higher μ_c . Avoiding excessively small values for W is also important to maximize η_r . The total efficiency $\eta_m \eta_r$ where η_m is the impedance matching efficiency. η_m is computed using a realistic value of 10 k Ω for the photo-mixer impedance. The observed efficiencies are low compared to antennas operating at microwave and millimeterwave frequency, but are actually better as compared with typical THz antennas[48] where η_m alone is less than 1% for a 10 k Ω photomixer– and despite the miniaturized size of the proposed antennas.

The radiation patterns in Fig. 4.14 resemble those of conventional (non-plasmonic) short

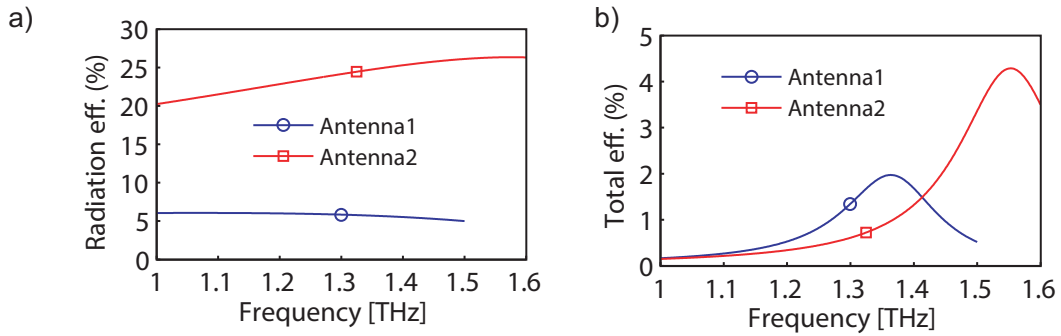


Figure 4.13 – Radiation efficiency (a) and total efficiency (b) of the plasmonic antenna, assuming that the antenna is connected with a 10 kΩ photomixer

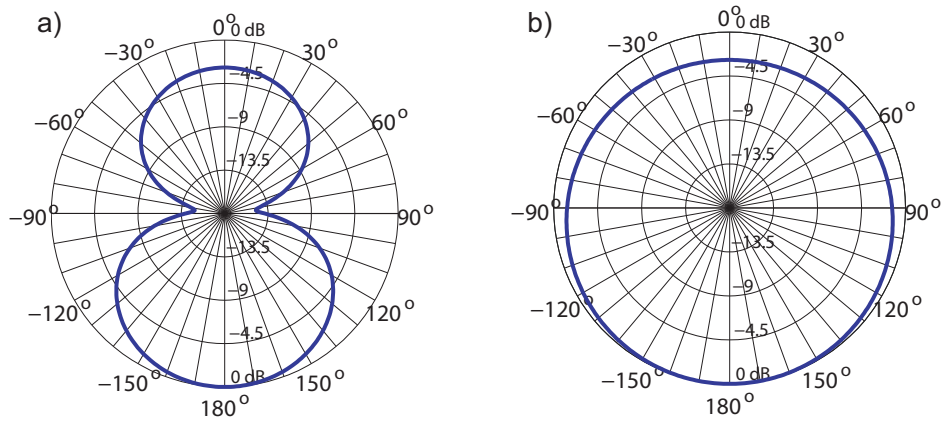


Figure 4.14 – Radiation pattern of the proposed graphene plasmonic dipole. a) E plane, b) H plane

dipoles. This is expected for such miniaturized antennas, since the current density is concentrated in the antenna phase center, leading to a radiation similar to the hertzian dipole. The THz radiation is mostly directed in the substrate direction, which is desired in case a dielectric lens is used to improve directivity[36]. It was also verified that adding such a lens has a negligible impact on the input impedance.

4.5.3 Frequency tuning

When a bias voltage is applied to graphene, the plasmon wavenumber can be controlled, and hence the operation frequency is expected to change. Because we are considering a photo-mixer as the source for the antenna, however, one must keep in mind that the photo-mixer also needs a bias DC voltage to operate. As a consequence, a stack of two graphene layers separated by a gate dielectric is considered rather than a single graphene layer. The dielectric is sufficiently thin to treat the graphene layers as a single one with the double of conductivity. The symmetry of graphene band structure ensures the same upper and lower conductivities (neglecting small residual unwanted doping) for initially undoped graphene. The final antenna, shown in Figure 4.15, allows then independent biasing of graphene patches

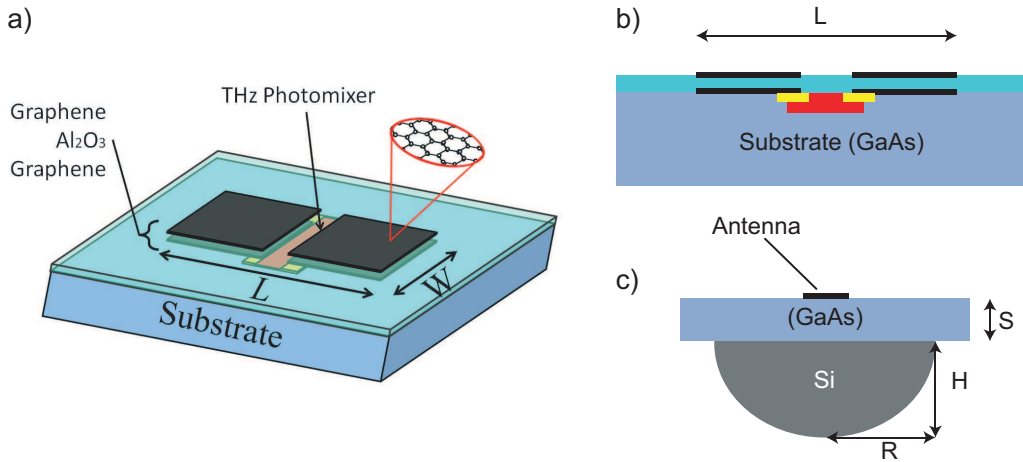


Figure 4.15 – Geometry of the tuneable graphene plasmonic dipole. a) 3D view of the structure. b) Cross section. c) Final system including the silicon lens

and photomixer, and can be integrated with a silicon lens commonly used to increase the directivity of terahertz antennas. This device has been studied theoretically and numerically in [JA10].

Each dipole arm is a set of two stacked graphene patches separated by a thin Al_2O_3 insulating film ($\epsilon_r = 9$, $\tan\delta = 0.01$). The intermediate Al_2O_3 layer has thickness of 100 nm, which is sufficiently large for capacitive quantum effects to be negligible but thin enough to preserve low bias voltage and good coupling between the patches, as discussed next. The antenna width W is $7 \mu\text{m}$ and the total length L is $11 \mu\text{m}$. The structure lies on a dielectric substrate (here GaAs, $\epsilon_r = 12.9$ and $\tan\delta = 0.001$) and includes a gap of $2 \mu\text{m}$ representing the THz photomixer.

Note that for a simpler technological implementation only the lower patches are directly connected to the photosource metallic electrodes. However, since both graphene layers are only separated by an electrically very thin 100 nm dielectric, they are very strongly capacitively coupled and behave as a single layer whose conductivity is approximately twice that of an individual layer. This behavior is assumed in the following explanations and analytical considerations, and is verified based on full-wave simulations. The parameters of the silicon lens are $S = 160 \mu\text{m}$, $H = 572 \mu\text{m}$, $R = 547 \mu\text{m}$, $\epsilon_r = 11.66$, $\tan\delta = 0.0002$). High quality is assumed, with $\tau = 1 \text{ ps}$.

Figure 4.16 illustrates the effect of different μ_c on the antenna input impedance. One can notice a wide tuning range of more than one octave and a very uniform and high impedance peak. The reason for this uniformity is discussed in the circuit model presented below.

Figure 4.17 illustrates the radiation efficiency of the antenna and the total efficiency (including also return loss due to source antenna impedance mismatch) with a $10\text{k}\Omega$ photomixer. Figure 4.18 demonstrates that the behavior of the antenna is very similar to a simplified case of a single layer 2D material with the double of conductivity of graphene. It also shows that the

4.5. Graphene tuneable plasmonic dipole

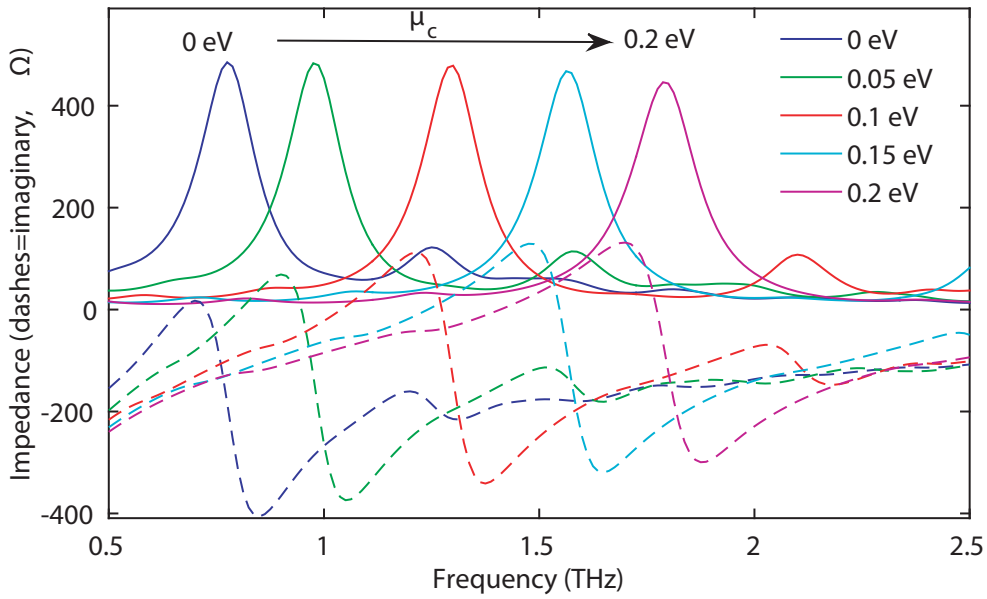


Figure 4.16 – Input impedance of the tuneable graphene plasmonic antenna upon variation in the Fermi level.

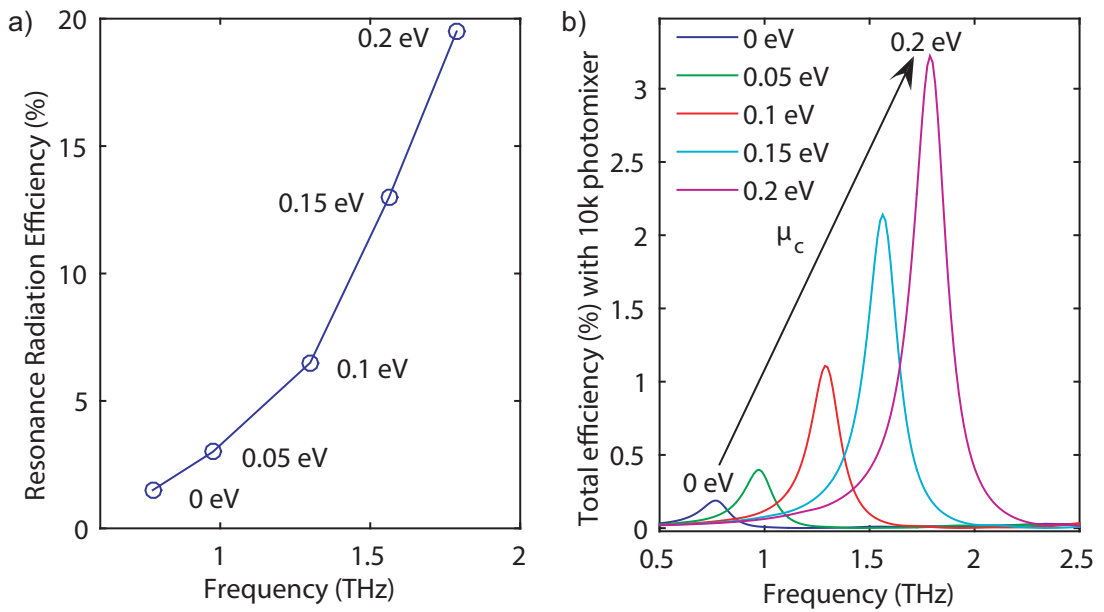


Figure 4.17 – Efficiency of the tuneable plasmonic graphene antenna. a) Radiation efficiency at the resonance working point for various Fermi level values b) Total efficiency with a 10 k Ω photomixer

graphene stack leads to higher efficiency and operating frequencies if compared to a single layer antenna.

Finally Figure 4.19 shows the normalized radiation pattern in two separate cases with and without the silicon lens.

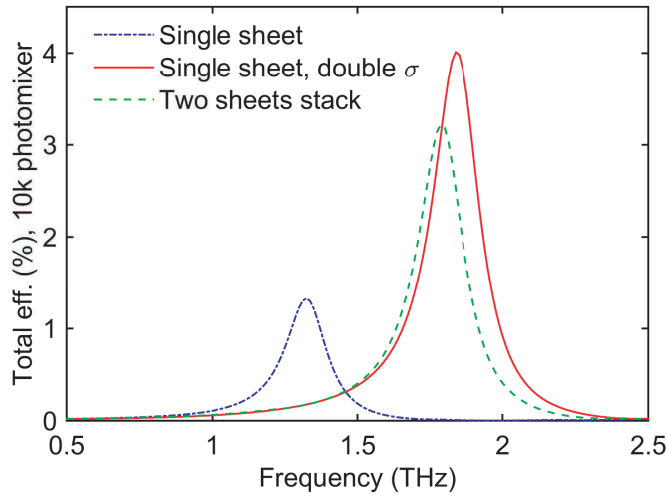


Figure 4.18 – Total efficiency comparison for with a single layer antenna with the same Fermi level and geometry and a single layer with doubled conductivity

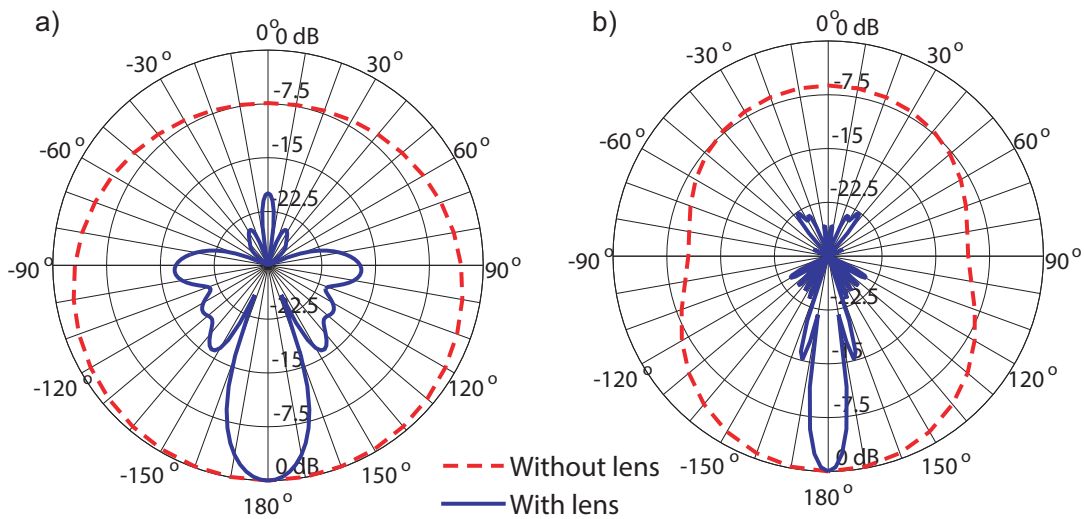


Figure 4.19 – Radiation pattern of the proposed graphene tuneable dipole. a) $\mu_c = 0\text{eV}$, $f = 0.8\text{THz}$. b) $\mu_c = 0.2\text{eV}$, $f = 1.8\text{THz}$

4.5.4 Circuit model

A circuit model of the graphene dipole (Figure 4.20) has been developed[CA27]. The circuit model allows a complete understanding of the working principles of the antenna as well as providing a tool to scale the antenna for different frequencies and applications. First a transmission line (TL) model is derived for the plasmons. While the propagation constant is already well known, the impedance of this model is non trivial, and its definition has been selected so that two conditions are satisfied:

- the total current on the graphene strip must be equal to the current on the equivalent TL

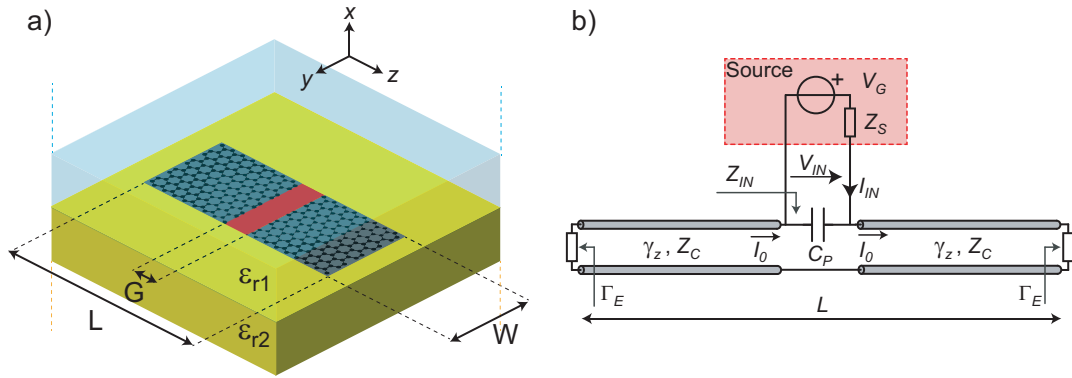


Figure 4.20 – Circuit model of the graphene plasmonic dipole

(in other words the current in the equivalent TL model is the so-called *natural currents*).

- Since losses are localized in graphene, they are modeled by a resistance in series with the inductor of the TL equivalent LC cell.

Following this definition and computing the power associated to the plasmonic mode with a Poynting vector integral, the impedance is computed as [CA27]:

$$\text{Re}(Z_c) = \frac{\text{Im}(\gamma_z)\omega}{2W|\sigma|^2} \left(\frac{\epsilon_0\epsilon_{r1}}{|\gamma_{x1}|^2\text{Re}(\gamma_{x1})} + \frac{\epsilon_0\epsilon_{r2}}{|\gamma_{x1}|^2\text{Re}(\gamma_{x2})} \right) \quad (4.41)$$

$$\text{Im}(Z_c) = \frac{\text{Re}(\gamma_z)}{\text{Im}(\gamma_z)} \text{Re}(Z_c) \quad (4.42)$$

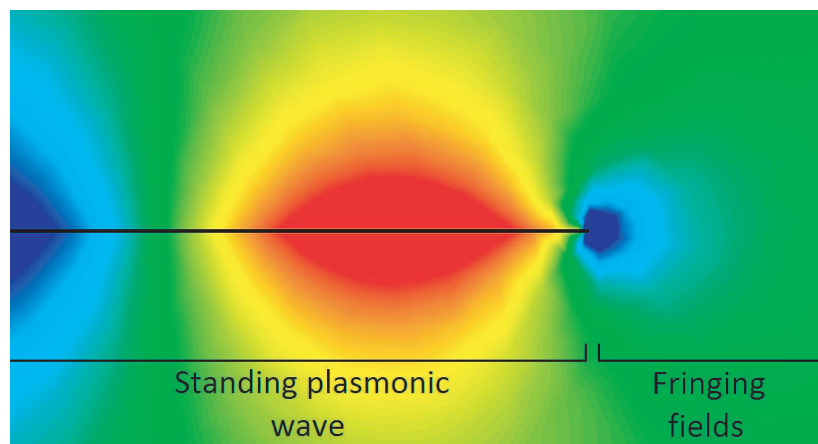


Figure 4.21 – Detail of the plasmonic fringing fields at the end of a ribbon waveguide

The model include a parasitic capacitor to model the fringing fields in the gap of the antenna,

Chapter 4. Graphene plasmonics for antenna applications

while the two extremities are terminated by a load to model the reflection coefficient of plasmons at the edges (see Figure 4.21). Importantly, the reflection coefficient is constant and independent of graphene properties and antenna geometries, and found from simulations to have a phase of approximately $-\pi/2$.

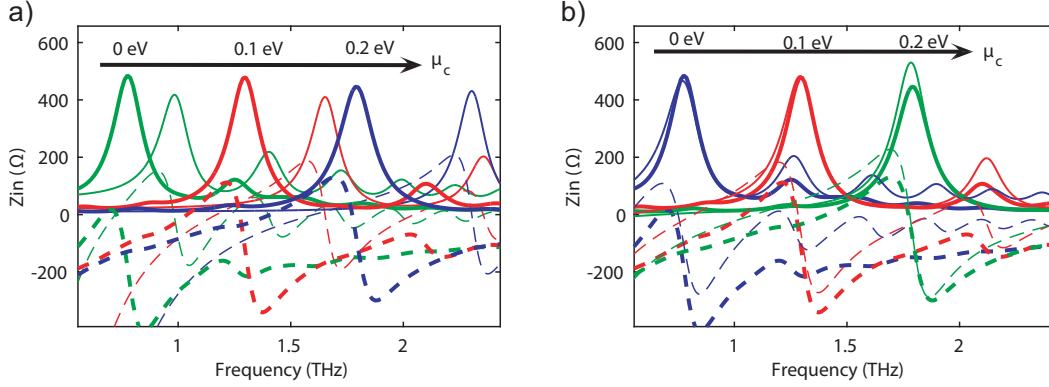


Figure 4.22 – Comparison of impedance between model and full wave simulations. Thick curves represent the full wave results and thin ones the circuit model. a) Model without parasitic elements. b) Model with parasitic elements

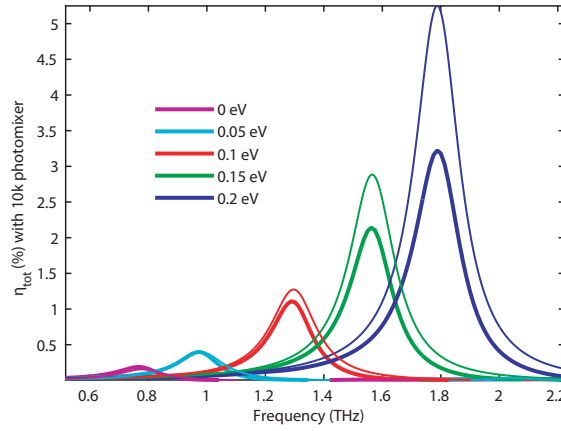


Figure 4.23 – Total efficiency comparison. Thick curves represent the full wave results.

Figures 4.22 and 4.23 show that the agreement between input impedance and efficiency simulations increases, especially when the parasitic elements are added to the model.

In a simplified version of this model [JA10] it is possible to estimate that the real part of the input impedance at the resonance peak is:

$$Z_{in,r} \propto \frac{4\beta}{\alpha L \omega_r} = \frac{4}{\tau L} \quad (4.43)$$

which is independent of the operation frequency, explaining the smooth input impedance

reconfigurability.

4.5.5 Metal graphene hybrid antenna

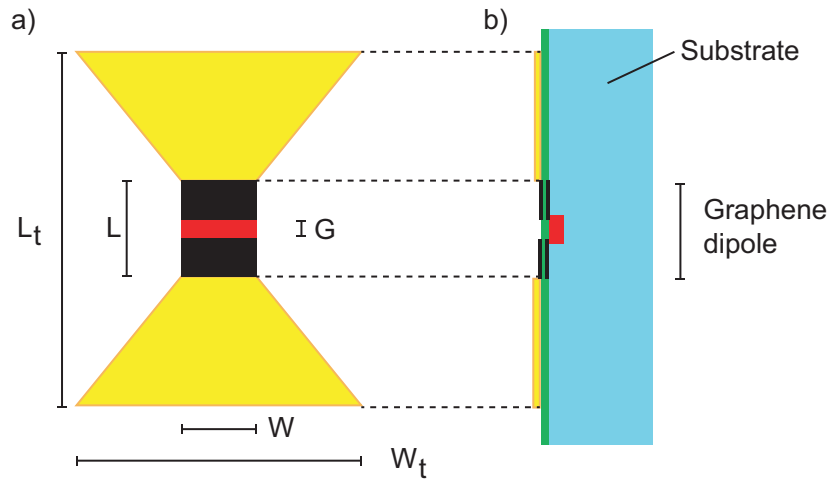


Figure 4.24 – Geometry of the proposed hybrid dipole. a) Top view. b) Cross section.

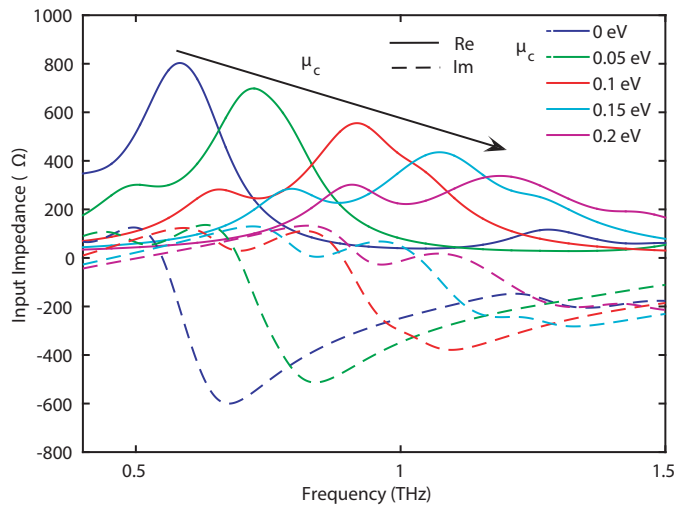


Figure 4.25 – Impedance tuning of the proposed hybrid dipole

Figure 4.24 illustrates a modified version of the frequency tunable antenna extended with two metal bow-tie metallic elements [CA21]. Figure 4.25 illustrates the input impedance of the hybrid graphene-metal antenna, while Figure 4.26 shows the achieved total and radiation efficiency. The metallic elements sensibly increase the radiation efficiency of the antenna (of roughly a factor of 3) while maintaining the frequency tuning capabilities. The overall size of the antenna, however, increases.

These results demonstrate that hybrid metallic graphene antenna are very promising, since they allow the use of reconfigurable properties of graphene while maximizing the radiation

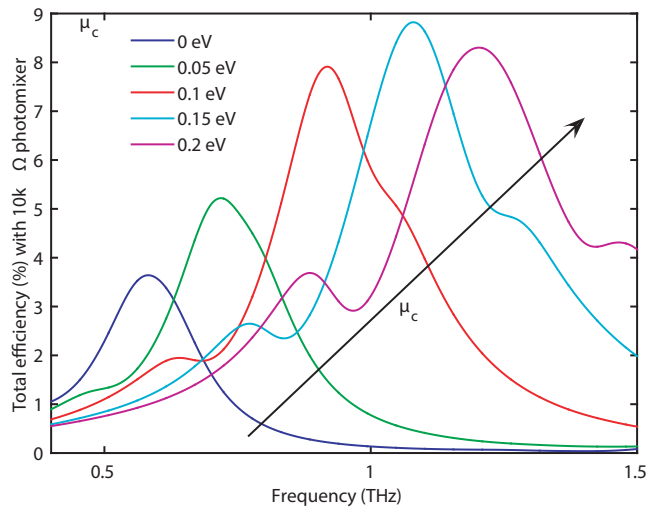


Figure 4.26 – Radiation efficiency of the proposed hybrid dipole

efficiency. This concept will be of fundamental importance for the experimental reflectarray demonstrated in Chapter 6.

4.5.6 Graphene plasmonic reflectarrays

Plasmonic reflectarrays can be implemented with graphene following similar design rules. They have been designed in collaboration with Dr. Eduardo Carrasco and can be found in [JA1, JA2].

4.6 Fabry-Perot infrared complex conductivity measurement

4.6.1 Introduction

The evaluation of graphene properties in the infrared band can be achieved using FTIR (Fourier Transform InfraRed spectroscopy) on graphene samples. This technique enables the measurement of transmittance or reflectance of graphene placed on a substrate. Unfortunately, this technique enables only the extraction of the real part of the conductivity, which is linked to the absorbance of the graphene sample. Part of the information is hence lost in the process. Importantly, the ratio of the real and imaginary conductivity, which is an indicator of the quality of the sample, cannot be observed directly.

Kramers-Kronig relations can be used to reconstruct the imaginary conductivity from the real one, but have several important limitations. Firstly, they only work with simple zero-pole resonances, so the accuracy can be easily spoiled in presence of e.g. Fabry-Perot resonances induced by the substrate. Importantly, graphene conductivity shows very broadband features, such as the interband step. Kramers-Kronig, on the contrary, are effective only in presence

4.6. Fabry-Perot infrared complex conductivity measurement

of sharp and narrowband features, while they are impractical for broadband effects as they require integration of a very broad frequency range, often outside the range of the instrument.

Because of the important limitations of Kramer-Kronig reconstruction, ellipsometry has been used to retrieve directly the complex conductivity of graphene [17]. Unfortunately mid infrared ellipsometry requires large spot size (in the order of two centimetres) and the method shown in [17] relies on CaF₂ substrates, preventing Fermi-Level tuning.

In collaboration with the Nanoelectronic Devices Laboratory (NANOLAB) and the BioNanoPhotonic Systems Laboratory (BIOS) at EPFL, a new method is being developed to measure the full complex conductivity of gated graphene at infrared frequencies using an FTIR setup. The method has the advantage of being able to resolve the conductivity in samples as small as 200 μm with the aid of a microscope connected to the FTIR setup. It consists in placing graphene over a special substrate composed of a pyrex support bonded to a 10 to 20 μm thick high resistivity silicon layer with a metallization on the back. The bonding can be achieved either with parylene or with anodic bonding. This structure is used also for the THz isolator described in Chapters 5, 6 and in Appendix A, where a more complete description including fabrication is available.

The thin silicon layer acts as a reflective Fabry-Perot etalon, namely a device showing strong and frequency-periodic absorption peaks in the reflectivity. The presence of graphene affect the shape of the peaks as noticed in [111]. There are two independent effects:

- The real part of the conductivity affects the depth of the peak;
- The imaginary part of the conductivity introduces a phase shift in the peak.

By comparing the peaks in a region of the substrate with and without graphene, its complex conductivity can be successfully measured. In addition, a thin gate oxide (here Al₂O₃) can be deposited on top of the sample prior to graphene transfer using ALD. A gate voltage can then be applied from graphene to the silicon layer and the Fermi level of graphene can be tuned. We verified that the interband step changes upon bias, as well as the features of the measured complex conductivity. The remainder of this section illustrates the obtained measurement results

4.6.2 Measurement results

Figure 4.27 illustrates an example of the reflection coefficient of the bare substrate for different frequencies. The periodicity in frequency is due to the thickness of the silicon etalon (10 μm) which behaves as a dielectric with relative permittivity of 11.6 in the infrared region. The absorption dips are

Figure 4.28 shows a single absorption dip measured on bare substrate and on graphene (biased at -16 V to increase graphene conductivity and better show the effect). It is evident that

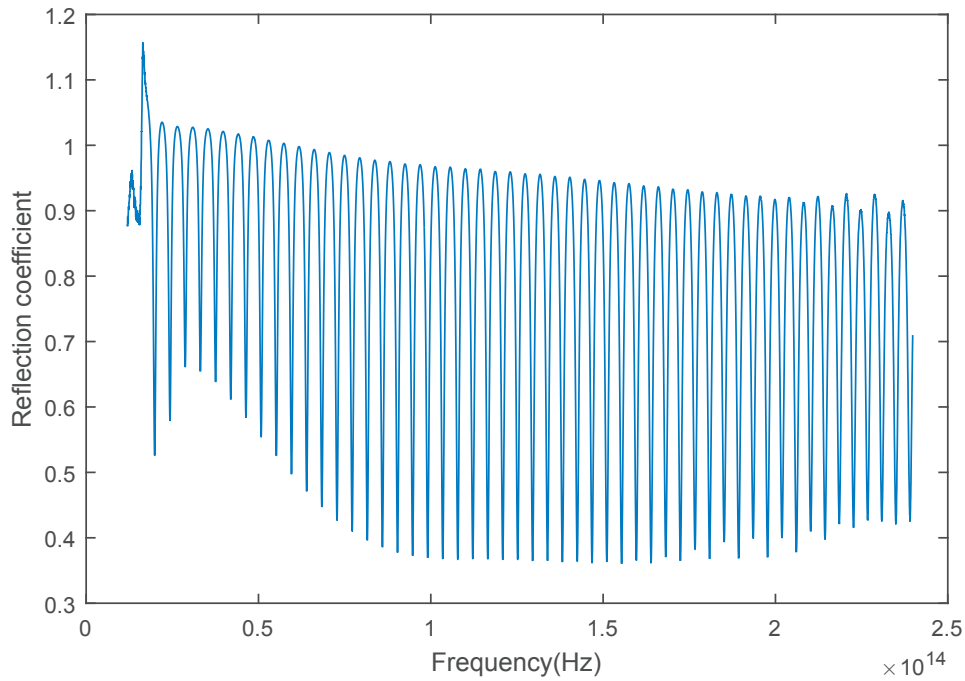


Figure 4.27 – Fabry-Perot periodic dips in the reflection coefficient of the bare substrate

graphene contributes to higher absorption (due to the real part of graphene conductivity) and to a frequency shift which correspond to an inductive behaviour, as expected for graphene in this frequency band.

Figure 4.29 shows an example of characterized complex conductivity for -4 V, and the corresponding fitting with Kubo formula, while figure 4.30 shows the conductivity for different biasing voltages. It is evident that, the larger the absolute value of the voltage, the larger is the frequency for the interband step, and also the the larger is the imaginary part of the conductivity, due to the increase of carrier number.

4.6. Fabry-Perot infrared complex conductivity measurement

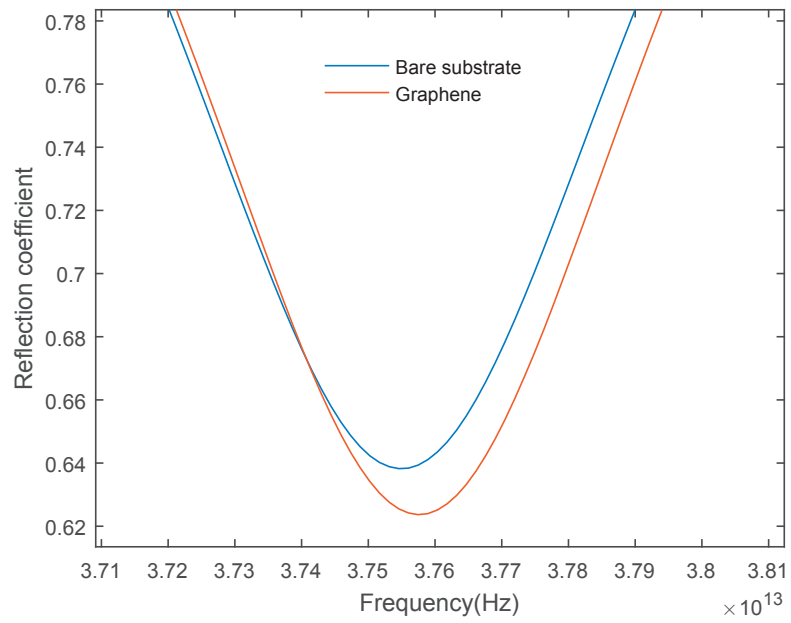


Figure 4.28 – Perturbation of a single Fabry-Perot absorption dip induced by graphene

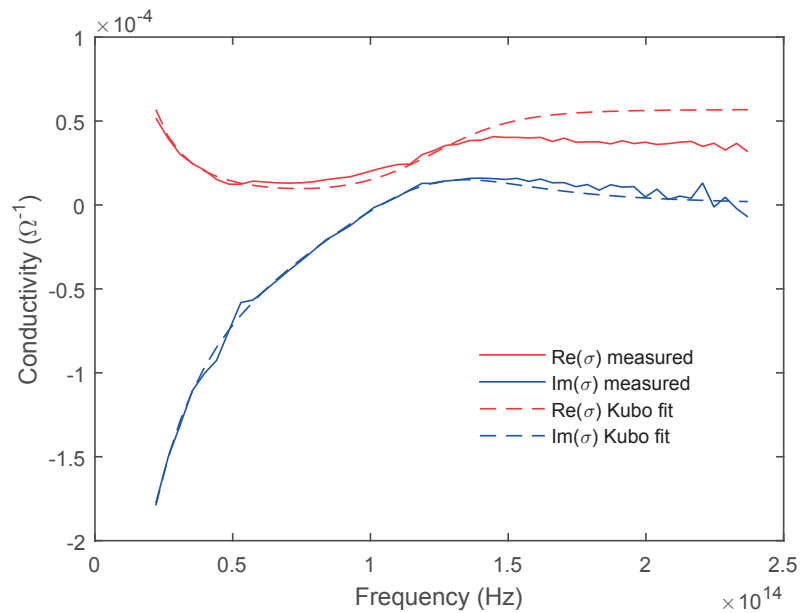


Figure 4.29 – Measured complex conductivity of graphene for gate voltage of -4V and corresponding fitting with Kubo formula, parameters $\tau=24.4$ fs, $\mu_c=0.253$ eV

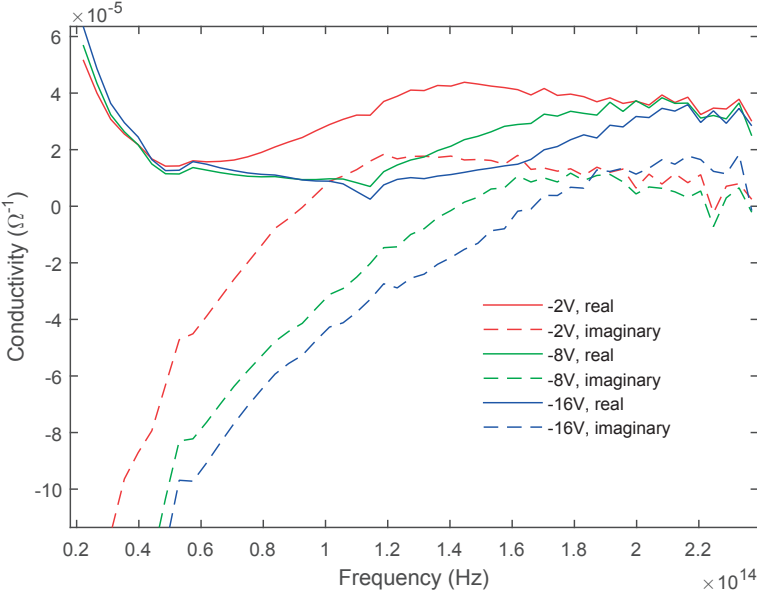


Figure 4.30 – Measured complex conductivity of graphene for different biasing voltages.

5 Non-reciprocal devices based on graphene

5.1 Introduction

This chapter contains the experimental results concerning devices exploiting non-reciprocal effects in graphene. Faraday rotation is a phenomenon observed when a linearly polarized electromagnetic wave propagates through a magneto-optical medium biased with a magneto-static field. The polarization is rotated upon propagation. Unlike chiral media, the rotation angle is independent of the propagation direction, and this implies non-reciprocity. Graphene exhibits this phenomenon in a wide range of frequencies [106, 105, 107, 108, 103, 21, 22, 110].

This phenomenon can be completely explained in the Maxwellian framework. In Chapter 2 we demonstrated that the conductivity tensor of graphene takes two equivalent scalar values for clockwise and counterclockwise waves:

$$\begin{aligned}\sigma_{\text{cw}} &= \sigma_{\text{d}} + j\sigma_{\text{o}} \\ \sigma_{\text{ccw}} &= \sigma_{\text{d}} - j\sigma_{\text{o}}\end{aligned}\tag{5.1}$$

It is easy to notice that at low frequency both σ_{d} and σ_{o} tend to be real. Hence σ_{cw} and σ_{ccw} have the same magnitude but different phases. If we consider Figure 5.1 we notice that graphene in empty space can be modeled for normally incident waves as a parallel admittance in a transmission line model. The admittance value is equal to either σ_{cw} or σ_{ccw} .

An incident linearly polarized wave can be decomposed in two circular polarizations, and each of the polarizations will undergo a different phase shift induced by graphene. Consequently the final transmitted wave is linearly polarized but slightly rotated. For higher frequencies, imaginary parts in the conductivity might induce also a difference in amplitude, and hence ellipticity in the transmitted wave.

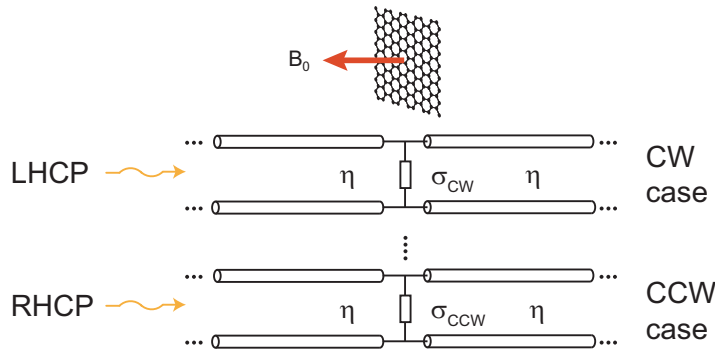


Figure 5.1 – Faraday rotation: circuit model

5.2 Faraday rotation

Faraday rotation on CVD graphene samples fabricated in collaboration with EPFL Nanolab has been measured in collaboration with University of Geneva, laboratory of prof. Alexey Kuzmenko. Following the fabrication process presented in Appendix refchap:fabricationoverview, CVD monolayer samples on a silicon substrate were fabricated and characterized in collaboration with University of Geneva (group of Dr. Alexey Kuzmenko). The samples were measured using a Fourier transform infrared spectrometer connected to a split-coil superconducting magnet. A polarizer was used to create a linearly polarized incident light, while an analyzer (i.e. a second polarizer) was used in front of the detector. Figure 5.2 shows the measured Faraday rotation, which reaches almost 3° for a single monolayer.

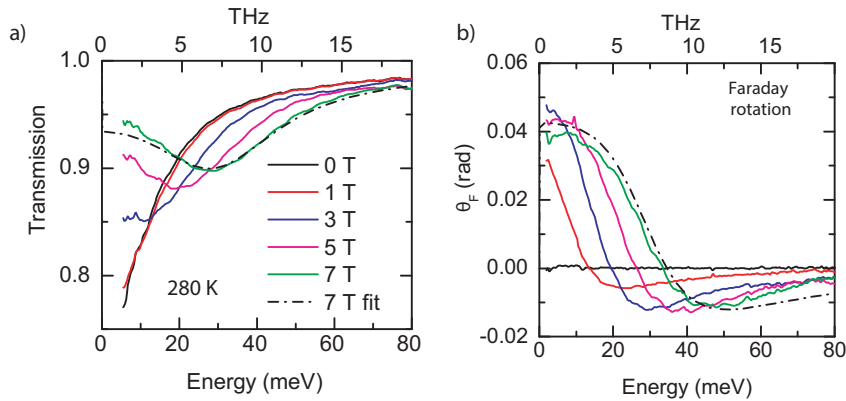


Figure 5.2 – Faraday rotation in CVD graphene. a) Transmission coefficient. b) Faraday rotation

5.3 Faraday rotation enhancement

Faraday rotation in graphene is limited by the low light-matter interaction for a uniform monolayer in presence of plane waves. Also, Faraday rotation is limited in frequency, dropping and oscillating for frequencies beyond 20 meV (approximately 5 THz), as shown in 5.2. There are, however, strategies to improve the light-matter interaction by either patterning graphene

or adding resonators such as metallic elements. These strategies are currently being explored, and this section summarizes the current status of this ongoing research by the author of this thesis.

5.3.1 Magnetoplasmonic enhanced Faraday rotator

Reference [28] illustrates how a pattern of graphene square can exhibit Faraday rotation even in frequency bands (e.g. 5 to 10 THz) where normally the ellipticity dominates, and the Faraday rotation is very small. This is achieved because the separating lines between the squares act as capacitors, compensating for the imaginary part of the conductivity due to plasmonic effects. Consequently, a peak in the Faraday rotation appears and can be controlled with the geometry of the pattern. This can be also understood considering the patches as magneto-plasmonic resonators.

An experiment to verify this phenomenon is currently in progress; a first prototype, shown in Figure 5.3, has been fabricated in EPFL CMI and measured in University of Geneva, in collaboration with Dr. Alexey Kuzmenko.

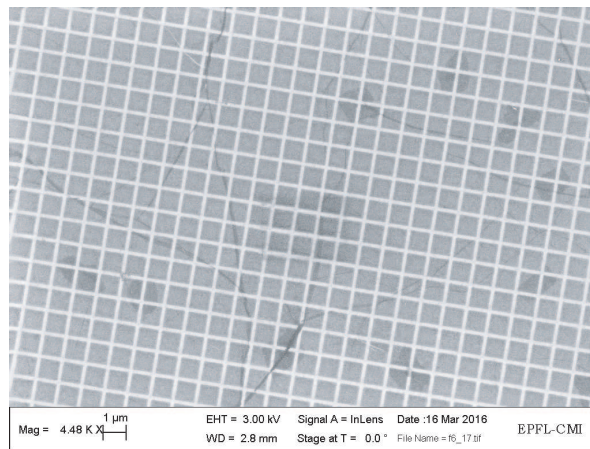


Figure 5.3 – Patterned graphene for plasmonically enhanced Faraday rotation

The squares pattern has a periodicity of $1 \mu\text{m}$ and the gaps separating the squares are 100 nm wide. The design was optimized to target a working frequency of 5 to 10 THz, where Faraday rotation in uniform graphene is null. The design was simulated in Ansys HFSS 15.0.

Figure 5.4 shows preliminary measurements (with magnetic field bias of 7T) of the fabricated device, showing excellent agreement with the numerical simulations for $\mu_c = 0.41 \text{ eV}$ and $\tau = 48 \text{ fs}$, confirming the concept of Faraday magneto-plasmonic enhancement and restoring at 6 THz the 3° of Faraday rotation that are normally observed for lower frequencies.

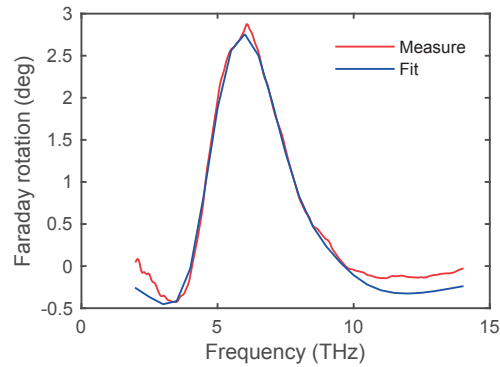


Figure 5.4 – Measured enhanced Faraday rotation at 7 T

5.3.2 Ring resonators enhanced Faraday rotator

Another experiment in progress aims to demonstrate that the Faraday rotation can also be enhanced with ring resonators. This case would also allow for electrostatic biasing, since graphene is not patterned. An experiment to verify this phenomenon is also currently in progress; the device, shown in Figure 5.5, has been fabricated in EPFL CMI and will be measured in University of Geneva, in collaboration with Dr. Alexey Kuzmenko. In this case the target is to increase the value of Faraday rotation and show ambipolarity with holes and electrons carriers. The measurements on the devices are currently ongoing.

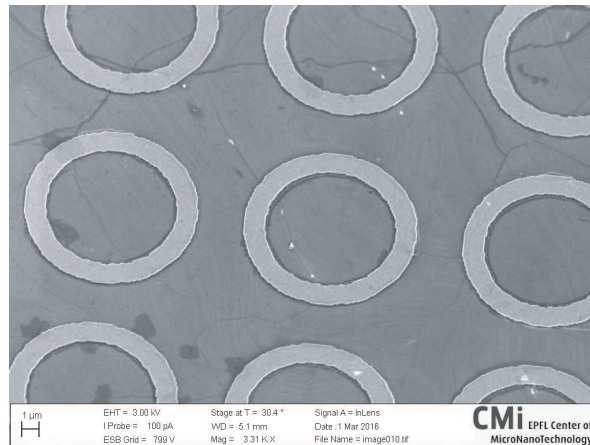


Figure 5.5 – Decorated graphene for enhanced Faraday rotation

5.4 Terahertz isolator based on graphene

Note: The graphene terahertz isolator is a collaboration between EPFL Laboratory of Electromagnetics and Antennas (design, data analysis), EPFL Nanoelectronic Devices Laboratory (fabrication) and University of Geneva (measurement). The work is published in [JA12].

5.4.1 Introduction

The realization of isolators at terahertz frequencies is a very important open challenge due to the intrinsic lossy terahertz propagation in the used non-reciprocal materials. In this chapter the design, fabrication and measurement of a terahertz non-reciprocal isolator (also known as optical diode) for circularly polarized waves based on magnetostatically biased monolayer graphene (operating in reflection) is reported. This is the first terahertz isolator (frequency between 1 and 10 THz) with insertion losses lower than 10 dB ever demonstrated experimentally. The device exploits the non-reciprocal optical conductivity of graphene and, in spite of its simple design, it exhibits almost 20 dB of isolation and only 7.5 dB of insertion loss at 2.9 terahertz. Operation with linearly polarized light can be achieved using quarter-wave-plates as polarization converters.

Several theoretical works have proposed devices based on magnetostatically biased graphene [103, 105, 106, 107, 108, 21, 110, 42], including isolators. In particular, a narrowband graphene isolator was recently measured at 20 GHz [103, 108]. Ferrite isolators have been demonstrated in the THz range [100], showing excellent operational bandwidth and eliminating the requirement for an external biasing magnetic field. However, currently available ferrite isolators are useful only up to 500 GHz and show prohibitive insertion losses in the order of tens of dB beyond this frequency [100]. This intrinsic limit is due to losses in ferrites, and motivates research in graphene and alternative materials. Precisely because of the losses in available magneto-optical materials, the realization of low loss non-reciprocal isolators is considered one of the most important challenges in terahertz science.

Apart from ferrite and graphene, alternative materials have also been proposed to achieve efficient terahertz non-reciprocity, and several works have been recently published presenting experimental characterization of the properties of these materials. One example is given by other free carrier based materials such as doped silicon [78]. In addition, thin films of HgTe exhibit interesting non-reciprocal properties due to a combination of band structure effects and high mobility carriers [101]. Ferrofluids have also been considered, since they exhibit good transparency in the THz band [99]. Another promising example are multiferroic materials, which show strong non-reciprocity and unidirectional propagation at terahertz frequencies [55, 56]. However, these materials have not been employed for the experimental demonstration of final isolator designs, and rarely the explored frequencies exceed 1.5 THz.

In the following we aim to exploit the non-reciprocity of magnetically biased monolayer graphene using a reflection configuration to achieve isolation for circularly polarized waves. The concept of isolator for circularly polarized light has been presented theoretically in a transmission configuration for graphene and other magneto-optical materials [65, 24], while strong circular dichroism was predicted for similar reflection structures [115].

The device presented in this contribution achieves isolation for circularly polarized waves at 3 THz and 7.5 THz, showing performances very close to the theoretical upper bound for non-reciprocal graphene devices⁴ with almost 20 dB of isolation and 7.5 dB of insertion loss.

Chapter 5. Non-reciprocal devices based on graphene

Excellent agreement between simulations and measurements is also demonstrated.

5.4.2 Working principle and Design

The proposed graphene terahertz isolator is a planar device, and it is illustrated in Figure 5.6a and 5.6b. A number N of graphene sheets are placed on a back-metallized thin silicon layer of $10\ \mu\text{m}$ thickness (for our device $N=3$). The sheets are separated by thin Poly(methyl methacrylate) (PMMA) layers (approximately $60\ \text{nm}$), while the thickness of the metallization (chromium and platinum) is $200\ \text{nm}$. The whole structure is bonded to a Pyrex wafer which has solely the function of mechanical support. A magnetostatic field B is applied orthogonally to graphene.

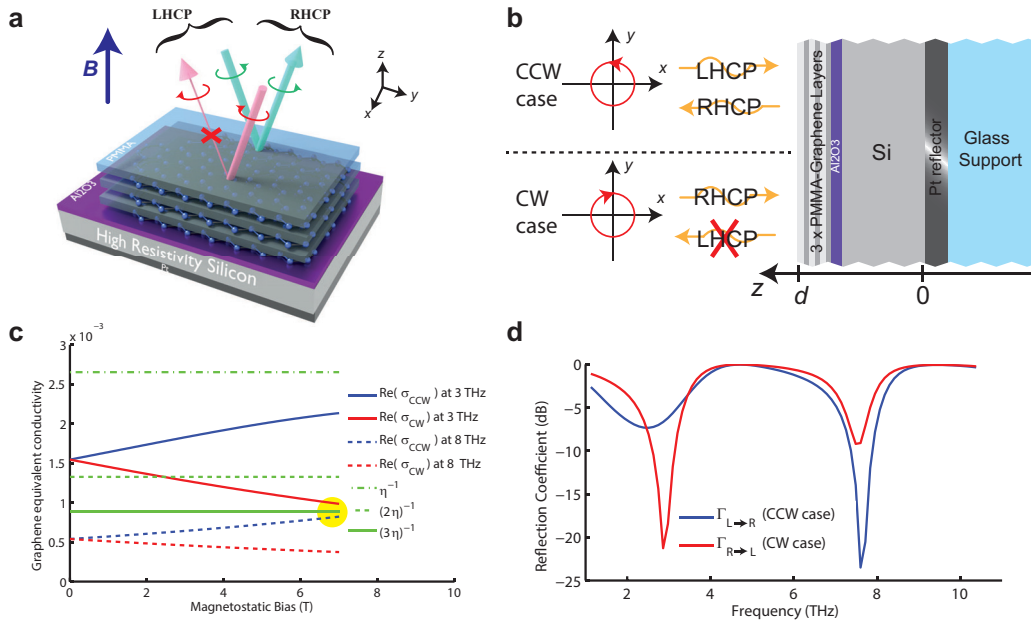


Figure 5.6 – The proposed graphene terahertz isolator. a) 3D view of the device. b) Cross section and schematics of the working principle. c) Magnetic field induced splitting of σ_{CW} and σ_{CCW} as a function of the bias B ($f = 3\ \text{THz}$ and $8\ \text{THz}$, $\mu_{\text{C}}=0.53\ \text{eV}$, $\tau=35\ \text{fs}$, $T=290\ \text{K}$) computed using Kubo formula. The real part of the equivalent conductivity for the clockwise and counter-clockwise cases is shown for monolayer graphene and compared with multiples of the free space impedance η . In yellow the area of interest for the design. d) Simulation of the reflection coefficients for wave converted from right-handed to left-handed or vice-versa, using the simplified model. Two working points are observed, however the direction of the isolation in the second one is reversed.

The device operation is based on reflecting incident LHCP (left hand circularly polarized) plane waves as RHCP (right hand circularly polarized) ones, while absorbing RHCP incident waves. The device thus achieves non-reciprocal unidirectional propagation and isolation for circularly polarized waves [65, 100, 78] because time reversal transformation preserves the handedness of the propagating wave (e.g. a time reversed LHCP is still LHCP). In addition, as explained later, simple reciprocal polarizers and polarization converters can be combined with this device to achieve terahertz isolation and source protection also for linearly polarized light.

5.4. Terahertz isolator based on graphene

Our device exploits Fabry-Perot resonances in the silicon layer to increase light-matter interaction in graphene. As a result, three monolayers of graphene are sufficient to obtain near perfect isolation. The principle of the isolator consists in creating for clockwise (CW) rotating waves (incident RHCP or reflected LHCP) a total surface impedance equal to the impedance η of free space (i.e. impedance matching), causing total absorption (reflection coefficient $\Gamma_{R \rightarrow L} = 0$). On the contrary, for counter-clockwise (CCW) ones (incident LHCP or reflected RHCP) the impedance is mismatched, and waves are reflected ($\Gamma_{L \rightarrow R} \neq 0$). This phenomenon can be completely understood by solving Maxwell's equations in the structure, and it is due to the fact that graphene conductivity can be expressed as a scalar quantity for circular polarization (Figure 5.6c), taking two different values σ_{CW} and σ_{CCW} in the CW and CCW cases respectively, as discussed for Faraday rotation.

To explain the device working principle, two models of the device will be used: a simplified analytical model and a full multilayer model. The former is used to find preliminary design rules and the second to refine the computation and fit the measured results. In both cases the incident and reflected beams are approximated as plane waves propagating normally with respect to the device. The approximation is motivated by the very small angle of the beams with respect to the normal (approximately 8 degrees) and by the spot diameter (in the order of millimetres) much larger than the wavelength of interest. The models then reduce the multilayer structure to a transmission line circuit model.

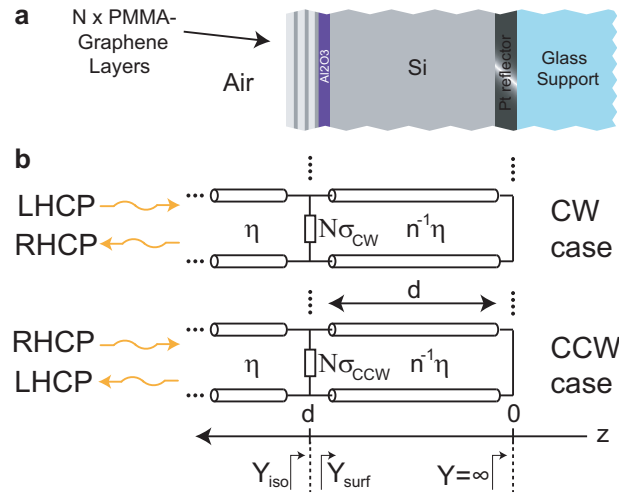


Figure 5.7 – Simplified transmission line circuit model of the isolator. a) Layered structure. b) Equivalent simplified circuit

In the simplified model it is assumed that the platinum reflector is a perfect conductor (and hence a short circuit in the model), the silicon is a lossless dielectric with $\epsilon_r = 11.66$ and graphene layers are assumed to be in parallel and of equal conductivity (so that the total conductivity of the graphene stack is N times the one of a single layer). The full model instead represent each PMMA layer as a layer of thickness 70 nm of a dielectric with $\epsilon_r = 2.4$ while platinum is described with a Drude model with plasma frequency $\omega_p = 7791 \text{ Trad} \cdot \text{s}^{-1}$ and

Chapter 5. Non-reciprocal devices based on graphene

collision frequency $\nu = 56$ THz [109]. Because Al_2O_3 has optical properties very similar to silicon, it is considered part of the silicon spacer.

Importantly, the layer structure is actually split in two circuit models, one for the CW case and the other for the CCW case. The only difference between these two cases is the conductivity of graphene, namely σ_{CW} and σ_{CCW} respectively. The CW case models the reflection from RHCP light to LHCP, which has to be optimized to minimize the reflection coefficient ($\Gamma_{\text{R} \rightarrow \text{L}} = 0$). In the other case (CCW) the isolator must reflect light from LHCP to RHCP ($\Gamma_{\text{L} \rightarrow \text{R}} \neq 0$). To reach this goal, we consider the simplified model and we find the condition such that the reflection in the CW case is minimized. It can be shown then that this choice, for this particular geometry, leads to a quasi-optimal design.

As well known from basic transmission line theory, the reflection coefficient for this structure is given by:

$$\Gamma_{\text{CW,CCW}} = \frac{1 - \eta N \sigma_{\text{CW,CCW}} + j n \cot(n k_0 d)}{1 + \eta N \sigma_{\text{CW,CCW}} - j n \cot(n k_0 d)} \quad (5.2)$$

where $n = \sqrt{\epsilon_r} = \sqrt{11.66}$ is the refractive index of silicon, k_0 is the wavenumber in vacuum, η is the free space impedance and we identified for simplicity $\Gamma_{\text{CCW}} \triangleq \Gamma_{\text{L} \rightarrow \text{R}}$ and $\Gamma_{\text{CW}} \triangleq \Gamma_{\text{R} \rightarrow \text{L}}$.

To satisfy the design condition $\Gamma_{\text{CW}} = 0$ the numerator must be set equal to 0:

$$1 - \eta N \sigma_{\text{CW,CCW}} + j n \cot(n k_0 d) = 0 \quad (5.3)$$

Because η and n are real, taking the real and imaginary part of Equation 5.3 two design rules can be obtained:

$$N \text{Re}(\sigma_{\text{CW}}) = \eta^{-1} \quad (5.4)$$

$$N \text{Im}(\sigma_{\text{CW}}) = n \eta^{-1} \cot(\omega n d c^{-1}) \quad (5.5)$$

After characterizing graphene at terahertz frequencies it was determined that for $N = 3$ the first design rule was satisfied for a field approximately equal to 7T. This fact is illustrated in Figure 5.6c which shows a real part for σ_{CW} of 0.87 mS, very close to $(3\eta)^{-1} \simeq 0.88$ mS.

The second rule, instead, can be used to determine d . Targeting a working frequency of 3 THz, we determined $d = 10 \mu\text{m}$.

Finally, if we assume that the two design rules are satisfied, we can compute the reflection

coefficient. In fact, noting that

$$\sigma_{\text{ccw}} = \sigma_{\text{cw}} - 2i\sigma_0 \quad (5.6)$$

we obtain:

$$\Gamma_{\text{CCW}} = \frac{j\eta N\sigma_0}{1 - j\eta N\sigma_0} \quad (5.7)$$

Clearly, the larger is B (and hence σ_0) the larger is the reflection, which implies that the isolator has lower insertion losses for high magnetostatic bias. The simulated performances of the device are shown in Figure 5.6d. The working principle of the device can also be explained in terms of Fabry-Perot resonances, as the cotangent periodicity predicts. Because of this, a second working point around 7.5 THz is possible and it is confirmed by the measurements. However, because of the frequency dispersion of graphene conductivity, in this second working point the design rules are actually satisfied for the CCW case, inverting the direction of the isolator. For higher frequencies graphene conductivity is too small, preventing other working points, which however could be targeted increasing the number of layers.

5.4.3 Measurement and elaboration

The device was fabricated (see fabrication in Appendix A) and measured using a Fourier transform infrared spectrometer connected to a split-coil superconducting magnet. A polarizer is used to create a linearly polarized incident light, while an analyzer (i.e. a second polarizer) is used in front of the detector (see Figure 5.8). The reflected elliptical polarization is mapped by repeating the measurement for different values of the angle θ between the two polarizers. The magnetostatic field is normal to the sample surface, while the light k vector is close to normal.

Figure 5.9 shows that the reflected polarization is identical to the incident one for $B = 0$ T. One can see that the normalized reflection shows strong absorption dips. These strong absorption features have a periodicity of 4.65 THz, corresponding to Fabry-Perot oscillation in a silicon layer of $9.43\mu\text{m}$ in very good agreement with the nominal value. Figure 5.8b show instead a rich polarization behaviour for $B = 7$ T. This is also shown better by the polarization diagrams in Figure 5.8c at selected frequencies of interest. At the first working point we also notice that the Kerr rotation ϕ goes up to 90° , and continues from -90° to 0° . The isolation and insertion loss of the device are defined as:

$$\text{ISO} \triangleq \frac{\max(\Gamma_{\text{R}\rightarrow\text{L}}, \Gamma_{\text{L}\rightarrow\text{R}})}{\min(\Gamma_{\text{R}\rightarrow\text{L}}, \Gamma_{\text{L}\rightarrow\text{R}})} \quad (5.8)$$

$$\text{IL} \triangleq \max(\Gamma_{\text{R}\rightarrow\text{L}}, \Gamma_{\text{L}\rightarrow\text{R}}) \quad (5.9)$$

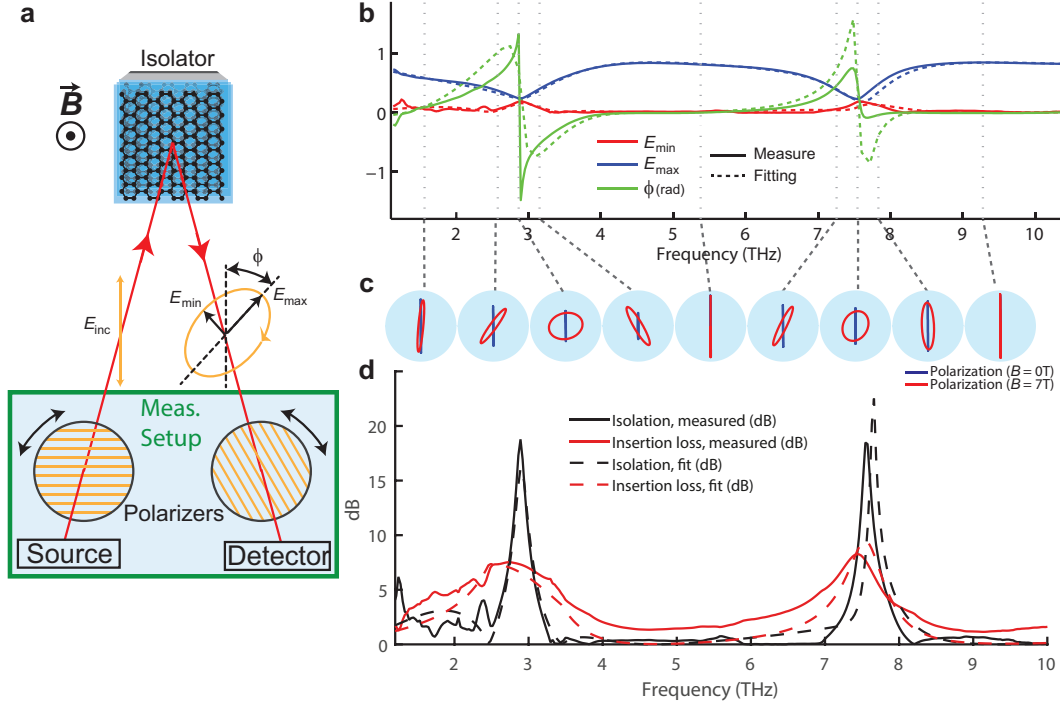


Figure 5.8 – Measured isolator performances. Measures have been performed at $T = 290$ K. a) Schematic of the measurement setup configuration and definition of elliptical polarization parameters. b) measured elliptical polarization parameters (major and minor axis E_{min} , E_{max} and Kerr rotation angle ϕ) as a function of frequency for $B = 0$ T and 7 T. E_{min} , E_{max} are normalized with respect to E_{inc} . The measures have been fitted (dashed traces) with the full multilayer model and the best fit is obtained for $\mu_c = 0.53$ eV, $\tau = 35$ fs, $d = 9.15 \mu\text{m}$, additional loss: 30%. c) Polarization state shown for some representative frequencies. d) The extracted performances (isolation and insertion loss expressed both as positive dB quantities) of the isolator for circularly polarized waves.

Even though our measurement setup is equipped only with linear polarizers, both these quantities can be computed accurately from the measured polarization parameters (obtained exciting the device with a linear polarization and mapping the reflected polarization with the analyser). The sought isolation and insertion loss can then be retrieved as:

$$\text{ISO} \triangleq \frac{E_{max} + E_{min}}{E_{max} - E_{min}} \quad (5.10)$$

$$\text{IL} \triangleq \frac{E_{max} + E_{min}}{E_{inc}} \quad (5.11)$$

$$(5.12)$$

where E_{max} and E_{min} are the major and minor axis of the mapped elliptical polarization of the reflected electric field and E_{inc} is the linearly polarized incident electric field. The full algorithm is actually more complex and it enables the compensation of polarizer imperfections, and it is explained in the Supplementary information of Ref [JA12].

The resulting performances are plotted in Figure 5.8d. At both working frequencies the

5.4. Terahertz isolator based on graphene

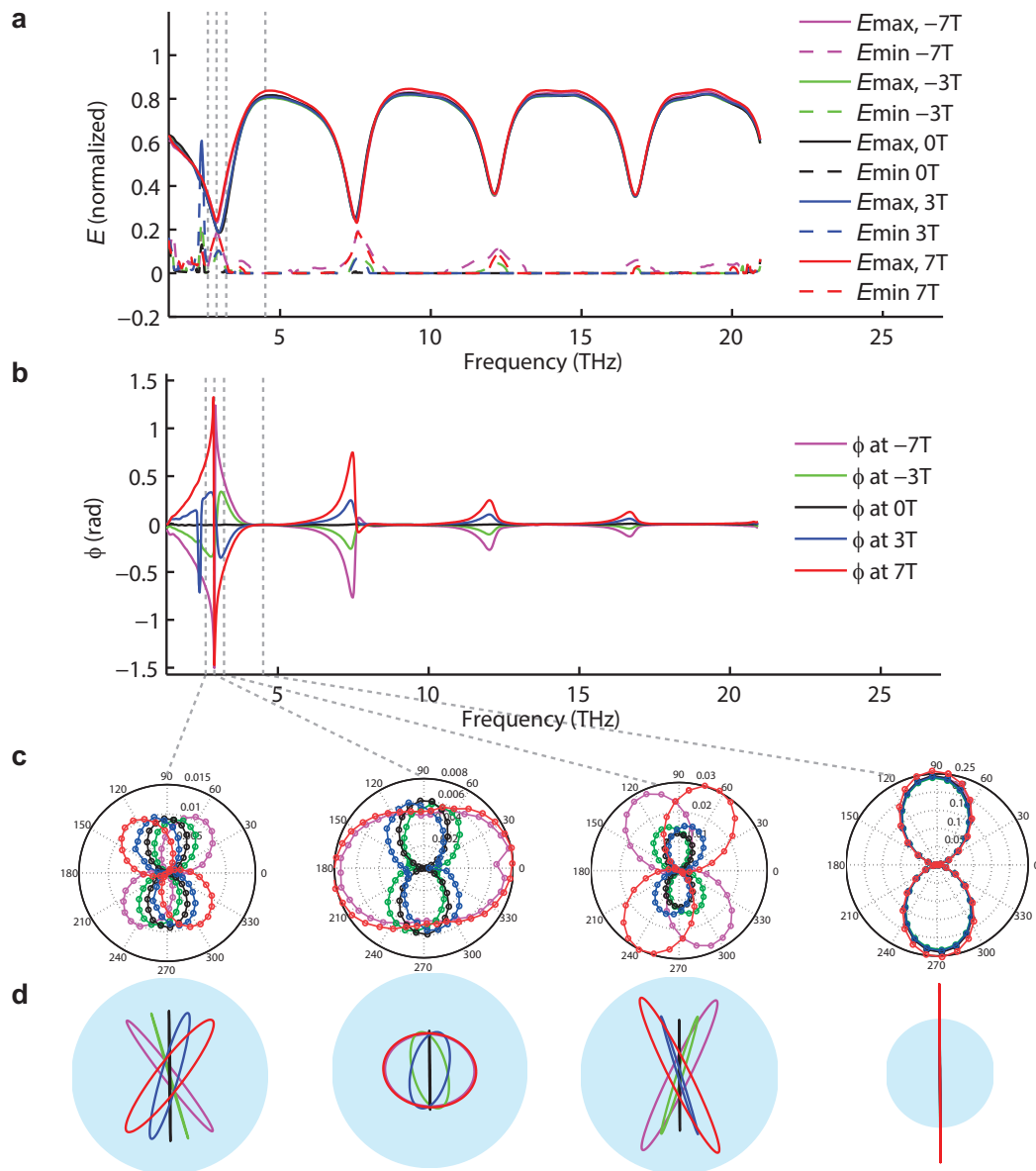


Figure 5.9 – Full device characterization. a,b) Polarization parameters. c) Raw power data for the five magnetic fields values at frequencies 2.6 THz, 2.9 THz, 3.2 THz, 4.5 THz. d) Corresponding fitted polarization plot (the reference light blue circle has a radius of 0.5). The performance of the device is shown, in the whole measured band up to 20 THz, in panels a and b. There is a striking difference between the behaviour in magnetic field at different frequencies: for $f = 4.5$ THz, the light stay polarized linearly with no noticeable influence of the magnetic field. For $f = 2.9$ THz on the contrary, a strong modification of the ellipticity of the light takes place. This variation is also accompanied by a rotation of the light polarization.

isolation reaches almost 20 dB (18.8 dB and 18.5 dB respectively) and the insertion loss is approximatively 7.5 dB. The results plotted in Figure 5.8b have been fitted with the full layered model reaching a very good agreement. Conductivity of graphene is computed using the Kubo formula, and the best fit is obtained for a graphene Fermi level $\mu_c=0.53$ eV, $\tau=35$ fs, $d=9.15$ μm , and the fitting improves sensibly if an additional overall loss of 30% is added to the model

Chapter 5. Non-reciprocal devices based on graphene

over the whole bandwidth. The high μ_c can be explained considering that graphene is still in contact with the PMMA on one or two sides, and hence is likely to be highly doped by substrate interactions. The 30% loss could be attributed to a systematic error due to the non-perfect planarity of the isolator, which caused part of the energy to be reflected out of the detector. Figure 5.9 shows the complete set of raw measures.

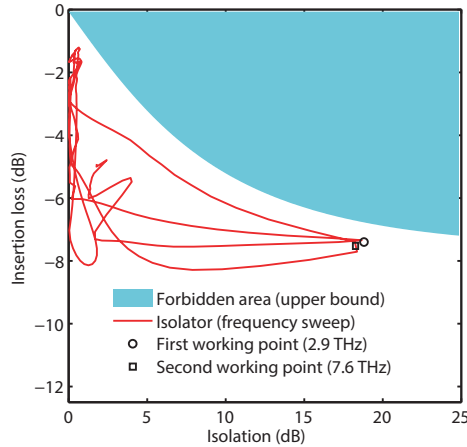


Figure 5.10 – Device optimality: representation of the measured device performances for $B = 7$ T in the Cartesian plane between isolation and insertion loss for different frequencies. On the same plot the non-reciprocity theoretical upper bound is represented for $\gamma_{NR}=0.295$, value found from the fitted graphene parameters. The working frequencies (showing a maximum in the isolation) are highlighted. Because the curves are very close to the theoretical bound the device is quasi-optimum with respect to it.

Figure 5.10 is a Cartesian plot of the isolation versus the insertion loss. The isolator upper bound, discussed in Chapter 3, is also represented. For the fitted parameters, it can be shown that the forbidden region is frequency-independent in the band from 0 THz to 20 THz. The performance of the device is just 1 dB below the theoretical upper bound which means that the device is near optimal.

While the presented isolator operates with circularly polarized light, it is clear that most terahertz applications need components able to handle linearly polarized waves. It is however quite simple to adapt our isolator to linear polarization operation using one or two quarter-wave plates (QWPs) as polarization converters, as shown in Figure 5.11a and 5.11b. This simple system can be used to protect a linearly polarized source from harmful reflections, which is one of the most important applications of non-reciprocal isolators [100].

The wave produced by the source could in fact propagate through the isolator but any reflected signal trying to propagate backwards in the isolator would be highly attenuated, protecting the source. If a linear polarizer is added after the source, then the latter is also protected from cross-polarized reflected light. Similarly, bandpass filters can be used in cascade with the isolator to protect the source from any unwanted signals having frequency outside the working band of the isolator..

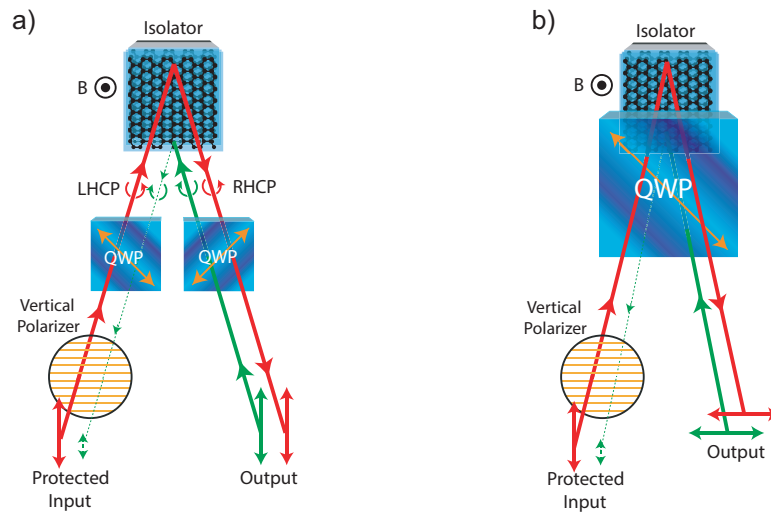


Figure 5.11 – Linearly polarized light operation: By combining the proposed isolator for circular polarization with simple quarter-wave plates (QWPs) it is possible to also achieve isolation for linearly polarized waves. The QWPs are placed with the optical axis (orange) at 4° thus acting as polarization converters from circular to linear polarization. Two configurations are proposed. Polarizers and/or filters can be used to completely protect a source from cross polarization or other frequency signals coming from the output port.

5.5 Conclusions

In this work we demonstrated the possibility of designing and implementing close to optimal terahertz isolators based on graphene. To achieve this goal, we proposed a reflection structure which exploits the Fabry-Perot resonances in a thin layer of silicon to obtain isolation using just three graphene monolayers. The operation of the device can be fully understood in the framework of Maxwell's Equations using a 2D linear conductivity tensor to model carrier dynamics in magnetostatically biased graphene. One of the most significant aspects of this design is its ability to be very close to the optimal performances available with the used graphene. Equivalent devices operating in transmission require more complicated structures or lead to suboptimal performances [JA8].

In addition it is worth mentioning some additional advantages related to this particular device geometry. First, due to the fact that the device is planar (i.e. operating for plane waves and not based on mono-modal waveguide ports), it works for incident waves having different \mathbf{k} vectors at the same time. Also, the isolator is expected to show modest frequency reconfigurability depending on the incidence angle, because the latter would affect the Fabry-Perot resonances. Electric field effect in gated graphene could be used to fine tune the device to virtually infinite isolation, as demonstrated also at microwave frequencies [108]. In fact, perfect isolation is obtained when the device surface impedance is equal to free space impedance, and electrostatic gating allows a fine tuning of the total impedance of the device.

Because the device exploits Fabry-Perot resonances, it is relatively narrowband; however the

absolute bandwidth is in the order of 50 GHz, which is an excellent value for telecommunications and for continuous wave applications. This value can possibly be increased using more complex designs including patterned graphene, added metal patterns and more complex multilayer structures[JA8]. The relative precision of the working frequency is given by the substrate thickness, and hence it can be controlled and fine-tuned in a precise way, in the technological process, by polishing or using additive dielectric depositions. Furthermore, for different angles of incidence, the working frequency is expected to change due to the reduced longitudinal wavelength of the wave, and this could be used to dynamically tune the operation frequency.

Finally, the reflection configuration of the device eliminates completely the input impedance mismatch (return loss) issue, which is instead a concern for any device operating in a transmission configuration. For waves with a non-zero incidence angle (as the case for practical application where receiver and transmitter are in separate locations) this fact is evident considering that the device is invariant to translation and hence it operates with a single diffraction order. This implies that the wave cannot possibly be reflected to the receiver. For normally incident waves, this is due to the fact that an incident left hand wave can only be reflected as right hand and vice versa, because the device is invariant to rotation.

The main drawbacks of our device are the need of high magnetic field (7 T) and an insertion loss of more than 7 dB. Both these issues cannot be solved by improving the design, since it is already quasi-optimum in this sense. Hence the only way to lower the insertion loss and reduce the required B biasing field is to use graphene with higher mobility, such as graphene encapsulated in hexagonal boron nitride with room temperature mobilities in the order of $100,000 \text{ cm}^2\text{V}^{-1}\text{s}^{-1}$. With a mobility of $40,000 \text{ cm}^2\text{V}^{-1}\text{s}^{-1}$ and a biasing field of 1 T (easily generated by rare earths permanent magnets) the insertion loss for perfect isolation would be as low as 0.3 dB according to the upper bound, paving the way to commercially relevant devices. These considerations are independent of the carrier density and, even if high mobility is available only for lower carrier density, the design can be adapted using a larger number of graphene layers.

6 Beam steering reflectarray at terahertz frequencies

6.1 Introduction

The objective of the work described in this chapter is the design, implementation and measurement of the first reconfigurable terahertz reflectarray using graphene as tunable material. This objective has been reached (although there are still wide margin for improvement) and the rest of this chapter describes the design, fabrication and measurement of this novel terahertz device.

Our implementation is based instead on a beam-steering reflectarray concept; a reflectarray is, in this context, a planar metasurface which reflects an incident beam of THz light (generated by an given illuminating source) in a direction which can be selected electronically with DC control signals to the reflectarray. The working principle of the proposed device is explained in the following section.

6.2 Reflectarray: working principle

The concept of reflectarray antenna is a very general one which covers several types of devices [8, 47, 9, 88, 12, 7, 38, 37, 10, 11, 81, 91, 92, 49, 79, 82, 131, 129, 128, 4, 117]. The main idea of the reflectarray is to create an electromagnetic beam with some given desired properties (e.g. in terms of width, direction, polarization, intensity profile, radiation pattern, etc.) by using a low profile (flat) metasurface illuminated by a source antenna. The surface is composed by a (quasi)periodical arrangement of cells, where each cell reflects the impinging wave with a certain phase delay (Figure 6.1). By carefully choosing the phase delay profile of the full surface, the final shape of the reflected beam can be designed precisely. Figure 6.1a shows an example of a simple design, where a progressive phase gradient is used to achieve anomalous reflection. This can be done, for example, varying the size of resonant elements and in turns the phase of each cell.

The most interesting property of reflectarrays is that it is possible to include tunable elements

Chapter 6. Beam steering reflectarray at terahertz frequencies

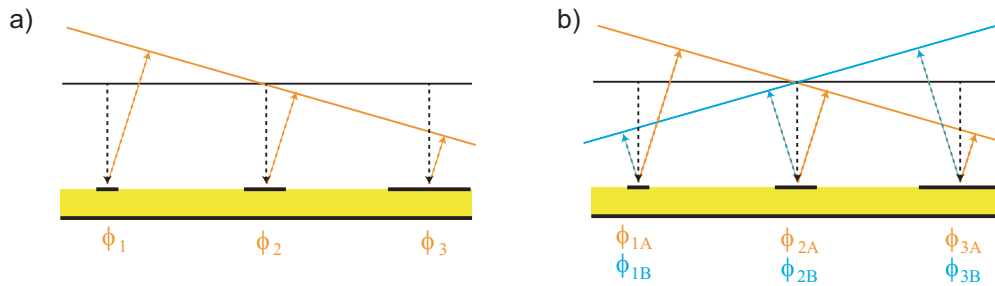


Figure 6.1 – Working principle for fixed and by-state dynamically reconfigurable reflectarrays, 2D view

in the reflective cells in order to control the reflective phase of each cell dynamically. Figure 6.1b shows an illustration of a simple example of this concept where each cell can be reconfigured to take two values for the phase reflection [58]. By tuning all the cells simultaneously with a common control signal, it is possible to select between two directions for the reflected beam.

A generalization of this concept is found in beam steering reflectarrays. In this case, typically, all the elements are identical, but their reflection phase can be controlled individually with separate control signals. The signals can then be selected in order to obtain the phase profile associated to the desired radiation pattern of the final antenna. Figure 6.2a shows the structure of this device. The size of the cells is subwavelength, and hence, when the same control signal is the same for all the cells, incident light is only reflected in the specular reflection, because of symmetry. Figure 6.2b shows the effect of modifying the control signal applied on the cells. For this demonstrator, beam steering in one dimension is proposed, in order to reduce the control signals to one for each column. More complex implementation can be designed to control the beam in two dimensions. Applying a periodic distribution of the control signals, the initial symmetry of the device is broken, and the new period will determine the direction of the reflected beam. By dynamically tuning the signals, beam steering becomes possible.

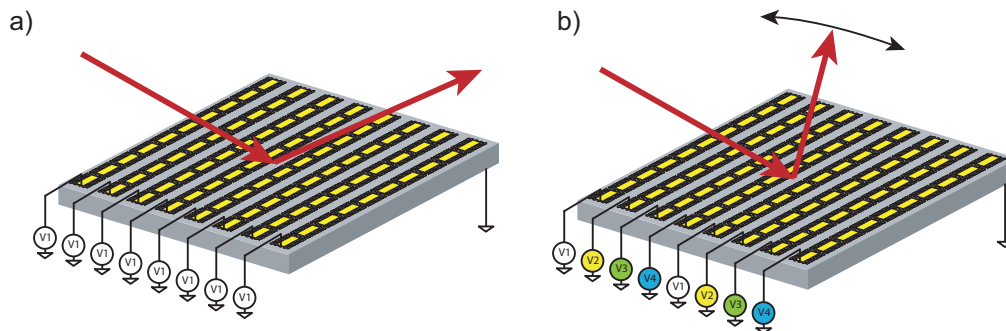


Figure 6.2 – Working principle for full beam steering reflectarray antennas.

In this project, the tunable elements in the cells are graphene FETs, which exhibit a conductivity depending on the applied gate voltage, which represents the control signal for our

implementation. Graphene elements are connected by column, so that all the elements in the same column have the same gating voltage and the same phase response. The substrate is instead connected to a reference voltage (ground). For gate oxides, ALD Al_2O_3 has been used.

Importantly, to increase the efficiency of the reflectarray, a ground plane (or reflector) has to be added below the structure. This is to prevent wasting energy in transmission and to increase the interaction of terahertz light and graphene at the same time. The top layer of the cell and the ground plane have to be spaced by a dielectric material with thickness in the order of the wavelength, which was one of the most important difficulties of the project.

More in general, the fabrication of the reflectarray has been very challenging, as it required the optimization of several clean room processes. However, the final process is now repeatable and reliable, and can be implemented with commonly available micro-nanofabrication infrastructures. To tackle these challenges, we first fabricated an intermediate demonstrator without graphene, to demonstrate fixed beam reflectarray operation and then we fabricated the final demonstrator with beam steering capabilities. All the prototypes were fabricated at EPFL Center of MicroNanoTechnology (CMi), graphene was provided by Cambridge University (Ferrari's Group) and from Graphenea. The remainder of this document first illustrates the fixed beam (no graphene) intermediate prototypes [JA4] and subsequently describes the final graphene based prototypes.

6.3 Fixed beam terahertz reflectarray

A fixed beam intermediate prototype was developed in collaboration with Dr. Hamed Hasani. This fixed beam reflectarray was designed to have deflection at different angles for each frequency, given a fixed incident wave. Fabrication is given in Appendix A.

Figure 6.3 shows the simulated reflection at the three design frequencies as a function of the geometrical parameters. Using these numerical simulations, the parameters have been optimized in order to obtain the phase gradients needed to achieve different beam directions at different frequencies.

The sample has been characterized at LEMA EPFL using a terahertz time domain system (Tera K15, THz-TDS measurement system from Menlo System GmbH), see Figure 6.4. In order to study the deflection capabilities, the receiver of the Tera K15 system has been mounted at a fixed angle of 30° from the normal incidence. On the other hand, the transmitter has been mounted on top of a rotary arm, which allows changing its position, and thus being able to measure at different incident angles. The reflectarray has then been mounted on a vertical surface along with a fully metallized substrate, which will act as reference mirror. The size of the THz beam has been adjusted to no more than 8 mm using an iris.

Figure 6.4 clearly illustrates that the incident beam is deflected in several directions according to its frequency. For frequencies outside the working bands the chip behaves as a mirror. For

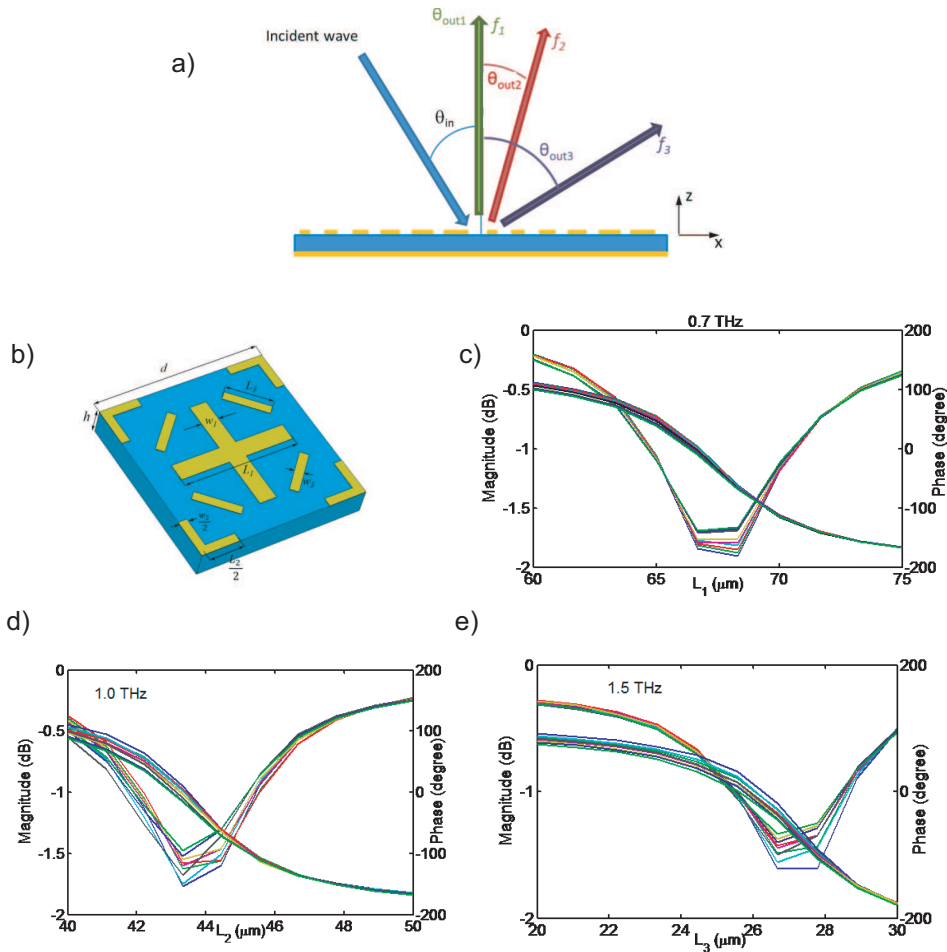


Figure 6.3 – Geometry and performance of the fixed beam reflectarray

the three working frequencies, the beam is deflected in three distinct angles corresponding to the design angles (0° , 20° and 50°), confirming that the intermediate prototype is fully functional.

6.4 Graphene beam steering reflectarray

Details on the fabrication of the graphene terahertz beam steerable reflectarray can be found in Appendix A. The design of the cell has been carried out in the numerical tool Ansys HFSS. First, graphene resistance has been measured in a fabricated gated graphene sample. We noticed that the graphene resistance can vary in a range between 800 ohm and 4000 ohm. For the used CVD graphene, the imaginary part of the conductivity in this frequency range can be neglected, and the real part is very close to the DC conductivity. This fact makes unfeasible to create a unit cell with a reflection phase changing uniformly with the voltage. Instead, a two state cell where the reflection coefficient has a phase variation of 180° in the two states is

6.4. Graphene beam steering reflectarray

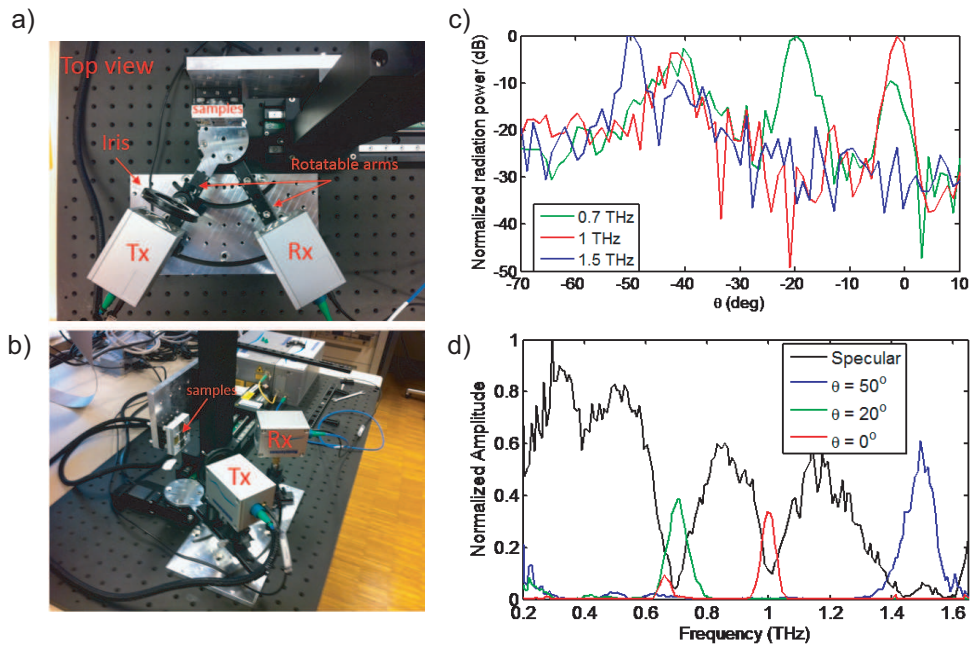


Figure 6.4 – Measurement of fixed beam terahertz reflectarray. a,b) Measurement setup with rotatable stages. c) Radiation pattern at the three design frequencies. d) Spectrum at the three design angles.

feasible.

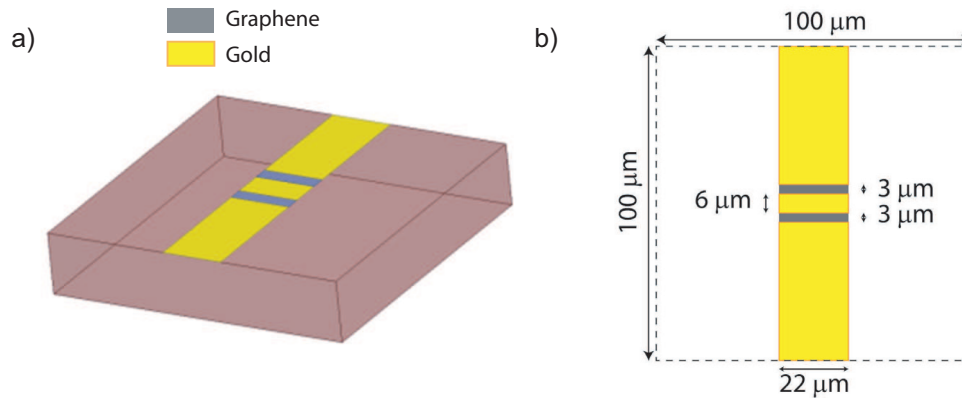


Figure 6.5 – Figure 14: Unit cell. a) Design in HFSS, b) Dimensions

Hence, the unit cell shown in Figure 6.5, based on a resonant cut-wire design with graphene in the gap working at frequency 1.2 THz, has been optimized to provide phase difference of 180° upon the two extreme values of graphene resistance (800 ohm and 4000 ohm), see Figure 6.6. The final layout includes 40×40 cells each having size of $100\mu\text{m} \times 100\mu\text{m}$ (Figure 6.7, 6.8, 6.9). Each column is piloted with an independent voltage provided by a control unit interfaced to a computer (Figure 6.10).

Chapter 6. Beam steering reflectarray at terahertz frequencies

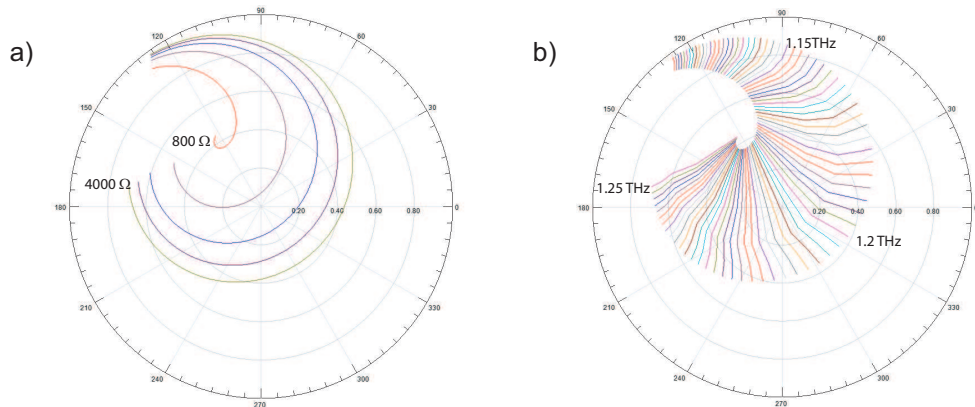


Figure 6.6 – Complex reflection coefficient of the period cell as a function of frequency and graphene resistance

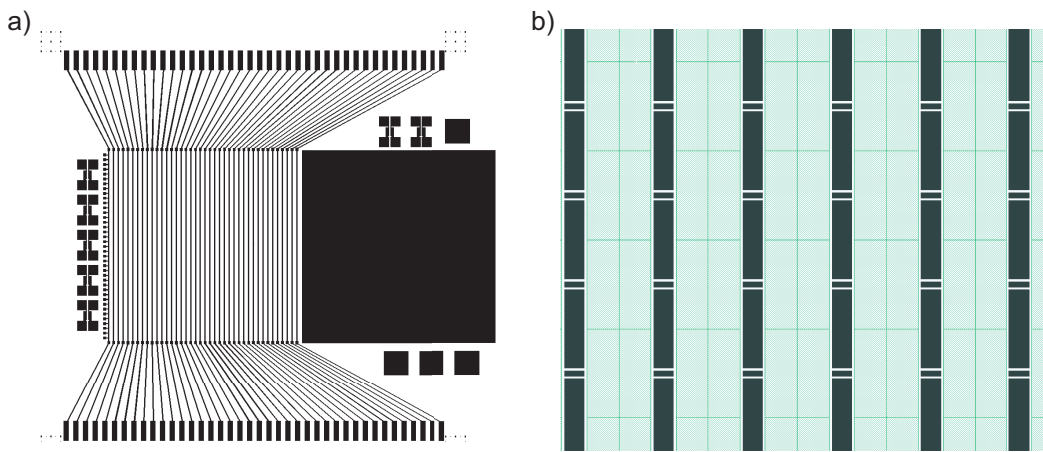


Figure 6.7 – Layout of the reflectarray (a) and details of the columns (b)

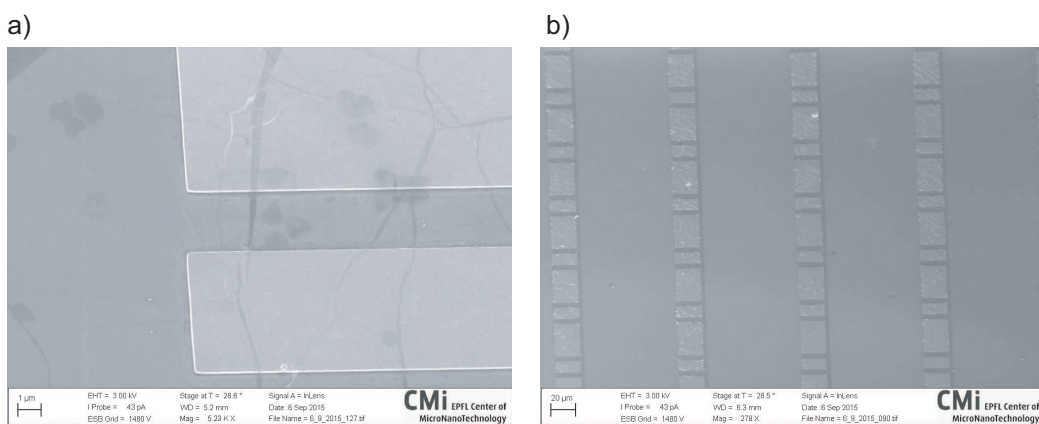


Figure 6.8 – SEM picture of reflectarray before (a) and after (b) graphene etching

Beam steering can be achieved by illuminating the reflectarray at 45° and then gating the columns with different voltages. For the final reflectarray sample, the Dirac point was found

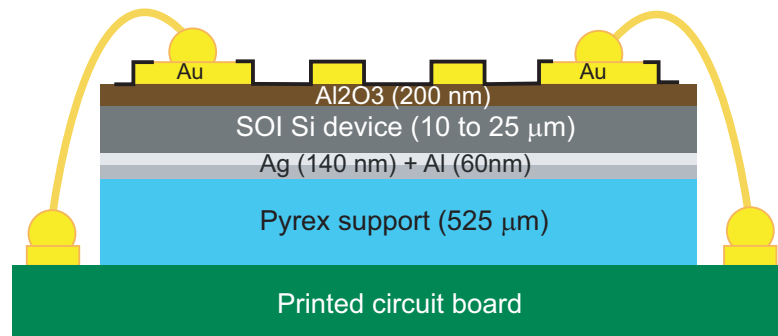


Figure 6.9 – Cross-section of the reflectarray mounted on the PCB

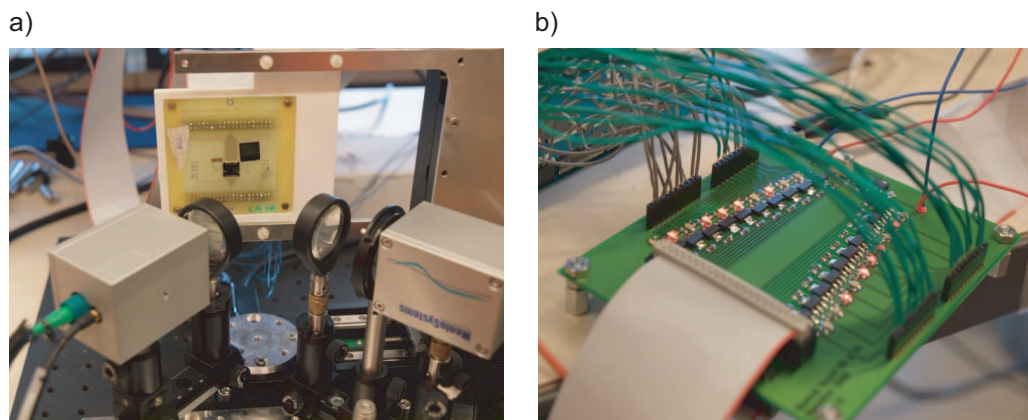


Figure 6.10 – Picture of the reflectarray mounted on the PCB (a) and of the control unit (b)

for a gate voltage of 7V, while -23V was used to obtain the high conductivity state in graphene. Each column was either gated with 7 (logical 1) or -23 V (logical 0). Patterns of logical 1s and 0s can be used to create a super-period in the reflectarray. For example the string ‘000111000111000111...’ shows a super-period of 6 columns. These patterns are referred in the following as “Period N ”, where N is the number of columns of the pattern periodicity. We use the adjective “Opposite” to designate the opposite pattern (each 1 is transformed to 0 and vice versa).

An Arduino board connected to a custom made array of CMOS control transistors has been used to change the gating pattern programmatically (Figure 6.10). The deflection angle can then be estimated according to anomalous reflection laws, see Table 6.1 for the full list of patterns and corresponding expected deflection angles. The chip was then measured scanning the receiver angle in the available range between -59° and -9° for control strings.

The first three plots of Figure 6.11 show the reflected power as a function of the measurement angle and of frequency for three patterns (with period 4, 6 and 10). The black arrow illustrates the presence of the beam in the central working frequency of 1.23 THz. The remaining ones show differential plots obtained measuring the reflectarray in one configuration and then

Chapter 6. Beam steering reflectarray at terahertz frequencies

Table 6.1 – Control strings for beam steering

Configuration	Control string	Angle
Period 4	00110011001100110011001100110011	-6°
Period 4, opposite	00111100110011001100110011001100	-6°
Period 5	0011000111001100011100110001110011000111	-13°
Period 5, opposite	1100111000110011100011001110001100111000	-13°
Period 6	0001110001110001110001110001110001110001	-17°
Period 6, opposite	1110001110001110001110001110001110001110	-17°
Period 8	0000111100001111000011110000111100001111	-24°
Period 8, opposite	1111000011110000111100001111000011110000	-24°
Period 10	0000011111000001111100000111110000011111	-28°
Period 10, opposite	1111100000111110000011111000001111100000	-28°

inverting all the control bits (see the opposite patterns in Table 6.1) and subtracting the radiation patterns in the two cases. This allows removing almost completely the specular reflection and obtaining a much clearer plot of the beam. The black arrows show clearly that the beam is steering accordingly to the control string.

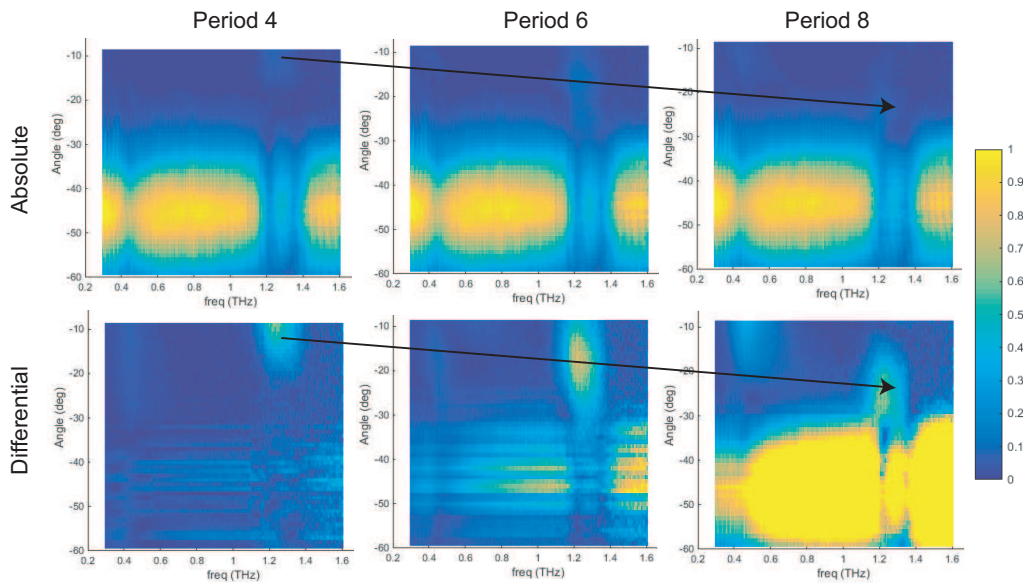


Figure 6.11 – Frequency versus angle dispersion plots. Absolute and differential data is shown

Figure 6.12 shows a plot of the radiation pattern normalized to its maximum value at the central working frequency of 1.23 THz. The curves in the plot are vertical slices of the differential patterns in figure 18, including in also the patterns with periodicity 5 and 10. The angles of the obtained maxima are in excellent agreement with the values predicted in Table 1. Importantly, the beams appear very wide (approximately 30°) because the reflectarray was measured with focused beams. For collimated beams the directivity is expected to be greatly improved.

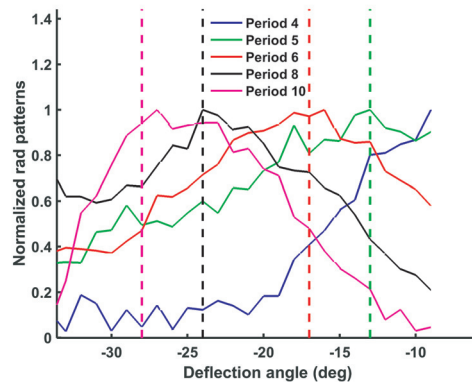


Figure 6.12 – Reflectarray radiation pattern (normalized to maximum value) showing beam scanning. Dashed lines are the expected direction of the beam using reflectarray theory

Finally, Figure 6.13 shows that if the bits of the control unit are shifted, the signal radiated in the beam can be modulated as in a PSK scheme. This is also the first time to the author's knowledge that such a complex modulation scheme is implemented in terahertz frequencies. Notice that the translational symmetry of the device guarantees constant amplitude of the PSK signal.

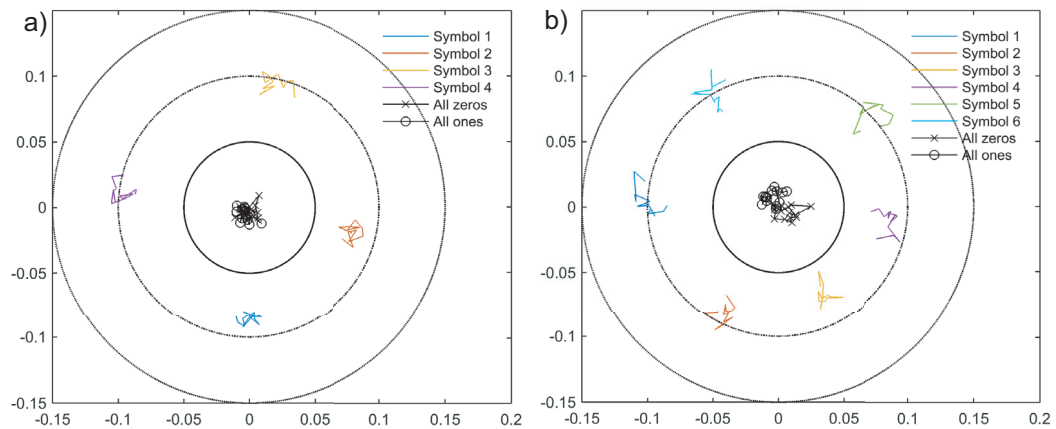


Figure 6.13 – PSK modulation schemes using periodicities of 4 and 6

6.5 Conclusions

The objectives within the Graphene Flagship project have been successfully reached, since beam steering at frequencies above 1 THz (1.2 to 1.3 THz) was obtained. Some optimization of the unit cell can be performed in order to reduce the specular reflection, which however goes beyond the scope of this initial demonstrator.

This is the first time that electronic beam steering has been demonstrated with a terahertz reflectarray, and the potential applications of this device are numerous. The steered signal has

Chapter 6. Beam steering reflectarray at terahertz frequencies

a bandwidth of almost 100 GHz. We believe that this device represents an important milestone in terahertz technology, which has been reached only thanks to the unique tunable properties of graphene. These exciting results will be further explored in the Core 2 phase of the Flagship, exploring new frequency ranges and gating schemes. Graphene tunability has been shown to greatly improve in the mid infrared range, and devices with even better performances are possible in that range.

7 Conclusions and perspectives

In this thesis a number of potential applications of graphene have been explored, and several experimental demonstrators have been obtained. The work performed in this thesis is a part of a much larger effort in bringing graphene and 2D materials on the market. Graphene research is, in fact, in a very delicate phase: whenever a new technology is discovered, the journey from the laboratory to the market is long and full of potential obstacles. The most important obstacle is beating existing technologies in terms of costs and performances. To cross the gap between research and commercialization, usually referred to as “valley of death”, it is very important to identify a set of applications where the new technology is clearly superior to the state of the art. For these reasons this thesis provided the following contributions:

- It developed a metric (the figure of merit of graphene deriving from the upper bound) to compare graphene potential for modulators and non-reciprocal components. This metric allows a fair comparison among various graphene types and with respect to competing technologies in terms of the expected device performances, like insertion loss. The metric demonstrated that graphene has a very high potential (which is still partly unused) for modulators at terahertz and especially in the mid infrared. It also demonstrated that the potential of graphene for non-reciprocal devices extends to the mid infrared, even if little Faraday rotation is observed in unpatterned graphene.
- It developed a new method to characterize complex conductivity of materials (which is at the moment still under development but showing already its usefulness in studying carrier’s dynamics without patterning).
- It developed several experimental demonstrators. Most notably, the terahertz reflectarray and terahertz isolators are very important contributions, since little or no available technologies exist to perform these functions in the terahertz range. While it is clear that graphene is not competitive in the microwave range for reconfigurable devices, it is one of the few choices for both terahertz non-reciprocity and modulation. We also predicted that a significant improvement is expected as soon as new methods to improve the mobility are developed, since both for modulation and non-reciprocity high values of μ (or τ) are beneficial for the graphene figure of merit.

Chapter 7. Conclusions and perspectives

- The developed devices have been created using commercial CVD graphene. This is very important, because many devices presented in literature use exfoliated samples instead. Exfoliated graphene possesses superior performances in terms of mobility, but the size of its samples is limited to few hundreds of micrometers, and hence it is not suitable for commercial applications (while of course it is extremely useful for research purposes to understand the ultimate potential of this material).

Several main conclusions can be drawn on the future of this technology from the point of view of the applications explored in this thesis. First, research efforts should focus especially in creating CVD graphene with high mobility and strategies to preserve the mobility during device fabrication are very important. This is not the first time that this conclusion is reached, but it is here particularly important and evident, especially in light of the developed graphene figure of merit and its dependence on mobility. Second, graphene is a winning technology for several terahertz applications. Besides the modulation, reflectarray and isolator applications presented here, several works in the literature have pointed out other possibilities in this frequency range. For example for terahertz detection [112] or to modulate the output of a quantum cascade laser [15]. As such, graphene can contribute to close the terahertz gap.

Future interesting research lines to continue the work of this thesis include:

- Improving the performances of the terahertz reflectarray with a fine tuned design.
- Implementing an experimental infrared beam steering reflectarrays using graphene. At infrared frequencies, in fact, graphene has the best potential for modulation and reconfigurability. This device would be an example of a spatial light modulator in reflection able to fully control the reflected beam. The easy integration of graphene with silicon technology could be exploited to create complex control networks to address a large area device.
- Integration of graphene tunable antennas, switches and reflectarrays in detectors, to tune detection frequency (hyper-spectral imaging) polarization and direction.
- Extending the isolator concept to higher frequencies (mid infrared). The graphene non-reciprocity figure of merit is, in fact, preserved up to frequencies in the order of tens of terahertz. The creation of non-reciprocal mid infrared components, possibly integrated directly in lasers, could contribute to the development of more robust sources, the protection of which is the main application of isolators.
- If better mobility is achieved, then the creation of miniaturized microwave non-reciprocal circuits would become an interesting avenue. In fact, while current ferrite non-reciprocal components are usually bulky, graphene could lead to much smaller and lighter devices. This provided that graphene mobility becomes sufficiently large at these frequencies to ensure large graphene non-reciprocity figure of merit even with a small biasing field.

Finally, the work presented in this thesis was a key contribution to the European Graphene Flagship Project (ramp up phase, tasks 5.4 and 5.5), and it opened very promising avenues to scale the presented devices at mid infrared (which will be one of the tasks of the Core 1 phase

of the Flagship Project), providing new understandings on the interaction between light and two-dimensional materials.

A Micro-nano fabrication of graphene devices

A.1 Introduction

This chapter summarizes the fabrication processes that have been used in the remainder of this thesis. All fabrication processes were performed in the Center of MicroNanoTechnology (CMi) at EPFL, except from graphene transfer which was done by external collaborators (Graphenea Inc. and Ferrari's Group at Cambridge University). Printed circuit boards (PCBs) were fabricated by the Atelier pour le routage et la fabrication de circuits imprimés (ACI).

A.2 Devices based on THz/IR silicon transmission substrate

A.2.1 Introduction

The first type of device is a general purpose transmission chip, on which graphene can be transferred and studied with several techniques. The used substrate is high resistivity silicon, which is transparent to infrared and terahertz radiation, and hence can be used to perform measurements on graphene at these frequencies in transmission. In addition, the chip has a top layer of silicon oxide (300 nm), which can be used to gate graphene tuning its conductivity. The chip is double side polished, to be compatible with optical measurement.

Figure A.1 illustrates the fabrication process of the transmission chip (additional details about the chip layout are given in the remaining chapters of the thesis). The starting substrate is a silicon high resistivity wafer purchased from Topsil Semiconducting Materials A/S with resistivity $\rho > 10\text{k}\Omega\text{cm}^{-1}$, thickness $525\ \mu\text{m}$, diameter 10 cm and $\langle 100 \rangle$ crystalline orientation (Figure A.1a). The wafer is first cleaned using a standard full RCA cleaning composed of three steps:

- **RCA1**: Solution of 5 parts of DI (deionized) water, 1 part of NH_4OH and 1 part of hydrogen peroxide H_2O_2 at 80° to remove organic impurities.
- **HF**: Solution of hydrofluoric acid HF and DI water 1:10 at room temperature to strip

Appendix A. Micro-nano fabrication of graphene devices

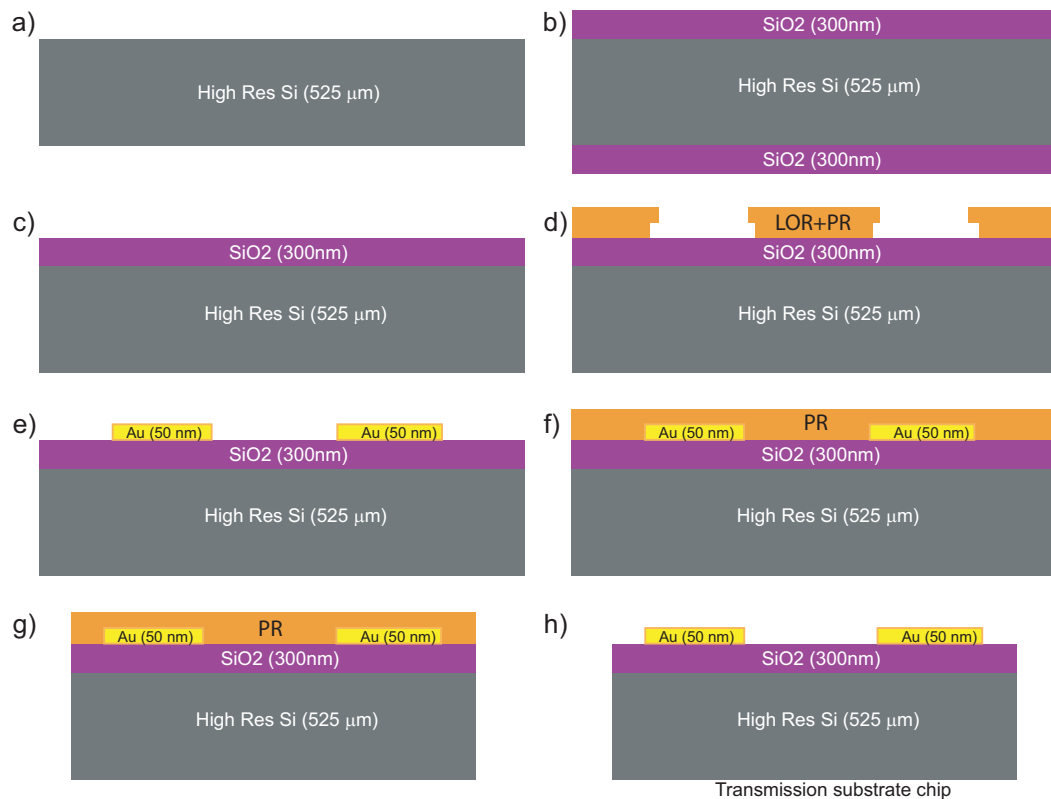


Figure A.1 – Process flow for THz/IR transmission chip. a) Initial high resistivity wafer. b) Dry oxidation c) Backside cleaning

native silicon oxide.

- **RCA2:** Solution of 6 parts of DI water, 1 part of hydrochloric acid HCl and 1 part of hydrogen peroxide H₂O₂ at 80° to remove metal contaminants.
- **SRD:** Spin rinse and dry (SRD) with deionized water.

Subsequently the wafer is dry-oxidized (Figure A.1b) at 1050 ° in a Centrotherm furnace until the gate oxide reaches a thickness of approximately 300 nm (actual thickness 275 nm). The oxide on the backside of the wafer is then etched (Figure A.1c) in an SPTS Advanced Plasma System (APS) module, to allow the possibility of contacting the silicon below to bias graphene.

Metal patterns are defined using a lift-off process with optical lithography. First the wafer is coated with a layer of LOR (lift-off resist) followed by a layer of AZ 1512 HS positive resist, using an EVG 150 automatic resist processing cluster. The wafer is exposed using a chrome mask (written using a DWL200 laser writing system) on a Süss MA6 UV exposure tool and developed in the EVG 150 (Figure A.1d). The LOR layer is underetched in the development, thus facilitating the lift-off. 50 nm of gold (after 5 nm of Cr for adhesion) are then evaporated on the wafer using a Leybold Optics LAB 600H ebeam evaporator. This evaporator is optimized for lift-off processes, and hence the ion beam is very directional preventing the deposition of metal on the photoresist edge. The lift-off is performed in Microposit remover 1165 for 48

A.2. Devices based on THz/IR silicon transmission substrate

hours and ultrasonication is performed if needed to help the release of the metal residues. The wafer is rinsed in IPA (isopropyl alcohol) and SRD is performed (Figure A.1e).

The wafer is coated with a layer of protective photo-resist using the EVG 150 (Figure A.1f) and dicing is performed using a DISCO DAD321 automatic dicer (Figure A.1g) and the chips are then cleaned from photoresist in a with Remover 1156 (two baths at 75° , coarse rinse followed by ultra-clean bath) and the final chips are dried (Figure A.1g).

A.2.2 Infrared and terahertz characterization of graphene

The substrates can be used as they are to study graphene at terahertz and infrared frequencies (Figure A.2). Graphene is transferred by external partners (Graphenea Inc. and Ferrari's Group at Cambridge University). Graphene is first grown using chemical vapor deposition (CVD) on a copper foil using a mixture of H₂ and CH₄ at approximately 1000C. Polymethyl methacrylate (PMMA) is spin coated on graphene and then the copper is chemically dissolved. Graphene is then transferred on the chip and, subsequently, the PMMA is dissolved in acetone and the chip is rinsed. The chip can then be used to characterize graphene at THz or to study the induced Faraday rotation. Metal contacts allows the study of DC conductivity (transport experiment) including electrostatic and magnetostatic bias.

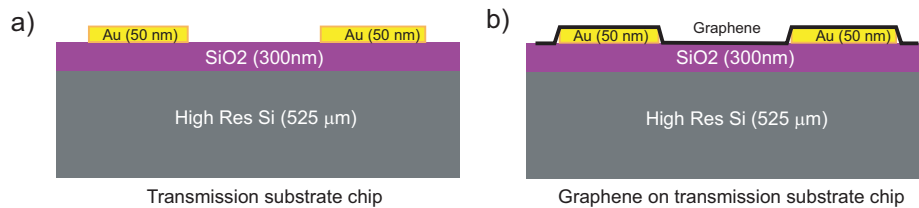


Figure A.2 – Process flow for graphene transfer. a) initial transmission chip. b) graphene transfer.

A.2.3 Magnetoplasmonic enhanced Faraday rotator

The magneto plasmonic Faraday rotators (fabricated but not yet characterized) have been manufactured starting with a transmission substrate chip (Figure A.3a) onto which graphene has been transferred (Figure A.3b). The graphene is then patterned using a standard e-beam process. First, the chip is dehydrated on a hot plate (200°) for 5 minutes. Then PMMA or ZEP resist are spin coated on graphene and the chip is baked for 5 minutes. E-beam exposure is done with doses from 600 to 1200 μCcm^{-2} with PMMA and from 180 to 280 μCcm^{-2} with ZEP. PMMA is developed in MiBK:IPA 1:3 for 1 minute and rinsed in IPA for 1 minute, while ZEP is developed in amyl-acetate for 1 minute and rinsed in 90:10 MiBK:IPA for 1 minute (Figure A.3c). Graphene was then dry-etched in oxygen plasma in an Alcatel 601 E system (Figure A.3d). The e-beam resist is then stripped in acetone. For PMMA stripping is easy and requires only 1 hour in acetone (followed by IPA rinse). ZEP is usually stripped with oxygen plasma or with specific solvents. However both these options damage or destroy graphene. Hence acetone is used, and to ensure complete removal of the resist the chip is first placed in acetone

Appendix A. Micro-nano fabrication of graphene devices

at 45° for 1 hour and then in acetone at room temperature for two days. The chip is then rinsed in IPA (Figure A.3e).

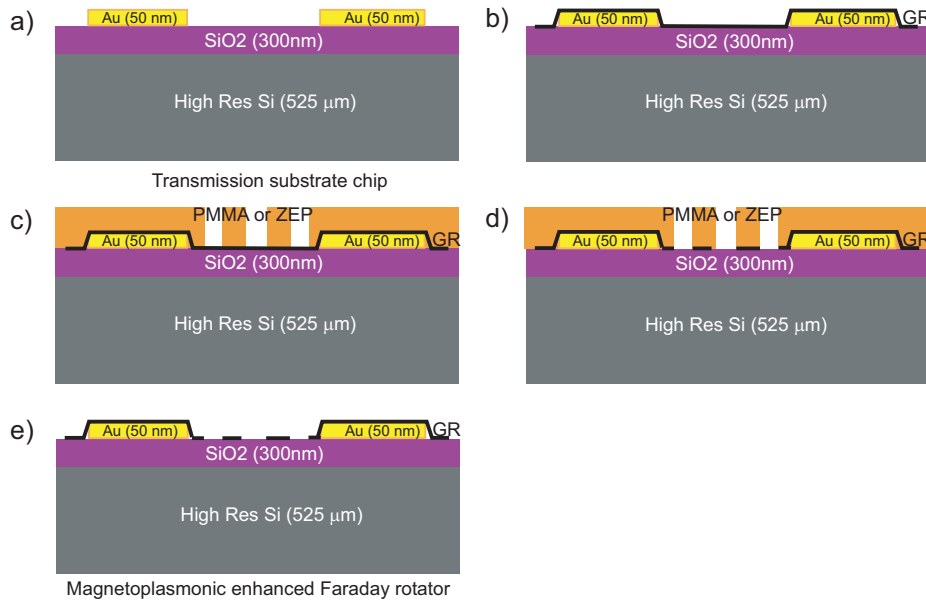


Figure A.3 – Process flow for graphene Magnetoplasmonic enhanced Faraday rotator. a) initial transmission chip. b) graphene transfer. c) PMMA or ZEP coating, ebeam exposure and development. d) Oxygen plasma etching. e) PMMA or ZEP stripping

A.2.4 Ring resonators enhanced Faraday rotator

The magneto plasmonic Faraday rotators (fabricated but not yet characterized) have been manufactured starting with a transmission substrate chip (Figure A.3a). Because the patterns are too small for optical lithography, they have been created using an e-beam lift-off process. First the chip is dehydrated for 5 min on a hot plate, then MMA is spin coated on the chip and baked for 5 minutes. Subsequently PMMA is spin coated and baked for 5 minutes. After e-beam exposure and development (same process of single PMMA layer), the MMA is under-etched, allowing easier lift-off (Figure A.3b). The chips cannot be evaporated directly, because of residues at the bottom of the windows in the resist. A de-scum step is required to improve metal adhesion (10 seconds in oxygen plasma in a Tepla Gigabatch). This de-scum step is required whenever PMMA - MMA lift-off is used. 50 nm of gold are then evaporated and lift-off is performed in acetone for two days. Chips are then rinsed in acetone (Figure A.3c). Graphene is then transferred on the substrate. Graphene (produced by Graphenea) does not break, allowing to conformally cover the gold patterns (Figure A.3d).

A.3. Reflection substrate based on SOI silicon device layer

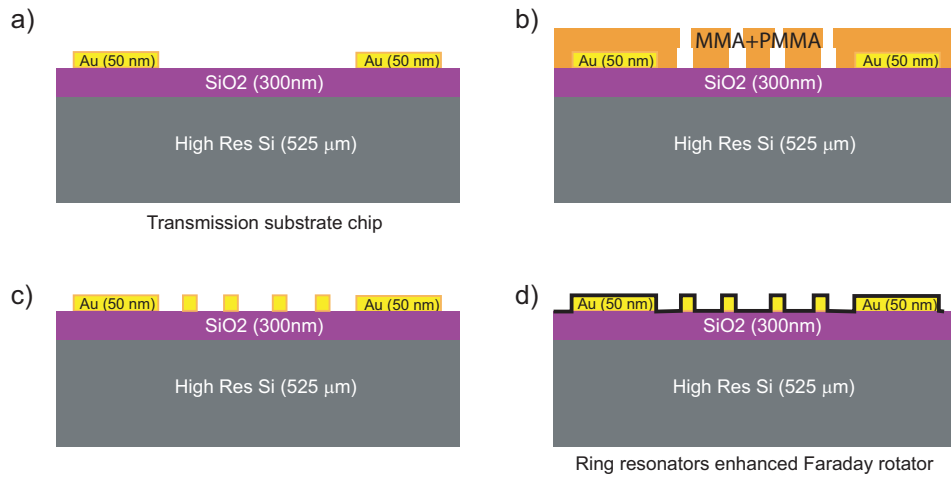


Figure A.4 – Process flow for Ring resonators enhanced Faraday rotator. a) initial transmission chip. b) MMA + PMMA coating, ebeam exposure and development. c) de-scum and gold evaporation and lift-off. d) graphene transfer.

A.3 Reflection substrate based on SOI silicon device layer

A.3.1 Introduction

Several devices developed in this thesis use a reflection stack based on a thin silicon layer bonded to a metallic retro reflector. These chips are fabricated by metallizing and bonding and SOI (Silicon on Insulator) wafer to a pyrex one, removing subsequently the handle and box layer of the SOI wafer. We developed two processes to obtain this result. The first one uses parylene bonding and was developed by Dr Clara Moldovan (EPFL, Nanolab). The second, developed by the PhD candidate, based on anodic bonding.

The parylene process is illustrated in Figure A.5. The starting substrate is an SOI wafer (Figure A.5a) with device layer of 10 to 25 μm , high resistivity silicon ($\rho > 1\text{k}\Omega\text{cm}^{-1}$), SiO_2 box layer and silicon handle layer. A layer of 200 nm of platinum is evaporated on the device layer (Figure A.5b). Then parylene is spin coated on a pyrex wafer and used as a glue to bond it to the device layer, using a Süss Substrate Bonder SB6. (Figure A.5c). The device layer is then removed by a first grinding (Figure A.5d) followed by dry etching in an Adixen AMS200 Etcher (Figure A.5e). Importantly, this process does not affect the device layer, that is protected by the SiO_2 box. Another dry etching step in the SPTS Advanced Plasma System (APS) module eliminates the box layer without affecting the device layer (Figure A.5f). Wafer is cleaned in SRD and an ALD Al_2O_3 layer is deposited (Figure A.5g) with a Beneq TFS200 system. A protective photoresist layer is spin coated (Figure A.5h) and the wafer is diced (Figure A.5i). The final chips are cleaned in Microposit remover 1165 (Figure A.5j).

Figure A.6 shows a FIB section of the parylene bonded reflection substrate.

Appendix A. Micro-nano fabrication of graphene devices

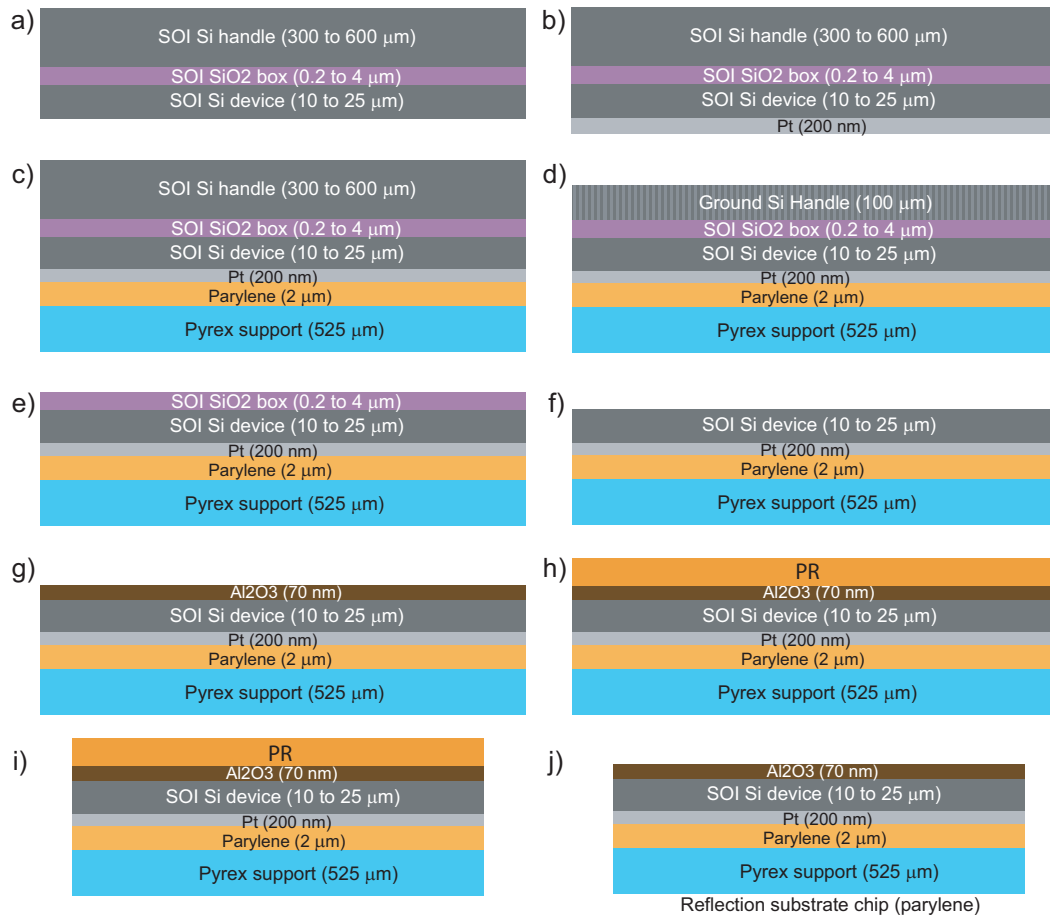


Figure A.5 – Process flow for reflection substrates (parylene bonding). a) initial SOI wafer. b) evaporation of 200 nm of platinum c) parylene coating and parylene bonding with pyrex support. d) grinding of handle layer. e) dry etching of remaining handle layer. f) dry etching of SiO₂ box. g) ALD deposition of Al₂O₃ h) protective photoresist coating. i) dicing. j) resist strip

The anodic bonding process is illustrated in Figure A.7. The starting SOI wafer (Figure A.7a) is evaporated with a layer of 140 nm of silver followed by 60nm of aluminum (Figure A.7b). For both layers an adhesion layer of 5 nm of chromium is used. Anodic bonding is performed between aluminum and pyrex using a Süss Substrate Bonder SB6 (Figure A.7c). The device layer is then removed by grinding (Figure A.7d) followed by dry etching (Figure A.7e). The box layer is removed with a bath of 49% HF which does not attack silicon(Figure A.7f). Importantly, the use of buffered oxide etch is to be avoided as it attacks aluminum potentially infiltrating the bonding. HF 49% also attacks aluminum, but at a much slower rate, so that it has no effect on the bonding. A protective photoresist layer is spin coated (Figure A.7g) and the wafer is diced (Figure A.7h). The final chips are cleaned in Microposit remover 1165 (Figure A.7i).

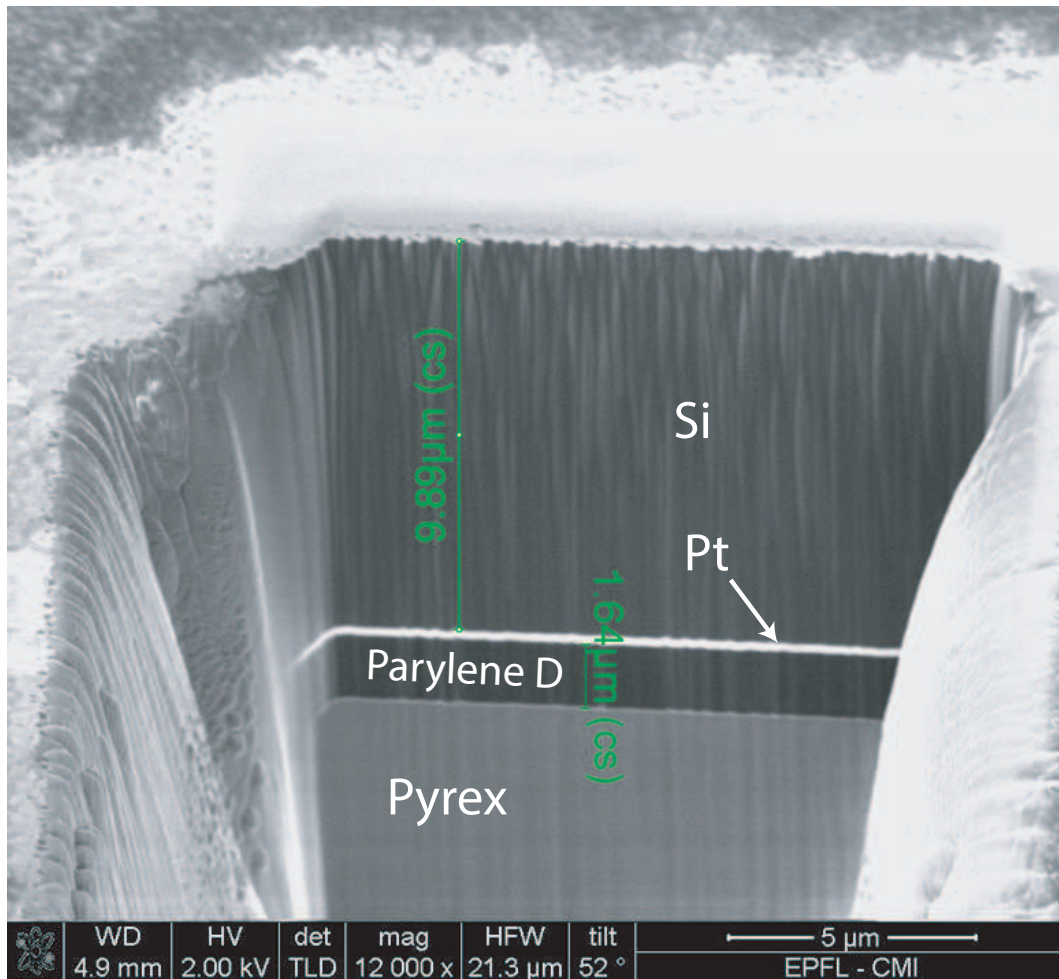


Figure A.6 – FIB section of reflection substrate

A.3.2 Graphene terahertz isolator

The fabrication of the terahertz isolator consists simply in transferring three layers of graphene (keeping the PMMA support layer) on the reflection stack (Figure A.8, performed by Graphenea Inc).

A.3.3 Fabry Perot based measurement of graphene conductivity

The measurement of complex conductivity of graphene is performed using a reflection substrate created with anodic bonding (although also parylene bonded chips have been tested successfully). Figure A.9 illustrate the sample preparation process. The reflection substrate chips (Figure A.9a) so not have an oxide gate, and after the resist stripping they might have organic contaminants. RCA1 cleaning is then very important prior to the subsequent ALD step (Figure A.9b) depositing 72 nm of Al_2O_3 . Graphene can be transferred (Figure A.9c) and optionally patterned (Figures A.9d,A.9e).

Appendix A. Micro-nano fabrication of graphene devices

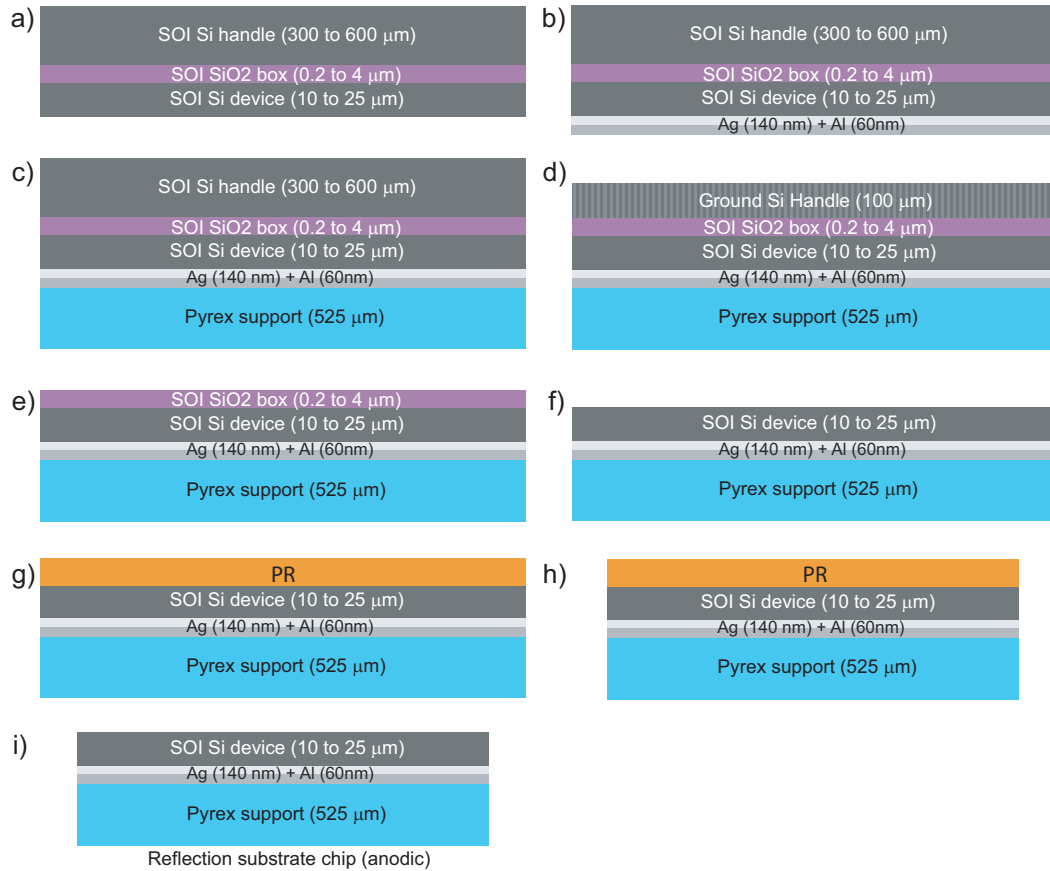


Figure A.7 – Process flow for reflection substrates (anodic bonding). a) initial SOI wafer. b) evaporation of 140 nm of silver and 60 nm of aluminum c) anodic bonding with pyrex support. d) grinding of handle layer. e) dry etching of remaining handle layer. f) wet HF etching of SiO₂ box. g) protective photoresist coating. h) dicing. i) resist strip and RCA1 cleaning

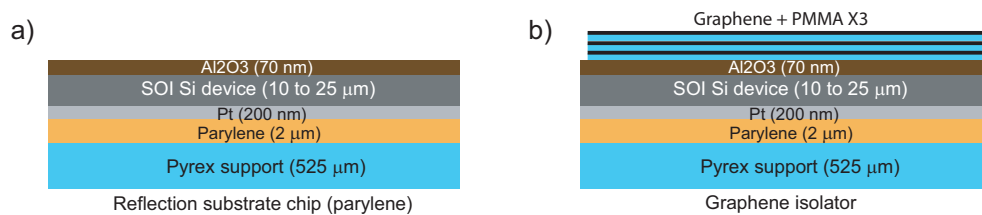


Figure A.8 – Process flow for the isolator. a) Initial reflection chip with parylene bonding and ALD Al₂O₃. b) transfer of three graphene layers keeping PMMA in between (by Graphenea)

A.3.4 Fixed beam terahertz multiband reflectarray

For the fixed beam reflectarray, no gate oxide is required, and the metal patterns are created using the usual e-beam lift-off process with 160 nm of silver, followed by 35 nm of gold. A chromium layer of 5 nm is used for adhesion (Figure A.10)

A.3. Reflection substrate based on SOI silicon device layer

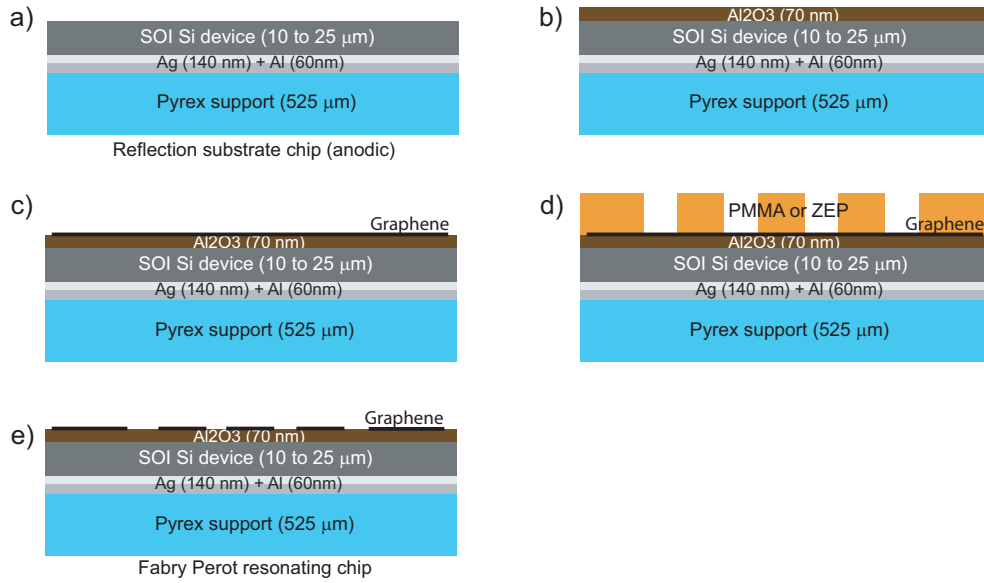


Figure A.9 – Process flow for Fabry Perot resonant chip. a) Initial reflection chip with anodic bonding. b) ALD deposition of Al_2O_3 . c) Graphene transfer. d) PMMA or ZEP coating, e-beam exposure and development. e) Graphene etching in oxygen plasma and resist strip.

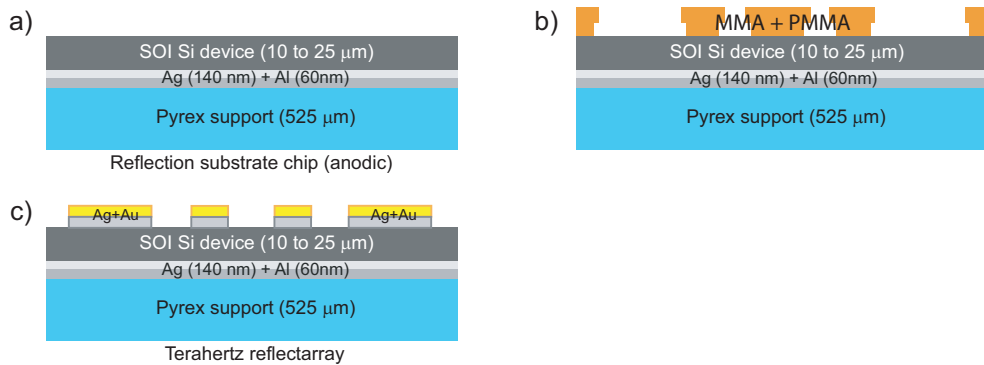


Figure A.10 – Process flow for the fixed beam terahertz multiband reflectarray. a) Initial reflection chip (anodic bonding). b) MMA + PMMA resist spin coat, ebeam exposure and developing. c) De-scum and silver (160 nm) and gold (35 nm) evaporation and liftoff in acetone

A.3.5 Graphene terahertz reflectarray

The graphene reflectarray is the most complex fabrication process presented in this thesis (Figure A.11). The initial reflection substrate with anodic bonding (Figure A.11a) is cleaned and a layer of ALD Al_2O_3 is deposited to form a gate oxide layer (Figure A.11b). Gold patterns are defined with e-beam liftoff (Figure A.11c, A.11d). Graphene is transferred and patterned using e-beam lithography with PMMA (Figure A.11e, A.11f, A.11g). The final chip is then glued wire-bonded to a printed circuit board (PCB).

Appendix A. Micro-nano fabrication of graphene devices

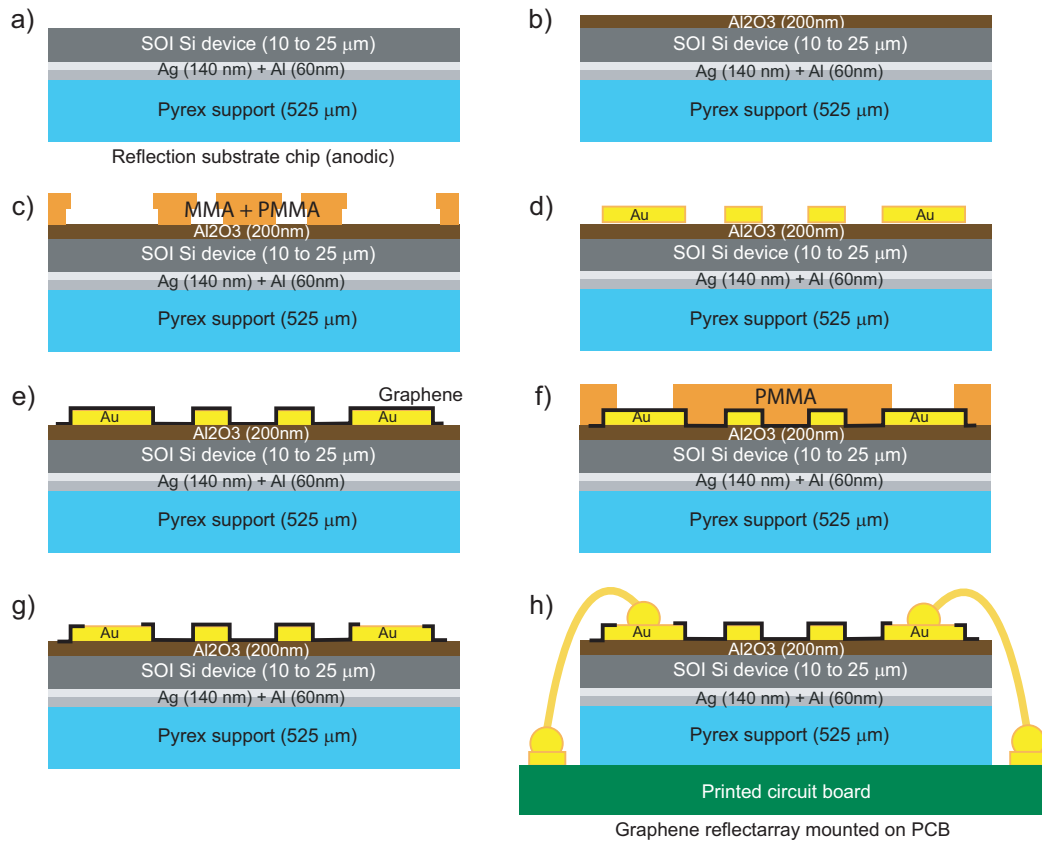


Figure A.11 – Process flow for graphene terahertz reflectarray. a) Initial reflection chip (anodic bonding). b) ALD deposition of Al_2O_3 . c) MMA + PMMA resist spin coat, ebeam exposure and developing. d) De-scum and gold (100 nm) evaporation and lift-off. e) Graphene transfer. f) PMMA coating, e-beam exposure and development, g) Graphene etching in oxygen plasma and resist strip. h) Chip gluing on the PCB and wirebonding.

Bibliography

- [1] I. F. Akyildiz, J. M. Jornet, and C. Han. Terahertz band: Next frontier for wireless communications. *Physical Communication*, 12:16–32, 2014.
- [2] S. Bae, H. Kim, Y. Lee, X. Xu, J.-S. Park, Y. Zheng, J. Balakrishnan, T. Lei, H. R. Kim, Y. I. Song, et al. Roll-to-roll production of 30-inch graphene films for transparent electrodes. *Nature nanotechnology*, 5(8):574–578, 2010.
- [3] D. B. Bennett, Z. D. Taylor, P. Tewari, R. S. Singh, M. O. Culjat, W. S. Grundfest, D. J. Sassoon, R. D. Johnson, J.-P. Hubschman, and E. R. Brown. Terahertz sensing in corneal tissues. *Journal of biomedical optics*, 16(5):057003–057003, 2011.
- [4] B. J. Bohn, M. Schnell, M. A. Kats, F. Aieta, R. Hillenbrand, and F. Capasso. Near-field imaging of phased array metasurfaces. *Nano Letters*, 15(6):3851–3858, 2015.
- [5] F. Bonaccorso, Z. Sun, T. Hasan, and A. C. Ferrari. Graphene photonics and optoelectronics. *Nat Photon*, 4(9):611–622, 2010. 10.1038/nphoton.2010.186.
- [6] H. Cao, Q. Yu, R. Colby, D. Pandey, C. Park, J. Lian, D. Zemlyanov, I. Childres, V. Drachev, E. A. Stach, et al. Large-scale graphitic thin films synthesized on ni and transferred to insulators: Structural and electronic properties. *Journal of Applied Physics*, 107(4):044310, 2010.
- [7] E. Carrasco, M. Arrebola, J. A. Encinar, and M. Barba. Demonstration of a shaped beam reflectarray using aperture-coupled delay lines for lmds central station antenna. *Antennas and Propagation, IEEE Transactions on*, 56(10):3103–3111, 2008.
- [8] E. Carrasco, M. Barba, and J. Encinar. Aperture-coupled reflectarray element with wide range of phase delay. *Electron. Lett*, 42(12):667–668, 2006.
- [9] E. Carrasco, M. Barba, and J. A. Encinar. Reflectarray element based on aperture-coupled patches with slots and lines of variable length. *Antennas and Propagation, IEEE Transactions on*, 55(3):820–825, 2007.
- [10] E. Carrasco, M. Barba, and J. A. Encinar. X-band reflectarray antenna with switching-beam using pin diodes and gathered elements. *Antennas and Propagation, IEEE Transactions on*, 60(12):5700–5708, 2012.

Bibliography

- [11] E. Carrasco, M. Barba, B. Reig, C. Dieppedale, and J. A. Encinar. Characterization of a reflectarray gathered element with electronic control using ohmic rf mems and patches aperture-coupled to a delay line. *Antennas and Propagation, IEEE Transactions on*, 60(9):4190–4201, 2012.
- [12] E. Carrasco, J. A. Encinar, and M. Barba. Bandwidth improvement in large reflectarrays by using true-time delay. *Antennas and Propagation, IEEE Transactions on*, 56(8):2496–2503, 2008.
- [13] E. Carrasco and J. Perruisseau-Carrier. Reflectarray antenna at terahertz using graphene. *Antennas and Wireless Propagation Letters, IEEE*, 12:253–256, 2013.
- [14] A. H. Castro Neto, F. Guinea, N. M. R. Peres, K. S. Novoselov, and A. K. Geim. The electronic properties of graphene. *Reviews of Modern Physics*, 81(1):109–162, 2009. RMP.
- [15] S. Chakraborty, O. P. Marshall, T. G. Folland, Y.-J. Kim, A. N. Grigorenko, and K. S. Novoselov. Gain modulation by graphene plasmons in aperiodic lattice lasers. *Science*, 351(6270):246–248, 2016.
- [16] N. Chamanara, D. Sounas, and C. Caloz. Non-reciprocity with graphene magnetoplasmons and application to plasmonic isolators. In *Electromagnetic Theory (EMTS), Proceedings of 2013 URSI International Symposium on*, pages 266–268. IEEE, 2013.
- [17] Y.-C. Chang, C.-H. Liu, C.-H. Liu, Z. Zhong, and T. B. Norris. Extracting the complex optical conductivity of mono- and bilayer graphene by ellipsometry. *Applied Physics Letters*, 104(26):261909, 2014.
- [18] E. Collett. *Field Guide to Polarization*. Field Guide Series. Society of Photo Optical, 2005.
- [19] K. B. Cooper, R. J. Dengler, N. Llombart, A. Talukder, A. V. Panangadan, C. S. Peay, I. Mehdi, and P. H. Siegel. Fast high-resolution terahertz radar imaging at 25 meters. In *SPIE Defense, Security, and Sensing*, volume 7671, pages 76710Y–76710Y–8, 2010. 10.1117/12.850395.
- [20] K. B. Cooper, R. J. Dengler, N. Llombart, B. Thomas, G. Chattopadhyay, and P. H. Siegel. Thz imaging radar for standoff personnel screening. *Terahertz Science and Technology, IEEE Transactions on*, 1(1):169–182, 2011.
- [21] I. Crassee, J. Levallois, A. L. Walter, M. Ostler, A. Bostwick, E. Rotenberg, T. Seyller, D. van der Marel, and A. B. Kuzmenko. Giant faraday rotation in single- and multilayer graphene. *Nat Phys*, 7(1):48–51, 2011. 10.1038/nphys1816.
- [22] I. Crassee, M. Orlita, M. Potemski, A. L. Walter, M. Ostler, T. Seyller, I. Gaponenko, J. Chen, and A. B. Kuzmenko. Intrinsic terahertz plasmons and magnetoplasmons in large scale monolayer graphene. *Nano Letters*, 12(5):2470–2474, 2012.

-
- [23] J. Dash, S. Ray, K. Nallappan, V. Kaware, N. Basutkar, R. G. Gonnade, A. V. Ambade, K. Joshi, and B. Pesala. Terahertz spectroscopy and solid-state density functional theory calculations of cyanobenzaldehyde isomers. *The Journal of Physical Chemistry A*, 119(29):7991–7999, 2015.
- [24] A. R. Davoyan, A. M. Mahmoud, and N. Engheta. Optical isolation with epsilon-near-zero metamaterials. *Optics Express*, 21(3):3279–3286, 2013.
- [25] A. Fallahi and C. Hafner. Analysis of semi-infinite periodic structures using a domain reduction technique. *JOSA A*, 27(1):40–49, 2010.
- [26] A. Fallahi, M. Mishrikey, C. Hafner, and R. Vahldieck. Analysis of multilayer frequency selective surfaces on periodic and anisotropic substrates. *Metamaterials*, 3(2):63–74, 2009.
- [27] A. Fallahi and J. Perruisseau-Carrier. Design of tunable biperiodic graphene metasurfaces. *Physical Review B*, 86(19):195408, 2012. PRB.
- [28] A. Fallahi and J. Perruisseau-Carrier. Manipulation of giant faraday rotation in graphene metasurfaces. *Applied Physics Letters*, 101(23):231605–4, 2012.
- [29] A. Fallahi, A. Yahaghi, H. Abiri, M. Shahabadi, and C. Hafner. Large overlapping subdomain method of moments for the analysis of frequency selective surfaces. *Microwave Theory and Techniques, IEEE Transactions on*, 58(8):2175–2187, 2010.
- [30] T. Fang, A. Konar, H. Xing, and D. Jena. Carrier statistics and quantum capacitance of graphene sheets and ribbons. *Applied Physics Letters*, 91(9):092109, 2007.
- [31] J. F. Federici, B. Schulkin, F. Huang, D. Gary, R. Barat, F. Oliveira, and D. Zimdars. Thz imaging and sensing for security applications—explosives, weapons and drugs. *Semiconductor Science and Technology*, 20(7):S266, 2005.
- [32] A. C. Ferrari and D. M. Basko. Raman spectroscopy as a versatile tool for studying the properties of graphene. *Nature nanotechnology*, 8(4):235–246, 2013.
- [33] A. C. Ferrari, F. Bonaccorso, V. Fal’Ko, K. S. Novoselov, S. Roche, P. Bøggild, S. Borini, F. H. Koppens, V. Palermo, N. Pugno, et al. Science and technology roadmap for graphene, related two-dimensional crystals, and hybrid systems. *Nanoscale*, 7(11):4598–4810, 2015.
- [34] A. K. Geim and K. S. Novoselov. The rise of graphene. *Nat Mater*, 6(3):183–191, 2007. 10.1038/nmat1849.
- [35] J. S. Gomez-Diaz and J. Perruisseau-Carrier. Graphene-based plasmonic switches at near infrared frequencies. *Opt. Express*, 21(13):15490–15504, 2013.
- [36] I. S. Gregory, C. Baker, W. R. Tribe, I. V. Bradley, M. J. Evans, E. H. Linfield, A. G. Davies, and M. Missous. Optimization of photomixers and antennas for continuous-wave terahertz emission. *Quantum Electronics, IEEE Journal of*, 41(5):717–728, 2005.

Bibliography

- [37] C. Guclu, J. Perruisseau-Carrier, and O. Civi. Proof of concept of a dual-band circularly-polarized rf mems beam-switching reflectarray. *Antennas and Propagation, IEEE Transactions on*, 60(11):5451–5455, 2012.
- [38] C. Guclu, J. Perruisseau-Carrier, and O. A. Civi. Dual frequency reflectarray cell using splitting elements with rf mems switches. In *Antennas and Propagation Society International Symposium (APSURSI), 2010 IEEE*, pages 1–4. IEEE, 2010.
- [39] M. S. Gupta. Power gain in feedback amplifiers, a classic revisited. *Microwave Theory and Techniques, IEEE Transactions on*, 40(5):864–879, 1992.
- [40] V. P. Gusynin and S. G. Sharapov. Transport of dirac quasiparticles in graphene: Hall and optical conductivities. *Physical Review B*, 73(24):245411, 2006. PRB.
- [41] V. P. Gusynin, S. G. Sharapov, and J. P. Carbotte. Magneto-optical conductivity in graphene. *Journal of Physics: Condensed Matter*, 19(2):026222, 2007.
- [42] Y. Hadad, A. R. Davoyan, N. Engheta, and B. Z. Steinberg. Extreme and quantized magneto-optics with graphene meta-atoms and metasurfaces. *ACS Photonics*, 1(10):1068–1073, 2014.
- [43] G. W. Hanson. Dyadic green’s functions and guided surface waves for a surface conductivity model of graphene. *Journal of Applied Physics*, 103(6):064302–8, 2008.
- [44] G. W. Hanson. Dyadic green’s functions for an anisotropic, non-local model of biased graphene. *Antennas and Propagation, IEEE Transactions on*, 56(3):747–757, 2008.
- [45] R. A. Horn and C. R. Johnson. *Matrix analysis*. Cambridge university press, 2012.
- [46] B. F. Hornecker. *Design of novel radiating elements for SATCOM phased arrays in Ku-Band*. PhD thesis, 2016.
- [47] J. Huang and J. Encinar. *Reflectarray Antennas*. IEEE Press Series on Electromagnetic Wave Theory. Wiley, 2007.
- [48] Y. Huang, N. Khiabani, Y. Shen, and D. Li. Terahertz photoconductive antenna efficiency. In *Antenna Technology (iWAT), 2011 International Workshop on*, pages 152–156. IEEE, 2011.
- [49] S. V. Hum and J. Perruisseau-Carrier. Reconfigurable reflectarrays and array lenses for dynamic antenna beam control: A review. *Antennas and Propagation, IEEE Transactions on*, 62(1):183–198, 2014.
- [50] M. Jablan, H. Buljan, and M. Soljagic. Plasmonics in graphene at infrared frequencies. *Physical Review B*, 80(24):245435, 2009. PRB.
- [51] M. Jablan, M. Soljagic, and H. Buljan. Plasmons in graphene: Fundamental properties and potential applications. *Proceedings of the IEEE*, 101(7):1689–1704, 2013.

- [52] P. U. Jepsen, D. G. Cooke, and M. Koch. Terahertz spectroscopy and imaging—modern techniques and applications. *Laser & Photonics Reviews*, 5(1):124–166, 2011.
- [53] L. Ju, B. Geng, J. Horng, C. Girit, M. Martin, Z. Hao, H. A. Bechtel, X. Liang, A. Zettl, Y. R. Shen, and F. Wang. Graphene plasmonics for tunable terahertz metamaterials. *Nat Nano*, 6(10):630–634, 2011. 10.1038/nnano.2011.146.
- [54] E. O. Kamenetskii. Nonreciprocal microwave bianisotropic materials: reciprocity theorem and network reciprocity. *IEEE Transactions on Antennas and Propagation*, 49(3):361–366, Mar 2001.
- [55] I. Kézsmárki, U. Nagel, S. Bordács, R. S. Fishman, J. H. Lee, H. T. Yi, S.-W. Cheong, and T. Rődm. Optical diode effect at spin-wave excitations of the room-temperature multiferroic bifeo 3. *Physical Review Letters*, 115(12):127203, 2015. PRL.
- [56] I. Kezsmarki, D. Szaller, S. Bordacs, V. Kocsis, Y. Tokunaga, Y. Taguchi, H. Murakawa, Y. Tokura, H. Engelkamp, T. Rődm, et al. One-way transparency of four-coloured spin-wave excitations in multiferroic materials. *Nat Commun*, 5, 2014.
- [57] K. S. Kim, Y. Zhao, H. Jang, S. Y. Lee, J. M. Kim, K. S. Kim, J.-H. Ahn, P. Kim, J.-Y. Choi, and B. H. Hong. Large-scale pattern growth of graphene films for stretchable transparent electrodes. *Nature*, 457(7230):706–710, 2009.
- [58] M. Kim, J. Jeong, J. K. Poon, and G. V. Eleftheriades. Vanadium-dioxide-assisted digital optical metasurfaces for dynamic wavefront engineering. *JOSA B*, 33(5):980–988, 2016.
- [59] S. J. Koester and M. Li. High-speed waveguide-coupled graphene-on-graphene optical modulators. *Applied Physics Letters*, 100(17):171107–4, 2012.
- [60] F. H. L. Koppens, T. Mueller, P. Avouris, A. C. Ferrari, M. S. Vitiello, and M. Polini. Photodetectors based on graphene, other two-dimensional materials and hybrid systems. *Nat Nano*, 9(10):780–793, 2014.
- [61] V. Kravets, R. Jalil, Y.-J. Kim, D. Ansell, D. Aznakayeva, B. Thackray, L. Britnell, B. Belle, F. Withers, I. Radko, et al. Graphene-protected copper and silver plasmonics. *Scientific reports*, 4, 2014.
- [62] C. A. Kulesa, M. C. Ashley, Y. Augarten, C. S. Bonner, M. G. Burton, L. Bycroft, J. Lawrence, D. H. Lesser, J. Loomis, D. M. Luong-Van, et al. Opportunities for terahertz facilities on the high plateau. *Proceedings of the International Astronomical Union*, 8(S288):256–263, 2012.
- [63] A. B. Kuzmenko, E. van Heumen, F. Carbone, and D. van der Marel. Universal optical conductance of graphite. *Physical Review Letters*, 100(11):117401, 2008. PRL.
- [64] S. H. Lee, M. Choi, T.-T. Kim, S. Lee, M. Liu, X. Yin, H. K. Choi, S. S. Lee, C.-G. Choi, S.-Y. Choi, X. Zhang, and B. Min. Switching terahertz waves with gate-controlled active graphene metamaterials. *Nat Mater*, 11(11):936–941, 2012. 10.1038/nmat3433.

Bibliography

- [65] X. Lin, Z. Wang, F. Gao, B. Zhang, and H. Chen. Atomically thin nonreciprocal optical isolation. *Sci. Rep.*, 4, 2014.
- [66] M. Liu, X. Yin, E. Ulin-Avila, B. Geng, T. Zentgraf, L. Ju, F. Wang, and X. Zhang. A graphene-based broadband optical modulator. *Nature*, 474(7349):64–67, 2011. 10.1038/nature10067.
- [67] I. Llatser, C. Kremers, A. Cabellos-Aparicio, J. M. Jornet, E. Alarcón, and D. N. Chigrin. Graphene-based nano-patch antenna for terahertz radiation. *Photonics and Nanostructures - Fundamentals and Applications*, 10(4):353–358, 2012.
- [68] I. Llatser, C. Kremers, D. N. Chigrin, J. M. Jornet, M. C. Lemme, A. Cabellos-Aparicio, and E. Alarcon. Characterization of graphene-based nano-antennas in the terahertz band. In *Antennas and Propagation (EUCAP), 2012 6th European Conference on*, pages 194–198. IEEE, 2012.
- [69] G. Lovat, G. W. Hanson, R. Araneo, and P. Burghignoli. Semiclassical spatially dispersive intraband conductivity tensor and quantum capacitance of graphene. *Phys. Rev. B*, 87:115429, Mar 2013.
- [70] Z. Lu and W. Zhao. Nanoscale electro-optic modulators based on graphene-slot waveguides. *J. Opt. Soc. Am. B*, 29(6):1490–1496, 2012.
- [71] H. Lyu, H. Wu, J. Liu, Q. Lu, J. Zhang, X. Wu, J. Li, T. Ma, J. Niu, W. Ren, et al. Double-balanced graphene integrated mixer with outstanding linearity. *Nano letters*, 15(10):6677–6682, 2015.
- [72] A. Martinez and Z. Sun. Nanotube and graphene saturable absorbers for fibre lasers. *Nature Photonics*, 7(11):842–845, 2013.
- [73] S. Mason. Power gain in feedback amplifier. *Circuit Theory, Transactions of the IRE Professional Group on*, CT-1(2):20–25, 1954.
- [74] A. S. Mayorov, R. V. Gorbachev, S. V. Morozov, L. Britnell, R. Jalil, L. A. Ponomarenko, P. Blake, K. S. Novoselov, K. Watanabe, T. Taniguchi, and A. K. Geim. Micrometer-scale ballistic transport in encapsulated graphene at room temperature. *Nano Letters*, 11(6):2396–2399, 2011.
- [75] X. Miao, S. Tongay, M. K. Petterson, K. Berke, A. G. Rinzler, B. R. Appleton, and A. F. Hebard. High efficiency graphene solar cells by chemical doping. *Nano letters*, 12(6):2745–2750, 2012.
- [76] C. F. Moldovan. *Enabling High Frequency Reconfigurable Functions with Graphene*. PhD thesis, 2016.
- [77] C. Montgomery, R. Dicke, and E. Purcell. *Principles of Microwave Circuits*. Electromagnetics and Radar Series. Institution of Engineering & Technology, 1948.

- [78] O. Morikawa, A. Quema, S. Nashima, H. Sumikura, T. Nagashima, and M. Hangyo. Faraday ellipticity and faraday rotation of a doped-silicon wafer studied by terahertz time-domain spectroscopy. *Journal of Applied Physics*, 100(3):033105, 2006.
- [79] P. Nayeri, M. Liang, R. A. Sabory-Garcia, M. Tuo, F. Yang, M. Gehm, H. Xin, and A. Z. Elsherbeni. 3d printed dielectric reflectarrays: low-cost high-gain antennas at sub-millimeter waves. *Antennas and Propagation, IEEE Transactions on*, 62(4):2000–2008, 2014.
- [80] T. Niu, A. Upadhyay, W. Withayachumnankul, D. Headland, D. Abbott, M. Bhaskaran, S. Sriram, and C. Fumeaux. Polarization-dependent thin-film wire-grid reflectarray for terahertz waves. *Applied Physics Letters*, 107(3):031111, 2015.
- [81] T. Niu, W. Withayachumnankul, B. S. Y. Ung, H. Menekse, M. Bhaskaran, S. Sriram, and C. Fumeaux. Experimental demonstration of reflectarray antennas at terahertz frequencies. *Optics Express*, 21(3):2875–2889, 2013.
- [82] T. Niu, W. Withayachumnankul, A. Upadhyay, P. Gutruf, D. Abbott, M. Bhaskaran, S. Sriram, and C. Fumeaux. Terahertz reflectarray as a polarizing beam splitter. *Optics Express*, 22(13):16148–16160, 2014.
- [83] K. S. Novoselov, V. I. Falko, L. Colombo, P. R. Gellert, M. G. Schwab, and K. Kim. A roadmap for graphene. *Nature*, 490(7419):192–200, 2012. [prime] 10.1038/nature11458.
- [84] K. S. Novoselov, A. K. Geim, S. V. Morozov, D. Jiang, Y. Zhang, S. V. Dubonos, I. V. Grigorieva, and A. A. Firsov. Electric field effect in atomically thin carbon films. *Science*, 306(5696):666–669, 2004.
- [85] P. M. Pardalos, A. Migdalas, and L. Pitsoulis. *Pareto optimality, game theory and equilibria*, volume 17. Springer Science & Business Media, 2008.
- [86] A. Y. Pawar, D. D. Sonawane, K. B. Erande, and D. V. Derle. Terahertz technology and its applications. *Drug Invention Today*, 5(2):157–163, 2013.
- [87] J. Perruisseau-Carrier. *Microwave periodic structures based on microelectromechanical systems (MEMS) and micromachining techniques*. PhD thesis, 2007.
- [88] J. Perruisseau-Carrier and A. K. Skrivervik. Monolithic mems-based reflectarray cell digitally reconfigurable over a 360 phase range. *Antennas and Wireless Propagation Letters, IEEE*, 7:138–141, 2008.
- [89] S.-W. Qu, W.-W. Wu, B.-J. Chen, H. Yi, X. Bai, K. B. Ng, and C. H. Chan. Controlling dispersion characteristics of terahertz metasurface. *Scientific reports*, 5, 2015.
- [90] A. Reina, X. Jia, J. Ho, D. Nezich, H. Son, V. Bulovic, M. S. Dresselhaus, and J. Kong. Large area, few-layer graphene films on arbitrary substrates by chemical vapor deposition. *Nano letters*, 9(1):30–35, 2008.

Bibliography

- [91] D. Rodrigo, L. Jofre, and J. Perruisseau-Carrier. Unit cell for frequency-tunable beamscanning reflectarrays. *Antennas and Propagation, IEEE Transactions on*, 61(12):5992–5999, 2013.
- [92] D. Rodrigo, L. Jofre, and J. Perruisseau-Carrier. Unit cell for frequency-tunable beamscanning reflectarrays. *Antennas and Propagation, IEEE Transactions on*, 61(12):5992–5999, 2013.
- [93] D. Rodrigo, O. Limaj, D. Janner, D. Etezadi, F. J. García de Abajo, V. Pruneri, and H. Altug. Mid-infrared plasmonic biosensing with graphene. *Science*, 349(6244):165–168, 2015.
- [94] D. Rodrigo, J. Romeu, S. Capdevila, and L. Jofre. A figure-of-merit for pattern reconfigurable antennas. *Antennas and Propagation, IEEE Transactions on*, 61(3):1448–1453, 2013.
- [95] P. Romano. *Adaptive Millimeter-Wave and THz Antenna Devices Based on Dielectric Elastomer Actuators*. PhD thesis, 2015.
- [96] T. Schaug-pettersen and A. Tonning. On the optimum performance of variable and nonreciprocal networks. *Circuit Theory, IRE Transactions on*, 6(2):150–158, 1959.
- [97] K. Sengupta and A. Hajimiri. A 0.28 thz power-generation and beam-steering array in cmos based on distributed active radiators. *Solid-State Circuits, IEEE Journal of*, 47(12):3013–3031, 2012.
- [98] B. Sensale-Rodriguez, R. Yan, M. M. Kelly, T. Fang, K. Tahy, W. S. Hwang, D. Jena, L. Liu, and H. G. Xing. Broadband graphene terahertz modulators enabled by intraband transitions. *Nat Commun*, 3:780, 2012. 10.1038/ncomms1787.
- [99] M. Shalaby, M. Peccianti, Y. Ozturk, M. Clerici, I. Al-Naib, L. Razzari, T. Ozaki, A. Mazhorova, M. Skorobogatiy, and R. Morandotti. Terahertz faraday rotation in a magnetic liquid: High magneto-optical figure of merit and broadband operation in a ferrofluid. *Applied Physics Letters*, 100(24):241107, 2012.
- [100] M. Shalaby, M. Peccianti, Y. Ozturk, and R. Morandotti. A magnetic non-reciprocal isolator for broadband terahertz operation. *Nat Commun*, 4:1558, 2013. 10.1038/ncomms2572.
- [101] A. M. Shuvaev, G. V. Astakhov, A. Pimenov, C. Brüne, H. Buhmann, and L. W. Molenkamp. Giant magneto-optical faraday effect in hgte thin films in the terahertz spectral range. *Physical Review Letters*, 106(10):107404, 2011. PRL.
- [102] A. Sihvola and S. Zouhdi. *Metamaterials and Plasmonics: Fundamentals, Modelling, Applications*. Springer Netherlands, Dordrecht, 2009.
- [103] H. S. Skulason, D. L. Sounas, F. Mahvash, S. Francoeur, M. Sijaj, C. Caloz, and T. Szkopek. Field effect tuning of microwave faraday rotation and isolation with large-area graphene. *Applied Physics Letters*, 107(9):093106, 2015.

- [104] C. Someda. *Electromagnetic Waves, Second Edition*. CRC Press, 2006.
- [105] D. Sounas and C. Caloz. *Novel Electromagnetic Phenomena in Graphene and Subsequent Microwave Devices Enabled by Multi-Scale Metamaterials*. INTECH Open Access Publisher, 2012.
- [106] D. L. Sounas and C. Caloz. Graphene-based non-reciprocal spatial isolator. In *Antennas and Propagation (APSURSI), 2011 IEEE International Symposium on*, pages 1597–1600. IEEE, 2011.
- [107] D. L. Sounas and C. Caloz. Gyrotropy and nonreciprocity of graphene for microwave applications. *Microwave Theory and Techniques, IEEE Transactions on*, 60(4):901–914, 2012.
- [108] D. L. Sounas, H. S. Skulason, H. V. Nguyen, A. Guermoune, M. Siaj, T. Szkopek, and C. Caloz. Faraday rotation in magnetically biased graphene at microwave frequencies. *Applied Physics Letters*, 102(19):191901–4, 2013.
- [109] P. Tassin, T. Koschny, M. Kafesaki, and C. M. Soukoulis. A comparison of graphene, superconductors and metals as conductors for metamaterials and plasmonics. *Nat Photon*, 6(4):259–264, 2012. 10.1038/nphoton.2012.27.
- [110] N. Ubrig, I. Crassee, J. Levallois, I. O. Nedoliuk, F. Fromm, M. Kaiser, T. Seyller, and A. B. Kuzmenko. Fabry-perot enhanced faraday rotation in graphene. *Optics Express*, 21(21):24736–24741, 2013.
- [111] B. Vasić and R. Gajić. Tunable fabry-perot resonators with embedded graphene from terahertz to near-infrared frequencies. *Optics Letters*, 39(21):6253–6256, 2014.
- [112] L. Vicarelli, M. S. Vitiello, D. Coquillat, A. Lombardo, A. C. Ferrari, W. Knap, M. Polini, V. Pellegrini, and A. Tredicucci. Graphene field-effect transistors as room-temperature terahertz detectors. *Nat Mater*, advance online publication, 2012. 10.1038/nmat3417.
- [113] A. T. Villeneuve and R. E. Harrington. Reciprocity relationships for gyrotropic media. *IRE Transactions on Microwave Theory and Techniques*, 6(3):308–310, July 1958.
- [114] W. A. Vitale. *Reconfigurable electronics based on metal-insulator transition: steep-slope switches and high frequency functions enabled by Vanadium Dioxide*. PhD thesis, 2016.
- [115] M. Wang, Y. Wang, M. Pu, C. Hu, X. Wu, Z. Zhao, and X. Luo. Circular dichroism of graphene-based absorber in static magnetic field. *Journal of Applied Physics*, 115(15):-, 2014.
- [116] Y. Wang, E. Plummer, and K. Kempa. Foundations of plasmonics. *Advances in Physics*, 60(5):799–898, 2011.
- [117] D. Wintz, P. Genevet, A. Ambrosio, A. Woolf, and F. Capasso. Holographic metalens for switchable focusing of surface plasmons. *Nano Letters*, 15(5):3585–3589, 2015.

Bibliography

- [118] C. Wolff, R. Rodríguez-Oliveros, and K. Busch. Simple magneto–optic transition metal models for time–domain simulations. *Optics Express*, 21(10):12022–12037, 2013.
- [119] Y. Wu, Y.-m. Lin, A. A. Bol, K. A. Jenkins, F. Xia, D. B. Farmer, Y. Zhu, and P. Avouris. High-frequency, scaled graphene transistors on diamond-like carbon. *Nature*, 472(7341):74–78, 2011.
- [120] C. Xu, Y. Jin, L. Yang, J. Yang, and X. Jiang. Characteristics of electro-refractive modulating based on graphene-oxide-silicon waveguide. *Opt. Express*, 20(20):22398–22405, 2012.
- [121] A. Yahaghi, A. Fallahi, H. Abiri, M. Shahabadi, C. Hafner, and R. Vahldieck. Analysis of frequency selective surfaces on periodic substrates using entire domain basis functions. *Antennas and Propagation, IEEE Transactions on*, 58(3):876–886, 2010.
- [122] H. Yan, T. Low, W. Zhu, Y. Wu, M. Freitag, X. Li, F. Guinea, P. Avouris, and F. Xia. Damping pathways of mid-infrared plasmons in graphene nanostructures. *Nat Photon*, 7(5):394–399, 2013.
- [123] Y. Yao, M. A. Kats, P. Genevet, N. Yu, Y. Song, J. Kong, and F. Capasso. Broad electrical tuning of graphene-loaded plasmonic antennas. *Nano Letters*, 13(3):1257–1264, 2013.
- [124] Y. Yao, M. A. Kats, R. Shankar, Y. Song, J. Kong, M. Loncar, and F. Capasso. Wide wavelength tuning of optical antennas on graphene with nanosecond response time. *Nano Letters*, 14(1):214–219, 2014.
- [125] Y. Yao, R. Shankar, M. A. Kats, Y. Song, J. Kong, M. Loncar, and F. Capasso. Electrically tunable metasurface perfect absorbers for ultrathin mid-infrared optical modulators. *Nano Letters*, 14(11):6526–6532, 2014.
- [126] Y. Yao, R. Shankar, P. Rauter, Y. Song, J. Kong, M. Loncar, and F. Capasso. High-responsivity mid-infrared graphene detectors with antenna-enhanced photocarrier generation and collection. *Nano Letters*, 14(7):3749–3754, 2014.
- [127] C. Yu, S. Fan, Y. Sun, and E. Pickwell-MacPherson. The potential of terahertz imaging for cancer diagnosis: A review of investigations to date. *Quantitative imaging in medicine and surgery*, 2(1):33–45, 2012.
- [128] N. Yu and F. Capasso. Flat optics with designer metasurfaces. *Nat Mater*, 13(2):139–150, 2014.
- [129] N. Yu, P. Genevet, M. A. Kats, F. Aieta, J.-P. Tetienne, F. Capasso, and Z. Gaburro. Light propagation with phase discontinuities: Generalized laws of reflection and refraction. *Science*, 334(6054):333–337, 2011.
- [130] S. Zanutto, F. Morichetti, and A. Melloni. Fundamental limits on the losses of phase and amplitude optical actuators. *Laser & Photonics Reviews*, pages n/a–n/a, 2015.

- [131] L. Zou, W. Withayachumnankul, C. M. Shah, A. Mitchell, M. Bhaskaran, S. Sriram, and C. Fumeaux. Dielectric resonator nanoantennas at visible frequencies. *Optics express*, 21(1):1344–1352, 2013.

Journal Articles

- [JA1] E. Carrasco, M. Tamagnone, J. R. Mosig, T. Low, and J. Perruisseau-Carrier. Gate-controlled mid-infrared light bending with aperiodic graphene nanoribbons array. *Nanotechnology*, 26(13):134002, 2015.
- [JA2] E. Carrasco, M. Tamagnone, and J. Perruisseau-Carrier. Tunable graphene reflective cells for thz reflectarrays and generalized law of reflection. *Applied Physics Letters*, 102(10):104103–4, 2013.
- [JA3] A. Fallahi, T. Low, M. Tamagnone, and J. Perruisseau-Carrier. Nonlocal electromagnetic response of graphene nanostructures. *Physical Review B*, 91(12):121405, 2015. PRB.
- [JA4] H. Hasani, M. Tamagnone, S. C. Cascante, C. F. Moldovan, P. Maoddi, A. M. Ionescu, C. Peixeiro, J. R. Mosig, A. K. Skrivervik, and J. Perruisseau-Carrier. Tri-band, polarization-independent reflectarray at terahertz frequencies: Design, fabrication, and measurement. *Terahertz Science and Technology, IEEE Transactions on*, PP(99):1–10, 2016.
- [JA5] C. F. Moldovan, W. A. Vitale, P. Sharma, M. Tamagnone, J. R. Mosig, and A. M. Ionescu. Graphene quantum capacitors for high frequency tunable analog applications. *Accepted in Nanoletters*, 2016.
- [JA6] M. Tamagnone, C. Craeye, and J. Perruisseau-Carrier. Comment on encoding many channels on the same frequency through radio vorticity: first experimental test. *New Journal of Physics*, 14(11):118001, 2012.
- [JA7] M. Tamagnone, C. Craeye, and J. Perruisseau-Carrier. Comment on reply to comment on encoding many channels on the same frequency through radio vorticity: first experimental test. *New Journal of Physics*, 15(7):078001, 2013.
- [JA8] M. Tamagnone, A. Fallahi, J. R. Mosig, and J. Perruisseau-Carrier. Fundamental limits and near-optimal design of graphene modulators and non-reciprocal devices. *Nature Photonics*, 8(7):556–563, 2014.

- [JA9] M. Tamagnone, J. S. Gomez-Diaz, J. R. Mosig, and J. Perruisseau-Carrier. Analysis and design of terahertz antennas based on plasmonic resonant graphene sheets. *Journal of Applied Physics*, 112(11):114915–4, 2012.
- [JA10] M. Tamagnone, J. S. Gomez-Diaz, J. R. Mosig, and J. Perruisseau-Carrier. Reconfigurable terahertz plasmonic antenna concept using a graphene stack. *Applied Physics Letters*, 101(21):214102–4, 2012.
- [JA11] M. Tamagnone, M. Martina, and G. Masera. An application specific instruction set processor based implementation for signal detection in multiple antenna systems. *Microprocessors and Microsystems*, 36(3):245–256, 2012.
- [JA12] M. Tamagnone, C. Moldovan, J.-M. Pouirol, A. B. Kuzmenko, A. M. Ionescu, J. R. Mosig, and J. Perruisseau-Carrier. Near optimal graphene terahertz non-reciprocal isolator. *Nature Communications*, 7, 2016.
- [JA13] M. Tamagnone and J. Mosig. Theoretical limits on the efficiency of reconfigurable and non-reciprocal graphene antennas. *IEEE Antennas and Wireless Propagation Letters*, PP(99):1–1, 2016.
- [JA14] M. Tamagnone and J. Perruisseau-Carrier. Predicting input impedance and efficiency of graphene reconfigurable dipoles using a simple circuit model. *Antennas and Wireless Propagation Letters, IEEE*, 13:313–316, 2014.
- [JA15] W. A. Vitale, C. F. Moldovan, M. Tamagnone, A. Paone, A. Schuler, and A. M. Ionescu. Steep-slope metal-insulator-transition vo2 switches with temperature-stable high i on. *Electron Device Letters, IEEE*, 36(9):972–974, 2015.
- [JA16] W. A. Vitale, M. Tamagnone, N. Emond, B. L. Drogoff, S. Capdevila, M. Chaker, J. R. Mosig, and A. M. Ionescu. Terahertz modulated scatterer technique enabled by current actuated vanadium dioxide switches. *Submitted*, 2016.

Conference Articles

- [CA1] E. Carrasco, M. Tamagnone, T. Low, M. Capstick, and J. R. Mosig. Mid-infrared reflectarrays based on an aperiodic graphene nanostrips array. In *10th European Conf. on Antennas and Prop (EuCAP 2016)*, 2016.
- [CA2] E. Carrasco, M. Tamagnone, T. Low, and J. R. Mosig. Dynamic reconfiguration of plasmonic reflectarrays using graphene: a review of the research led by prof. perruisseau-carrier. In *9th European Conference on Antennas and Propagation (EuCAP)*, number EPFL-CONF-209728, 2015.
- [CA3] E. Carrasco, M. Tamagnone, and J. Perruisseau-Carrier. Tunable graphene-based reflectarray element for reconfigurable beams. In *Antennas and Propagation (EuCAP), 2013 7th European Conference on*, pages 1779–1782. Ieee, 2013.
- [CA4] G. Gäumann, I. Crassee, N. Numan, J.-M. Poumirol, M. Tamagnone, J.-P. Wolf, and T. Feurer. High field terahertz spectroscopy on gated single layer graphene. In *5th EOS Topical Meeting on Terahertz Science & Technology (TST 2016)*, 2016.
- [CA5] H. Hasani, M. Tamagnone, S. Capdevila Cascante, C. F. Moldovan, M. A. Ionescu, C. Peixeiro, J. R. Mosig, and A. Skrivervik. Design, fabrication and characterization of terahertz reflectarrays based on a silicon substrate. In *International Conference on Metamaterials, Photonic Crystals and Plasmonics*, number EPFL-CONF-209723, 2015.
- [CA6] H. Hasani, S. Capdevila, M. Tamagnone, C. Moldovan, W. A. Vitale, A. M. Ionescu, C. Peixeiro, A. Skrivervik, and J. R. Mosig. Dual-band terahertz reflectarray integrated on a silicon substrate. In *ISAP 2016 (submitted)*, 2016.
- [CA7] C. F. Moldovan, W. A. Vitale, M. Tamagnone, J. R. Mosig, and A. M. Ionescu. Graphene quantum capacitors for high-q tunable lc-tanks for rf ics. In *ESSDERC 2016 (accepted)*, 2016.
- [CA8] C. F. Moldovan, K. Gajewski, M. Tamagnone, R. S. Weatherup, H. Sugime, A. Szumska, W. A. Vitale, J. Robertson, and A. M. Ionescu. Spatial variability in large area single and few-layer cvd graphene. In *Ultimate Integration on Silicon (EUROSIOI-ULIS), 2015 Joint International EUROSIOI Workshop and International Conference on*, pages 85–88. IEEE, 2015.

- [CA9] C. F. Moldovan, W. A. Vitale, M. Tamagnone, and A. Ionescu. Graphene rf nems shunt switches for analog and digital phase shifters. In *Solid-State Sensors, Actuators and Microsystems (TRANSDUCERS), 2015 Transducers-2015 18th International Conference on*, pages 2029–2032. IEEE, 2015.
- [CA10] J. R. Mosig, M. Tamagnone, and S. Capdevila Cascante. Graphene for antenna system applications at terahertz frequency range. In *Cambridge Graphene Centre Advanced Technology Lectures, Invited Talk*, number EPFL-TALK-209729, 2015.
- [CA11] J. Perruisseau-Carrier, J. S. Gomez-Diaz, E. Carrasco, M. Tamagnone, and A. Fallahi. Graphene nanophotonics methods and devices: what can we learn from the microwave field. In *Graphene Nanophotonics*, 2013.
- [CA12] J. Perruisseau-Carrier, M. Tamagnone, J. S. Gomez-Diaz, and E. Carrasco. Graphene antennas: Can integration and reconfigurability compensate for the loss? In *Microwave Conference (EuMC), 2013 European*, pages 369–372. Ieee, 2013.
- [CA13] J. Perruisseau-Carrier, M. Tamagnone, J. S. Gomez-Diaz, M. Esquius-Morote, and J. R. Mosig. Resonant and leaky-wave reconfigurable antennas based on graphene plasmonics. In *Antennas and Propagation Society International Symposium (APSURSI), 2013 IEEE*, pages 136–137. IEEE, 2013.
- [CA14] J. Poumirol, P. Liu, M. Tamagnone, C. F. Moldovan, J. Perruisseau-Carrier, J. Faist, and A. Kuzmenko. Electrically tunable terahertz magneto-absorption and faraday rotation in graphene. In *ImagineNano 2015*, number EPFL-CONF-209730, 2015.
- [CA15] P. Romano, M. Tamagnone, S. Capdevila Cascante, S. Rosset, H. Shea, and J. R. Mosig. Stretchable and transparent thz reflectarrays based on pdms. In *International Conference on Metamaterials, Photonic Crystals and Plasmonics*, number EPFL-CONF-209722, 2015.
- [CA16] M. Tamagnone. Gate-controlled mid-infrared light bending with aperiodic graphene nanoribbons array. In *Webinar IOP*, 2015.
- [CA17] M. Tamagnone, S. Capdevila, H. Hasani, P. Romano, A. Skrivervik, J. Perruisseau-Carrier, J. R. Mosig, W. A. Vitale, C. Moldovan, and A. M. Ionescu. Performance evaluation of novel technologies for terahertz reflectarrays. In *Microwave Integrated Circuits Conference (EuMIC), 2015 10th European*, pages 393–396. IEEE, Sept 2015.
- [CA18] M. Tamagnone, S. Capdevila, H. Hasani, W. A. Vitale, C. Moldovan, A. M. Ionescu, A. Skrivervik, and J. R. Mosig. Novel technologies for fixed and tuneable terahertz reflectarrays. In *10th European Conf. on Antennas and Prop (Eucap 2016)*, 2016.
- [CA19] M. Tamagnone, S. Capdevila, and J. R. Mosig. Numerical simulation and design of electromagnetic devices based on graphene. In *Graphene Flagship Workshop*, 2015.





- [CA20] M. Tamagnone, S. Capdevila Cascante, H. Hasani, C. F. Moldovan, M. A. Ionescu, A. Skrivervik, and J. R. Mosig. Evaluation of graphene for terahertz reflectarray antennas. In *Graphene Week 2015*, number EPFL-CONF-209719, 2015.
- [CA21] M. Tamagnone, J. S. G. Diaz, J. Mosig, and J. Perruisseau-Carrier. Hybrid graphene-metal reconfigurable terahertz antenna. In *2013 IEEE MTT-S International Microwave Symposium Digest (MTT)*, 2013.
- [CA22] M. Tamagnone, A. Fallahi, J. R. Mosig, and J. Perruisseau-Carrier. Theoretical limits of graphene terahertz non-reciprocal devices. In *9th European Conference on Antennas and Propagation (EuCAP)*, number EPFL-CONF-209727, 2015.
- [CA23] M. Tamagnone, A. Fallahi, and J. Perruisseau-Carrier. Theoretical upper bounds on the performance of graphene reconfigurable devices. In *Eucap 2014, 8th European Conf. on Antennas and Prop.*, number EPFL-CONF-198229, 2014.
- [CA24] M. Tamagnone, J. Gomez Diaz, J. Perruisseau-Carrier, and J. R. Mosig. High-impedance frequency-agile thz dipole antennas using graphene. In *Antennas and Propagation (EuCAP), 2013 7th European Conference on*, pages 533–536. Ieee, 2013.
- [CA25] M. Tamagnone, C. Moldovan, J.-M. Poumirol, A. B. Kuzmenko, A. M. Ionescu, and J. R. Mosig. Experimental demonstration of unidirectional terahertz waves propagation using graphene. In *META 2016 conference (accepted)*, 2016.
- [CA26] M. Tamagnone, C. Moldovan, J.-M. Poumirol, A. B. Kuzmenko, A. M. Ionescu, J. Perruisseau-Carrier, and J. R. Mosig. Experimental demonstration of a terahertz non-reciprocal isolator based on graphene. In *10th European Conf. on Antennas and Prop (Eucap 2016)*, 2016.
- [CA27] M. Tamagnone and J. Perruisseau-Carrier. A circuit model for reconfigurable graphene plasmonic dipoles. In *Eucap 2014, 8th European Conf. on Antennas and Prop.*, number EPFL-CONF-198237, 2014.
- [CA28] M. Tamagnone and J. Perruisseau-Carrier. Fundamental theoretical limits of graphene tunable and non-reciprocal devices. In *Graphene Conference*, number EPFL-CONF-198222, 2014.
- [CA29] M. Tamagnone and J. Perruisseau-Carrier. Reconfigurable graphene metasurfaces: determining and approaching theoretical upper bounds. In *META'14, 5th Intern. Conf. on Metamaterials, Photonic Crystals and Plasmonics*, number EPFL-CONF-198227, 2014.
- [CA30] M. Tamagnone, J. S. Silva, S. Capdevila, J. R. Mosig, and J. Perruisseau-Carrier. The orbital angular momentum (oam) multiplexing controversy: Oam as a subset of mimo. In *Antennas and Propagation (EuCAP), 2015 9th European Conference on*, pages 1–5. IEEE, 2015.

Conference Articles

- [CA31] W. A. Vitale, M. Tamagnone, N. Émond, B. Le Drogoff, S. Capdevila, A. Skrivervik, M. Chaker, J. R. Mosig, and A. M. Ionescu. Vanadium dioxide devices for energy efficient communications, sensing and energy harvesting in terahertz wireless sensor networks (wsn). In *E-MRS 2016 Spring Meeting*, 2016.
- [CA32] W. A. Vitale, M. Tamagnone, C. F. Moldovan, N. Émond, E. A. Casu, L. Petit, B. L. Drogoff, M. Chaker, J. R. Mosig, and A. M. Ionescu. Field-enhanced design of steep-slope vo₂ switches for low actuation voltage. In *ESSDERC 2016 (Accepted)*, 2016.

Michele Tamagnone

Ph.D. Student (Electrical Engineering)
Advisor: Prof. Juan Ramon Mosig (EPFL, LEMA)
Co-advisor: Prof. Adrian Mihai Ionescu (EPFL, NANOLAB)
Laboratory of Electromagnetics and Antennas
Institute of Electrical Engineering, School of Engineering,
Ecole Polytechnique Fédérale de Lausanne (EPFL), Switzerland.
ORCID : [0000-0002-9812-2449](https://orcid.org/0000-0002-9812-2449)

Contact  ELB-037, STI-IEL-LEMA, Station 11, EPFL, 1015 Lausanne, Switzerland
 +41 216932682
 +41 216932673
 michele.tamagnone@epfl.ch

Web <http://people.epfl.ch//michele.tamagnone>

Personal Born 18th of July 1986, Italian nationality
Speaks Italian, English, basic French
Has driving license

RESEARCH INTERESTS

Interdisciplinary topics at the frontier of Electromagnetics, Photonics and Solid State Physics

- Graphene for electromagnetic and nano-photonic applications, from microwaves to infrared
- Terahertz science and technology
- Micro-Nano technology and fabrication
- Reconfigurable systems, modulators and switches based on graphene and other 2DEGs
- Magneto-optics, non-reciprocal phenomena and one-way light propagation
- Vanadium dioxide for microwave and terahertz switches and metasurfaces
- Numerical methods for electrodynamics problems, including 2D materials based devices
- Quantum optics, classical and quantum information theory, quantum computing
- Tunable metamaterials and plasmonic systems
- Theoretical limits of photonic devices
- Flexible electronics for electromagnetic applications
- Multiple antenna systems (MIMO) and extensions to optics
- Structured light, orbital angular momentum of light
- Wave phenomena.

EDUCATION AND PROFESSIONAL EMPLOYMENT

Apr 2012 – Today	Ph.D. Student in Electrical Engineering <i>Ecole Polytechnique Fédérale de Lausanne (EPFL), Switzerland.</i> Advisor: Prof. Juan Ramon Mosig (EPFL, LEMA) Co-Advisor: Prof. Adrian Mihai Ionescu (EPFL, NANOLAB)
Jul 2010 – Mar 2012	Microprocessor HW and SW design <i>Auconel S.r.l. (Druento, Torino, Italy)</i>
Oct 2008 – Jul 2010	M.Sc. in Electrical Engineering (110/110 cum laude) <i>Polytechnic of Turin, Italy</i> <i>Polytechnic of Milan, Italy</i> , from double degree program <i>Alta Scuola Politecnica</i> <i>University of Illinois at Chicago (UIC)</i> , from double degree program <i>TOP-UIC</i>
Oct 2005 – Jul 2008	B.Sc. in Electrical Engineering (110/110 cum laude) <i>Polytechnic of Turin, Italy</i>

PROFESSIONAL ACTIVITY AND TEACHING

- Chair of convened session on “Applications of graphene and low dimensional materials” at EuCAP 2016 (European Conference on Antennas and Propagation)
- Journal Reviewing: *Applied Physics Letters*, *Antenna and Wireless Propagation Letters*, *IEEE Transactions on Terahertz Science and Technology*, *IEEE Transactions on Antennas and Propagation*, *Optical Materials Express*, *Superlattices and Microstructures*, *IEEE Communication Letters*, *Radioengineering*, *IET Electronics Letters*, *APL Photonics*.
- Conference reviewing: EuCAP 2015, META 2015, EuCAP 2016.
- Teaching assistant for the course *Rayonnement et Antennes* (Radiation and Antennas) at EPFL (2012/2013, 2013/2014 and 2014/2015)

RESEARCH PROJECTS

- **European Graphene Flagship:** European graphene Flagship (Contract No. CNECT-ICT-604391), Ramp up phase, Work Package 5 (Optoelectronics), task 5.5 (Long wavelength photodetectors): *Fabrication and characterization of graphene-based THz reflectarrays.*
- **Hasler Project n° 11149:** *Advanced Adaptive Electromagnetic Surfaces — Design and Micro/Nanotechnology Implementation.*
- **Swiss National Science Foundation , Project n° 133583:** *Reconfigurable Microwave Technology for Novel Telecom and Sensing Applications.*

ATTENDED DOCTORAL COURSES

- European School of Antennas (ESoA) Course “**Terahertz Technologies and Applications**”, Barcelona 4-8 June 2012, held by Prof. Luis Jofre et al, **passed**.
- EPFL doctoral course “**RF MEMS for communications applications**”, Doctoral School of Microsystems and Microelectronics, June 2012, held by Prof. Adrian M. Ionescu, **passed**.
- EPFL doctoral course “**Advanced topics in microwaves and antennas**”, Doctoral School of Electrical Engineering and Microelectronics, June 2013 held by Prof. Anja Skrivervik, and Dr. Zürcher Jean-François, **grade 6/6**.
- EPFL doctoral course “**Integral equations in Electromagnetics**”, Doctoral School of Electrical Engineering, July 2014 held by Prof. Juan R. Mosig, **grade 6/6**.
- EPFL doctoral course “**Advanced topics in electromagnetic compatibility**”, Doctoral School of Electrical Engineering, January 2016, held by Prof. Rachidi-Haeri Farhad, **grade 6/6**.
- EPFL doctoral course “**Quantum Information Theory and Computation**”, Doctoral School of Computer and Communication Sciences, Doctoral School of Photonics, January 2016 held by Prof. Nicolas Macris, **grade 6/6**.

AWARDS AND SCHOLARSHIPS

- *IEEE Antenna and Propagation Piergiorgio L. E. Uslenghi AWPL Prize Paper Award* (\$1000), 2015, For the paper “Predicting Input Impedance and Efficiency of Graphene Reconfigurable Dipoles Using a Simple Circuit Model”
- *Optime Prize* (Master of Science level) 2010 – 2011
For study merits promoted by Unione Industriale di Torino
- *TOP-UIC scholarship* (10'000\$) 2008 – 2010
For the tuition fees of University of Illinois at Chicago
- *Optime Prize* (Bachelor of Science level) 2008 – 2009
For study merits promoted by Unione Industriale di Torino
- *Physics Olympiad* 2005:
One of the ten winners of the Italian national competition and best experimental test.
- *Mathematical Olympiad* 2005:
Bronze medal at the Italian national competition.

CERTIFICATIONS (GRE, LANGUAGES, COMPUTER)

- GRE (Graduate Record Examinations) General Test (October 2011)

Verbal	160 / 170	Percentile: 86%
Quantitative	168 / 170	Percentile: 96%
Analytical Writing	3.5 / 6	Percentile: 38%

- GRE (Graduate Record Examinations) Subject Test Physics (October 2011)

Physics	990 / 990	Percentile: 95%
---------	-----------	-----------------

- English language certifications

Name	Score	Released by	Date
Preliminary English Test (PET)	Pass with Merit	University of Cambridge	March 2004
TOEFL Internet based	107/120	ETS	February 2010
IELTS	7.5/9	British Council	November 2011

- French language certification

Name	Score	Released by	Date
French Intensive Module A1	6 (Excellent)	EPFL Language Center	September 2012

- Computer Certifications

Name	Released by	Date
European Computer Driving License (ECDL)	CEPIS, AICA	April 2005

SOFTWARE

- Operating systems:** Windows, Linux, DOS
- Numerical EM/photonics softwares:** Ansys HFSS, CST (basics), Lumerical (basics), MWoffice
- Analysis tools:** Matlab & Simulink, Mathematica, OriginLab (basics), Modelsim, Orcad, P-Spice
- Layout editors:** Ledit, Cadence Virtuoso (basics), Orcad, Autocad, Layout Beamer
- Programming languages:** C, C++, NETC, VB 6.0, VB.NET, Visual Studio 2005, Matlab, Java, SQL, ASP.NET, Assembly 8x86, Assembly Freescale HCS12, Assembly PIC18, LabView
- Hardware description languages:** SystemC, VHDL
- Graphical Softwares:** Illustrator, Blender, POV-ray, GIMP, Inkscape, Autocad
- Miscellaneous:** Microsoft Office, LaTeX, Endnote, VMware

CLEAN ROOM AND EXPERIMENTAL SKILLS

- 18 months of clean room experience in the Center of MicroNanoTechnology (CMi) at EPFL. Fabrication of tunable graphene and vanadium dioxide terahertz and infrared metasurfaces, stretchable PDMS terahertz metamaterials and graphene quantum capacitors. Experienced in several fabrications techniques including:
 - Optical lithography (positive and negative resist, mask fabrication, lift-off)
 - E-beam lithography (PMMA, PMMA-MMA lift-off, ZEP, HSQ), Layout Beamer.
 - E-beam evaporation (metals and dielectrics) including shadow mask processes, Atomic Layer Deposition (ALD) for high-k dielectrics, sputtering, thermal annealing.
 - Dry etching (O₂ plasma graphene patterning, Si, oxides, metals)
 - Ion Beam Etching (IBE)
 - Focused Ion Beam (FIB) for device cross sections and direct graphene patterning.
 - Wet etching (Si, oxides, metals)
 - Wafer bonding (Anodic or parylene-based)
 - Polydimethylsiloxane (PDMS) processes for flexible electronics
 - Wafer dicing, PCB fabrication and wire-bonding.
- Experienced in several measurement and imaging setups including:
 - Angle resolved terahertz time domain spectroscopic setup with imaging stages
 - Standard optical microscopy (bright field / dark field)
 - Scanning electron microscopy (SEM)
 - Focused Ion Beam (FIB) imaging and patterning
 - Atomic Force Microscopy (AFM)
 - Mechanical profilometer
 - Thin film characterization via spectroscopic reflectometer and spectroscopic ellipsometer.
 - Fourier transform infrared spectroscopy (FTIR)
 - High vacuum cryogenic probe station for DC and RF on wafer measurement
 - Semiconductor device analyzer
 - Vector Network Analyzer (VNA)